Sami Kaappa

Analysis and Applications of Electronic Structure in Gold and Silver Nanoclusters

UNIVERSITY OF JYVÄSKYLÄ

FACULTY OF MATHEMATICS
AND SCIENCE

Sami Kaappa

Analysis and Applications of Electronic Structure in Gold and Silver Nanoclusters

Esitetään Jyväskylän yliopiston matemaattis-luonnontieteellisen tiedekunnan suostumuksella
julkisesti tarkastettavaksi yliopiston Ylistönrinteen salissa FYS1
syyskuun 13. päivänä 2019 kello 12.

Academic dissertation to be publicly discussed, by permission of
the Faculty of Mathematics and Science of the University of Jyväskylä,
in Ylistönrinne, auditorium FYS1, on September 13, 2019 at 12 o'clock noon.

JYVÄSKYLÄN YLIOPISTO
UNIVERSITY OF JYVÄSKYLÄ

JYVÄSKYLÄ 2019

Editors

Hannu Häkkinen

Department of Physics, Department of Chemistry, University of Jyväskylä

Timo Hautala

Open Science Centre, University of Jyväskylä

ABSTRACT

Gold and silver nanoclusters are understood as atomically precise particles that consist of a metal core of more than 2 atoms that are usually protected and stabilized by a monolayer of organic molecules; these molecules are called ligands. In this thesis, gold and silver nanoclusters are examined through their electronic structure at the level of density functional theory. New analytical methods are developed and applied by considering the symmetry of the clusters more thoroughly than before. Gold clusters incorporating a new type type of ligand, N-heterocyclic carbenes, are studied with computational methods to explain the experimental findings. The scanning tunnelling microscope image of a large ligand-protected, atomically precise silver cluster is analyzed with the help of density functional theory and a pattern recognition algorithm that has been developed for this study. The results and the new methods both produce a wider understanding of metal nanoclusters and pave the way for research of new types of ligand-protected metal nanoclusters and their applications.

Keywords: gold, silver, nanoclusters, symmetry, density functional theory, scanning tunnelling microscopy, N-heterocyclic carbenes

Author   Sami Kaappa
                          Department of Physics
                          Nanoscience Center
                          University of Jyväskylä
                          Finland

Supervisor   Academy Professor Hannu Häkkinen
                          Department of Physics
                          Department of Chemistry
                          Nanoscience Center
                          University of Jyväskylä
                          Finland

Co-Supervisor   University Researcher Sami Malola
                          Department of Physics
                          Nanoscience Center
                          University of Jyväskylä
                          Finland

Reviewers   Professor Christine M. Aikens
                          Department of Chemistry
                          Kansas State University

                          Professor Henrik Grönbeck
                          Department of Physics
                          Competence Centre for Catalysis
                          Chalmers University of Technology

Opponent   Associate Professor Nicola Gaston
                          Department of Physics
                          The University of Auckland

PREFACE

This thesis was written during the spring of 2019. It compiles and explains my main scientific research from the past three and half years, which I have spent working as a member of academy professor Hannu Häkkinen's research group at University of Jyväskylä. Two of the peer-reviewed publications in this thesis are works of only the people of Nanoscience Center in Jyväskylä, while the three others are accomplished in projects involving strong international collaboration.

My work is theoretical and computational research on nanometer-scale chemical particles that comprise cores of multiple Au or Ag atoms and protecting ligands on the exterior. These objects are called metal nanoclusters. During the work, I have enjoyed both the revelations of chemical and physical phenomena and their origins, and the development of the computational and analytical methods for the sake of better understanding of the fundamental essence and properties of metal nanoclusters.

<div align="right">

In Jyväskylä, August 12, 2019
Sami Kaappa

</div>

ACKNOWLEDGEMENTS

LIST OF ABBREVIATIONS

DFT	Density functional theory
KS	Kohn-Sham
LR-TDDFT	Linear-response time-dependent density functional theory
TD-DFPT	Time-dependent density functional perturbation theory
GPAW	Grid projector-augmented wave (code package)
PBE	Perdew-Burke-Ernzerhof exchange-correlation functional
LDA	Local density approximation
BEEF	Bayesian error estimation functional
vdW	van der Waals
TCM	Transition contribution map
$\mathbf{Y}_{lm}$	Spherical harmonics with quantum numbers l and m
NHC	N-heterocyclic carbene
iPr	isopropyl
Bn	Benzene
2-Np	2-Naphtyl
PET	Phenyl ethyl thiol
TBBT	Tert-butyl benzene thiol
HOMO	Highest occupied molecular orbital
LUMO	Lowest unoccupied molecular orbital
PDOS	Projected density of states
SPDOS	Symmetry projected density of states
SPM	Scanning probe microscopy
STM	Scanning tunnelling microscopy
LDOS	Local density of states
L-He, L-N	Liquid Helium and liquid Nitrogen

LIST OF FIGURES

LIST OF TABLES

CONTENTS

LIST OF INCLUDED ARTICLES

PI   Rosalba Juarez-Mosqueda, **Sami Kaappa**, Sami Malola, Hannu Häkkinen. Analysis of the Electronic Structure of Non-Spherical Ligand-Protected Metal Nanoclusters: The Case of a Box-like Ag_{67}. *The Journal of Physical Chemistry C*, **121**(20), 10698-10705, (2016).

PII   **Sami Kaappa**, Sami Malola, Hannu Häkkinen. Point Group Symmetry Analysis of the Electronic Structure of Bare and Protected Metal Nanocrystals. *The Journal of Physical Chemistry A*, **122**(43), 8576-8584, (2018).

PIII Mina R. Narouz, Kimberly M. Osten, Phillip J. Unsworth, Renee W.Y. Man, Kirsi Salorinne, Shinjiro Takano, Ryohei Tomihara, **Sami Kaappa**, Sami Malola, Cao-Thang Dinh, J. Daniel Padmos, Kennedy Ayoo, Patrick J. Garrett, Masakazu Nambo, J. Hugh Horton, Edward H. Sargent, Hannu Häkkinen, Tatsuya Tsukuda, Cathleen M. Crudden. N-Heterocyclic carbene-functionalized magic number gold nanoclusters. *Nature Chemistry*, **11**(5), 419-425, (2019).

PIV   Mina R. Narouz, Shinjiro Takano, Paul A. Lummis, Tetyana I. Levchenko, Ali Nazemi, **Sami Kaappa**, Sami Malola, Seyedehgoonay Yousefalizadeh, Kevin G. Stamplecoskie, Hannu Häkkinen, Tatsuya Tsukuda, Cathleen Crudden. N-Heterocyclic carbene-stabilized Au_{13} superatom clusters. *ChemRxiv*, doi:10.26434/chemrxiv.7498748, (2018).

PV   Qin Zhou, **Sami Kaappa**, Sami Malola, Hui Lu, Dawei Guan, Yajuan Li, Haochen Wang, Zhaoxiong Xie, Zhibo Ma, Hannu Häkkinen, Nanfeng Zheng, Xueming Yang, Lansun Zheng. Real-space imaging with pattern recognition of a ligand-protected Ag_{374} nanocluster at sub-molecular resolution. *Nature Communications*, **9**(1), 2948, (2018).

In article [PI], the author carried out the jellium calculations, developed the projection algorithm and code, developed the selection rules, performed the atomistic calculations on the predicted structures, and participated in writing the draft. He developed the point group symmetry analysis algorithm and code, carried out all the calculations, and prepared the first draft of [PII]. In [PIII] and [PIV], the author carried out all the DFT calculations excluding the NMR simulations, and contributed in writing the drafts regarding the computational parts. In [PV], the author developed the pattern recognition algorithm and code, carried out all the calculations except the simulation of the line scan, and participated in writing the draft. The author has also contributed to the following publications:

LIST OF OTHER ARTICLES

API   Mohammad J. Alhilaly, Megalamane S. Bootharaju, Chakra P. Joshi, Tabot M. Besong, Abdul-Hamid Emwas, Rosalba Juarez-Mosqueda, **Sami Kaappa**, Sami Malola, Karim Adil, Aleksander Shkurenko, Hannu Häkkinen, Mohamed Eddaoudi, Osman M. Bakr. $[Ag_{67}(SPhMe_2)_{32}(PPh_3)_8]^{3+}$: Synthesis, Total Structure, and Optical Properties of a Large Box-Shaped Silver Nanocluster. *The Journal of American Chemical Society*, **138**(44), 14727–14732, (2016).

APII   Liane S. Slaughter, Kevin M. Cheung, **Sami Kaappa**, Huan H. Cao, Qing Yang, Thomas D. Young, Andrew C. Serino, Sami Malola, Jana M. Olson, Stephan Link, Hannu Häkkinen, Anne M. Andrews and Paul S. Weiss. Patterning of supported gold monolayers via chemical lift-off lithography. *Beilstein Journal of Nanotechnology*, **8**, 2648–2661, (2017).

APIII   Cunfa Sun, Nisha Mammen, **Sami Kaappa**, Peng Yuan, Guocheng Deng, Chaowei Zhao, Juanzhu Yan, Sami Malola, Karoliina Honkala, Hannu Häkkinen, Boon K. Teo, Nanfeng Zheng. Atomically Precise, Thiolated Copper–Hydride Nanoclusters as Single-Site Hydrogenation Catalysts for Ketones in Mild Conditions. *ACS Nano*, **13**(5), 5975–5986, (2019).

APIV   Hui Shen, Guocheng Deng, **Sami Kaappa**, Sami Malola, Boon K. Teo, Hannu Häkkinen, Nanfeng Zheng, Tongde Tan, Yinzi Han, Shuichao Lin. Highly Robust but Surface-Active: N-Heterocyclic Carbene-Stabilized Au_{25} Nanocluster as a Homogeneous Catalyst. *ChemRxiv*, Preprint online. doi:10.26434/chemrxiv.8015651 (2019).

APV   Sami Malola, **Sami Kaappa**, Hannu Häkkinen. The Role of Nanocrystal Symmetry in the Crossover Region from Molecular to Metallic Gold Nanoparticles. *The Journal of Physical Chemistry C* (Just Accepted) doi:10.1021/acs.jpcc.9b05863 (2019)

1   INTRODUCTION

By speaking of metal nanoclusters in general, we speak about a large and diverse set of molecules with 2 or more metal atoms where the valence electrons of the metal atoms form shell structures similar to that of an atom. Gold and silver nanoclusters are often found in well-defined geometries, surrounded by stabilizing ligands of organic, inorganic or halide nature [1, 2, 3, 4, 5]. In contrast, metal nanoparticles are understood as individual metal structures with ill-defined or varying atomic structures which nevertheless are usually formed in a beautiful crystal lattice geometry [6, 7, 8, 9]. Nanoparticles are often characterized only by their size distribution and the properties are usually scalable with the size of the particle, whereas in nanoclusters this is not the case but at least the atomically-precise composition is known, often also the atomic structure. Another distinctive feature between metal nanoparticles and clusters is the electronic structure, which is metal-like in particles (no gap between occupied and unoccupied electronic states) and molecule-like in clusters. In nanoclusters, a change of 1 in the metal atom count may therefore alter the stability and optical properties of the system extremely in a similar way as in organic molecules. An example of a widely studied cluster $[Au_{25}(PET)_{18}]^-$ (PET = phenyl ethyl thiol) is illustrated in fig. 1.

The intriguing chemical and optical properties of metal nanoclusters have awaken an ever-growing field of applications, including catalytic activity [10, 11, 12, 13, 14, 15, 16], chemical sensing [17, 18, 19, 20], biolabelling [21, 22, 23], solar cell technology [24, 25, 26, 27] and imaging [28, 29] among others.

The history of nanocluster research is not too old, although the soluble, "colloidal" gold is known to have been used in medical purposes in the Middle Ages [6]. The atomic precision of phosphine-protected nanoclusters was achieved in late 1960s [30, 31], whereas the first thiol-protected Au cluster was crystallized only in 2007, as the crystal structure of $Au_{102}(p\text{-MBA})_{44}$ (p-MBA = para-mercapto benzoic acid) was resolved by Kornberg et al. by
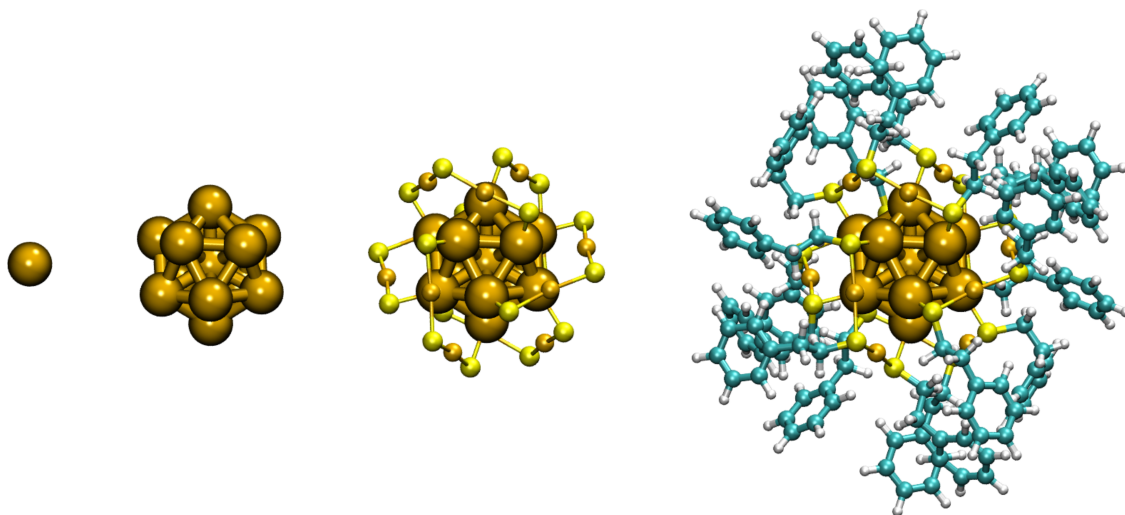
FIGURE 1 Structure of $[Au_{25}(PET)_{18}]^-$ (PET=phenyl ethyl thiol). The icosahedral gold core is formed around the central Au atom. The S-Au-S units are bound to the gold core. The alkyl chains are bonded to sulphur atoms. Colors: Golden Au, Yellow S, Cyan C, White H.

x-ray crystallography [32].

As noted in the famous study of Knight et al. [33], small metal clusters have systematically specific atom counts in which they appear more abundant than in the other atom counts. These numbers are called magic numbers and they are understood in the same way as the most stable electron numbers for individual atoms: once a special number of electrons is achieved, both the ionization energy and the electron affinity are highly increased and the system lies in a relaxed state. If a single electron is added to the atom, the system becomes unstable and the extra electron can be lost with only a little effort. It is found that the *aufbau* principle that sets the occupation order of electron states in atoms is also obeyed in sodium clusters as noted already by Knight et al. Also structural magic numbers have been used to explain the abundance of certain atom counts [34]. This thinking is based on completing shells of atoms in certain geometries, such as icosahedra or cuboctahedra.

This thesis regards ligand-protected gold and silver clusters. The relation to sodium, which was the target of studies for Knight et al., is that also gold and silver have a single *s*-electron at the highest occupied electron energy level. In addition to the electrostatic potential of the nuclei, the most substantial difference between gold and silver is the underlying atomic electron states such as the next highest *d*-electrons that also have their effect to the interactions of the atoms to their chemical environment. The effect of *d*-electrons becomes emergent for example in Au-Ag mixed-metal clusters [35, 36, 37] where the metal atoms do not behave equally since the *d*-levels lie deeper in energy in Ag than in Au. The electron configuration of silver and gold are thus $[Kr]4d^{10}5s^1$ and $[Xe]4f^{14}5d^{10}6s^1$, respectively. In the solid state, the single valence electron is shared among the other metal atoms

which results in metallic properties of the solids, such as conductivity and shininess. A similar phenomenon is understood in metal clusters where the s-electrons are delocalized inside the metal core, and in that case the wave functions of electrons inherit the symmetry of the atomic structure. In mathematical terms, this is because the eigenfunctions of the Hamiltonian belong to the same symmetry group as the Hamiltonian itself, as is explained in section 2.2.2.

Whereas the metallic valence electrons delocalize over the metal core, the binding of protecting ligands to the surface of the core can decrease the number of delocalized electrons by their covalent bonding. In 2008, it was realized [38] that also the ligand-protected nanoclusters obey the magic number series with a simple formula of

$$n_c = N_m - N_l - q \qquad (1)$$

where the number of delocalized core electrons n_c is obtained by subtracting the number of electrons N_l withdrawn by ligands and the total charge of the cluster q from the number of valence electrons of the metal N_m. In addition to s-electrons, the superatom model has been applied to d-electrons of transitions metal clusters [39].

As said, the original idea of superatoms [33] leans heavily on the approximation of bare metal clusters as spherically symmetric objects. In perfectly spherical potential such as a jellium[1] sphere, the electrons follow the occupation order relative to that of atoms [42]: As the number of electrons is increased in the system, 1S is filled first with 2 electrons and then 1P with 6 electrons due to degeneracy of the P-states. The beginning of the series shows as 1S, 1P, 1D, 2S, 1F, 2P, 1G, and so forth, and the corresponding magic numbers are 2, 8, 18, (20,) 34, (40,) 58... with weaker magic numbers in brackets as they are relatively close in energy to the next shell filling. That is, the whole idea of magic numbers is based on the degeneracy of some states due to symmetry. As of the notation, it is a common practice that the superatom states are written in capital letters (1S, 1P etc.) that correspond to their atomic counterparts in lowercase letters. The number of the notation gives the number of radial maxima and minima of the function, while the letter refers to the number of angular nodes, $l = 0, 1, 2, \ldots$, in the series of spherical harmonics that are denoted as Y_{lm}.

A long-used method to resolve the symmetries of the electron wave functions in nanoclusters is to project the functions to spherical harmonics [38, 43, 44, 45]. If we can assume that the delocalized electrons in metal cores form trajectories close to shapes of spherical harmonics, the advantage of the projection is thus in determining which shells are occupied in the spherical notation (1S, 1P, ...). This information is shown to be a powerful tool

---

[1] Jellium means simple modelling of metals as homogeneous positive background charge that has predicted properties of simple metals quite accurately despite its simplicity [40, 41]. The only parameter in jellium model is the density of the background charge.

in explaining the electronic stability of ligand-protected metal clusters. For example, in $[Au_{13}(PH_3)_{10}Cl_2]^{3+}$ [38] and $[Au_{25}(SR)_{18}]^-$ [46], the highest occupied states show clear P-type shape whereas the lowest unoccupied states are of D-type ($l = 1$ and $l = 2$ in Y_{lm} notation, respectively). That is, due to symmetry these states are near to degenerate and a stabilizing gap between the occupied and unoccupied states is formed.

Many of the nanoclusters appear with highly symmetrical metal cores, for example $[Au_{13}(PR_3)_{10}Cl_2]^{3+}$ [47], $Au_{25}(SR)_{18}$ [48] and its silver analogue $Ag_{25}(SR)_{18}$ [49], $Au_{38}(SR)_{24}$ [50], $Au_{144}(SR)_{60}$ [51], and the cubic clusters in ref. [52], just to mention few. However, the electronic structures of all these clusters have been systematically analyzed in terms of spherical symmetry. Once the crystal structure of the silver cluster $[Ag_{67}(SPhMe_2)_{32}(PPh_3)_8]^{3+}$ was resolved [53] and identified to possess the cuboidal shape, we took a different approach and considered the box-like shape in the analysis; this is presented in article [PI]. The methodology introduced there is valid only for box-shaped systems, and therefore we continued the work on non-spherical systems in article [PIII] where we utilized group theory in order to characterize the wave functions by their shapes. A direct application of the symmetry representations of the single-electron wave functions that we suggest in the article makes the simulations of optical spectra more efficient for highly symmetric molecules.

In history, the most studied Au and Ag clusters with ligand protection are protected with thiols [54, 48, 49, 50, 32, 51, 49, 35] and/or phosphines [55, 56, 47, 57, 53, 58, 59]. Also alkynyl ligands [60, 61, 62] have been shown to act as stabilizing monolayers on metal particles. In terms of delocalized valence electrons, thiols that stabilize the surface of nanoclusters are considered as electrophiles that reduce the number of superelectrons according to equation 1. The bond between phosphine and gold is considered as electron-neutral, whereas the halides as well as alkynyls are electrophiles, localizing some of the valence electrons of the metal to the bond. In articles [PIII] and [PIV], we report the atomically precise structures of N-heterocyclic carbene stabilized Au nanoclusters which is the first time for clusters including more than three Au atoms [63]. Considering this thesis, I will present our computational results on the respective clusters that were obtained using the density functional theory and that strongly support the experimental findings.

Nanoclusters can be realized with various methods experimentally. Mass spectrometry is used to evaluate the chemical composition of molecules. The x-ray diffraction (XRD) methods are used to resolve the atomic structure of the cluster in the crystallized form directly; success of XRD is a high-priority wish also for a computational scientist since the atomic structure contains much of the information that is required for reliable theoretical work on the system. Nuclear magnetic resonance spectroscopy can be used to probe chemical bonds or existence of certain atoms in the molecule. For

example, in article [PIII], NMR was used to verify the existence of the Au-C bond before the crystal structure was attained, and in reference [64] NMR could be utilized in predicting the existence of hydride in the copper core of $[Cu_{25}H_{10}(SR)_{18}]^{3-}$ that could not be seen in the crystal structure. In contrast, imaging of nanoclusters with real-space methods, such as scanning probe microscopy (SPM) has shown to be an extremely difficult task. This is due to the high curvature of small particles and the physical size of the scanning tip, leading to convolution effects that reduce the resolution of imaging. In this thesis, I will present our work on the successful scanning tunnelling microscopy (STM) of $Ag_{374}(TBBT)_{113}Br_2Cl_2$ (TBBT = tert-butyl benzene thiol) nanocluster at sub-molecular resolution and our theoretical work therein that is originally reported in article [PV].

My work on nanoclusters has thus been theoretical via computational modelling. Considering the sizes and numbers of electrons, the mostly used computational modelling method in nanocluster research is the density functional theory (DFT). The theory leans on the formulation of Kohn and Sham [65] where the electrons are modelled in a non-interacting potential that produces the same electron density as the real, interacting potential. The theory can also be cast in the time-dependent (TDDFT) form, which can be used to follow the response of the system to external perturbations such as electromagnetic radiation. The use of TDDFT is beneficial in that it provides straightforward data to be compared to experimental data that is easy and efficient to obtain for solvated clusters.

There are a couple of direct approximations that are assumed while modelling nanoclusters with DFT. Most commonly the solvation is excluded although this might have some effects on stability [66] or even optical response of molecules [67, 68]. In some studies, the large thiols are reduced to smaller ligands in simulations to achieve smaller computational cost [69, 70, 71] although this approach is becoming less relevant for small systems as computational methods and machinery become more efficient. In the works concerning this thesis, the solvents are not taken into consideration, and calculations on the atomistic model of $[Ag_{67}(SR)_{32}(PR_3)_8]^{3+}$ in article [PI] and on $Au_{108}S_{24}(PR_3)_{16}$ in article [PII] were performed with smaller ligands than with which the cluster was actually synthesized and characterized to achieve less computational requirements for the calculation. The approximation that is built in DFT machinery is the analytically unsolved form of the functional that describes the non-Coulombic interactions between electrons, but this is discussed more in section 2.1.2.

This thesis is constructed as follows: In chapter 2, the theoretical methodology of my work is represented and discussed. In chapter 3, I will go through the results of the articles of this thesis with slightly deeper touch than what is reported in the published articles. Finally, chapter 4 summarizes and presents conclusions regarding my work, and future perspectives of the field of nanocluster research are offered. At the end of this book, the

published articles are reprinted.

2   THEORETICAL BACKGROUND

Chemical elements can be examined at different levels of theory of which the density functional theory (DFT) is a widely used compromise between accuracy and computational efficiency [72, 73, 74, 75, 76]. We use DFT to model metal nanoclusters comprising of up to 374 metal atoms and the 117 protecting ligands [PV]. In this chapter, I will go through the computational methods including fundamentals of DFT simulations and the analytical machinery that I used in the research of this thesis and the underlying theoretical considerations.

2.1   Density functional theory

There are numerous well-written derivations for the density functional theory, and therefore I will only provide the minimal formulation of the theory and exclude the fine details. The reader is guided to refs. [73, 76] for further information.

2.1.1   Formulation

According to the postulates of quantum mechanics, the total energy of any system is obtained as an eigenvalue of the Hamiltonian operator $\hat{H}$. For electrons interacting in an external potential, the eigenvalue problem of the total energy can be written as

$$\hat{H}\Psi = \left(\hat{T} + \hat{V}_{\text{ext}} + \hat{W}\right)\Psi = E\Psi \tag{2}$$

where $\hat{T}$ is the kinetic energy operator, $\hat{V}_{\text{ext}}$ is the external potential and $\hat{W}$ describes the interaction between electrons. The eigenvectors (Ψ) of this equation are termed as wave functions. Generally, the only varying term in Eq. 2 is the external potential $\hat{V}_{\text{ext}}$; the kinetic energy term and the electron-electron interaction term always have the same form. The problem in solving eq. 2 is that the equation is a second order differential equation with

solutions Ψ of dimension 3N due to three coordinates for each of the N electrons. DFT tackles this problem so that the wave function Ψ can eventually be separated to N functions with 3 dimensions which are vastly easier to solve.

The density functional theory is based on the Hohenberg-Kohn (HK) theorem which states that there is a unique mapping between the external potential of the system and the ground state density [77]. The ground state is understood as the state that corresponds to the smallest eigenvalue E. A straightforward conclusion can be drawn that all the properties of an electron system can be derived from the ground state electron density.

The Kohn-Sham (KS) approach acknowledges the importance of the correct ground state electron density and aims to produce it by introducing a new Hamiltonian

$$\hat{H}_s = \hat{T} + \hat{V}_s \tag{3}$$

with no electron-electron interaction term [65]. The potential $\hat{V}_s$ is considered in such a way that the reference Hamiltonian $\hat{H}_s$ produces the same ground state density as the Hamiltonian with the real potential in Eq. 2. This way, Eq. 3 can actually be separated for each individual state since there are no interactions between the electrons but they only exist in a new external potential. The separation leads us to the so-called Kohn-Sham equations for single-particle states [65]

$$\left(-\frac{1}{2}\nabla^2 + v_s(\mathbf{r}) \right) \phi_i(\mathbf{r}) = \varepsilon_i \phi_i(\mathbf{r}), \tag{4}$$

$$n(\mathbf{r}) = 2 \sum_{i=1}^{N/2} |\phi_i(\mathbf{r})|^2 \tag{5}$$

where $v_s(\mathbf{r})$ is the potential for a single electron, and ε_i and $\phi_i(\mathbf{r})$ are the eigenenergies and eigenstates of the single-electron Hamiltonian, that is the operator on the left-hand side of the equation 4. The most essential variable in DFT, that is the ground state density $n(\mathbf{r})$, is given by Eq. 5. In equations 4 and 5, the spin-degeneracy was already taken into account by assuming that two electrons occupy a state with exactly the same energy but with antiparallel spins; this is why the factor 2 appears and the summation is taken to only half of the number of electrons N. The advantage of introduction of $\hat{V}_s$ is evident here, as equation 4 is a second order differential equation of only 3 dimensions with contrast to the 3N-dimensional Schrödinger equation 2. Here, as well as in the following formulations, the atomic units are used in the equations, taken that $m = \hbar = e^2/(4\pi\varepsilon_0) = 1$ where m is the electron mass.

The problem is still to determine the potential $\hat{V}_s$ which was introduced by moving from the interacting picture to the non-interacting one. Let us write the expectation value of $\hat{T}$ in the single-particle basis Φ_s (i.e. eigenfunctions

of the Hamiltonian in Eq. 3) as

$$T_s = \langle \Phi_s | \hat{T} | \Phi_s \rangle . \tag{6}$$

Now let us define the exchange-correlation energy E_{xc} as the difference in kinetic and electron interaction energy between the interacting and non-interacting systems:

$$E_{xc} = (T - T_s) + (W - E_H) \tag{7}$$

where E_H is the Hartree energy, corresponding to the classical Coulombic interaction, that has

$$E_H = \frac{1}{2} \int d\mathbf{r} d\mathbf{r}' \frac{n(\mathbf{r}) n(\mathbf{r}')}{|\mathbf{r} - \mathbf{r}'|} . \tag{8}$$

In equation 7, all the terms are functionals of the electron density. Taking the functional derivative of that equation with respect to $n(\mathbf{r})$ gives [73]

$$v_s = v_0 + v_H + v_{xc} \tag{9}$$

where each potential v targets a single-particle state in equation 4, and v_0 acts as the real external potential. Finally, the exchange-correlation potential is defined as

$$v_{xc}(\mathbf{r}) = \frac{\delta E_{xc}}{\delta n(\mathbf{r})} . \tag{10}$$

The two latter equations complete the Kohn-Sham equations that can be used to calculate the properties of any electron system self-consistently once either the exchange-correlation energy E_{xc} or potential v_{xc} is specified.

2.1.2 Exchange-correlation functionals

The exchange-correlation (xc) effect can be thought of as a hole in the probability density that an electron creates in the vicinity of itself. The exchange part of this contribution can be realized by looking into a non-interacting system and denoting that the probability of two like-spin particles occupying the same position at the same time is 0; this can be considered as a consequence of the Pauli exclusion principle. The correlation part of E_{xc} is defined as including all the other correlations between the electrons, but the analytical form for these effects is not known.

The simplest model for exchange and correlation effects of electrons is offered by the local density approximation (LDA). It assumes slowly-varying density in that the density is locally uniform, i.e. its gradient is taken to be zero everywhere. The total xc-energy can therefore be written as a functional of the electron density n as

$$E_{xc}^{LDA} = \int d\mathbf{r}\, n(\mathbf{r}) \varepsilon_{xc}(n(\mathbf{r})) \tag{11}$$

where the density can be considered as a weight for the single-electron xc-energies $\varepsilon_{xc}(n(\mathbf{r}))$ that depend on the density only locally. The exchange part of ε_{xc} can be determined analytically [73] to be

$$\varepsilon_x^{\text{LDA}}(n(\mathbf{r})) = -\frac{3}{4}\left(\frac{3}{\pi}\right)^{1/3} n(\mathbf{r})^{1/3}, \tag{12}$$

and an example of a widely used LDA correlation functional is constructed by Perdew and Wang [78]. In contrast, if the gradient of the density is accounted for to the first order, the energy can be written as [79, 80]

$$E_{xc}^{\text{GGA}} = \int d\mathbf{r}\, f(n(\mathbf{r}), \nabla n(\mathbf{r})) \tag{13}$$

which is a functional of both the density and the gradient of the density at each point in space. The acronym GGA stands for generalized gradient approximation.

2.1.2.1 PBE

In this work, a GGA method called PBE [81] after its founders Perdew, Burke and Ernzerhof was mainly used. The derivation for the form of E_{xc}^{PBE} lies on satisfying some known limits and tendencies: the limits of slowly and rapidly varying densities, the scaling of the correlation energy to a constant under uniform scaling of the density in the high-density limit ($n(\mathbf{r}) \to \lambda^3 n(\lambda\mathbf{r})$ with $\lambda \to \infty$), the scaling of exchange energy to λ under the same scaling of n, correct spin-scaling, repeating LDA results for nearly-uniform density scaling, and the Lieb-Oxford bound which states that

$$E_{xc} \geq -1.679 \int d\mathbf{r}\, n^{4/3}. \tag{14}$$

The functional that obeys all of these requirements is given as

$$E_{xc}[n_+, n_-] = E_x[n_+, n_-] + E_c[n_+, n_-] \tag{15}$$
$$= \int d\mathbf{r}\, n\, \varepsilon_x^{\text{unif}}(n) F_x(s) + \int d\mathbf{r}\, n\left(\varepsilon_c^{\text{unif}}(r_s, \xi) + H(r_s, \xi, t)\right)$$

where unif refers to uniform electron gas and subscripts $+$ and $-$ denote the two spin states. The exchange enhancement factor $F_x(s)$ has the form of

$$F_x(s) = 1 + \kappa - \kappa/(1 + \mu s^2/\kappa) \tag{16}$$

with $\kappa = 0.804$ and s as a dimensionless density gradient $s = |\nabla n|/2k_F n$ with $k_F = (3\pi^2 n)^{1/3}$. The gradient-dependent part of the correlation energy, H, is written as

$$H = (e^2/a_0)\gamma\phi^3 \ln\left[1 + (\beta/\gamma)t^2 \frac{1 + At^2}{1 + At^2 + A^2t^4}\right], \tag{17}$$

where

$$A = \frac{\beta}{\gamma\left(\exp\left(-\varepsilon_c^{\text{unif}}/(\gamma\phi^3 e^2/a_0)\right) - 1\right)} \tag{18}$$

and $a_0 = \hbar^2/me^2$, $\beta = 0.066725$ and $\gamma = 0.031091$ are constants, and $\phi(\xi) = [(1+\xi)^{2/3} + (1-\xi)^{2/3}]/2$ is a spin-scaling factor that is a function of the relative spin polarization $\xi = (n_+ - n_-)/n$. The function t is another dimensionless gradient factor with $t = |\nabla n|/2\phi k_s n$, where $k_s = (4k_F/\pi a_0)^{1/2}$. The argument r_s in eq. 15 refers to Seitz radius and is just another form of the density as $r_s = (4\pi n/3)^{1/3}$. In the articles of this thesis, mostly spin-paired calculations are carried out with $n_+ = n_-$ everywhere, resulting in $\xi = 0$ and $\phi(\xi = 0) = 1$. The correlation energy per particle $\varepsilon_c^{\text{unif}}$ is considered "well-established" [81] and used as such as derived in ref. [78].

PBE is probably the most cited functional in the history of DFT due to the compromise for its generality, accuracy and computational simplicity. The systems considered in this thesis comprise of heavy metal atoms in different oxidation states covered with thiols, phosphines, halides and organic molecules. We use PBE due to its ability to model these kind of diverse systems where only metal–metal and covalent bonds dominate the systems with no strong electron correlations. The number of electrons in the system is also quite high for *ab initio* calculations, so a computationally light functional is mandatory to perform the calculations in reasonable times.

2.1.2.2 Bayesian Error Estimation Functional BEEF

Van der Waals (vdW) interactions are not generally described by the simplest xc-functionals. As many nanoclusters have large pi-conjugated ligands as the protecting layer, it is reasonable to ask whether these long-range interactions are important on the stability and properties of the clusters.

In the article considering the NHC-protected Au_{13} clusters [PIV], the xc-functional called BEEF-vdW [82] (Bayesian Error Estimation Functional with van der Waals) was used to include the vdW interactions into the xc-functional. The BEEF-vdW is built in inspiration of machine learning techniques combining multiple functionals and training the parameters in multiple data sets. The form of the exchange energy relies on the general form of exchange in GGA approaches as

$$E_x^{\text{GGA}}[n, \nabla n] = \int d\mathbf{r}\, \varepsilon_x^{\text{unif}}(n)\, F_x(s) \tag{19}$$

similar to PBE. In BEEF-vdW, the exchange enhancement factor F_x is described as an expansion in 30 Legendre polynomials in BEEF-vdW; the coefficients for the expansion are acquired via machine learning techniques by teaching various data sets to the functional. The correlation energy is a combination of LDA [78], PBE [81] and a functional called vdW-DF2 [83] that is invented to describe the van der Waals effects accurately. The form for the

global correlation energy is thus

$$E_c = \alpha_c E_c^{\text{LDA}} + (1 - \alpha_c) E_c^{\text{PBE}} + E_c^{\text{vdW-DF2}} \tag{20}$$

which brings an extra parameter α_c to the total xc-energy. A total of 31 parameters are then optimized while training the functional with various training sets.

Also BEEF-vdW is fabricated to describe many different types of interactions between atoms (covalent, metallic, long-range etc.), making it an appealing functional for our needs. The computational cost therein is mostly limited by the in-built vdW-DF2 functional.

2.1.3 Linear response time-dependent density functional theory

In the articles of this thesis, the optical response of nanoclusters was modelled in linear response time-dependent density functional theory (LR-TDDFT) using Casida's formalism [84]. An alternative for the LR-TDDFT that operates in frequency-space is the real-time propagation TDDFT [85, 86] where the Kohn-Sham wave functions are straightforwardly propagated in time in an external electric field. However, we wish to characterize single peaks of the optical spectra in terms of the Kohn-Sham states which is possible via the transition contribution map analysis, explained in section 2.1.4.

The linear-response formalism is based on matrix Ω that is calculated as

$$\Omega_{ip,jq} = \delta_{i,j}\delta_{p,q}(\varepsilon_q - \varepsilon_j)^2 + 2\sqrt{(f_i - f_p)(\varepsilon_p - \varepsilon_i)}K_{ip,jq}\sqrt{(f_j - f_q)(\varepsilon_q - \varepsilon_j)} \tag{21}$$

where the subscripts i, j and p, q refer to occupied and unoccupied Kohn-Sham states, respectively. The transition coupling matrix K has elements of

$$K_{ip,jq} = \int d\mathbf{r}d\mathbf{r}' \, \Phi_{ip}(\mathbf{r}) f_{Hxc}(\mathbf{r}, \mathbf{r}') \Phi_{jq}^*(\mathbf{r}') \tag{22}$$

where Φ is the pair density, containing the product of Kohn-Sham wave functions ϕ as

$$\Phi_{ip}(\mathbf{r}) \equiv \phi_i^*(\mathbf{r})\phi_p(\mathbf{r}) \tag{23}$$

and the kernel f_{Hxc} contains the Hartree and exchange-correlation parts as

$$f_{Hxc}(\mathbf{r}, \mathbf{r}') = f_H(\mathbf{r}, \mathbf{r}') + f_{xc}(\mathbf{r}, \mathbf{r}') = \frac{1}{|\mathbf{r} - \mathbf{r}'|} + \left.\frac{\delta v_{xc}[n](\mathbf{r}, \mathbf{r}')}{\delta n}\right|_{n_0}. \tag{24}$$

The eigenvalue problem of Ω is subsequently solved as

$$\Omega F = \omega^2 F \tag{25}$$

that produces a set of (squared) eigenfrequencies $\{\omega_I^2\}$ and a respective set of eigenvectors $\{F_I\}$ that are used in composing the optical spectrum as

$$f_I = \frac{2}{3}\sum_{j,q}(f_q - f_j)(\varepsilon_q - \varepsilon_j)\left|F_I^{jq} \, \vec{\mu}_{jq}\right|^2 \tag{26}$$

that offers the oscillator strengths f_I at respective energies ω_I. Here f_i and ε_i are the occupation number and the energy of the ith Kohn-Sham state, respectively. The factor μ_{jq} contains the dipole moment for a transition $j \rightarrow q$ as

$$\vec{\mu}_{jq} = -e \int d\mathbf{r} \, \phi_q^*(\mathbf{r}) \, \hat{\mathbf{r}} \, \phi_j(\mathbf{r}) \tag{27}$$

2.1.4 Optical transition analysis

Simulations of optical spectra of molecules is offered by the LR-TDDFT formalism, and individual electron-hole transitions could be examined directly from the data therein. However, we wish to look at distinct spectral features and the contributions from all transitions to them. To do this, we use the implementation of time-dependent density functional perturbation theory (TD-DFPT) [87] and transition contribution map (TCM) technique that was originally developed to study the origin of plasmons in gold nanoclusters [70].

The theory is based on the time-dependent Kohn-Sham equations with a small perturbation that in our case describes the effect of the electromagnetic field. The transition contribution map (TCM) is written as a function of the two energy axes of occupied and unoccupied energies, and the numerical delta peaks of the electron-hole transitions are broadened with Gaussian kernels for both axes. The function of TCM is written as [70]

$$
TCM(\varepsilon_{\mathrm{occ}}, \varepsilon_{\mathrm{unocc}}) = \sum_i^{\mathrm{occ}} \sum_p^{\mathrm{unocc}} \left| C_{ip}^{\omega,\mathrm{abs}} \right|^2 \times \exp\left[-\left(\frac{\varepsilon_{\mathrm{occ}} - \varepsilon_i}{\Delta\varepsilon} \right)^2 \right] \tag{28}
$$

$$
\times \exp\left[-\left(\frac{\varepsilon_{\mathrm{unocc}} - \varepsilon_p}{\Delta\varepsilon} \right)^2 \right],
$$

where $\varepsilon_{\mathrm{occ}}$ and $\varepsilon_{\mathrm{unocc}}$ are the energy axes of occupied and unoccupied states, respectively, ε_i and ε_p are the energies of the states between which the $i \to p$ transition occurs, and $\Delta\varepsilon$ is the Gaussian broadening parameter. The exponential functions are introduced only to broaden the squared absorption intensity coefficients $C_{ip}^{\omega,\mathrm{abs}}$, that are written as

$$
C_{ip}^{\omega,\mathrm{abs}} = \sqrt{\Delta n_{ip}} \left(C_{ip}^{\omega,\mathrm{Im}} - C_{ip}^{-\omega,\mathrm{Im}} \right). \tag{29}
$$

Here Δn_{ip} is the occupation difference between occupied state i and unoccupied state p, and $C_{ip}^{\omega,\mathrm{Im}}, C_{ip}^{-\omega,\mathrm{Im}}$ are matrix elements of the supervectors that are solutions to the linear equation of [87]

$$
\begin{pmatrix} \tilde{E} + K\tilde{N} + \omega & K\tilde{N} & -\eta & 0 \\ K\tilde{N} & \tilde{E} + K\tilde{N} - \omega & 0 & -\eta \\ \eta & 0 & \tilde{E} + K\tilde{N} + \omega & -K\tilde{N} \\ 0 & \eta & -K\tilde{N} & \tilde{E} + K\tilde{N} - \omega \end{pmatrix} \begin{pmatrix} C^{\omega,\mathrm{Re}} \\ C^{-\omega,\mathrm{Re}} \\ C^{\omega,\mathrm{Im}} \\ C^{-\omega,\mathrm{Im}} \end{pmatrix}
$$

$$
\tag{30}
$$

$$
= \begin{pmatrix} -\mu^{\mathrm{laser}} \\ -\mu^{\mathrm{laser}} \\ 0 \\ 0 \end{pmatrix}.
$$

Here, $\tilde{E}_{pi,qj} = (\varepsilon_q - \epsilon_j)\delta_{ij}\delta_{pq}$ is the energy difference of the Kohn-Sham states, K is the K-matrix from the Casida formalism, already encountered in

eq. 22, $\tilde{N}_{pi,qj} = (n_j - n_q)\delta_{ij}\delta_{pq}$ is the occupation difference of the Kohn-Sham states, η is the Lorentzian spectral broadening parameter (that is included for numerical stability), and

$$\mu_{q,j}^{\text{laser}} = -e\hat{r}_{\text{laser}} \cdot \int d\mathbf{r}\, \phi_q^*(\mathbf{r})\mathbf{r}\, \phi_j(\mathbf{r}) \tag{31}$$

is the dipole moment of the transition between states q and j.

2.1.5 GPAW: Real-space grid implementation

When DFT is implemented in chemical applications, that is in systems with multiple atoms, a problem arises due to the requirement for the orthogonality of all the Kohn-Sham wavefunctions. This is due to the electron states in very low energies (core states of atoms) that are confined in very small volumes compared to the size of the system; To require orthogonality of the respective wave functions we would have to use either very fine grid or a huge set of basis functions.

The calculations presented in this thesis were carried out using the code GPAW [88, 89], which is a real-space grid implementation of DFT that uses the projector-augmented wave (PAW) method [90] to overcome the core electron issue.

In the PAW formalism, the all-electron wave functions are obtained from a linear transformation

$$|\Psi_n\rangle = \hat{T}\,|\tilde{\Psi}_n\rangle \tag{32}$$

that maps the smoothly behaving auxiliary wave function $\tilde{\Psi}_n$ to the true one. We require the transformation to be applied only inside a pre-determined augmentation sphere with radius R^a for atom a to obtain the smoothly behaving core states. Therefore we have the transformation operator defined through partial waves $|\phi_i^a\rangle$, smooth partial waves $|\tilde{\phi}_i^a\rangle$ and projector functions $|p_i^a\rangle$ as [90]

$$\hat{T} = 1 + \sum_a \sum_i (|\phi_i^a\rangle - |\tilde{\phi}_i^a\rangle)\,\langle p_i^a|. \tag{33}$$

These functions are also pre-determined for each atom a, requiring that inside the augmentation sphere $\tilde{\phi}_i^a$ is smooth and outside the sphere we have the condition

$$\tilde{\phi}_i^a(\vec{r}) = \phi_i^a(\vec{r}) \tag{34}$$

so that the transformation is only unity in that region by eq. 33. Also, the projector functions are fully localized inside the augmentation sphere.

Once we know how to construct Ψ_n, we define the core electron densities inside the augmentation sphere and their smooth counterparts for each atom and use them to construct the all-electron density. Also, compensation charges are added to the smooth charge density inside the augmentation spheres to fix the norm-conservation that is not built-in in $\tilde{\Psi}_n$. The final

atom-specific piece of the PAW total energy is the correction to the Kohn-Sham potential to make the effective potential smooth inside the augmentation spheres. With these elements, the difficult behaviour of the core states is compensated, and the electron density, effective potential and total energy of a system can be determined as in DFT scheme.

GPAW is a real-space grid implementation of the PAW method, and the implementation is simple: The wave functions, densities and potentials are represented as discrete scalar fields at the grid, and their derivatives are calculated with finite difference methods. The integrals of the 3D functions become only sums over the grid points.

2.1.6   Jellium

The word jellium refers to a simple way of modelling metals and their electronic structure and properties. In a jellium system, the lattice of atoms is modelled as a homogeneous background charge where the electrons are confined to. Due to the lack of atomic positions, only the valence electrons that in real systems are strongly delocalized in the metal atomic lattice are taken into consideration. Note that this type of a model system is used to construct the LDA approximation for the exchange-correlation functional as explained in section 2.1.2.

In GPAW framework, we calculate the electronic ground states of finite jellium systems by introducing the size, shape, location and charge density of the positive background charge via the Poisson solver that is used to solve the contributions of Coulombic interactions to the total energy within the unit cell. The electrons that we want to model are then inserted into the system simply by the total charge keyword in the GPAW calculator (see manual for GPAW [89]). That is, if we want to examine an 8-electron jellium system, we set `charge=-8`. To obtain an electronically neutral system, the density of the background charge must then be set in such a way that it integrates to +8(e).

2.2 Group theory in chemistry

This section explains the fundamentals of group theory and the basic information required to implement group theory in chemistry. More thorough theory and ideas are offered by references [91, 92].

2.2.1 Introduction to group theory

In general, group theory describes groups of abstract elements which obey the following rules [91]:

1. Closure: if a and b are members of a group, then $c = ab$ is also a member of the same group

2. Associativity: if a, b and c are members of the same group, then $a(bc) = (ab)c$

3. Unit element: A group contains an element a for which $ab = ba = b$ for each b of the group

4. Inverse: For element a of the group, there is an inverse of that element in the group so that $a^{-1}a = 1$ where 1 stands for the unit element

In this context, the multiplication operation can be, for example, multiplication, sum, dot product, or anything that can bind any two elements and produce a new element of that group. Thus, the interelement operation is a property of the group so that each rule above is satisfied. Especially, a group can consist of matrices, and, essentially in molecular chemistry, matrices that describe rotations in 3-dimensional space. The multiplication operation between these group members is the ordinary matrix multiplication.

For example, point group D_5 consists of 10 rotational transformations: the trivial transformation that does nothing, 2 antiparallel rotations of $2\pi/5$ radians around the z axis, 2 antiparallel rotations of $4\pi/5$ radians around the z axis, and 5 rotations of π radians around axes that are perpendicular to z and have equivalent angles ($2\pi/5$) between each other. The symmetry axes of a shape which belongs to the point group D_5 are shown in figure 2 (the images are generated using VMD software [93]). The notation of C_n gives the symmetry axis with respect to rotations of $2\pi/n$ rad.

To determine the crystallographic point group of a molecule, we seek for all coordinate transformations that keep the atomic configuration of the molecule invariant. These transformations, or the corresponding 3x3 matrices, form a group. A special matrix that is included in each point group is the unit matrix which satisfies the third requirement of a group as described above. For later purposes, we define a class of group elements. By definition, two elements T_1 and T_2 of group G belong to the same class if there
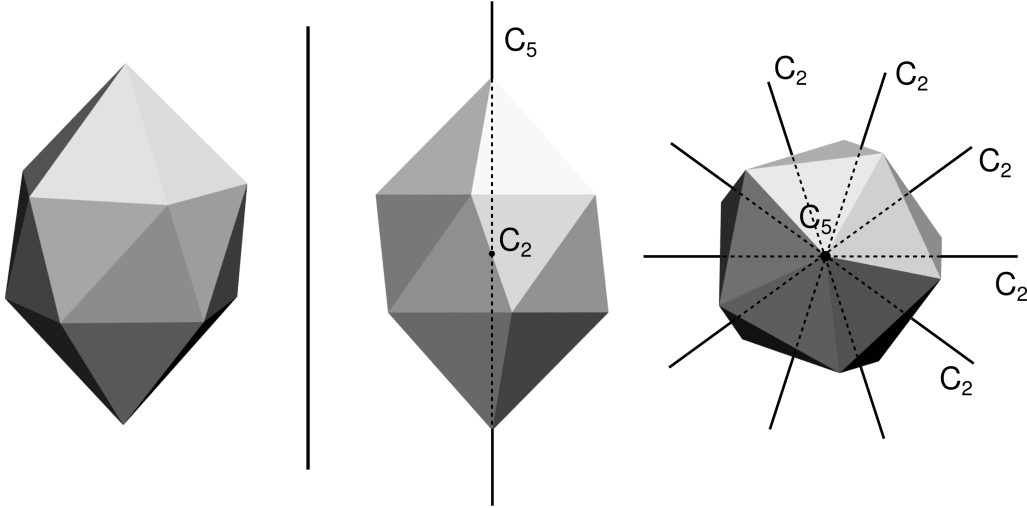
FIGURE 2   Illustration of a particle which transforms in point group D_5. Left, the shape of the particle is shown. In the middle, the particle is shown from a perspective along one of the C_2 axes. The main axis (C_5) axis is shown. On right, the shape is shown from perspective along the C_5 axis, and each of the C_2 axes are shown.

exists an element $X \in G$ that has

$$T_1 = X T_2 X^{-1}. \tag{35}$$

In D_5 group, the trivial operator forms its own class (as in every point group), and the 2 rotations of $2\pi/5$, 2 rotations of $4\pi/5$ and 5 rotations of π form distinct classes.

To make use of a point group, we define the representations of a group as all possible sets of matrices that have the same multiplication table as the group members with the condition

$$M(T_1)M(T_2) = M(T_1 T_2) \quad \forall\, T_1, T_2 \in G_1 \tag{36}$$

where M is the mapping between the two groups: $M : G_1 \rightarrow G_2$ and T_1 and T_2 are members of group G_1. A multiplication table includes the results of multiplications between each two group members. Due to the closure requirement above, the table elements are also members of the group. If a representation consists of $d \times d$ matrices, the representation is then d-fold degenerate. It can be shown [91] that a point group has infinitely many representations, but they can be built only of a few which are called irreducible representations. That is, the irreducible representations act as a basis of a group that can be linearly combined to obtain any representation of the group.

To continue with our example of point group D_5, let us introduce its irreducible representations. The representation A_1 consists of 1×1 matrices with elements of 1, so it trivially satisfies the same multiplication table as the rotational matrices that correspond to the rotations explained above.

TABLE 1 Explanations of shorthand notations for symmetry representations of point groups.

A, B	Single degeneracy
E	Double degeneracy
T	Triple degeneracy
G	Quadruple degeneracy
H	5-fold degeneracy
Subindices 1,2	Symmetric, Antisymmetric with respect to (i) π rad rotation around secondary axis or (ii) vertical mirroring
Prime, double-prime	Symmetric, Antisymmetric with respect to horizontal mirroring
Subindices g, u	*gerade*, *ungerade*: Symmetric, Antisymmetric with respect to inversion

The second representation, A_2, is also 1-dimensional but they consist of elements 1 and -1. It can be verified by building the multiplication table that the π rad rotations along the secondary axes correspond to the elements of -1 and the others have 1. The notations A_1 and A_2 are explained in table 1. The other two representations of group D_5 are 2-dimensional, that is they consist of 2×2 matrices. The first one, E_1, has the following matrices:

$$E = \begin{pmatrix} 1 & 0 \\ 0 & 1 \end{pmatrix} \tag{37}$$

$$C_{5,1} = \begin{pmatrix} \cos\left(\frac{2\pi}{5}\right) & -\sin\left(\frac{2\pi}{5}\right) \\ \sin\left(\frac{2\pi}{5}\right) & \cos\left(\frac{2\pi}{5}\right) \end{pmatrix}, C_{5,2} = \begin{pmatrix} \cos\left(\frac{2\pi}{5}\right) & \sin\left(\frac{2\pi}{5}\right) \\ -\sin\left(\frac{2\pi}{5}\right) & \cos\left(\frac{2\pi}{5}\right) \end{pmatrix} \tag{38}$$

$$C_{5,1}^2 = \begin{pmatrix} \cos\left(\frac{4\pi}{5}\right) & -\sin\left(\frac{4\pi}{5}\right) \\ \sin\left(\frac{4\pi}{5}\right) & \cos\left(\frac{4\pi}{5}\right) \end{pmatrix}, C_{5,2}^2 = \begin{pmatrix} \cos\left(\frac{4\pi}{5}\right) & \sin\left(\frac{4\pi}{5}\right) \\ -\sin\left(\frac{4\pi}{5}\right) & \cos\left(\frac{4\pi}{5}\right) \end{pmatrix} \tag{39}$$

$$C_{2,1}' = \begin{pmatrix} \cos\left(\frac{4\pi}{5}\right) & \sin\left(\frac{4\pi}{5}\right) \\ \sin\left(\frac{4\pi}{5}\right) & -\cos\left(\frac{4\pi}{5}\right) \end{pmatrix} C_{2,2}' = \begin{pmatrix} \cos\left(\frac{8\pi}{5}\right) & \sin\left(\frac{8\pi}{5}\right) \\ \sin\left(\frac{8\pi}{5}\right) & -\cos\left(\frac{8\pi}{5}\right) \end{pmatrix}, \ldots \tag{40}$$

where E refers to the trivial element, C_5 to a $2\pi/5$ rotation around the main axis and C_2' to π rotations around a secondary axis. The second subindices distinguish between the different elements of the classes. The series of C_2' continues with three more matrices with different arguments of the *sin* and *cos* based on the rotation axis. The final representation E_2 is very similar to E_1 but still orthogonal to the other representations. The multiplication tables for E_1 and E_2 can naturally be verified to be similar to the transformations of the group.

2.2.2 Symmetry representations of wave functions

The first important theorem of group theory concerning quantum mechanics is that the coordinate transformations that leave the stationary Hamilto-

TABLE 2 Character table for point group D_5.

	E	$2\,C_5$	$2\,(C_5)^3$	$5\,C_2'$
A_1	1	1	1	1
A_2	1	1	1	−1
E_1	2	$2\cos(2\pi/5)$	$2\cos(4\pi/5)$	0
E_2	2	$2\cos(4\pi/5)$	$2\cos(2\pi/5)$	0

nian invariant form a group that satisfies all the requirements above. The second important theorem implies that degenerate eigenfunctions of the Hamiltonian form a basis for a representation of the group of the Hamiltonian, that is, a single irreducible representation can be assigned to an eigenvalue of the Hamiltonian. These theorems are proven e.g. in ref. [91].

Then, how to determine the corresponding representations for a wave function? The basis functions of a d-dimensional representation Γ of group G are defined as $\psi_1(\vec{r}), \psi_2(\vec{r}), \ldots, \psi_d(\vec{r})$ for which the transformations $P(T)$ give a linear combination [91]

$$P(T)\psi_n(\vec{r}) = \sum_{m=1}^{d} \Gamma(T)_{mn}\psi_m(\vec{r}) \tag{41}$$

with coefficients that are the matrix elements of $\Gamma(T)$. Actually, the matrices $\Gamma(T)$ have still only of the coefficients of the linear combination, but it can be shown that the sets of these matrices can be considered as representations of group G. The equation 41 can be inversed to have

$$\Gamma(T)_{nn} = \frac{1}{N} \int d\vec{r}\, \psi_n^{\dagger}(\vec{r})\, P(T)\, \psi_n(\vec{r}) \tag{42}$$

for basis functions normalized to N. From eq. 42 we see that the diagonal elements of the representation matrices can be obtained from the overlap integral of the wave function and its transformation. In fact, this is exactly how we determine the representations for the wave functions in article [PII].

Moreover, the matrices that form the representations of a group can be reduced to their traces (sums of diagonal values) that are called characters, to construct a character table. In a character table, the rows correspond to different representations and for each column, the characters of representations for a single coordinate transformation are given. It is convenient to present character tables in a class-collected form, such as the one in table 2 for group D_5, which means that the elements are grouped to classes. Thus, each class is shown as a single column which is possible because each class member has the same set of characters, as can be seen from eqs. 38, 39 and 40.

Character tables have some useful properties. Considering the form of the table where the elements are not collected to classes, the rows are orthonormal to each other and they normalize to the order of the group that is the

number of group elements. Also, the number of irreducible representations equals to the number of classes which makes the (class-collected) character table a square matrix. Therefore, any vector whose length equals to the number of rows of the character table can be described as a linear combination of the rows. Another property of the table is that the sum of the squares of the degeneracies of representations (first column of the character table) equals to the number of elements in the group.

Our target is to assign symmetry representations to the Kohn-Sham states that correspond to eigenvalues and eigenfunctions of the non-interacting Hamiltonian as introduced in the formalism of the density functional theory. This can be done by considering the wave functions as bases for representations of the point group of the atomic structure. For a wave function, we apply each transformation of the group and calculate the overlap integrals as in eq. 42. The overlap integrals form a vector which we reduce by combining the overlaps to classes as in constructing the character table; after that, we have a vector whose length corresponds to the dimension of the character table. The vector is then written as a linear combination of the rows of the table and coefficients for different irreducible representations are obtained. If the molecular system is close enough to symmetry of the point group, high single coefficients are achieved and a single representation can be assigned to a wave function.

2.2.3 Selection rules

The representations of Kohn-Sham states can be used to devise selection rules for optical transitions in molecules. If ψ_i^r and ψ_j^p are functions that transform as representations Γ^r and Γ^p, respectively, and Q^q is an operator that transforms as representation Γ^q, the Wigner-Eckart theorem states that

$$\int \mathrm{d}\vec{r}\, \psi_i^r Q^q \psi_j^p = 0 \tag{43}$$

if Γ^r does not appear in the reduction of $\Gamma^p \otimes \Gamma^q$ ([91], p.99). The "appearance" is described later. The product $\otimes$ between representations is called direct product that gives another representation $\Gamma^{p\otimes q}$ of the same group whose characters χ are given directly by the characters of Γ^p and Γ^q [91]:

$$\chi(T) = \chi^p(T)\chi^q(T). \tag{44}$$

The vector of χ's can be reduced to single irreducible representations as

$$\Gamma^p \otimes \Gamma^q = \Gamma^{p\otimes q} = \sum_{i=1}^{n} C_i^{p\otimes q}\Gamma^i \tag{45}$$

where C_i are coefficients and Γ^i are the irreducible representations of the group. For example, for D_5 group, the following direct products apply:

$$A_2 \otimes A_2 = A_1 \tag{46}$$
$$A_2 \otimes E_1 = E_1 \tag{47}$$
$$E_1 \otimes E_1 = A_1 \oplus A_2 \oplus E_2 \tag{48}$$
$$E_1 \otimes E_2 = E_1 \oplus E_2 \tag{49}$$
$$A_1 \otimes \Gamma^i = \Gamma^i \tag{50}$$

that is, the direct product of any representation with A_1 gives the same representation, since its characters are only multiplied by one. The sum of representations is notated by symbol $\oplus$ which indicates that the representation is not described by only one irreducible representation but many, and we say that these irreducible representations appear in the reducible representation.

The perturbation of an electromagnetic wave can be described via a field vector $\vec{k}$ that can be considered to transform as some representation in each point group. In D_5, the representations for functions $f_x(x,y,z) = x$, $f_y(x,y,z) = y$ and $f_z(x,y,z) = z$ are E_1, E_1 and A_2, respectively. Therefore, a general function that describes $\vec{k}$ as

$$g_{\vec{k}}(x,y,z) = \hat{r}(x,y,z) \cdot \vec{k} = k_x x + k_y y + k_z z \tag{51}$$

with constants $k_x, k_y, k_z \neq 0$ has a representation of $\Gamma(g) = E_1 \oplus A_2$. For example, let us consider ψ_j^p that transforms as E_2 in group D_5. The direct product between ψ_j^p and g then gives

$$\Gamma(\psi_j^p) \otimes \Gamma(g) = E_2 \otimes (E_1 \oplus A_2) \tag{52}$$
$$= (E_2 \otimes E_1) \oplus (E_2 \otimes A_2)$$
$$= E_1 \oplus E_2 \oplus E_1.$$

That is, the reduction of $\Gamma(\psi_j^p) \times \Gamma(g)$ does not contain representations A_1 and A_2, indicating that transitions $E_2 \to A_1$ and $E_2 \to A_2$ are dipole forbidden in point group D_5 (Eq. 43). As the rules can be determined for each representation $\Gamma(\psi_j^p)$, we can tabulate the dipole selection rules as in table 3 for group D_5. The utilization of the dipole selection rules in LR-TDDFT calculations is described and discussed later in section 3.1.3.

TABLE 3 Dipole selection rules for point group D_5. The ones and zeros denote allowed
and forbidden transitions, respectively.

	A_1	A_2	E_1	E_2
A_1	0	1	1	0
A_2	1	0	1	0
E_1	1	1	1	1
E_2	0	0	1	1

2.3 Bader charge analysis

As atoms are put together to form molecules, their electron distribution is
perturbed in that some atoms become more electrically positive and some
become more negative than they are as free atoms. In DFT, the electron dis-
tribution, or density, is the function that describes the whole system and
determines its properties. To examine how the density is changed among
the atoms of the system compared to free atoms, we use the Bader charge
analysis and its grid-based, so-called near-grid implementation [94, 95, 96].

The idea of the analysis is quite simple and intuitive. It relies on assigning
the grid points to each atom where the division is based on the zero-flux
surfaces in the density. The total charge of an atom is then given by inte-
grating (or summing over grid points) the electron density at the assigned
points. In the near-grid method, the lattice-bias error that occurs in more
simple methods is fixed by refining the boundaries of the volumes assigned
to different atoms.

2.4 Tersoff-Hamann method

In article [PV], we performed simulations of scanning tunnelling micro-
scope (STM) images on a nanoparticle. The simulations were run according
to Tersoff-Hamann method, named after its founders [97], as implemented
in the Atomic Simulation Environment (ASE) package [98, 99]. The deriva-
tion of the method begins with the so-called Bardeen's formalism for the
tunnelling current between the tip and the sample as

$$I = \frac{2\pi e}{\hbar} \sum_{\mu,\nu} f(E_\mu)[1 - f(E_\nu + eV)] |M_{\mu\nu}|^2 \delta(E_\mu - E_\nu) \tag{53}$$

where μ and ν refer to the tip and the sample, respectively, $f(E)$ is the Fermi
function, or occupation at energy E and $M_{\mu\nu}$ is the tunnelling matrix ele-
ment between tip and sample states μ and ν, respectively. Acting in low
temperatures, the Fermi functions become step-like.

The problem is then to evaluate $M_{\mu\nu}$. According to Bardeen's tunnelling

theory, it has

$$M_{\mu\nu} = \frac{\hbar^2}{2m} \int d\mathbf{S} \cdot (\psi_\mu^* \nabla \psi_\nu - \psi_\nu \nabla \psi_\mu^*) \tag{54}$$

where the integrand is merely the current density. Tersoff and Hamann then showed that after expanding the sample wave functions in k-space and representing the tip wave functions as spherical objects, the formulation for the current is reduced to the form of

$$I \propto \sum_{E_\nu < E_F - eV}^{E_\nu < eV} |\psi_\nu(\mathbf{r}_0)|^2 \tag{55}$$

where $\mathbf{r}_0$ is the position of the midpoint of the tip and V is the applied voltage. That is, the right hand side of equation 55 has the local density of states (LDOS) which is calculated based on the occupied states whose energies are above eV (this is true for $V < 0$; for $V > 0$, unoccupied states are used). This formulation is called the *s*-wave approximation due to neglecting the possibility of angular dependence of the tip wave functions.

To evaluate the currents from the LDOS according to eq. 55, we need a conversion factor between those quantities. The approximations that we do are the same that are introduced by Hofer et al. [100]: (i) The tunnelling current passes through a circular cross section with 2 Å radius, (ii) the wave functions decay in the same way as the electron states at the Fermi level of metal surface with work function of 4 Å, and (iii) we set $\psi_\nu = \psi_\mu$ in eq. 54. Naturally, we also expect that there are no chemical phenomena occuring between the tip and the sample. In this work, the isovalues of the LDOS were therefore transformed into current by relation

$$I(\mathbf{r}) = (5000\, n(\mathbf{r}))^2 \tag{56}$$

so that the density $n(\mathbf{r})$ is given in units of Å^{-3} and thus the current is obtained in nanoamperes. Thus, it is true that these approximations are quite crude considering that we model STM images of an organic layer of ligands that surround a metallic nanoparticle. However, we assume that the detailed structure of images is not required, as the comparison of the simulated and experimental images is reduced to comparison of the extremum coordinates of the data. The comparison algorithm is discussed in the next section.

2.5 Pattern recognition in topographic data

The problem that we addressed in article [PV] was that we wanted to simulate the STM image of the $Ag_{374}(SR)_{113}Br_2Cl_2$ nanocluster, but we did not know about the orientation in which the particle resided on the surface. To resolve that, we developed an algorithm that compares sets of topographic

data with each other and calculates single-valued distances between the images. Simply put, the algorithm fits the coordinates of the local maxima and minima in the contour maps and calculates the mean distance of the resulting nearest neighbours.

The algorithm in its full form can be set as follows:

```
E := Experimental image
Cᵢ := Simulated image with index i
We start with i = 0.
```

$E := $ Experimental image
$C_i := $ Simulated image with index i
We start with $i = 0$.

1. Apply Gaussian smoothing for E and C_i.
2. Find N_{max} local maxima and N_{min} local minima of E and save the coordinates to containers S_E^{max} and S_E^{min}.
3. Find M_{max} local maxima and M_{min} local minima of C_i and save the coordinates to S_i^{max} and S_i^{min}.
4. Set $X_i^{min} = \infty$
5. Translate coordinates of S_E^{max} and S_E^{min} so that the coordinates of the total maximum coordinates of E are shifted to origin.
6. Translate coordinates of S_i^{max} and S_i^{min} so that the coordinates of the total maximum coordinates of C_i are shifted to origin.
7. Find nearest neighbours between sets S_E^{max} and S_i^{max} and make a paired array P_i of those.
8. Find nearest neighbours between sets S_E^{min} and S_i^{min} and append the pairs to P_i.
9. Fit the pairs of coordinates, i.e. minimize the root mean square (RMS) distance between them by rotations and translations.
10. Calculate the RMS distance between the fit coordinates and save it to X_i.
11. Set $X_i^{min} = min(X_i, X_i^{min})$.
12. Rotate C_i by 1/50 of the full circle and continue to step 5 until the full circle is regarded.
13. Save X_i^{min}.
14. Go to the next simulated image, i.e. increase i by 1 and continue from step 1 until all images are compared to E.

In this way, we reduce the problem of comparing two images to comparison of two sets of coordinates which is computationally much faster and also simpler. Mathematically this means that we do not try to fit two functions $f(x, y)$ and $g(x, y)$ and determine their distance, but we fit coordinates of sets $F = \{[x_1, y_1], [x_2, y_2], [x_3, y_3] \dots\}$ and $G = \{[\tilde{x}_1, \tilde{y}_1], [\tilde{x}_2, \tilde{y}_2], [\tilde{x}_3, \tilde{y}_3] \dots\}$ and calculate the distance between F and G.

The first stage is to apply Gaussian convolution to the images. The smoothing is done for the experimental images in order to remove the artefacts of the imaging such as scratch-like patterns that are due to the movement of the tip; see figure 3a. For the simulated images, the smoothing is done in order to remove the discrete cusps in the contour, that result from the numerical method of implementing the Tersoff-Hamann method, and in that way take into account the imperfection of the experimental image that are caused by the tip convolution effects. If the smoothing was not done for the simulated images, the local minima and maxima would exist in positions where they certainly can not exist in the experimental STM image. The effect of the Gaussian smoothing is illustrated in figure 3.

The parameters N_{max}, N_{min}, M_{max} and M_{min} are chosen is such a way that the most descriptive extremum points of the experimental data are sought. "The most descriptive" means that we search the extremum points in the middle area of the image since the tip convolution effect is more significant at the edges of the cluster due to its curvature. From the simulated images, we thus obtain more local extremum coordinates from which we finally end up with the nearest neighbours to the experimental set of points. This means that $N_{max} < M_{max}$ and $N_{min} < M_{min}$. In article [PV] we used $N_{max} = 10$, $N_{min} = 3$, $M_{max} = 20$, and $M_{min} = 20$.

The translation of the top point coordinates on top of each other ensures that we compare reasonable pairs of coordinates. The top coordinates are fixed because we expect that the topmost point of the nanocluster image is the most accurately determined site of the system, since the tip convolution effects are minimal there.

The search for the nearest neighbours was implemented through the `KDTree` package of the Scientific Python library `scipy` [101]. The minimization of the distance between two sets of coordinates was done using the algorithm introduced by Arun et al. [102]. Since the fitting algorithm requires fixed pairs of coordinates, we have to minimize the obtained distances in the case of a single simulated image with respect to rotations around the topmost coordinates to go through all the possible pairs of coordinates. The whole script can be downloaded from the web link http://r.jyu.fi/uNF .
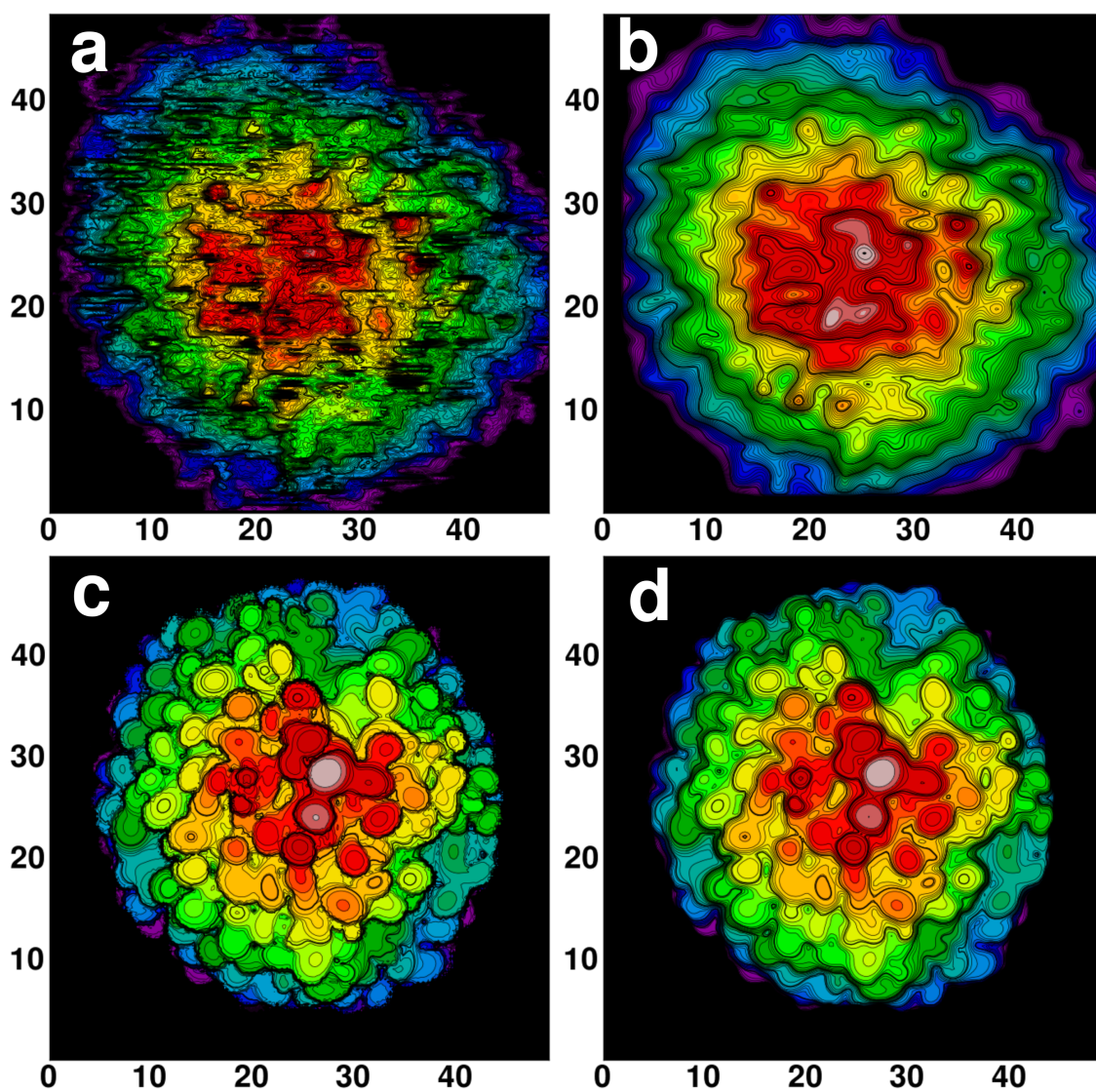
FIGURE 3 Effect of Gaussian smoothing on STM images. (a) Original experimental STM image. (b) Experimental image with Gaussian smoothing. (c) Original simulated STM image. (d) Simulated image with Gaussian smoothing.

3 RESULTS

I will go through the results of articles [PI], [PII], [PIII], [PIV] and [PV] in this particular order. The theoretical analysis of the box-shaped cluster Ag_{67} [PI] gave birth to motivation to study the symmetries of the metal nanoclusters in more detail in article [PII]. Once the first Au cluster (with more than 3 metal atoms) incorporating N-heterocyclic carbene ligands was synthesized and analyzed in article [PIII], the study was straightforwardly continued to article [PIV] where the analysis of tridecagold Au-NHC clusters was continued also with the aid of the symmetry analysis. The scanning tunnelling microscope images of silver cluster Ag_{374} are simulated and analyzed in article [PV].

3.1 Role of symmetry in nanoclusters

3.1.1 Projection to jellium states

In addition to the useful examination in spherical terms, the idea of superatoms and series of electronic magic numbers could be generalized to lower symmetries if only the relative energies of the states could be solved analytically. An exception to the unsolved systems is the infinitely deep potential well, for which the electron states are solved already in elementary classes. In 3-dimensional space, this system is represented by the particle-in-box picture and the energies of the electron states are given by [103] (p. 304)

$$E = \frac{\pi^2}{2} \left(\frac{n_x^2}{L_x^2} + \frac{n_y^2}{L_y^2} + \frac{n_z^2}{L_z^2} \right) \tag{57}$$

with eigenfunctions of

$$\Psi(\mathbf{r}) = \sqrt{\frac{8}{L_x L_y L_z}} \sin\left(\frac{\pi n_x x}{L_x}\right) \sin\left(\frac{\pi n_y y}{L_y}\right) \sin\left(\frac{\pi n_z z}{L_z}\right). \tag{58}$$
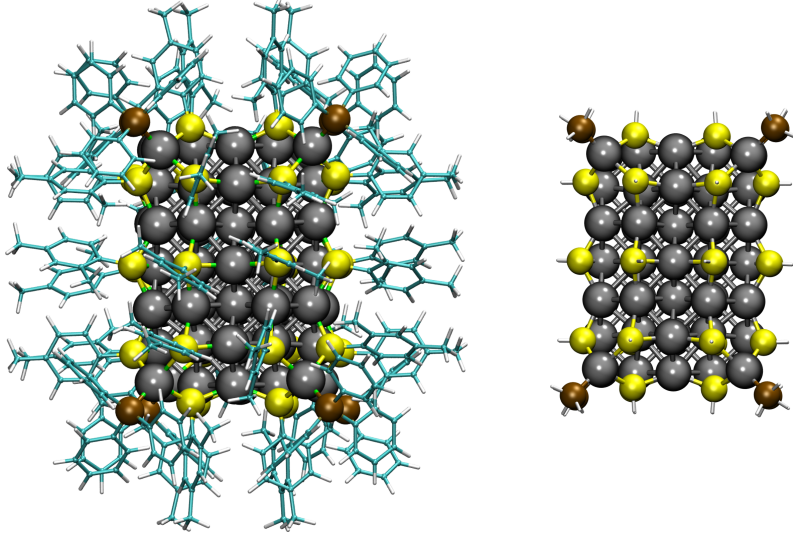
FIGURE 4   Crystal structure of $[Ag_{67}(SPhMe_2)_{32}(PPh_3)_8]^{3+}$ and the corresponding structure with minimal ligands -SH and -PH₃.

where n_x, n_y, n_z are integers. That is, the states can be characterized by their nodal multiplicities along each cartesian axis as (n_x, n_y, n_z).

In 2016, crystal structure of the silver cluster $[Ag_{67}(SPhMe_2)_{32}(PPh_3)_8]^{3+}$ was resolved [53] and interestingly, it showed a pure box-like symmetry. In [PI], we analyze the electronic structure of the particular cluster, although minimal ligands –SH and –PH₃ were used (see figure 4). Encouraged by the predictive power of spherical jellium systems on magic numbers of spherical metal clusters, we calculated the electron states for a jellium system with similar size and shape as the metal core of the minimal-ligand model $[Ag_{67}(SH)_{32}(PH_3)_8]^{3+}$. The edge lengths of the jellium box were set to the average distances between the nuclei of the outermost silver atoms. The electron count in the jellium calculation was 32, corresponding to the calculated delocalized electron count using the formula of Eq. 1. The total background charge was +44e, homogeneously distributed to the volume of the jellium box. This number was obtained by balancing the total charge of the jellium system to the total Bader charge of the core in the atomistic model which is +12e (+44e - 32e = +12e).

Analogously to projection to spherical harmonics, we projected the Kohn-Sham (KS) wavefunctions of the atomistic calculation to the wavefunctions of the jellium calculation. Since the jellium wave functions $\{\phi^j\}$ span a proper orthonormal basis, the projection coefficients of the atomistic wave functions $\{\phi^a\}$ to the jellium wave function basis are given by

$$C_{kl}^{ja} = \left\langle \phi_k^j \middle| \phi_l^a \right\rangle = \int d\mathbf{r} \left(\phi_k^j(\mathbf{r}) \right)^\dagger \phi_l^a(\mathbf{r}) = \int d\mathbf{r}\, \phi_k^j(\mathbf{r}) \phi_l^a(\mathbf{r}) \tag{59}$$

where the last equality stands for real-valued functions $\phi_k^j(\mathbf{r})$ which is true for our case. Here we already assume normalized wave functions, and thus
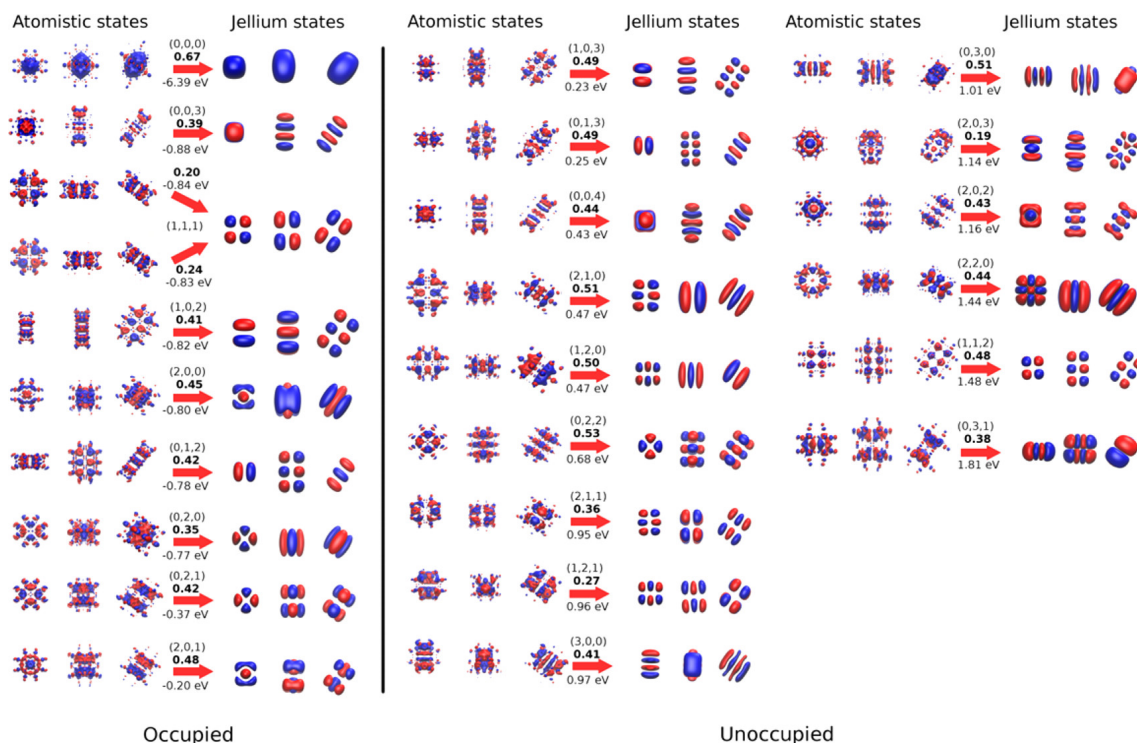
FIGURE 5   The highest overlap weights for projections of atomistic states to jellium states. The KS wave functions are visualized from 3 different perspectives. The number of nodes in (x,y,z) directions are shown with the weight in bold font. The energies of the atomistic states with respect to the Fermi level are shown. Reprinted with permission from Rosalba Juarez-Mosqueda, Sami Kaappa, Sami Malola, Hannu Häkkinen. Analysis of the Electronic Structure of Non-Spherical Ligand-Protected Metal Nanoclusters: The Case of a Box-like Ag_{67}. *The Journal of Physical Chemistry C*, 121(20), pp. 10698-10705, **2016**. Copyright 2016 American Chemical Society.

the coefficients satisfy

$$\sum_l \left| \mathcal{C}_{kl}^{ja} \right|^2 = 1. \tag{60}$$

The jellium states were characterized by their nodal multiplicities by visual inspection. In figure 5, the best correspondences between the sets of wave functions are illustrated. Firstly, both the jellium and the atomistic wave functions show the nodal structure along each axis of the cluster edge as predicted by the mathematical model of infinitely deep potential box (Equations 57 and 58) although the "well" is definitely not infinitely deep in the case of the silver cluster. The superatom state that corresponds to the 1S state in spherical terms is visualized as the upmost occupied state in figure 5 with nodal multiplicity of 0 in all directions. Most of the similarities in fig. 5 are distinct already by visual inspection, which is confirmed by the numerical analysis, i.e. the high weights. Some cases are less clear: for example the connection of the two states of atomic calculations at energies –0.83 eV and –0.84 eV to the jellium state with (1,1,1) nodal multiplicity is not trivial at least along the z axis.
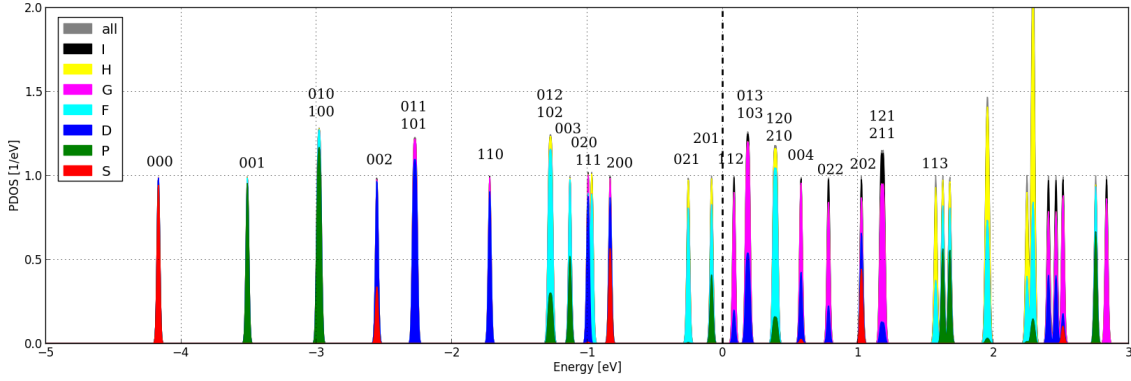
FIGURE 6   Density-of-states with spherical projection on the states of the jellium particle that corresponds to the silver core of $[Ag_{67}(SH)_{32}(PH_3)_8]^{3+}$.

The energetic order of the states can be compared to the mathematical description of the 3D potential well in equation 57. In a cubic system, the directions x, y, z would be equal, but now the edge of the box that is parallel to the z axis is longer than those of x and y. For example, we note that (1,0,2) is lower in energy than the fewer-node states (2,0,0) and (0,2,0) which is true also for the mathematical model, where the (1,0,2) state would have energy of

$$E(1,0,2) = \frac{\pi^2}{2}\left(\frac{1^2}{8.2^2} + \frac{0^2}{8.2^2} + \frac{2^2}{12.3^2}\right) = 0.204 \tag{61}$$

and the (2,0,0) and (0,2,0) would have larger energies of

$$E(2,0,0) = E(0,2,0) = \frac{\pi^2}{2}\left(\frac{2^2}{8.2^2} + \frac{0^2}{8.2^2} + \frac{0^2}{12.3^2}\right) = 0.293 \tag{62}$$

where the dimensions of the box were given in Ångstroms. In cubic system with $L_x = L_y = L_z$ the order of these multiplicities would be reversed. However, this analogue does not hold throughout the states of Ag_{67}. We observe that (0,0,3) is at even lower energies than (1,0,2), whereas the mathematical model predicts that it has the energy of 0.293 which is equal to (2,0,0) and (0,2,0) with these dimensions. This contradiction can be ascribed to various complex factors that make the mathematical model too simple to describe the system: the finite depth of the potential well of Ag_{67}, the effect of the ligand layer, and the atomistic structure of the corners of the box, where the silver atom lattice is broken and the sulphur atoms are dwelled into the lattice.

As previously unpublished information, figure 6 shows the energy levels of the jellium system. The energy order of the few highest occupied states is different from the atomistic calculations in that the (0,1,2) and (0,2,1) states are below (0,0,3) in energy, which is also predicted by the model of infinite well. The next states up to Fermi level appear in the same order than those of the atomistic calculation with some minor shift of (1,1,1) state which is anyway very close to the adjacent (2,0,0) and (0,2,0). Thus, we conclude that the power of the spherical jellium model in predicting the energetic order of

the states with certain symmetries can not be quantitatively generalized to other shapes as such. The fundamental difference therein is that the spherical potential is always spherical regardless of the distance from the center of the potential, which is true for both an atom and a spherical jellium particle. In contrast, the decaying shape of the potential of, say, box-shaped background charge is not box-shaped anymore in the distance from the origin but also starts to approach spherical shape further away from the potential box.

In article [PI], the optical response of the $[Ag_{67}(SH)_{32}(PH_3)_8]^{3+}$ cluster was investigated thoroughly in terms of the projections to the jellium states and the nodal multiplicities. The most surprising observation therein is that the dipole selection rules of the mathematical model of the infinite well are not sufficient in describing the allowed transitions in the atomistic model. In the particle-in-box model, only the number of nodes of the photon field direction can change, and the change is an odd number. This is due to the symmetry properties of the sinusoidal wave functions when their dipole moments are calculated in the form of equation 27.

In more realistic systems such as the silver cluster, we observe that in addition to the photon field direction also the number of nodes in other directions can change, and the change is an even number. We account this drastic difference for the finite depth of the potential well and the effect of ligands to the states, resulting in wave functions that cannot be considered as perfectly sinusoidal. Also, the mathematical model describes the energy levels and the respective wave functions for a single electron, whereas in the case of nanoclusters there are interactions between electrons that affects the shapes of the wave functions. For fine details of our analysis, see [PI] and its Supplementary material.

Consequently to the more realistic description of selection rules described above, the total change in the number of nodes is odd, and the selection rules can be visualized as in figure 7, where also the transition contributions for a single peak of the optical spectrum are shown. The TCM in the figure is calculated for the photon field parallel to the long axis of the cluster (z), which means that only the selection rules labelled as z in the figure are relevant. Indeed, the most intense contribution A comes from odd-odd-odd $\rightarrow$ odd-odd-even transition which is considered as allowed according to the selection rules. The transitions B, C, E, F, G and I are between even-even-odd and even-even-even states, and H and most of D are of type even-odd-even $\rightarrow$ even-odd-odd parities, obeying the selection rules flawlessly.

Using DFT, we also predicted possible atomic structures of $[Ag_{46}(SH)_{24}(PH_3)_8]^{2+}$ and $[Ag_{88}(SH)_{40}(PH_3)_8]^{2-}$ [PI] which are conjugates of the Ag_{67} cluster in that there is only a difference of $Ag_{21}(SH)_8$ unit between the structures. The electronic stability of the predicted structures is depicted by the HOMO-LUMO gaps that are larger than that of Ag_{67} (Ag_{46}:
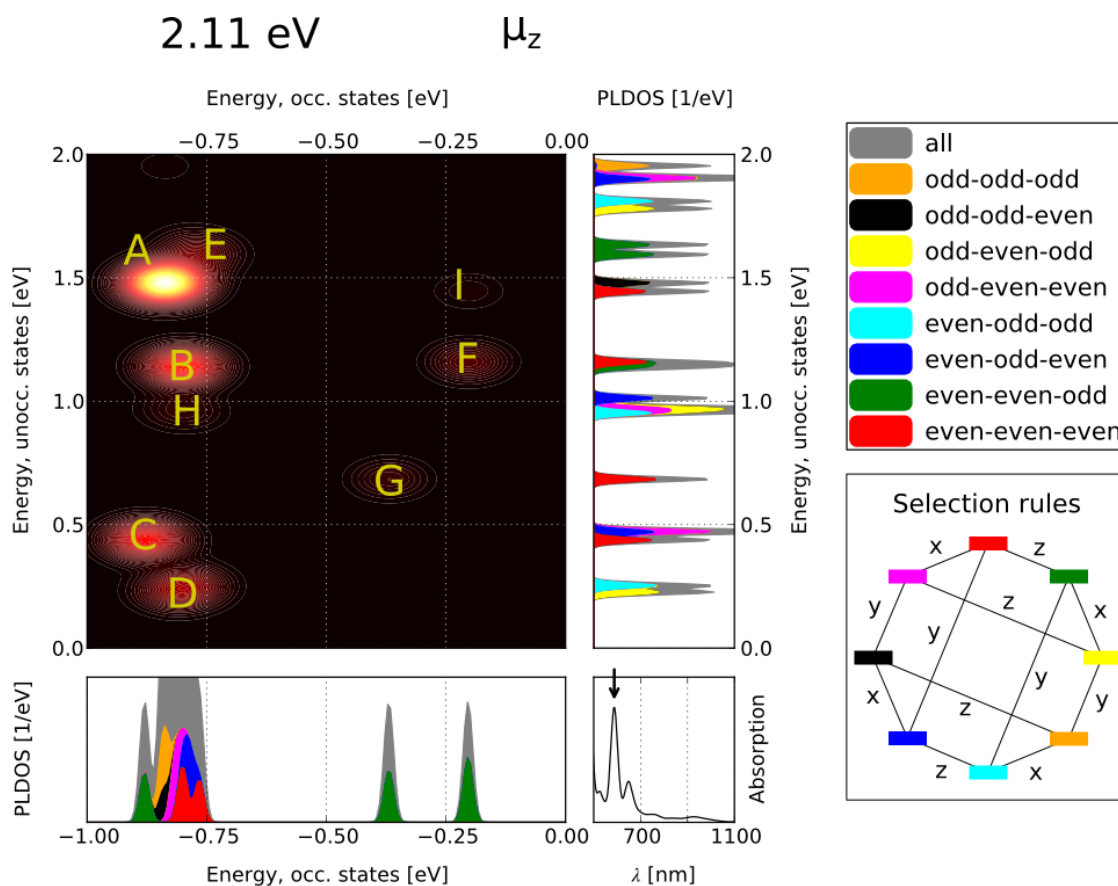
FIGURE 7 DFPT-based transition contributions for a single peak in the optical spectrum of the atomistic model of $[Ag_{67}(SH)_{32}(PH_3)_8]^{3+}$. The lower energy panel shows the density-of-states of the occupied states and the vertical energy panel has the unoccupied states. The contour map shows the intensities of the transition contributions between occupied and unoccupied states. The labels A-I distinguish between the contour spots. The coloring of the DOS is chosen as to describe the parity of the nodal multiplicities in x,y,z directions, and the same coloring is used in visualizing the selections rules in the rightmost lower corner of the figure. There, the labels x,y,z denote allowed transitions between the states that are connected by the respective line. Reprinted with permission from Rosalba Juarez-Mosqueda, Sami Kaappa, Sami Malola, Hannu Häkkinen. Analysis of the Electronic Structure of Non-Spherical Ligand-Protected Metal Nanoclusters: The Case of a Box-like Ag_{67}. *The Journal of Physical Chemistry C*, 121(20), pp. 10698-10705, **2016**. Copyright 2016 American Chemical Society.

1.0 eV, Ag_{88}: 0.46 eV, Ag_{67}: 0.36 eV). The structure of Ag_{88} could still be elongated by adding more $Ag_{21}(SH)_8$ units, but these systems were not examined in the work. This kind of embryonic growth of cuboidal silver clusters was experienced later, as another family of silver clusters was found and crystallized [52]. In $Ag_{14}(SPhF_2)_{12}(PPh_3)_8$, $Ag_{38}(SPhF_2)_{26} (P^nBu_3)_8$ and $[Ag_{63} (SPhF_2)_{36} (P^nBu_3)_8]^+$, the corners of the box-shaped Ag cores are again covered by phosphine ligands while the sulfur atoms occupy the faces of the Ag cubes. Analysis similar to Ag_{67}, that is the projection of wavefunctions to those of a jellium system, could be devised also for those cases.

3.1.2   Point group symmetry analysis

The applicability of the analysis that was done in the case of Ag_{67} is very limited as it is only valid for cuboidal structures. In article [PII] we report utilization of a more general tool, group theory, to represent the symmetries of wavefunctions of symmerical nanoclusters. Group theory has long been used in chemistry in describing rotational symmetries of molecules and spatial symmetries of atomic lattices, and the fundamentals of the group theory as it is used in chemistry and in ref. [PII] are given in section 2.2. In the paper, we characterize the Kohn-Sham wavefunctions of metal nanoclusters in the point group symmetry representations and compare those to the spherical Y_{lm} expansions which is the traditional way of analyzing the symmetries of the wave functions in metal nanoclusters.

We begin with unprotected clusters Ag_{55}^- and Au_{20}. The silver cluster was studied in three different geometries possessing point groups of icosahedral I_h, decahedral D_{5h} and cuboctahedral O_h of which the icosahedral state is known to be energetically the most stable one [104]. The structure of that has been shown to exist in weakly distorted form of the perfect icosahedron [105] but in [PII] we consider an undistorted structure to make our point of the symmetries and their role. The gold cluster Au_{20} is considered as a tetrahedron with T_d group that has been suggested based on the photoelectron spectrum by Li et al. [106].

For icosahedral and cuboctahedral Ag_{55}^-, the states that comprise of the *s*-shell valence electrons of Ag have relatively distinct spherical symmetry due to the high symmetry of the atomic structures. In contrast, the states of decahedral Ag_{55}^- have greater deviation from the spherical harmonics, and the tetrahedral Au_{20} is so far from a sphere that the states can not be characterized in spherical terms. However, another story is attained by describing the states with representations in the respective point groups, where an unambiguous representation can be assigned to each state near the Fermi level.

The valence electron number of Ag_{55}^- is 56, and according to the superatom model this corresponds to filled states up to 1G which is occupied with 16 electrons, that is it lacks 2 electrons from the shell-filling 18 electrons. For

each of the three Ag_{55}^- geometries, the 1G state is observed at around the Fermi level but in split form due to broken symmetries. For icosahedral Ag_{55}^-, the states with 1G spherical symmetry are split in energy to states with 4- and 5-fold degenerate G_g and H_g representations, respectively, of the I_h point group. In the decahedron, the spherical superatom states of 1G degeneracy are more difficult to be determined unambiguously, but it seems to be split again to both sides of the Fermi level. According to the analysis in D_{5h} point group the respective states have doubly degenerate forms of E_2'', E_1'' and E_2' at around –0.9 eV and E_1' right above the Fermi level.

In the case of the cuboctahedral Ag_{55}^-, the splitting of the 1G offers a possible route with which symmetry breaking can be seen as a factor in stabilizing a system electronically. Namely, in the density-of-states of cuboctahedral Ag_{55}^-, a gap is formed between the HOMO and LUMO. This cannot happen in spherical systems with 56 electrons due to the electron-shy 1G which always appears as a 9-fold degenerate set of states in perfectly spherical potentials. The gap formation is due to the symmetry breaking and the splitting of 1G in such a way that a single A_{1g} state with 2 electrons is left unoccupied and not degenerate with the occupied E_g, T_{1g} and T_{2g} states that are also split of the 1G spherical state. This observation solidifies the somewhat trivial idea that there can be different electronic magic numbers in systems with different geometries.

In the case of tetrahedral Au_{20}, the valence electron number is 20 which is one of the (spherical) magic numbers introduced earlier. According to the superatom model, 20 electrons fill 1S, 1P, 1D and 2S states with 2, 6, 10 and 2 electrons, respectively. However, the Y_{lm} analysis shows that the states do not appear in shapes of clear spherical symmetries, although the degenerate highest occupied states can be considered close to D symmetry which splits to E and T_2 representations in the T_d group. This suggests that the order of 1D and 2S states is inversed with respect to the *aufbau* principle and the 2S is at lower energies and/or mixed with the Au(d) electron states below -1.5 eV from the Fermi level. All of this is said assuming that the spherical magic numbers are still relevant in systems where the states do not show spherically symmetric shapes.

On top of bare clusters, we analyzed the states of 7 large ligand-protected Ag and Au clusters whose crystal structures have been verified experimentally. Throughout this section, we will refer to these clusters by their metal atom count.

Let us go through each cluster one at a time. In many cases, the ligand layer possesses lower symmetry than the metal core, and thus the assignment of symmetry representations in the point group of the core results in smaller weights than in the unprotected clusters. An example of this is Ag_{136} where the analysis was restricted only to the volume of a pentagonal bipyramid of Ag_{54} since the surface silver atoms on top of the bipyramid are structured

in an irregular pattern in the crystal structure. Despite the cluttered exterior, some of the states appear with very unambiguous correspondence to a single representation inside the core. A conclusion therein is that the ligand layer and the low-symmetrical Ag surface do not completely spoil the shape of the potential in the metal core but some of the states there are shaped only by the potential formed by the Ag_{54} core with D_{5h} point group symmetry.

Ag_{136} has 70 free valence electrons from the silver atoms according to eq. 1. This could be considered as a shell-filling number with filling up to 2D and 3S states, but according to the DFT calculation, there is no gap between the occupied and unoccupied states with the charge state -1. According to the calculation, there is a 0.3 eV gap above the first unoccupied state, suggesting that the existence of 70 free valence electrons is not enough to produce a HOMO-LUMO gap in this system which is not close to spherical. We would like to emphasize here that we are aware of the difficulties in determining the exact charge state of a large cluster in its crystalline form, since the number of counter-ions that balance the charge can not be necessarily determined in the lattice unambiguously. Therefore, the real charge state of Ag_{136} could be also –3 considering the possibility for an error in determining the charge state based on the crystal structure, which would most probably result in a considerable gap at the Fermi level. Despite this aspect, the spherical model can not explain the electronic stability of Ag_{136} since 72 does not appear in the magic number series.

A different situation is that of Ag_{141} where a distinct HOMO-LUMO gap is formed but at valence electron number of 88 that is not one of the magic numbers in spherical terms. In point group D_5, the maximum degeneracy of representations is 2 (for E_1 and E_2 representations), which suggests that an energy gap between degenerate states exists at least every 4 electrons. The unfortunate fact here is that the energy levels of different symmetry representations of D_5 cannot be placed in a fixed order since the dimensions of a particle with D_5 symmetry can vary (that can be understood by looking at figure 2), resulting in shifts of states with certain symmetry representation along the energy axis. Therefore, no fixed magic numbers can be ascribed

TABLE 4   List of large ligated clusters that were analyzed in article [PII]. The numbers of valence electrons are given in column n_c as obtained by eq. 1. The point group is shown in which the symmetry analysis was run.

Chemical composition	n_c	Point group	Reference
$[Ag_{136}(TBBT)_{64}Cl_3]^-$	70	D_{5h}	[107]
$[Ag_{141}(SAd)_{40}Br_{12}]^+$	88	D_5	[108]
$Au_{70}S_{20}(PPh_3)_{12}$	30	D_{2d}	[109]
$Au_{108}S_{24}(P(CH_3)_3)_{16}$	60	T_d	[110]
$Au_{144}(SCH_3)_{60}$	84	I_h	[111]
$[Au_{146}(p\text{-}MBA)_{57}]^{3-}$	92	C_{2v}	[112]
$Au_{246}(SPhCH_3)_{80}$	166	D_5	[113]

to a point group.

The same analysis can be applied to Au_{70} and Au_{108} with valence electron counts of 30 and 60, respectively. In these clusters, the sulfide ligands appear formally as S^{2-} that decrease the valence electron number by 2 per ion. For Au_{70}, the HOMO state actually shows superatom character of S symmetry. However, the facts that 30 is not part of the magic number series and no other state shows clear spherical symmetry prohibit the assignment of spherical superatom character to Au_{70}. The same conclusions apply for Au_{108} with its non-magical 60 valence electrons. In contrast, the point group symmetry analysis shows clean symmetry representations for all states for both Au_{70} and Au_{108}, and the gap is formed beautifully and expectedly between states that are non-degenerate in symmetry.

Of the ligand-protected clusters in article [PII], the icosahedral Au_{144} shows the largest Y_{lm} coefficients for single spherical functions, which we account for the symmetry group of I_h that has in total of 120 symmetry operations. To compare, D_5, D_{5h} and T_d groups have 10, 20 and 24 operations, respectively. In the article, we go through the splitting of the spherical terms to the icosahedral representations according to the tables in ref. [114] and observe that the splitting occurs exactly as expected. However, the closed (metal-like) density of states around the Fermi level can be explained no better by the icosahedral analysis in comparison to Y_{lm} expansion. In both cases, states with 11-fold H symmetry in Y_{lm} analysis and 5-fold degeneracy in H_g representation in I_h analysis are split to both sides of the Fermi level, explaining the absence of the HOMO-LUMO gap with the 84 valence electrons in the system.

The point group of Au_{146} is C_{2v}, which only has singly-degenerate representations. Therefore, this point group has potential magic numbers after every two electrons, and thus it is in general impossible to explain the electronic stability of a cluster obeying that point group in terms of symmetry, since a gap might occur between any two spin-paired states. Therefore, all the states with spherical symmetry are also split to singly-degenerate representations as the C_{2v} symmetry is introduced. Most probably, this is the reason to the small amount of information offered by Y_{lm} analysis in the case of electron states of Au_{146}. Naturally, a possible HOMO-LUMO gap in a (large) cluster of C_{2v} group might occur due to other factors than symmetry, such as size, dimensions, and effects of ligands.

Finally, Au_{246} shows already more degeneracy in the states than Au_{146}, which is expected by the D_5 point group where there are two-degenerate representations. According to the calculation, there is no accountable HOMO-LUMO gap for Au_{246}, but the Fermi level lies between an occupied A_2 and unoccupied E_2 states which are less than 0.05 eV apart from each other. After the two E_2 states, there is a larger gap of 0.18 eV. The number of free valence electrons of Au in the cluster is 166 that corresponds to a spherical

shell-filling up to 1G(58), 2D(68), 3S(70), 1H(92), 2F(106), 3P(112), 1I(138), 2G(156) and 3D(166) where the cumulative electron number is shown in parentheses. However, the Y_{lm} analysis shows that the states near the Fermi level appear in non-spherical shapes, again indicating that the spherical model is not valid in the case of Au_{246} obeying the D_5 point group. Also, the absence of the HOMO-LUMO gap refers to this.

Of the large ligand-protected clusters studied in article [PII], only Au_{144} has electron states that can be characterized in spherical terms. For each particle, the analysis in the respective point group shows that the states transform very similarly to the representations of the group, regardless of the lower-symmetry ligand layer. Interestingly, the poor sphericity of the states is true also for Au_{108}, Au_{146} and Au_{246} although they can be considered rather spherical by visual inspection. Thus, we conclude that the sphericity of a large cluster and, essentially, its electronic states is determined by the symmetry class rather than the deviation in the radius of the metal core, which is the intuitive way of determining sphericity. As a technical consequence, this appoints to a major problem in modelling (large) clusters with the spherical jellium model, which totally neglects the true symmetry of the potential in the system that apparently has a large effect to the electronic structure of the system.

The main conclusion of the comparison of Y_{lm} and assignments to symmetry representations for ligand-protected clusters is the same as in the case of the bare clusters: The Y_{lm} analysis is still a superior tool in explaining the stability of systems that have high symmetry, but the group representations offer more accurately the character of each state in the symmetry group of the cluster, regardless of its sphericity. The information of the group representations can also be used in explaining the electronic stability of the clusters, although to a lesser extent than spherical analysis. It can also manifest the fine details of the electronic structure, such as the degeneracy of the states and their distribution on the energy axis.

3.1.3 Applying selection rules to LR-TDDFT

In article [PII], we utilized the symmetry representations of the cuboctahedral Ag_{55}^- to enhance the performance of the LR-TDDFT calculation by applying the dipole selection rules in to the calculation of the optical spectrum. The selection rules were determined as explained in section 2.2.3. The observed result was as expected in that nothing happened to the spectrum when the forbidden transitions were neglected. However, the run time was only 21% of the full LR-TDDFT calculation. That is, the same result was obtained with only approximately a fifth of effort once the symmetry representations of the states were known.

Our implementation of applying the selection rules was carried out simply

by removing all dipole forbidden transitions from the Kohn-Sham transition list that is given to the GPAW program before the calculation of the Ω matrix (see section 2.1.3). However, we acknowledge that this is not theoretically an exact way of simulating the optical spectrum due to the form of the spectral oscillator strengths (eq. 26) and the eigenvectors F_I that have large contributions from the K matrix introduced in equation 22. In that equation, single transitions couple to each other and the mere dipole selection rules do not apply there; i.e. a non-zero matrix element of K might well include an integral over Φ_{ip} and Φ_{jq} of which, say Φ_{ip}, refers to a dipole-forbidden transition $i \rightarrow p$. In that case, the matrix element has an effect on the eigenvectors F_I and a contribution to the optical spectrum follows.

The possibility of neglecting weak transitions in calculation of the optical spectrum is examined e.g. in ref. [115] where the authors represent their results on suppressing single transitions based on the dipole moments while using time-dependent density functional tight binding model for various molecules. Their conclusion is that truncating weak enough single transitions leads to minor or insignificant changes in the spectrum, which is similar to our observation. Especially in the case of fullerene, they address the fine performance of the truncation of transitions with low oscillator strengths to the symmetry of the system and the consequent zero oscillator strengths of the dipole forbidden transitions. The threshold for oscillator strength being 0.001 leads to truncation of 75% of the transitions in their work. Considering the icosahedral symmetry of fullerene, 74/100 intersymmetry transitions are forbidden in the respective I_h group. This gives a reason to speculate that using the threshold of 0.001 they have mostly removed the symmetry-forbidden transitions from the calculation.

Nevertheless, our result indicates that the dipole forbidden transitions play a very unimportant role in the optical response of cuboctahedral Ag_{55}^-. This result cannot be generalized to all molecules since the transitions can couple to each other in theory, but it might provide a reasonable approximation while dealing with large systems where a calculation of optical spectrum is computationally too tedious to be performed. For example, the symmetry analysis for Ag_{141} showed very distinct representations for states [PII], and the requirements to calculate the optical spectrum could be considerably reduced by neglecting the dipole forbidden transitions in the LR-TDDFT calculation which scales as $\mathcal{O}(N^2)$ where N is the number of single Kohn-Sham transitions.
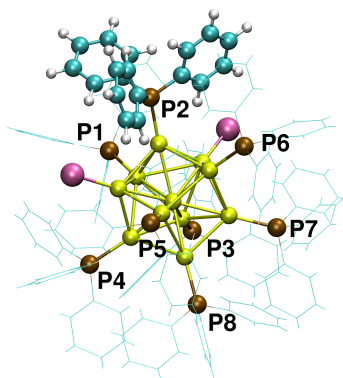
FIGURE 8   Structure of $[Au_{11}(PPh_3)_8Cl_2]^+$ with phosphine site labels. Reprinted with permission from Mina R. Narouz, Kimberly M. Osten, Phillip J. Unsworth, Renee W.Y. Man, Kirsi Salorinne, Shinjiro Takano, Ryohei Tomihara, Sami Kaappa, Sami Malola, Cao-Thang Dinh, J. Daniel Padmos, Kennedy Ayoo, Patrick J. Garrett, Masakazu Nambo, J. Hugh Horton, Edward H. Sargent, Hannu Häkkinen, Tatsuya Tsukuda, Cathleen M. Crudden. N-Heterocyclic carbene-functionalized magic number gold nanoclusters. *Nature Chemistry*, 11(5), pp. 419-425, **2019**. Copyright 2019 Nature Research.

3.2   Au nanoclusters protected by N-heterocyclic carbenes

3.2.1   Ligand exchange of PPh$_3$ to NHC in Au$_{11}$

In article [PIII], we report synthesis and characterization of clusters derived from $[Au_{11}(PPh_3)_8Cl_2]^+$ [55] where one or more of the phosphine ligands are exchanged to N-heterocyclic carbenes (NHCs); see figure 8 for the structure and the labels of the phosphine sites P1–P8. NHCs are a family of organic molecules with a divalent carbon atom which are long known to stabilize metal complexes, metal nanoparticles and metal surfaces [116, 117, 118, 119] and to be active in organic and organometallic catalysis [120, 121, 122]. Therefore, the coordination of NHC on Au is well known and it is found to bind to Au surfaces with a simple top-site bond, similar to the bond between Au and phosphine. Yet, only one magic number gold cluster incorporating NHC ligands is known, that is the trigold-NHC cluster reported by Sadighi and Bertrand [63, 123]. Our study presents the first crystal structure of an NHC-stabilized magic number gold cluster larger than that of three atoms along with synthesis and experimental evidence of the activity in the electrocatalytic reduction of CO_2 to CO. If we assume that the bond between Au and NHC is similar to Au-phosphine bond in terms of counting of superelectrons, the cluster is considered as an 8-electron superatom with 11 Au(s) electrons, 2 electron-withdrawing chlorine atoms and the total charge of +1.

To support the experimental findings, we performed DFT calculations on the studied systems.   Starting from the well-known structure of $[Au_{11}(PPh_3)_8Cl_2]^+$, we replaced each phoshine ligand with NHC molecules with side groups of methyl (Met), ethyl (Et) and isopropyl (iPr). For these

TABLE 5   Ligand exchange energies in electron volts according to eq. 63. Different columns have energies for different types of NHC side groups: isopropyl (iPr), ethyl (Et) and methyl (Met).

	iPr	Et	Met
P1	−0.64	−0.37	−0.47
P2	**−0.93**	**−0.82**	**−0.80**
P3	−0.73	−0.75	−0.74
P4	−0.55	−0.59	−0.60
P5	−0.41	−0.16	−0.54
P6	−0.40	−0.32	−0.47
P7	−0.75	−0.44	−0.67
P8	+0.05	−0.25	−0.46

systems, we calculated the change in total energy in the reaction of

$$[\mathrm{Au}_{11}\,(\mathrm{PPh_3})_8\,\mathrm{Cl_2}]^+ + \mathrm{NHC} \quad \rightarrow \quad [\mathrm{Au}_{11}\,(\mathrm{PPh_3})_7\,\mathrm{NHC}\,\mathrm{Cl_2}]^+ + \mathrm{PPh_3}. \tag{63}$$
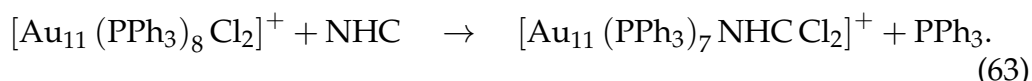
See table 5 for results. The first observation is that most of the energies are negative, relating to thermodynamically favourable reaction. The exchange of NHC-iPr to site P8 shows unfavourable binding that is probably due to steric effects caused by interactions of the NHC with the adjacent phosphines. Unlike for other sites, there is no neighbouring Cl ligand next to P8 which would allow more space for the ligand reaching out from the gold surface. It has to be pointed out that we only used PBE functional to model the exchange-correlation effects in Au_{11} clusters, and therefore the long-range interactions were neglected that could affect the obtained energies and optimal structures. However, the calculations on $[\mathrm{Au}_{13}(\mathrm{NHC})_9\mathrm{Cl_3}]^{2+}$, discussed in the next section, imply that inclusion of the van der Waals interactions do not have a critical effect on the system which is very similar to Au_{11}.

Another major point that can be read from the energetics is that P2 is the most optimal exchange site for each type of NHC with different side groups. For P2 exchanged systems, also the gap between the highest occupied and lowest unoccupied molecular orbitals (HOMO and LUMO) appears to be largest of all sites with values of 2.01 eV, 2.00 eV and 1.96 eV for Met-NHC, Et-NHC and iPr-NHC substituted species. See Supplementary information of [PIII] for more data.

As a historical anecdote, the DFT calculations were performed before the crystal structure of the monosubstituted $[\mathrm{Au}_{11}(\mathrm{PPh_3})_7\mathrm{NHC}\text{-}\mathrm{iPr}\,\mathrm{Cl_2}]^+$ was obtained. In the crystal structure, the NHC is substituted to the P2 phosphine site, exactly as our DFT calculations predicted beforehand. The most accountable difference between the PBE-predicted structure and the crystal structure is that the phenyl rings of the phosphine ligands are oriented slightly differently, as illustrated in figure 9. In the crystal structure, the phosphine at P1 is oriented so that the phenyl rings are further away from
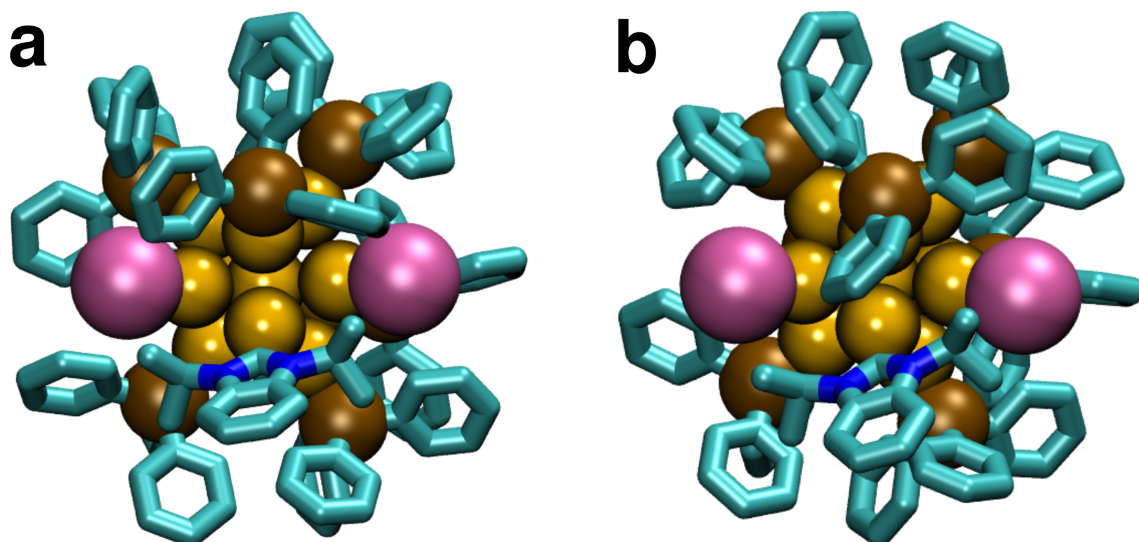
FIGURE 9 (a) The PBE prediction of structure for $[Au_{11}(PPh_3)_7NHC\text{-}iPr\,Cl_2]^+$ and (b) the crystal structure. Reprinted with permission from Mina R. Narouz, Kimberly M. Osten, Phillip J. Unsworth, Renee W.Y. Man, Kirsi Salorinne, Shinjiro Takano, Ryohei Tomihara, Sami Kaappa, Sami Malola, Cao-Thang Dinh, J. Daniel Padmos, Kennedy Ayoo, Patrick J. Garrett, Masakazu Nambo, J. Hugh Horton, Edward H. Sargent, Hannu Häkkinen, Tatsuya Tsukuda, Cathleen M. Crudden. N-Heterocyclic carbene-functionalized magic number gold nanoclusters. *Nature Chemistry*, 11(5), pp. 419-425, **2019**. Copyright 2019 Nature Research.

the neighbouring chlorines than in the predicted structure.

To account for the effect of substitution of phosphine to NHC even further, we investigated the Bader charges of the different atoms and ligands in both the non-subsituted Au_{11} and the crystal structure that was optimized with the PBE functional. The previously unpublished results are summarized in table 6. By examining the average charges of different Au atoms of the systems, we observe that the middle atom has withdrawn an accountable amount of electron density, compared to a free atom. Of the surface atoms, Au that binds to Cl is slightly positively charged. The essential difference between the substituted and non-substituted species is that the Au that binds to NHC is now positively charged, in contrast to the phosphine-coordinated Au atoms which preserve their negative Bader charge when NHC is introduced at P2. The average charge of the Cl ligands remains the same in the exchange, and that of PPh_3 is decreased from +0.38 |e| to +0.37 |e| in average. The Bader charge of the NHC ligand attached to Au_{11} is +0.34 |e|, that is slightly lower than that of PPh_3. The exchange of a ligand thus changes the charge distribution of the system so that the Au core becomes less negative as (i) NHC tends to donate less electron density to Au compared to PPh_3 and (ii) PPh_3 donates slightly less charge to Au in the substituted system. In some sense, the introduction of NHC to the cluster seems to decrease the strength of the interaction between Au and PPh_3.

TABLE 6 Bader charges of various atoms and ligands in PBE-optimized $[Au_{11}(PPh_3)_8 Cl_2]^+$ and crystal structure of $[Au_{11}(PPh_3)_7 NHC\text{-}iPr Cl_2]^+$. The numbers are in units of elementary charge.

	No NHC	NHC at P2
Au(-Cl)	+0.06	+0.05
Au(-PPh$_3$)	–0.10	–0.10
Au(-NHC)	–	+0.06
Au (middle)	–0.27	–0.28
Au (total)	–0.95	–0.81
Cl (total)	–1.12	–1.12
PPh$_3$ (total)	+3.04	+2.60
NHC (total)	–	+0.34

The optical properties of $[Au_{11}(PPh_3)_7 NHC\text{-}iPr Cl_2]^+$ were studied using LR-TDDFT and TCM analysis. In figure 10a, different calculated spectra are compared to the experiment. Good correspondence with the calculated and the experimental curves was obtained by shifting the computed spectra by 0.4 eV up in energy. The redshift of computed spectral features can be attributed to various factors, such as the rather simple model for exchange and correlation effects or solvation effects [124, 68]. After the shift, peaks at around 310 nm and 420 nm match well in addition to the decaying tail of the spectral curve after 550 nm. The peaks at 310 nm and 420 nm are analyzed using TCM (fig. 10b and 10c). The analysis indicates that large contributions to the transitions occur from both Au(s) and Au(d) states to the unoccupied states of the phenyl rings of the phosphine ligands, and that the states localized to vicinity of NHC do not play major role in the optical response at this energy range.

The colors in the density-of-states of the TCM images describe the localization of the electronic states to different parts of the molecule. To analyze the localization, we first transform each Kohn-Sham wave function to density by taking the square of the function. Then, Bader analysis is performed to the resulting density. The resulting charges are then grouped into the four classes of Au, Cl, PPh$_3$ and NHC by summing up the respective charges. The sums are the weights that determine the height of the colored parts of the states in the figures 10b,c. As a sidenote, the weights trivially add up to the normalization factor of the Kohn-Sham state.

3.2.2 All-NHC stabilized Au$_{13}$

After the first NHC-stabilized gold cluster was crystallized, more were to come. In article [PIV], we report the crystal structure and characterization of another gold cluster where the icosahedral Au$_{13}$ is fully protected by NHCs and chlorine: The formula of the studied system is $[Au_{13}(NHC)_9 Cl_3]^{2+}$ with straightforward analogy to the long-known phosphine protected $[Au_{13}(PMe_2Ph)_{10}Cl_2]^{3+}$ [47] with a difference of 1 ligand and respective charge state. The superelectron number in both systems is 8 due to for-
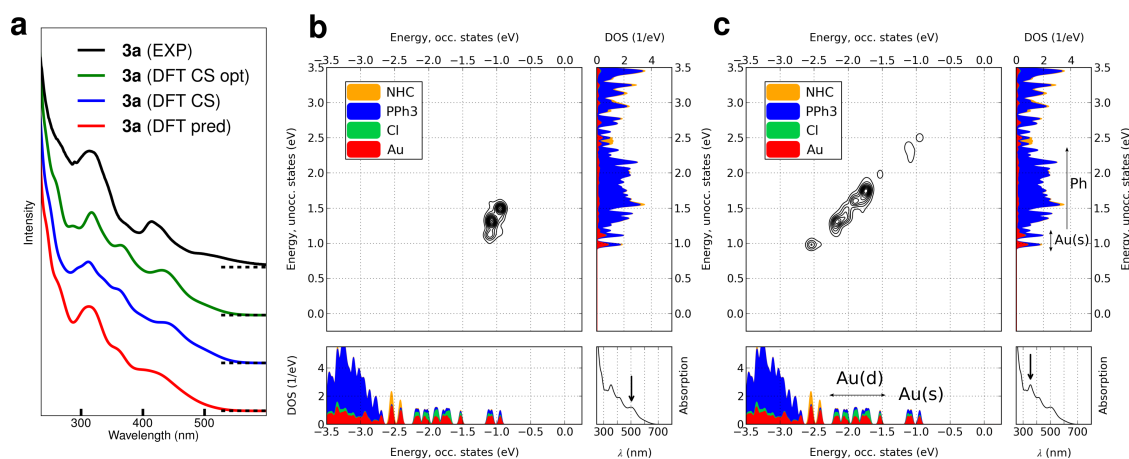
FIGURE 10   Optical response of NHC-iPr substituted Au_{11}. (a) Optical spectra. **3a** refers to $[Au_{11}(PPh_3)_7NHC\text{-}iPr\,Cl_2]^+$, CS refers to crystal structure and opt and pred refer to optimized and predicted structures. The computed spectra are manipulated by blueshifting them by 0.4 eV. (b) and (c) Transition contribution maps of the peaks shown in the lower right corners of the respective maps. In (c), some of the states are assigned by their spatial localization. Reprinted with permission from Mina R. Narouz, Kimberly M. Osten, Phillip J. Unsworth, Renee W.Y. Man, Kirsi Salorinne, Shinjiro Takano, Ryohei Tomihara, Sami Kaappa, Sami Malola, Cao-Thang Dinh, J. Daniel Padmos, Kennedy Ayoo, Patrick J. Garrett, Masakazu Nambo, J. Hugh Horton, Edward H. Sargent, Hannu Häkkinen, Tatsuya Tsukuda, Cathleen M. Crudden. N-Heterocyclic carbene-functionalized magic number gold nanoclusters. *Nature Chemistry*, 11(5), pp. 419-425, **2019**. Copyright 2019 Nature Research.

mation of a formal Au_{13}^{5+} core.

The crystal structure was acquired for the cluster incorporating NHC-Bn (benzyl) ligands. In addition to that, DFT calculations were performed for NHC-CH_2(2-Np) (2-naphtyl) ligand by replacing the side groups of the ligands by hand starting from the crystal structure. The NHC-2-naphtyl protected cluster was also characterized from experiments although the crystal structure could not be obtained. According to DFT calculations, the binding energies of NHC-Bn were 1.99 eV for Au(1) (the notation for Au atoms is given in figure 11), 2.26 eV for Au(2) and 2.29 eV for Au(4). The difference of Au(1) to the other sites can be accounted for the number of neighbouring Cl sites which is 1 for Au(1) and 2 for the other NHC sites.

Another observation that indicates a different nature of Au(1) to the other NHC sites are the Au-NHC bond lengths within the crystal structure which are in average 2.10 Å for Au(1) and 2.03 Å for the rest. For reference, the Au-NHC bond length was 2.05 Å in the crystal structure of $[Au_{11}(PPh_3)_7NHC\text{-}iPr\,Cl_2]^+$. We speculate that this might again be an effect of either stericity of the surface or the distribution of charge between different ligands. Indeed, when van der Waals effects were taken into account by the exchange-
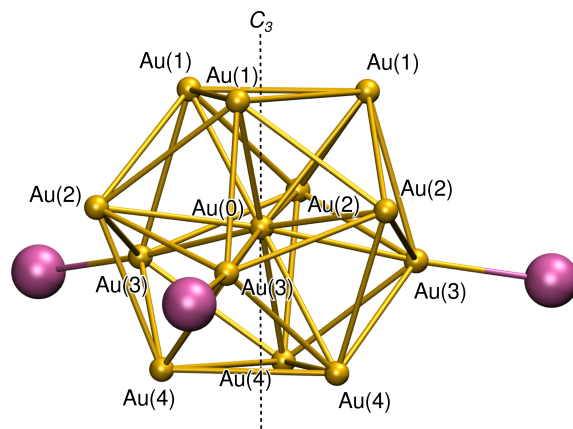
FIGURE 11   Gold core and chlorine ligands of $[Au_{13}(NHC)_9Cl_3]^{2+}$.

correlation functional BEEF (see section 2.1.2.2), the binding energy was 2.62 eV at Au(1) site. This is 0.63 eV higher than with PBE, manifesting the role of long-range interactions between the π electrons of the phenyl rings.

In addition to binding energies, the HOMO-LUMO gaps of 1.96 eV and 1.95 eV for NHC-Bn and NHC-CH_2(2-Np) clusters, respectively, were obtained with PBE functional and they further indicate high stability of the systems. The BEEF functional gives a gap of 1.98 eV for NHC-Bn cluster which is very close to the one calculated with PBE. This indicates that the functional does not affect too much on the states of Au(s) electrons, but more likely validates that the difference in the binding energy is due to the interactions between the organic ligands.

The Bader charge analysis, summarized in table 7, repeats the difference between gold atoms that are neighbours to one and two chlorine sites. The central Au atom exhibits reduction of –0.27 |e| (according to PBE functional) which is very close to the Au atom in the middle site of $[Au_{11}(PPh_3)_7NHC\text{-}iPrCl_2]^+$ that had –0.28 |e|. In accordance to the case of Au_{11}, each surface atom binding to NHC or Cl appears with positive Bader charge. However, the average Bader charge of Au(1) atoms is slightly but substantially lower than that of the rest of the surface Au atoms. Also the NHC ligands at Au(1) sites have smaller Bader charge than the other carbenes, which again demonstrates the weaker interaction between Au and NHC further away from Cl. While comparing BEEF calculations to PBE in terms of Bader charges, we notice that BEEF suggests larger charge for the surface Au atoms and lesser electron density donation from NHCs than PBE.

The major difference between the phosphine-protected Au_{11} and the all-NHC Au_{13} in terms of Bader charge is the total charge of the Au core, which is highly negative in Au_{11} and highly positive in Au_{13}. This difference was already encountered in the previous section where we noted that the Au atoms that bind to PPh_3 are negative in Bader charge and the one binding to NHC was positive. This suggests a fundamental difference in binding of phosphine and NHC to Au clusters although they coordinate to the surface

TABLE 7   Bader charges of various atoms in Au_{13} calculated with both PBE and BEEF functionals. The numbers are in units of elementary charge.

	PBE	BEEF
Au(0)	−0.27	−0.26
Au(1)	+0.03	+0.05
Au(2)	+0.05	+0.08
Au(3)	+0.06	+0.09
Au(4)	+0.05	+0.07
NHC(1)	+0.36	+0.34
NHC(2)	+0.37	+0.34
NHC(4)	+0.38	+0.36
Au (total)	+0.33	+0.62
Cl (total)	−1.65	−1.73
NHC (total)	+3.33	+3.10
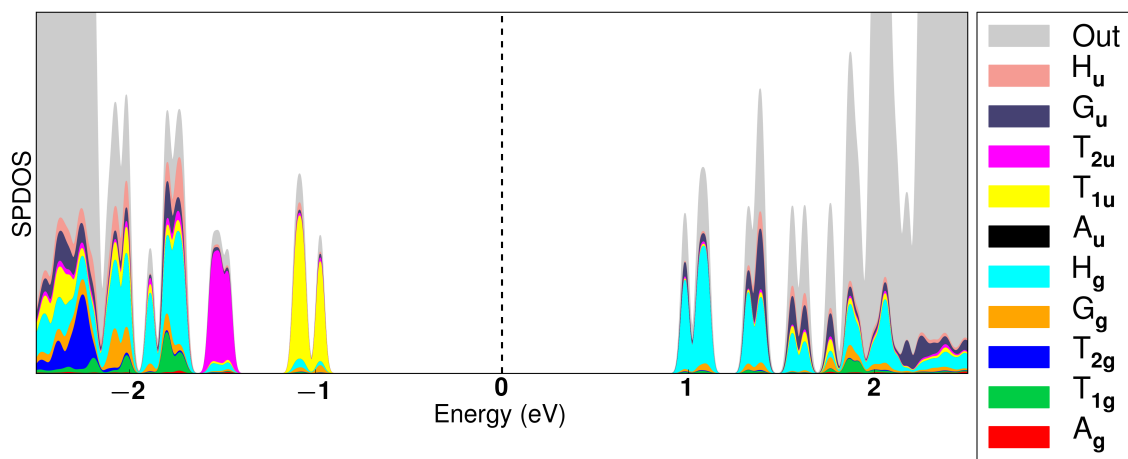
FIGURE 12   Density of states with I_h symmetry analysis of $[Au_{13}(NHC\text{-}Bn)_9Cl_3]^{2+}$. The figure is reproduced from article [PIV].

in a similar way and can be exchanged, as observed in article [PIII].

Whereas the Au_{11} cluster shows no symmetry above C_s of the gold core, the icosahedral geometry of the core of Au_{13} makes it tempting to analyze the electron states in point group representations similarly to what was done in article [PII]. The analysis along with the density-of-states is shown in fig. 12. The highest occupied states that transform as representation T_{1u} in I_h group appear as slightly split in degeneracies of 2 and 1. In spherical terms, the three HOMOs are the 1P states which can be seen already by visual inspection of the states. Also, the representation of the spherical harmonics of P-symmetry is T_{1u} in I_h group [114].

The small splitting of the three HOMOs can be understood by broken symmetry. Firstly, we observe that the chlorine atoms lie approximately at the equator of the cluster, considering the rotational axis C_3 in fig. 11. If we

imagine that this plane is the xy-plane, then the 2 degenerate states that are at lower energies are $1P_x$ and $1P_y$, and the single HOMO is $1P_z$ which is not degenerate to the two in-plane states due to the asymmetry of the ligand layer. The orientation of the HOMO having the node at this xy-plane validates this picture. Similarly, the first few LUMOs are 1D states which transform as five-fold H_g representations in I_h group.

The comparison of the experimental and calculated optical spectra are shown in figure 13a. The peaks at 310–320 nm match well between the curves, as well as the peaks at around 410 nm. The lowest peak of the simulations is at 550 nm which is 60 nm lower than the lowest peaks of the measured spectra at 490 nm. This accounts for 0.28 eV in energy, which is of the same order of magnitude as the global shift that we assumed in the case of Au_{11}. The lowest peak was analyzed with TCM (figure 13b) which shows that the peak arises mostly of the HOMO–LUMO transition. According to the symmetry analysis, the transition is correctly dipole allowed.

The measured emission spectrum of $[Au_{13}(NHC\text{-}CH_2\text{-}2\text{-}Np)_9Cl_3]^{2+}$ shows a peak at around 730 nm with high quantum yield. We investigated the origin of the emission and performed calculations on the excited states of both $NHC\text{-}CH_2(2\text{-}Np)$ and NHC-Bn protected clusters. The spin-polarized calculations were run by forcing a single electron to be excited onto the first unoccupied Kohn-Sham state in both cases and relaxing the systems. The resulting energies of the excited systems were 1.68 eV and 1.61 eV higher than those of the ground states of NHC-Bn and $NHC\text{-}CH_2(2\text{-}Np)$ protected clusters, respectively. The energies correspond to wavelengths of 738–770 nm, thus agreeing well with the experimental energy of the peak for the cluster with 2-napthyl-NHCs. This result thus agrees with the simple description of fluorescence that after excitation, the vibrational state of the system is relaxed and de-excitation occurs from the vibrational ground state of the electronically excited system to the electronic ground state.

Let us summarize the two last sections relating to NHC-stabilized clusters. The DFT calculations were able to predict the correct binding site of the NHC in $[Au_{11}(PPh_3)_7NHC\,Cl_2]^+$ and reproduced the shape of the optical spectrum of the NHC-iPr substituted cluster with good correspondence. The exchange of phosphine ligands to NHC showed energetically favourable reaction towards binding of NHC. The calculations on tridecagold cluster $[Au_{13}NHC_9\,Cl_3]^{2+}$ also showed high binding energy of NHC on the cluster and agreement of the optical response to the experimental data. The calculations also suggest that the binding energy of NHC on Au clusters is dependent on the site due to steric effects and charge distribution. The inclusion of van der Waals effects in describing the electron interactions in $[Au_{13}NHC_9\,Cl_3]^{2+}$ indicated higher binding energy of NHC comparing to PBE functional, but the size, shape and electron density of the cluster did not change substantially between the two functionals.
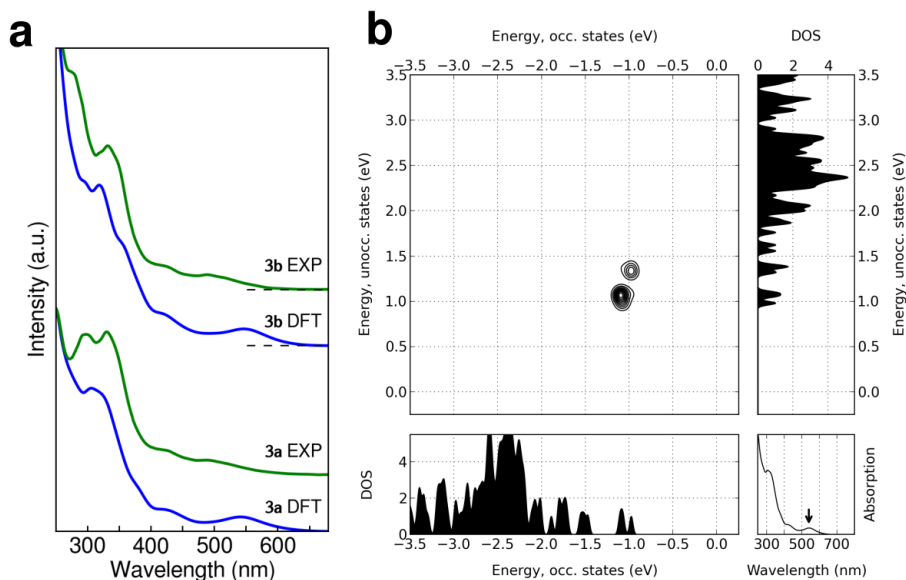
FIGURE 13   (a) Experimental and simulated optical spectra of $[Au_{13}(NHC)_9Cl_3]^{2+}$. 3a
refers to NHC-Bn and 3b refers to NHC-CH$_2$-2-Np ligated clusters. (b) TCM
of a single transition in NHC-Bn cluster.

3.3   Numerical analysis of STM images of nanoclusters

The electronic structure of nanoparticles can be applied to simulations of
the scanning probe microsopes as explained in section 2.4 for scanning tun-
nelling microscopy (STM). In article [PV], we show, for the first time, STM
images of an atomically precise nanoparticle with sub-molecular resolu-
tion. We wanted to model the STM images with DFT and Tersoff-Hamann
model, but we lacked the knowledge of the orientation of the cluster on
the substrate, and we therefore had no direct way of analyzing the exper-
imental results in theoretical means. Therefore, the images of the ligand-
protected silver particle with molecular formula of $Ag_{374}(TBBT)_{113}Br_2Cl_2$
(TBBT = tert-butyl benzene thiol) were simulated in 1665 orientations using
Tersoff-Hamann method as implemented in the ASE package [98], and the
orientation of the particle on the substrate was sought using a self-built pat-
tern recognition algorithm that is explained in section 2.5.

First of all, we confirm that sub-molecular resolution is achieved by exam-
ining the peak-to-peak distances of the line-scans at the central part of the
cluster, where the tip-convolution effects are minimal. The line-scans in
several STM image show peak-to-peak distances of the topographic data
ranging from 0.3 to 0.6 nm. The DFT simulations of the STM images of the
particle imply that the peak-to-peak distance between two methyl groups
is approximately 0.3 nm and the peak-to-peak distance between two TBBT
ligands is approximately 0.6 nm. Therefore, we conclude that the peaks that
are present in STM images correspond to peaks caused by single methyl
groups at the surface of the particle, and that the sub-molecular resolution

is evident.

The main result of my work is shown in figure 14d. The figure shows the distance between each simulated STM image and the experimental image which is shown in figure 14a. The white dots on top of the STM images denote the positions of the extremum points that are compared between the experimental and simulated images. The data points with the same color in figure 14d represent similar perspective and set of maxima and minima, which are, in some cases, not close to each other in the orientation numbers; this is only due to the order in which the orientations were walked through. In addition, it is notable that similar set of colored data points exist quite symmetrically on both sides of the midmost orientation number of 883. This is simply caused by the close-to C_2 symmetry of the ligand layer, and the walk-through of the orientations is such that the symmetrical orientations are regarded in the opposite order than those of the first 883 orientations. We would like to emphasize that the limit of 1.1 Å beneath which the data points are coloured is not well defined but it is just roughly the lower boundary of the main band of the data points.

The imaging procedure offers two different images: the first image is recorded while the tip moves from left to right, and another image is recorded as the tip comes back from right to left by the same trace. After a trace is finished to both directions, the tip is moved a bit forward and another trace is recorded for both images. Here, the first image is shown in figure 14a, and the re-trace image is shown in figure 14b. Naturally, we ran the comparison analysis for this image also. The results are given in figure 15. The colors of the data points there refer to the same colors in figure 14d, indicating that mostly the same calculated images are found to fit to both the first and the re-trace image. From this result, we draw two conclusions. Firstly, the measurement does not affect too much on the sample. This is an important observation because of the validation on our assumption that we are imaging something that really exists on the surface of the sample, and the scanning tip or the tunnelling electrons do not affect the surface too much. Secondly, the result implies that the comparison method is not too sensitive on the fine details of the local density of states (LDOS) that are different between the two traces.

The critical question on our analysis is whether the accuracy and applicability of the method for comparison is substantial in distinguishing between different sets of coordinates. To test this, we took a single simulated image with orientation index 600 and compared each calculated figure to that one. However, before the analysis, the local extremum points were perturbed (i.e. shifted randomly) by up to 1 and 2 Å in both x and y directions. The results are shown in figure 16. For the smaller perturbation, the analysis is with no doubt able to find the correspondent set of coordinates for the extremum points and the respective images. Even in the case of the random shifts up to 2 Å, the correct images (red data points in figure 16) are unam-
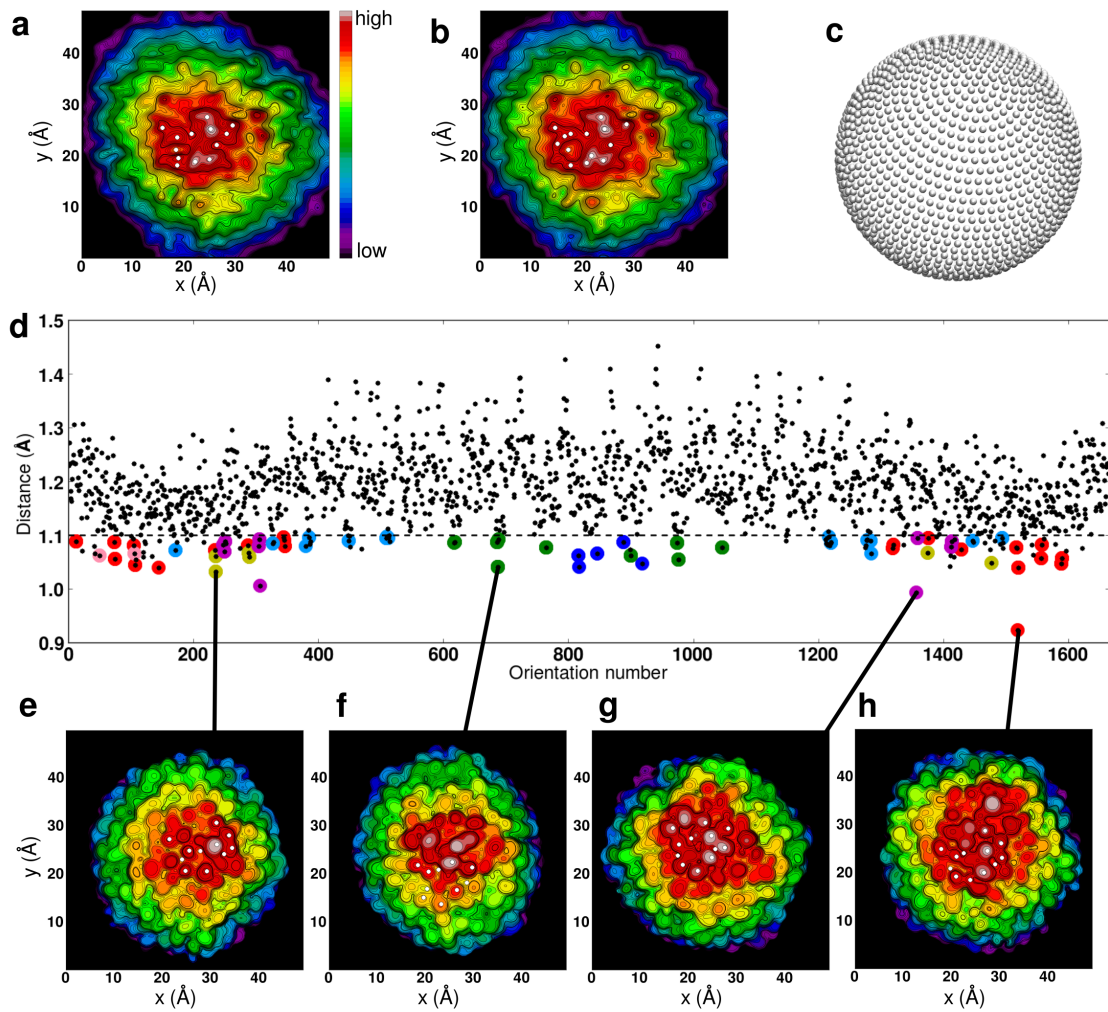
FIGURE 14   Comparison of STM images. (a) Experimental STM image for which the comparison is carried out. (b) Re-trace image of the same particle. (c) Illustration of the distribution of perspectives where the STM simulations were calculated. (d) Distances between each simulated image and the experimental image. (e-h) Simulated images of the selected perspectives, connected with lines to figure d. Reprinted with permission from Qin Zhou, Sami Kaappa, Sami Malola, Hui Lu, Dawei Guan, Yajuan Li, Haochen Wang, Zhaoxiong Xie, Zhibo Ma, Hannu Häkkinen, Nanfeng Zheng, Xueming Yang, Lansun Zheng. Real-space imaging with pattern recognition of a ligand-protected Ag$_{374}$ nanocluster at sub-molecular resolution. *Nature Communications*, 9(1) p. 2948, **2018**. Copyright 2018 Nature Research.
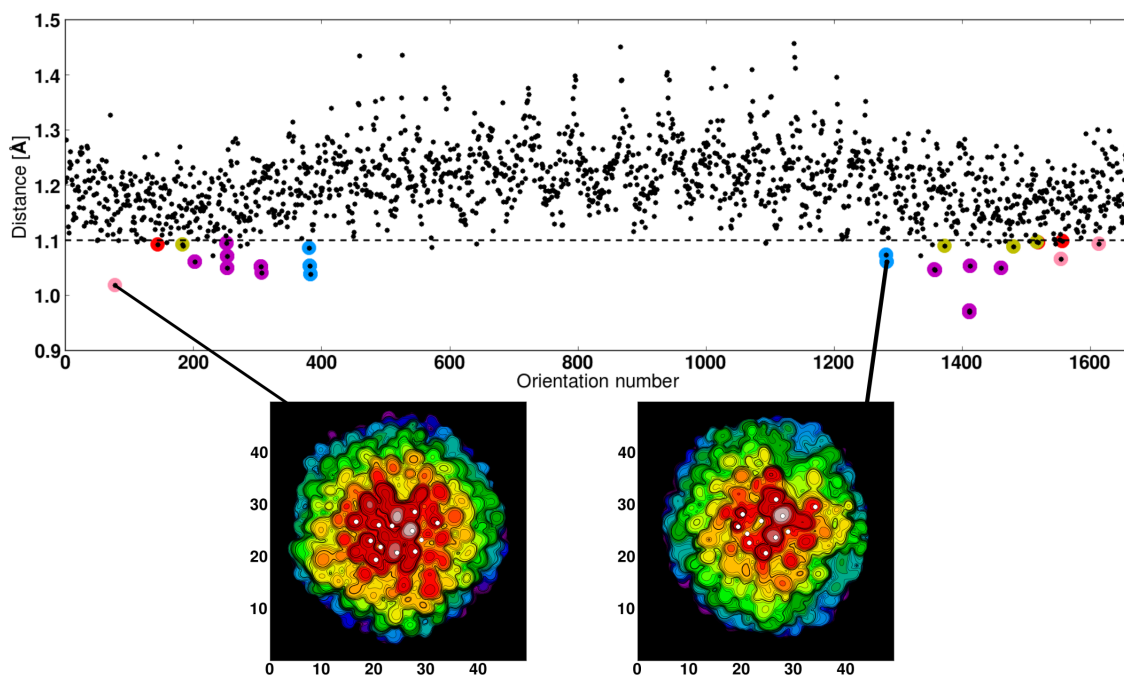
FIGURE 15   Comparison of simulated STM images and the re-trace image in figure 14b. The colors of the data points match with the ones in figure 14d. Reprinted with permission from Qin Zhou, Sami Kaappa, Sami Malola, Hui Lu, Dawei Guan, Yajuan Li, Haochen Wang, Zhaoxiong Xie, Zhibo Ma, Hannu Häkkinen, Nanfeng Zheng, Xueming Yang, Lansun Zheng. Real-space imaging with pattern recognition of a ligand-protected Ag$_{374}$ nanocluster at submolecular resolution. *Nature Communications*, 9(1) p. 2948, **2018**. Copyright 2018 Nature Research.

biguously found among the best candidates.

To examine the effect of possible thermal movement of the tert-butyl ends of the TBBT ligands, we simulated the STM images of TBBT on Au(111) surface. The thiol was relaxed on top of the Au(111) surface using PBE functional, and three different rotational barriers were determined. The rotation of the mere tert-butyl group with respect to the benzene ring (figure 17a) resulted in a barrier of 0.08 eV. The corresponding barrier for rotation of the whole ligand (figure 17b) was smaller, 0.04 eV. The tilting of the ligand with respect to the Au surface, shown in figure 17c, was remarkably more expensive with 0.27 eV barrier. The experiments were carried out in ultra-high vacuum chamber with liquid-helium temperature, and the corresponding Arrhenius probability factor for the smallest barrier is 10^{-51} in that temperature. As the typical rotational frequency of the rotations of such organic molecules is of the order of 10^9 1/s, the 120° rotation of a single thiol is expected to happen of the order of every 10^{42} seconds. Whereas this result was obtained for a single thiol on a clean surface, the barriers are assumably even larger for the thiols on top of a cluster because of the interactions and steric hindrance of the neighbouring ligands. This result strongly suggests that the cluster is in very frozen state in the environment where the experiment is carried out, which means that the thermal effects do not al-
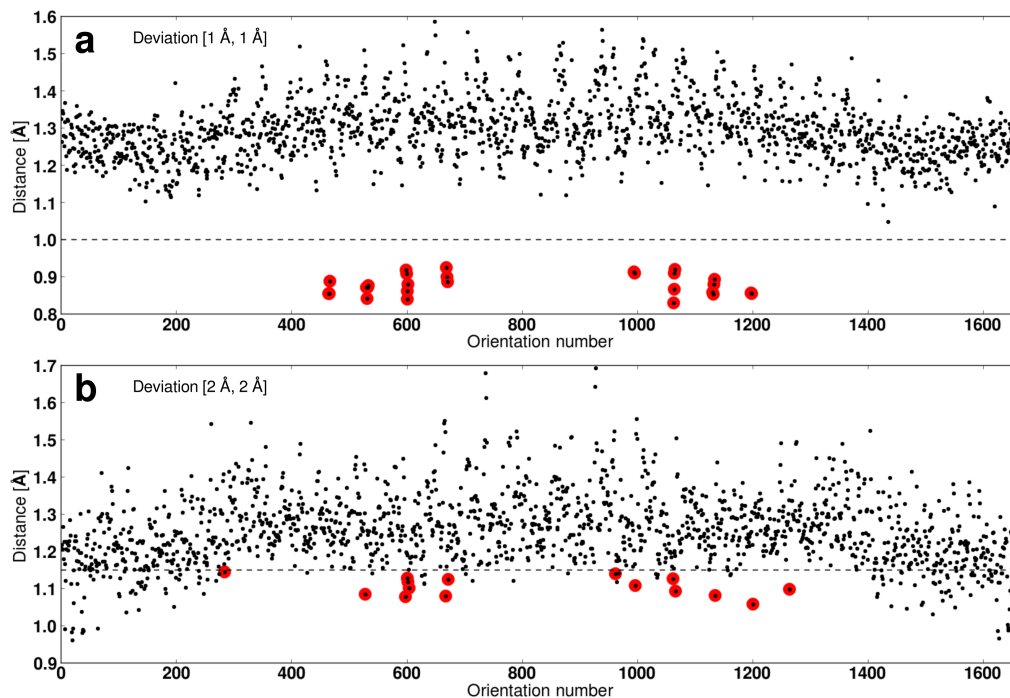
FIGURE 16 Comparison of each simulated image to image no. 600. The extremum points of the reference image are deviated in *x* and *y* randomly by picking numbers from uniform distribution between (a) –1 and 1 Å and (b) –2 and 2 Å. Reprinted with permission from Qin Zhou, Sami Kaappa, Sami Malola, Hui Lu, Dawei Guan, Yajuan Li, Haochen Wang, Zhaoxiong Xie, Zhibo Ma, Hannu Häkkinen, Nanfeng Zheng, Xueming Yang, Lansun Zheng. Real-space imaging with pattern recognition of a ligand-protected Ag$_{374}$ nanocluster at sub-molecular resolution. *Nature Communications*, 9(1) p. 2948, **2018**. Copyright 2018 Nature Research.

ter the surface of the cluster during the measurement. To set the reaction rate to a scale, the time for a single thiol rotation to take place in liquid nitrogen would be of the order of 10^{-6} seconds and in room temperature 10^{-9} seconds. This strongly suggests that low temperatures are required in STM imaging of ligand-protected systems in sub-molecular resolution. According to both simulations on TBBT and STM images in liquid nitrogen temperature, we conclude that the respective temperature ($\approx$ 77 K) sets a rough upper limit for the temperature where sub-molecular resolution can be achieved in such systems.

In an ideal case, where the cluster would possess its exact crystal structure even when lying on the substrate, where the scanning tip would produce a flawless image of the LDOS of the cluster, and where the Tersoff-Hamann method would give the coordinates of the LDOS extrema correctly, we would obtain zero distance between the STM image and the corresponding simulated image. However, there are unknown uncertainties in each of these assumptions that result in non-zero distances. To test how the thermally induced rotations of the thiols would relate to our pattern recognition algorithm, we performed the distance measurements of the images for the
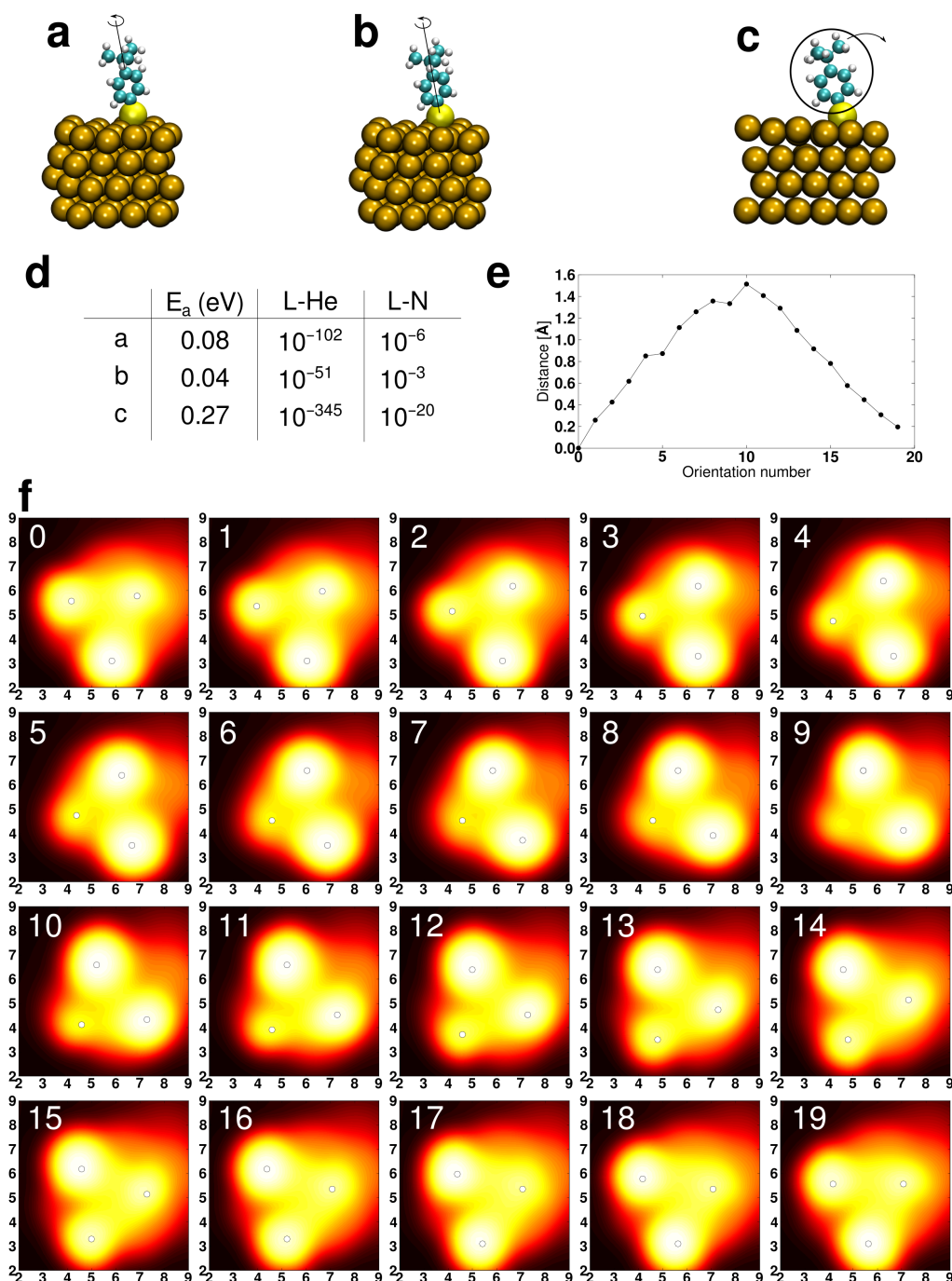
FIGURE 17 Thermal movement of tert-butyl benzene thiols. Rotations of (a) tert-butyl group, (b) the whole thiol, and (c) tilting of the thiol are illustrated. (d) The corresponding barriers (E_a) and Arrhenius probability factors in liquid helium (L-He) and liquid nitrogen (L-N) temperatures for different rotations. (e) Distances between image 0 and the images shown in (f). In (f), the white dots appoint to the positions of the local maxima of the LDOS. Reprinted with permission from Qin Zhou, Sami Kaappa, Sami Malola, Hui Lu, Dawei Guan, Yajuan Li, Haochen Wang, Zhaoxiong Xie, Zhibo Ma, Hannu Häkkinen, Nanfeng Zheng, Xueming Yang, Lansun Zheng. Real-space imaging with pattern recognition of a ligand-protected Ag_{374} nanocluster at submolecular resolution. *Nature Communications*, 9(1) p. 2948, **2018**. Copyright 2018 Nature Research.

simulated TBBT-on-Au(111) systems by comparing each rotated system to the structural ground state which is the image 0 in figure 17f. The distances are shown in figure 17e, and the evolution of the distance with respect to the rotation angle is quite trivial: The curve begins from 0 and increases linearly to 1.5 Å, which is roughly half of the methyl-methyl distance in a TBBT molecule, and then decreases back to 0 when the total rotation of 120° is achieved.

The average value of the distances in figure 17e is thus approximately 0.8 Å. That is, if the orientation of the tert-butyl groups in the ligands of the Ag_{374} cluster is random, the expectation value of the distance from the crystal structure would be 0.8 Å. Now, the distribution of the data points in figures 14d, 15 and 16 are somewhat similar to each other in that the smallest distances are between 0.9 Å and 1.0 Å and the lower limit of the main band of the data points can be placed at approximately 1.1 Å. Thus, we conclude that the best distances of 0.9 Å are quite good, since the value of 0.8 Å can be considered as an order of error that results from the rotations of the thiols or their tert-butyl ends, meaning that already those rotations cause an (average) error of 0.8 Å.

Let us summarize what we did here. We simulated STM images of the TBBT protected Ag_{374} nanoparticle and developed a numerical analysis method to resolve the orientation of the cluster on the surface. Using one of the simulated images as a dummy test image, we showed that the analysis is accurate enough to find the correct image out of the 1665 images, but the unambiguous orientation of the real cluster could not be achieved due to factors that cause uncertainty in the structure of the cluster and the accuracy of the imaging. We believe that these uncertainties dominate over the error in Tersoff-Hamann method that we used to simulate the STM images, since we are finally interested only of the extremum coordinates of the STM data. We also showed that low temperatures are definitely required in STM imaging with sub-molecular resolution.

4 CONCLUSIONS

In this thesis, I showed how the electronic structure of Au and Ag nanoclusters can be analyzed in different ways, how the calculations are able to predict and explain experimental data, and how it can be used in imaging applications. Using theoretical tools, we also showed the difference in bonding nature of phosphine and NHC ligands to gold although they behave similarly at atomic structural level. All of the electronic structure modelling was done on the density functional theory (DFT) level, and the optical properties of the clusters were studied using the time-dependent DFT (TDDFT). On top of that, the electronic structure was further analyzed in terms of symmetry and charge distribution, and it was applied to simulate scanning tunnelling images together with a homemade analytical technique for topographic pattern recognition.

In article [PI], the cuboidal symmetry of the silver cluster $[Ag_{67}(SH)_{32}(PH_3)_8]^{3+}$ was used in order to characterize its electronic states by relating them to the jellium particle with the same geometry and connecting the system to the mathematical description of a single quantum particle trapped in a box-shaped potential. Also, a new set of selection rules was designed for cuboidal systems in terms of the nodal structure of the electronic states. This study shows how calculations on non-spherical jellium particles can be utilized in research of real, atomistic particles at the DFT level of electronic structure. This study also illustrates the connection of particle-in-box model to real systems and describes the challenges in doing so. Also, the possible embryonic growth of the particular Ag_{67} cluster was predicted.

The article [PII] concerns the symmetry of nanoclusters in point groups, and the electronic structures of the large clusters studied there were shown to inherit the real symmetry of the particles rather than spherical symmetry. It was observed that the electronic states of large Au and Ag nanoclusters can not be described in spherical terms in most cases, but the states show clean characters in terms of point group representations. Despite the power of projection to spherical harmonics in explaining the stability of magic-

number clusters, the non-spherical symmetry could be, in some cases, regarded as an electronically-stabilizing factor of systems where the spherical symmetry is strongly split, resulting in decrease of degeneracy. The long-known dipole selection rules were applied in calculation of the optical response of the particles, resulting in great reduction in the computational effort required to obtain the optical spectrum of highly symmetrical particles. The approximation in the method is that the dark modes (coupling of dipole-forbidden transitions) are neglected which are generally taken into account by the LR-TDDFT machinery. However, we claim that this approach makes it possible to produce optical spectra of larger systems than with the full calculation.

Thus, the results of article [PII] set the current understanding of large noble metal nanoclusters questionable. Their electronic stability is widely understood as a consequence of the number of metallic valence electrons that are fit to the series of electronic magic numbers. That is, they are fit to spherical model. But in fact, no cluster is found to have both a notable HOMO-LUMO gap and spherical symmetry of the states, and the latter is not even observed for clusters that have weaker than icosahedral symmetry. The series of magic numbers results from the model of spherical jellium particles, but regarding the results in [PII], this model seems highly insufficient in describing the electronic states of ligand-protected clusters with 70 or more noble metal atoms. An interesting exception is $Au_{102}(SR)_{44}$ that is shown to be a 58-electron superatom with correct shell closing and spherical symmetry of the states [125], but the cluster was not studied here. Unfortunately, assignment of the point group representations is no better in explaining the stability only based on the number of valence electrons, since the energetic order of the states with certain representations can not be predicted unlike with spherical terms. However, we acknowledge that on top of symmetry there are various factors that affect the electronic structure and stability of clusters such as size, dimensions, atomic packing and effects of ligands. Together these factors form the energies of the electronic states and determine the behaviour of the system under external perturbations such as solvents, ions, force fields and light. As long known, the other factors, especially atomic packing and protecting ligands play an increasing role while the number of metal atoms in a cluster increases.

In small systems however, the magic numbers are superior in explaining the stability of close-to spherical clusters. After decades of thiols and phosphines dominating the Au nanocluster protection, the synthesis and crystallographic characterization of magic-size Au clusters with N-heterocyclic carbene ligands as stabilizing units were finally successful in articles [PIII] and [PIV]. We analyze the 8-electron superatoms Au_{11} and Au_{13} and their electronic structure with density functional theory and analytical methods built on top of DFT: LR-TDDFT, transition contribution maps, symmetry analysis, and Bader charge analysis. Along with the studies, the density functional theory demonstrated its power by predicting the correct bind-

ing site of NHC on the monosubstituted $[Au_{11}(PPh_3)_7 NHC\,Cl_2]^+$ before the actual crystal structure was obtained. Also, the high electronic stability of NHC-substituted Au_{11} and all-NHC stabilized Au_{13} was manifested by DFT, and the simulated optical spectra were found to agree well with the experimental data. The calculations on binding energies and electronic charge distributions also revealed interesting differences between different binding sites for NHC.

The computational studies on the NHC-protected Au clusters showed the remarkably stronger binding of NHC on Au in comparison to the triphenyl phosphine ligands. The long-known analogues of the studied clusters incorporating phosphines as stabilizing ligands gives a reason to assume that the synthesis of more NHC-protected clusters will take place. This is already predicted by the DFT calculations for Au_6 and Au_{25} [126] of which the latter is already reported to be synthesized [127].

In article [PV], the electronic structure of the large silver cluster Ag_{374} was used in order to simulate the scanning tunnelling microscopy (STM) images via the local density of states (LDOS) calculated with DFT. Since we did not know about the orientation of the cluster on the substrate, we developed a numerical method to resolve it. The method is based on fitting the local extremum points of the height profiles of the STM images. The study presents, for the first time, successful and indisputable STM imaging of an atomically precise metal nanoparticle with sub-molecular resolution. With the help of STM simulations, we show that low temperatures are required in order to suppress the thermally induced transformations of the ligands and to achieve such a resolution. We belive that after this work, there is not a long way to go in resolving the atomistic structures of ligand-protected nanoparticles with real-space imaging. The real-space imaging of nanoparticles could provide a totally new tool in investigating the properties of nanoparticles and their correlations with sizes, shapes and structures.

To put it all together, the DFT-level electronic structure was analyzed and applied to explain properties of gold and silver nanoclusters. The results and the new methods introduced in this thesis have both produced a wider understanding of metal nanoclusters and paved the way for research of new types of metal nanoclusters and their applications. From my perspective, the future of computational nanoscience is increasingly moving towards the world of machine learning, that is able to predict for example new types of nanostructures and exchange-correlation functionals and produce novel multi-dimensional optimization algorithms [128, 129, 130, 131]. About metal nanoclusters, I would say that the field is heading towards commercial applications little by little since already dozens of structures are known well and can be characterized with systematic and standard methods. More fundamental research is still to be done on the mechanisms of catalytic processes and luminescent effects, not to mention the synthetic reaction pathways of clusters.

58

YHTEENVETO (FINNISH SUMMARY)

Kulta- ja hopeananoklusterit ovat atomirakenteeltaan täsmällisiä molekyylejä, jotka koostuvat yli kahdesta metalliatomin ytimestä ja sitä usein suojaavasta ja vakauttavasta orgaanisesta molekyylikerroksesta. Tässä väitöskirjassa kulta- ja hopeananoklustereiden tutkimus kohdistuu niiden elektronirakenteeseen, jota mallinnetaan tiheysfunktionaaliteorian tasolla. Tutkimuksessa kehitetyillä menetelmillä voidaan analysoida symmetristen klustereiden elektronirakennetta tarkemmin ja syvemmin kuin aikaisemmin. Työn soveltavammassa osassa elektronirakennelaskuja hyödynnettiin tutkittaessa kultaklustereita, joihin kiinnittyy uudentyyppinen suojaava molekyyli. Lisäksi työssä mallinnettiin suuren, suojatun hopeaklusterin pyyhkäisytunnelointimikroskooppikuvaa ja analysoitiin sitä varta vasten kehitetyllä hahmontunnistusmenetelmällä. Väitöskirjan työn tulokset ja uudet menetelmät sekä auttavat ymmärtämään metallinanoklustereiden ominaisuuksia yhä paremmin että edistävät niiden tutkimusta ja soveltamista käytännön ratkaisuihin.

REFERENCES

[1] P. Jena and Q. Sun, Super atomic clusters: Design rules and potential for building blocks of materials, *Chem. Rev.*, **118**(11), 5755–5870, (2018)

[2] T. Tsukuda and H. Häkkinen, *Protected Metal Clusters: From Fundamentals to Applications*, vol. 9. Elsevier, 1 ed., (2015)

[3] R. Jin, C. Zeng, M. Zhou, and Y. Chen, Atomically precise colloidal metal nanoclusters and nanoparticles: Fundamentals and opportunities, *Chem. Rev.*, **116**(18), 10346–10413, (2016)

[4] R. Jin, Atomically precise metal nanoclusters: stable sizes and optical properties, *Nanoscale*, **7**(5), 1549–1565, (2015)

[5] H. Qian, M. Zhu, Z. Wu, and R. Jin, Quantum sized gold nanoclusters with atomic precision, *Acc. Chem. Res.*, **45**(9), 1470–1479, (2012)

[6] M. C. Daniel and D. Astruc, Gold nanoparticles: Assembly, supramolecular chemistry, quantum-size-related properties, and applications toward biology, catalysis, and nanotechnology, *Chem. Rev.*, **104**(1), 293–346, (2004)

[7] Y. Xia, Y. Xiong, B. Lim, and S. Skrabalak, Shape-controlled synthesis of metal nanocrystals: Simple chemistry meets complex physics?, *Angew. Chem. Int. Ed.*, **48**(1), 60–103, (2009)

[8] J. L. West and N. J. Halas, Engineered nanomaterials for biophotonics applications: Improving sensing, imaging, and therapeutics, *Annu. Rev. Biomed. Eng.*, **5**(1), 285–292, (2003)

[9] R. L. Johnston, Metal nanoparticles and nanoalloys, *Frontiers of Nanoscience*, **3**, 1–42, (2012)

[10] G. Li and R. Jin, Atomically precise gold nanoclusters as new model catalysts, *Acc. Chem. Res.*, **46**(8), 1749–1758, (2013)

[11] G. Hogarth, S. E. Kabir, and E. Nordlander, Cluster chemistry in the noughties: new developments and their relationship to nanoparticles, *Dalton Trans.*, **39**(27), 6153–6174, (2010)

[12] G. Li, D.-e. Jiang, S. Kumar, Y. Chen, and R. Jin, Size dependence of atomically precise gold nanoclusters in chemoselective hydrogenation and active site structure, *ACS Catal.*, **4**(8), 2463–2469, (2014)

[13] S. Yamazoe, K. Koyasu, and T. Tsukuda, Nonscalable oxidation catalysis of gold clusters, *Acc. Chem. Res.*, **47**(3), 816–824, (2014)

[14] H. Yamamoto, H. Yano, H. Kouchi, Y. Obora, R. Arakawa, and H. Kawasaki, N,N-Dimethylformamide-stabilized gold nanoclusters as a catalyst for the reduction of 4-nitrophenol, *Nanoscale*, **4**(14), 4148–4154, (2012)

[15] O. Lopez-Acevedo, K. A. Kacprzak, J. Akola, and H. Häkkinen, Quantum size effects in ambient CO oxidation catalysed by ligand-protected gold clusters, *Nat. Chem.*, **2**, 329–334, (2010)

60

[16] Q.-Y. Zhang and L. Zhao, Chiral metal cluster and nanocluster complexes and their application in asymmetric catalysis, *Tetrahedron Lett.*, **59**(4), 310 – 316, (2018)

[17] A. George, E. S. Shibu, S. M. Maliyekkal, M. S. Bootharaju, and T. Pradeep, Luminescent, freestanding composite films of Au_{15} for specific metal ion sensing, *ACS Appl. Mater. Interfaces*, **4**(2), 639–644, (2012)

[18] C. J. Ackerson, P. D. Jadzinsky, J. Z. Sexton, D. A. Bushnell, and R. D. Kornberg, Synthesis and bioconjugation of 2 and 3 nm-diameter gold nanoparticles, *Bioconjugate Chem.*, **21**(2), 214–218, (2010)

[19] S. Basu, A. Paul, and A. Chattopadhyay, Zinc mediated crystalline assembly of gold nanoclusters for expedient hydrogen storage and sensing, *J. Mater. Chem. A*, **4**(4), 1218–1223, (2016)

[20] L.-Y. Chen, C.-W. Wang, Z. Yuan, and H.-T. Chang, Fluorescent gold nanoclusters: Recent advances in sensing and imaging, *Anal. Chem.*, **87**(1), 216–229, (2015)

[21] V. Marjomäki, T. Lahtinen, M. Martikainen, J. Koivisto, S. Malola, K. Salorinne, M. Pettersson, and H. Häkkinen, Site-specific targeting of enterovirus capsid by functionalized monodisperse gold nanoclusters, *Proc. Natl. Acad. Sci. U.S.A.*, **111**(4), 1277–1281, (2014)

[22] S. Xu, X. Lu, C. Yao, F. Huang, H. Jiang, W. Hua, N. Na, H. Liu, and J. Ouyang, A visual sensor array for pattern recognition analysis of proteins using novel blue-emitting fluorescent gold nanoclusters, *Anal. Chem.*, **86**(23), 11634–11639, (2014)

[23] H. Lin, L. Li, C. Lei, X. Xu, Z. Nie, M. Guo, Y. Huang, and S. Yao, Immune-independent and label-free fluorescent assay for Cystatin C detection based on protein-stabilized Au nanoclusters, *Biosens. Bioelectron.*, **41**, 256 – 261, (2013)

[24] Y.-S. Chen, H. Choi, and P. V. Kamat, Metal-cluster-sensitized solar cells. a new class of thiolated gold sensitizers delivering efficiency greater than 2%, *J. Am. Chem. Soc.*, **135**(24), 8822–8825, (2013)

[25] P. Oelhafen and A. Schüler, Nanostructured materials for solar energy conversion, *Solar Energy*, **79**(2), 110 – 121, (2005)

[26] A. S. Kuznetsov, V. K. Tikhomirov, M. V. Shestakov, and V. V. Moshchalkov, Ag nanocluster functionalized glasses for efficient photonic conversion in light sources, solar cells and flexible screen monitors, *Nanoscale*, **5**(21), 10065–10075, (2013)

[27] R. Bauld, M. Hesari, M. S. Workentin, and G. Fanchini, Tessellated gold nanostructures from $Au_{144}(SCH_2CH_2Ph)_{60}$ molecular precursors and their use in organic solar cell enhancement, *Nanoscale*, **6**(13), 7570–7575, (2014)

[28] A. Samanta, B. B. Dhar, and R. N. Devi, Ultrasmall gold cluster arrays encapsulated in silica nanospheres: Applications in fluorescence imaging and catalysis, *J. Phys. Chem. C*, **116**(2), 1748–1754, (2012)

[29] L. Zhang and E. Wang, Metal nanoclusters: New fluorescent probes for sensors and bioimaging, *Nano Today*, **9**(1), 132 – 157, (2014)

[30] L. Malatesta, L. Naldini, G. Simonetta, and F. Cariati, Triphenylphosphine-gold(0) gold(I) compounds, *Chem. Commun. (London)*, (11), 212–213, (1965)

[31] F. Cariati and L. Naldini, Trianionoeptakis (triarylphosphine) undecagold cluster compounds, *Inorganica Chim. Acta*, **5**(172), (1971)

[32] P. Jadzinsky, G. Calero, C. Ackerson, D. Bushnell, and R. Kornberg, Structure of a thiol monolayer-protected gold nanoparticle at 1.1 å resolution, *Science (New York, N.Y.)*, **318**, 430–433, (2007)

[33] W. D. Knight, K. Clemenger, W. A. de Heer, W. A. Saunders, M. Y. Chou, and M. L. Cohen, Electronic shell structure and abundances of sodium clusters, *Phys. Rev. Lett.*, **52**(24), 2141–2143, (1984)

[34] T. Martin, Shells of atoms, *Phys. Rep.*, **273**(4), 199 – 241, (1996)

[35] H. Yang, Y. Wang, H. Huang, L. Gell, L. Lehtovaara, S. Malola, H. Häkkinen, and N. Zheng, All-thiol-stabilized Ag_{44} and $Au_{12}Ag_{32}$ nanoparticles with single-crystal structures, *Nat. Comm.*, **4**(2422), (2013)

[36] R. Juarez-Mosqueda, S. Malola, and H. Häkkinen, Stability, electronic structure, and optical properties of protected gold-doped silver $Ag_{29-x}Au_x$ (x = 0-5) nanoclusters, *Phys. Chem. Chem. Phys.*, **19**(21), 13868–13874, (2017)

[37] Q. Li, S. Wang, K. Kirschbaum, K. J. Lambright, A. Das, and R. Jin, Heavily doped $Au_{25-x}Ag_x(SC_6H_{11})_{18}^-$ nanoclusters: silver goes from the core to the surface, *Chem. Commun.*, **52**(29), 5194–5197, (2016)

[38] M. Walter, J. Akola, O. Lopez-Acevedo, P. D. Jadzinsky, G. Calero, C. J. Ackerson, R. L. Whetten, H. Grönbeck, and H. Häkkinen, A unified view of ligand-protected gold clusters as superatom complexes, *Proc. Natl. Acad. Sci. U.S.A.*, **105**(27), 9157–9162, (2008)

[39] J. T. A. Gilmour and N. Gaston, On the involvement of d-electrons in superatomic shells: the group 3 and 4 transition metals, *Phys. Chem. Chem. Phys.*, **21**(15), 8035–8045, (2019)

[40] N. D. Lang and W. Kohn, Theory of metal surfaces: Work function, *Phys. Rev. B*, **3**(4), 1215–1223, (1971)

[41] N. D. Lang and W. Kohn, Surface-dipole barriers in simple metals, *Phys. Rev. B*, **8**(12), 6010–6012, (1973)

[42] M. Brack, The physics of simple metal clusters: self-consistent jellium model and semiclassical approaches, *Rev. Mod. Phys.*, **65**(3), 677–732, (1993)

[43] A. Fernando, K. L. Weerawardene, D. M., N. V. Karimova, and C. M. Aikens, Quantum mechanical studies of large metal, metal oxide, and metal chalcogenide nanoparticles and clusters, *Chem. Rev.*, **115**(12), 6112–6216, (2015)

[44] B. Yoon, P. Koskinen, B. Huber, O. Kostko, B. von Issendorff, H. Häkkinen, M. Moseler, and U. Landman, Size-dependent structural evolution and chemical reactivity of gold clusters, *ChemPhysChem*, **8**(1), 157–161, (2007)

[45] D. Schebarchov and N. Gaston, Throwing jellium at gallium — a systematic superatom analysis of metalloid gallium clusters, *Phys. Chem. Chem. Phys.*, **13**(47), 21109–21115, (2011)

[46] J. Akola, M. Walter, R. L. Whetten, H. Häkkinen, and H. Grönbeck, On the structure of thiolate-protected Au_{25}, *J. Am. Chem. Soc.*, **130**(12), 3756–3757, (2008)

[47] C. E. Briant, B. R. C. Theobald, J. W. White, L. K. Bell, D. M. P. Mingos, and A. J. Welch, Synthesis and X-ray structural characterization of the centred icosahedral gold cluster compound $[Au_{13}(PMe_2Ph)_{10}Cl_2](PF_6)_3$; the realization of a theoretical prediction, *J. Chem. Soc., Chem. Commun.*, (5), 201–202, (1981)

[48] M. W. Heaven, A. Dass, P. S. White, K. M. Holt, and R. W. Murray, Crystal structure of the gold nanoparticle $[N(C_8H_{17})_4][Au_{25}(SCH_2CH_2Ph)_{18}]$, *J. Am. Chem. Soc.*, **130**(12), 3754–3755, (2008)

[49] C. P. Joshi, M. S. Bootharaju, M. J. Alhilaly, and O. M. Bakr, $[Ag_{25}(SR)_{18}]^-$: The "golden" silver nanoparticle, *J. Am. Chem. Soc.*, **137**(36), 11578–11581, (2015)

[50] H. Qian, W. T. Eckenhoff, Y. Zhu, T. Pintauer, and R. Jin, Total structure determination of thiolate-protected Au_{38} nanoparticles, *J. Am. Chem. Soc.*, **132**(24), 8280–8281, (2010)

[51] N. Yan, N. Xia, L. Liao, M. Zhu, F. Jin, R. Jin, and Z. Wu, Unraveling the long-pursued Au_{144} structure by x-ray crystallography, *Sci. Adv.*, **4**(10), (2018)

[52] H. Yang, J. Yan, Y. Wang, H. Su, L. Gell, X. Zhao, C. Xu, B. K. Teo, H. Häkkinen, and N. Zheng, Embryonic growth of face-center-cubic silver nanoclusters shaped in nearly perfect half-cubes and cubes, *J. Am. Chem. Soc.*, **139**(1), 31–34, (2017)

[53] M. J. Alhilaly, M. S. Bootharaju, C. P. Joshi, T. M. Besong, A.-H. Emwas, R. Juarez-Mosqueda, S. Kaappa, S. Malola, K. Adil, A. Shkurenko, H. Häkkinen, M. Eddaoudi, and O. M. Bakr, $[Ag_{67}(SPhMe_2)_{32}(PPh_3)_8]^{3+}$: Synthesis, total structure, and optical properties of a large box-shaped silver nanocluster, *J. Am. Chem. Soc.*, **138**(44), 14727–14732, (2016)

[54] H. Häkkinen, The gold-sulfur interface at the nanoscale., *Nat. Chem.*, **4**(6), 443–455, (2012)

[55] L. C. McKenzie, T. O. Zaikova, and J. E. Hutchison, Structurally similar triphenylphosphine-stabilized undecagolds, $Au_{11}(PPh_3)_7Cl_3$ and $[Au_{11}(PPh_3)_8Cl_2]Cl$, exhibit distinct ligand exchange pathways with glutathione, *J. Am. Chem. Soc.*, **136**(38), 13426–13435, (2014)

[56] L. D. Menard, S.-P. Gao, H. Xu, R. D. Twesten, A. S. Harper, Y. Song, G. Wang, A. D. Douglas, J. C. Yang, A. I. Frenkel, R. G. Nuzzo, and R. W. Murray, Sub-nanometer Au monolayer-protected clusters exhibiting molecule-like electronic behavior: Quantitative high-angle annular dark-field scanning transmission electron microscopy and electrochemical characterization of clusters with precise atomic stoichiometry, *J. Phys. Chem. B*, **110**(26), 12874–12883, (2006)

[57] H. Qian, W. T. Eckenhoff, M. E. Bier, T. Pintauer, and R. Jin, Crystal structures of Au_2 complex and Au_{25} nanocluster and mechanistic insight into the conversion of polydisperse nanoparticles into monodisperse Au_{25} nanoclusters, *Inorg. Chem.*, **50**(21), 10735–10739, (2011)

[58] H. Yang, J. Yan, Y. Wang, H. Su, L. Gell, X. Zhao, C. Xu, B. K. Teo, H. Häkkinen, and N. Zheng, Embryonic growth of face-center-cubic silver nanoclusters shaped in nearly perfect half-cubes and cubes, *J. Am. Chem. Soc.*, **139**(1), 31–34, (2017)

[59] X.-K. Wan, Z.-W. Lin, and Q.-M. Wang, Au_{20} nanocluster protected by hemilabile phosphines, *J. Am. Chem. Soc.*, **134**(36), 14750–14752, (2012)

[60] Z.-J. Guan, J.-L. Zeng, S.-F. Yuan, F. Hu, Y.-M. Lin, and Q.-M. Wang, $Au_{57}Ag_{53}(CCPh)_{40}Br_{12}$: A large nanocluster with C_1 symmetry, *Angew. Chem. Int. Ed.*, **57**(20), 5703–5707, (2018)

[61] J.-L. Zeng, Z.-J. Guan, Y. Du, Z.-A. Nan, Y.-M. Lin, and Q.-M. Wang, Chloride-promoted formation of a bimetallic nanocluster $Au_{80}Ag_{30}$ and the total structure determination, *J. Am. Chem. Soc.*, **138**(25), 7848–7851, (2016)

[62] S.-S. Zhang, F. Alkan, H.-F. Su, C. M. Aikens, C.-H. Tung, and D. Sun, $[Ag_{48}(C-CtBu)_{20}(CrO_4)_7]$: An atomically precise silver nanocluster co-protected by inorganic and organic ligands, *J. Am. Chem. Soc.*, **141**(10), 4460–4467, (2019)

[63] T. J. Robilotto, J. Bacsa, T. G. Gray, and J. P. Sadighi, Synthesis of a trigold monocation: An isolobal analogue of $[H_3]^+$, *Angew. Chem. Int. Ed.*, **51**(48), 12077–12080, (2012)

[64] C. Sun, N. Mammen, S. Kaappa, P. Yuan, G. Deng, C. Zhao, J. Yan, S. Malola, K. Honkala, H. Häkkinen, B. K. Teo, and N. Zheng, Atomically precise, thiolated copper-hydride nanoclusters as single-site hydrogenation catalysts for ketones in mild conditions, *ACS Nano*, **13**(5), 5975–5986, (2019)

[65] W. Kohn and L. J. Sham, Self-consistent equations including exchange and correlation effects, *Phys. Rev.*, **140**(4A), A1133–A1138, (1965)

[66] S. M. Neidhart, B. M. Barngrover, and C. M. Aikens, Theoretical examination of solvent and R group dependence in gold thiolate nanoparticle synthesis, *Phys. Chem. Chem. Phys.*, **17**(12), 7676–7680, (2015)

[67] A. Sánchez-González, A. Munoz-Losa, S. Vukovic, S. Corni, and B. Mennucci, Quantum mechanical approach to solvent effects on the

optical properties of metal nanoparticles and their efficiency as excitation energy transfer acceptors, *J. Phys. Chem. C*, **114**(3), 1553–1561, (2010)

[68] L. Bernasconi, M. Sprik, and J. Hutter, Time dependent density functional theory study of charge-transfer and intramolecular electronic excitations in acetone-water systems, *J. Chem. Phys.*, **119**(23), 12417–12431, (2003)

[69] H. Häkkinen, M. Walter, and H. Grönbeck, Divide and protect: Capping gold nanoclusters with molecular gold-thiolate rings, *J. Phys. Chem. B*, **110**(20), 9927–9931, (2006)

[70] S. Malola, L. Lehtovaara, J. Enkovaara, and H. Häkkinen, Birth of the localized surface plasmon resonance in monolayer-protected gold nanoclusters, *ACS Nano*, **7**(11), 10263–10270, (2013)

[71] R. D. Senanayake, A. V. Akimov, and C. M. Aikens, Theoretical investigation of electron and nuclear dynamics in the $[Au_{25}(SH)_{18}]^{-1}$ thiolate-protected gold nanocluster, *J. Phys. Chem. C*, **121**(20), 10653–10662, (2017)

[72] D. Sholl and J. A. Steckel, *Density Functional Theory: A Practical Introduction*. John Wiley & Sons, Incorporated, (2009)

[73] R. Parr and W. Yang, Density-functional theory of the electronic structure of molecules, *Annu. Rev. Phys. Chem.*, (1995)

[74] K. Burke, Perspective on density functional theory, *J. Chem. Phys.*, **136**(15), 150901, (2012)

[75] A. D. Becke, Perspective: Fifty years of density-functional theory in chemical physics, *J. Chem. Phys.*, **140**(18), 18A301, (2014)

[76] U. von Barth, Basic density-functional theory—an overview, *Phys. Scr.*, **T109**, 9–39, (2004)

[77] P. Hohenberg and W. Kohn, Inhomogeneous electron gas, *Phys. Rev.*, **136**(3B), B864–B871, (1964)

[78] J. P. Perdew and Y. Wang, Accurate and simple analytic representation of the electron-gas correlation energy, *Phys. Rev. B*, **45**(23), 13244–13249, (1992)

[79] D. C. Langreth and M. J. Mehl, Beyond the local-density approximation in calculations of ground-state electronic properties, *Phys. Rev. B*, **28**(4), 1809–1834, (1983)

[80] A. D. Becke, Density-functional exchange-energy approximation with correct asymptotic behavior, *Phys. Rev. A*, **38**(6), 3098–3100, (1988)

[81] J. P. Perdew, M. Ernzerhof, and K. Burke, Generalized gradient approximation made simple, *Phys. Rev. Letters*, **77**(18), 3865–3868, (1996)

[82] J. Wellendorff, K. T. Lundgaard, A. Møgelhøj, V. Petzold, D. D. Landis, J. K. Nørskov, T. Bligaard, and K. W. Jacobsen, Density functionals for surface science: Exchange-correlation model development with bayesian error estimation, *Phys. Rev. B*, **85**(23), 235149, (2012)

[83] K. Lee, E. D. Murray, L. Kong, B. I. Lundqvist, and D. C. Langreth, Higher-accuracy van der Waals density functional, *Phys. Rev. B*, **82**(8), 081101, (2010)

[84] M. E. Casida, Time-dependent density functional response theory for molecules, in *Recent Advances in Density Functional Methods* (D. P. Chong, ed.), vol. 1, p. 155, World Scientific, Singapore, (1995)

[85] K. Yabana and G. F. Bertsch, Time-dependent local-density approximation in real time, *Phys. Rev. B*, **54**(7), 4484–4487, (1996)

[86] K. Yabana, T. Nakatsukasa, J.-I. Iwata, and G. F. Bertsch, Real-time, real-space implementation of the linear response time-dependent density-functional theory, *Phys. Status Solidi B*, **243**(5), 1121–1138, (2006)

[87] L. Lehtovaara and M. A. L. Marques, Simple preconditioning for time-dependent density functional perturbation theory, *J. Chem. Phys.*, **135**(1), 014103, (2011)

[88] J. Enkovaara, C. Rostgaard, J. J. Mortensen, J. Chen, M. Dulak, L. Ferrighi, J. Gavnholt, C. Glinsvad, V. Haikola, H. A. Hansen, H. H. Kristoffersen, M. Kuisma, A. H. Larsen, L. Lehtovaara, M. Ljungberg, O. Lopez-Acevedo, P. G. Moses, J. Ojanen, T. Olsen, V. Petzold, N. A. Romero, J. Stausholm-Möller, M. Strange, G. A. Tritsaris, M. Vanin, M. Walter, B. Hammer, H. Häkkinen, G. K. H. Madsen, R. M. Nieminen, J. K. Nørskov, M. Puska, T. T. Rantala, J. Schiötz, K. S. Thygesen, and K. W. Jacobsen, Electronic structure calculations with GPAW: a real-space implementation of the projector augmented-wave method., *J. Phys. Condens. Matter*, **22**(25), 253202, (2010)

[89] GPAW Web page: https://wiki.fysik.dtu.dk/gpaw/index.html

[90] P. E. Blöchl, Projector augmented-wave method, *Phys. Rev. B*, **50**(24), 17953–17979, (1994)

[91] J. F. Cornwell, *Group Theory in Physics: An Introduction*. Elsevier Science and Technology, (1997)

[92] K. C. Molloy, *Group Theory for Chemists: Fundamental Theory and Applications*. Woodhead Publishing Limited, (2013). Second Edition

[93] W. Humphrey, A. Dalke, and K. Schulten, VMD – Visual Molecular Dynamics, *J. Molec. Graphics*, **14**, 33–38, (1996)

[94] R. F. W. Bader, *Atoms in Molecules: A Quantum Theory*. Oxford University Press, New York, (1990)

[95] W. Tang, E. Sanville, and G. Henkelman, A grid-based bader analysis algorithm without lattice bias, *J. Phys. Condens. Matter*, **21**(8), 084204, (2009)

[96] Bader Charge Analysis web page: http://theory.cm.utexas.edu/henkelman/code/bader/

[97] J. Tersoff and D. R. Hamann, Theory and application for the scanning tunneling microscope, *Phys. Rev. Lett.*, **50**(25), 1998–2001, (1983)

[98] A. H. Larsen, J. J. Mortensen, J. Blomqvist, I. E. Castelli, R. Christensen, M. Dułak, J. Friis, M. N. Groves, B. Hammer, C. Hargus, E. D. Hermes, P. C. Jennings, P. B. Jensen, J. Kermode, J. R. Kitchin, E. L. Kolsbjerg, J. Kubal, K. Kaasbjerg, S. Lysgaard, J. B. Maronsson, T. Maxson, T. Olsen, L. Pastewka, A. Peterson, C. Rostgaard, J. Schiøtz, O. Schütt, M. Strange, K. S. Thygesen, T. Vegge, L. Vilhelmsen, M. Walter, Z. Zeng, and K. W. Jacobsen, The atomic simulation environment — a python library for working with atoms, *J. Phys. Condens. Matter*, **29**(27), 273002, (2017)

[99] ASE Web page: https://wiki.fysik.dtu.dk/ase/index.html

[100] W. A. Hofer, A. S. Foster, and A. L. Shluger, Theories of scanning probe microscopes at the atomic scale, *Rev. Mod. Phys.*, **75**(4), 1287–1331, (2003)

[101] E. Jones, T. Oliphant, P. Peterson, *et al.*, SciPy: Open source scientific tools for Python, (2001–). http://www.scipy.org/

[102] K. S. Arun, T. S. Huang, and S. D. Blostein, Least-squares fitting of two 3-D point sets, *IEEE Trans. Pattern Anal. Mach. Intell.*, **PAMI-9**(5), 698–700, (1987)

[103] M. Beck, *Quantum Mechanics : Theory and Experiment*. New York : Oxford University Press, (2012)

[104] H. Häkkinen, M. Moseler, O. Kostko, N. Morgner, M. A. Hoffmann, and B. v. Issendorff, Symmetry and electronic structure of noble-metal nanoparticles and the role of relativity, *Phys. Rev. Lett.*, **93**(9), 093401, (2004)

[105] D. Schooss, M. N. Blom, J. H. Parks, B. v. Issendorff, H. Haberland, and M. M. Kappes, The structures of Ag_{55}^+ and Ag_{55}^-: Trapped ion electron diffraction and density functional theory, *Nano Lett.*, **5**(10), 1972–1977, (2005)

[106] J. Li, X. Li, H.-J. Zhai, and L.-S. Wang, Au_{20}: A tetrahedral cluster, *Science*, **299**(5608), 864–867, (2003)

[107] H. Yang, Y. Wang, X. Chen, X. Zhao, L. Gu, H. Huang, J. Yan, C. Xu, G. Li, J. Wu, A. J. Edwards, B. Dittrich, Z. Tang, D. Wang, L. Lehtovaara, H. Häkkinen, and N. Zheng, Plasmonic twinned silver nanoparticles with molecular precision, *Science*, **7**, 12809, (2016)

[108] L. Ren, P. Yuan, H. Su, S. Malola, S. Lin, Z. Tang, B. K. Teo, H. Häkkinen, L. Zheng, and N. Zheng, Bulky surface ligands promote surface reactivities of $[Ag_{141}X_{12}(S\text{-}Adm)_{40}]^{3+}$ (X = Cl, Br, I) nanoclusters: Models for multiple-twinned nanoparticles, *J. Am. Chem. Soc.*, **139**(38), 13288–13291, (2017)

[109] S. Kenzler, C. Schrenk, A. R. Frojd, H. Häkkinen, A. Z. Clayborne, and A. Schnepf, $Au_{70}S_{20}(PPh_3)_{12}$: an intermediate sized metalloid gold cluster stabilized by the Au_4S_4 ring motif and Au-PPh_3 groups, *Chem. Commun.*, **54**(3), 248–251, (2018)

[110] S. Kenzler, C. Schrenk, and A. Schnepf, $Au_{108}S_{24}(PPh_3)_{16}$: A highly symmetric nanoscale gold cluster confirms the general concept of metalloid clusters, *Angew. Chem. Int. Ed.*, **56**(1), 393–396, (2017)

[111] O. Lopez-Acevedo, J. Akola, R. L. Whetten, H. Grönbeck, and H. Häkkinen, Structure and bonding in the ubiquitous icosahedral metallic gold cluster $Au_{144}(SR)_{60}$, *J. Phys. Chem. C*, **113**(13), 5035–5038, (2009)

[112] S. Vergara, D. A. Lukes, M. W. Martynowycz, U. Santiago, G. Plascencia-Villa, S. C. Weiss, M. J. de la Cruz, D. M. Black, M. M. Alvarez, X. López-Lozano, C. O. Barnes, G. Lin, H.-C. Weissker, R. L. Whetten, T. Gonen, M. J. Yacaman, and G. Calero, MicroED structure of $Au_{146}(p\text{-}MBA)_{57}$ at subatomic resolution reveals a twinned FCC cluster, *J. Phys. Chem. Letters*, **8**(22), 5523–5530, (2017)

[113] C. Zeng, Y. Chen, K. Kirschbaum, K. J. Lambright, and R. Jin, Emergence of hierarchical structural complexities in nanoparticles and their assembly, *Science*, **354**(6319), 1580–1584, (2016)

[114] A. Gelessus, W. Thiel, and W. Weber, Multipoles and symmetry, *J. Chem. Educ.*, **72**(6), 505–508, (1995)

[115] R. Rüger, E. van Lenthe, Y. Lu, J. Frenzel, T. Heine, and L. Visscher, Efficient calculation of electronic absorption spectra by means of intensity-selected time-dependent density functional tight binding, *J. Chem. Theory Comput.*, **11**(1), 157–167, (2015)

[116] P. de Frémont, N. Marion, and S. P. Nolan, Carbenes: Synthesis, properties, and organometallic chemistry, *Coord. Chem. Rev.*, **253**(7), 862 – 892, (2009)

[117] A. V. Zhukhovitskiy, M. J. MacLeod, and J. A. Johnson, Carbene ligands in surface chemistry: From stabilization of discrete elemental allotropes to modification of nanoscale and bulk substrates, *Chem. Rev.*, **115**(20), 11503–11532, (2015)

[118] K. Salorinne, R. W. Y. Man, C.-H. Li, M. Taki, M. Nambo, and C. M. Crudden, Water-soluble N-heterocyclic carbene-protected gold nanoparticles: Size-controlled synthesis, stability, and optical properties, *Angew. Chem. Int. Ed.*, **56**(22), 6198–6202, (2017)

[119] C. A. Smith, M. R. Narouz, P. A. Lummis, I. Singh, A. Nazemi, C.-H. Li, and C. M. Crudden, N-heterocyclic carbenes in materials chemistry, *Chem. Rev.*, **119**(8), 4986–5056, (2019)

[120] D. Enders, O. Niemeier, and A. Henseler, Organocatalysis by N-heterocyclic carbenes, *Chem. Rev.*, **107**(12), 5606–5655, (2007)

[121] C. Crudden and D. Allen, Stability and reactivity of N-heterocyclic carbene complexes, *Coord. Chem. Rev.*, **248**, 2247–2273, (2004)

[122] F. Glorius, *N-Heterocyclic Carbenes in Transition Metal Catalysis.* Springer-Verlag Berlin Heidelberg, 1 ed., (2007)

[123] L. Jin, D. S. Weinberger, M. Melaimi, C. E. Moore, A. L. Rheingold, and G. Bertrand, Trinuclear gold clusters supported by cyclic

(alkyl)(amino)carbene ligands: Mimics for gold heterogeneous catalysts, *Angew. Chem. Int. Ed.*, **53**(34), 9059–9063, (2014)

[124] C. M. Aikens, Effects of core distances, solvent, ligand, and level of theory on the tddft optical absorption spectrum of the thiolate-protected Au_{25} nanoparticle, *J. Phys. Chem. A*, **113**(40), 10811–10817, (2009)

[125] O. Lopez-Acevedo, P. A. Clayborne, and H. Häkkinen, Electronic structure of gold, aluminum, and gallium superatom complexes, *Phys. Rev. B*, **84**, 035434, (2011)

[126] D. MacLeod Carey and A. Munoz-Castro, Evaluation of N-heterocyclic carbene counterparts of classical gold clusters; bonding properties of octahedral CAu_6, icosahedral $Au_{13}Cl_2$, and bi-icosahedral $Au_{25}Cl_2$ cores from relativistic DFT calculations, *J. Phys. Chem. C*, **123**(19), 12466–12473, (2019)

[127] H. Shen, G. Deng, S. Kaappa, S. Malola, B. K. Teo, H. Häkkinen, N. Zheng, T. Tan, Y. Han, and S. Lin, Highly Robust but Surface-Active: N-Heterocyclic Carbene-Stabilized Au_{25} Nanocluster as a Homogeneous Catalyst, (2019). doi:10.26434/chemrxiv.8015651.v1

[128] C. Zeni, K. Rossi, A. Glielmo, A. Fekete, N. Gaston, F. Baletto, and A. De Vita, Building machine learning force fields for nanoclusters, *J. Chem. Phys.*, **148**(24), 241739, (2018)

[129] K. Ryan, J. Lengyel, and M. Shatruk, Crystal structure prediction via deep learning, *J. Am. Chem. Soc.*, **140**(32), 10158–10168, (2018)

[130] A. P. Bartók, S. De, C. Poelking, N. Bernstein, J. R. Kermode, G. Csányi, and M. Ceriotti, Machine learning unifies the modeling of materials and molecules, *Sci. Adv.*, **3**(12), (2017)

[131] O. Isayev, C. Oses, C. Toher, E. Gossett, S. Curtarolo, and A. Tropsha, Universal fragment descriptors for predicting properties of inorganic crystals, *Nat. Comm.*, **8**(15679), (2017)

ORIGINAL PAPERS

PI

ANALYSIS OF THE ELECTRONIC STRUCTURE OF NON-SPHERICAL LIGAND-PROTECTED METAL NANOCLUSTERS: THE CASE OF A BOX-LIKE AG$_{67}$

by

Rosalba Juarez-Mosqueda, Sami Kaappa, Sami Malola &
Hannu Häkkinen (2016)

The Journal of Physical Chemistry C, 121(20), 10698–10705

Analysis of the Electronic Structure of Non-Spherical Ligand-Protected Metal Nanoclusters: The Case of a Box-Like Ag₆₇

Rosalba Juarez-Mosqueda,[†,§] Sami Kaappa,[†,§] Sami Malola,[†] and Hannu Häkkinen[*,†,‡]

†Department of Physics and ‡Department of Chemistry, Nanoscience Center, University of Jyväskylä, FI-40014 Jyväskylä, Finland

ⓢ Supporting Information

ABSTRACT: In this work we introduce a new strategy to investigate the electronic shell structure of ligand-protected metal nanoclusters of polyhedral core shape. The central idea is to identify the symmetry of the Kohn−Sham molecular orbitals of an atomistic structure based on their projection onto the electronic states of a jellium system with a similar shape of the background charge density. Herein, we study the connection between a reduced atomistic model of the recently reported box-like $[Ag_{67}(SR)_{32}(PR_3)_8]^{3+}$ nanocluster and a jellium box consisting of 32 free electrons. With this approach, we determine the symmetry of electronic states of the metal core and identify those that are involved in the lowest metal-to-metal electronic transitions. Furthermore, we define a new transition selection rule for ligand-protected metal nanoclusters with rectangular cuboid-like core. This rule differs from the one of a particle in an infinitely deep 3D potential well. The approach presented here is complementary to the angular momentum analysis of "superatom orbitals" of spherical or near spherical metal nanoclusters and opens the door to understand and predict the electronic properties and stability of several existent and new ligand-protected metal nanoclusters with nonspherical cores.
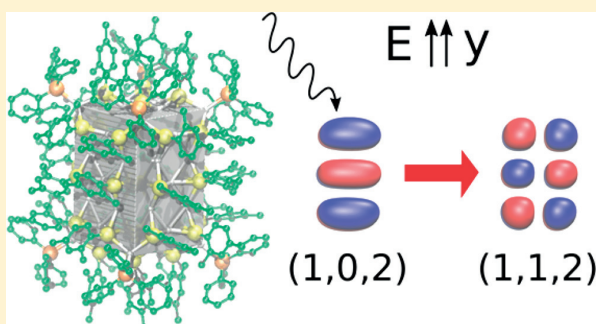
■ INTRODUCTION

Valence electrons of small 1−2 nm sized metal nanoclusters consisting of less than a few hundred atoms are often delocalized over the full cluster volume, leading to quantized valence electron states.[1−4] The size and the shape of the confinement strongly affect the energies and symmetries of these states. Occupying the states by the Pauli principle gives a sequence of electron-shell-closing numbers, which for spherical or near-spherical systems resemble closely to shell-filling numbers of ordinary atoms. Hence the terms of "artificial atom" or "superatom" have been used in the context of cluster physics already for a long time.[1−5] Despite the stability factors, the low coordinated atoms at the surface of small nanoclusters tend to react with foreign atoms and molecules especially in nonclosed shell nanoclusters.[6−8] Less reactive surfaces can be achieved with ligated metal nanoparticles that all have a common structure of a metallic core overlaid by organic molecules such as thiols, phosphines, and alkynyls. Synthesis of the ligated metal nanoclusters can be made with molecular precision and the choice of ligands affects their overall structure, size and physical, chemical, and biological properties.[9−16] As a consequence of the stabilizing factors from the metal−ligand interface, ligand-protected metal nanoclusters can also be very stable in nonspherical shapes.[17−20] Developments in synthesis of stable nonspherical shaped nanoclusters extend the already vast variety of intriguing properties of these systems to be used in different applications.

Häkkinen and collaborators[21,22] laid out two principles concerning both the geometric and electronic structure of ligand-protected metal nanoclusters in 2006−2008. First, the atomic structure of theses clusters can generally be understood by the "Divide and Protect" concept, whereby the metal atoms (M) could be found in the cluster in two chemical (formal oxidation) states, in the neutral state in the central metal core and in the +1 state if bound to electron-withdrawing ligands (X) inside the ligand layer.[21] Second, as the chemical formula of these clusters can be written in a simplest form as $(M_m X_x L_s)^q$, where additionally L denotes a weakly (coordinating) bound ligand and q a possible overall charge of the cluster, the number of the "metallic" ("free") electrons n in the system can be calculated simply from the equation

$$n = m - x - q$$

when M is assumed to be a monovalent metal and X a one-electron withdrawing ligand.[22] Generalisation of the equation to multivalent metals and ligands is straightforward.

The number of electron withdrawing ligands and the number of valence electrons of metal atoms in the nanocluster thus determine the electronic structure, which includes, among all,

the superatomic orbitals delocalized over the metallic core. For the spherical nanoclusters, electronic shells close when the free valence electrons of the superatom system equals magic numbers 2, 8, 18, 34, 58, 92, 138,... indicating increased electronic stability. For a spherical ligand-protected nanocluster, the projection of the electron states onto spherical harmonics directly reveals their superatomic nature.[22] To date, the applicability of this approach has been restricted to spherical symmetry, and hence to spherical and close-to-spherical nanoclusters.

Recently, several ligand-protected metal nanoclusters have been reported that are far from spherical shape.[17−20] As an example, Alhilaly et al.[17] synthesized an unprecedented box-like shaped silver nanocluster formed by 67 Ag atoms (Ag_{67}) protected by thiol and phosphine ligands. This new nanocluster, formulated as $[Ag_{67}(SPhMe_2)_{32}(PPh_3)_8]^{3+}$, has been fully characterized by X-ray diffraction and electrospray ionization mass spectrometry (ESI-MS). The authors attribute the shape and stability of the cluster partly to the thiols, but most importantly to the phosphine ligands at each corner of the box. They also reported the optical spectrum of this $[Ag_{67}(SPhMe_2)_{32}(PPh_3)_8]^{3+}$ compound, which shows highly structured absorption peaks in the visible region. Their results underline the importance of the protecting ligands in determining the shape and size of the cluster core.

In this work, we extend the analysis of electronic shells of spherical superatoms to nonspherical shapes. The idea is based on the projection of the molecular orbitals of the atomistic cluster onto quantum states of a jellium system with similar background charge density as in the metal core of the real system. Using this approach we analyze the symmetries of the electronic states for the box-like $[Ag_{67}(SPhMe_2)_{32}(PPh_3)_8]^{3+}$ nanocluster[17] using a simplified $[Ag_{67}(SH)_{32}(PH_3)_8]^{3+}$ model. Moreover, we analyze the electronic transitions related to the absorption peaks of the highly structured optical spectrum and obtain a new transition selection rule for ligand protected metal nanoclusters with rectangular cuboid-like core. In contrast to the transition selection rule for a particle in a 3D infinite potential well, this new rule considers the effect of the electron−electron interactions and the finite potential well of the real nanoclusters.

■ COMPUTATIONAL METHODS

The electronic structure calculations of both the atomistic $[Ag_{67}(SH)_{32}(PH_3)_8]^{3+}$ and the jellium models were performed using the projector augmented-wave (PAW) method as implemented in the GPAW code-package (grid-based projector-augmented wave method).[23,24] The wave functions were represented by using a real-space with grid spacing of 0.2 Å. The coordinates of the atomistic model were built from the experimental $[Ag_{67}(SPhMe_2)_{32}(PPh_3)_8]^{3+}$ crystal structure[17] by replacing the true ligands with −SH and −PH$_3$ groups. All the atomic positions in the $[Ag_{67}(SH)_{32}(PH_3)_8]^{3+}$ model were optimized using the convergence criterion of 0.05 eV/Å as a maximum value for the forces acting on individual atoms.

Based on the electron count formula for ligand protected nanoclusters,[22] the $[Ag_{67}(SR)_{32}(PR_3)_8]^{3+}$ system consists of 32 superatom electrons ($n = 67-32 - (+3) = 32$), since the phosphine ligands do not withdraw or donate electrons to the system. The jellium model was therefore designed as 32 electrons confined in an ion density box of the same shape and dimensions as the metal core of the atomistic model (see Figure 1). To take the effect of the ligand layer into account in the jellium model, an ion charge of $+44e$ was used to yield an effective charge of $+12e$ ($+44e − 32e = +12e$, e stands for the positive unit charge). The value $+12e$ was obtained from the Bader charge analysis[25] by taking the sum of the atomic charges of the sixty-seven silver atoms in the $[Ag_{67}(SH)_{32}(PH_3)_8]^{3+}$ cluster.

The ground state calculations for the $[Ag_{67}(SH)_{32}(PH_3)_8]^{3+}$ and jellium models were performed using the Kohn−Sham formulation of the density functional theory (DFT) as implemented in GPAW. The exchange and correlation energy for the atomistic calculations was approximated by using the generalized gradient-corrected PBE[26] functional. The jellium calculations were performed using local-density approximation (LDA)[27] that, in contrast to the PBE functional, neglects the gradient of the electron density. Nevertheless, this effect is very small in jellium calculations since the gradients are relatively small.

To identify symmetry of the electronic states, the Kohn−Sham molecular orbitals of the atomistic model were projected onto the jellium states and the overlaps were calculated through the integrals $O_{ij} = \int \phi_i(\vec{r})\psi_j(\vec{r}) \, d\vec{r}$, where $\psi_j(\vec{r})$ and $\phi_i(\vec{r})$ are the sets of wave functions from the atomistic and jellium calculations, respectively (see more details in the Supporting Information (SI)). The square of the overlap between $\psi_j(\vec{r})$ and $\phi_i(\vec{r})$ was used as a quantitative measure in characterizing the symmetry of the atomic state. The nodal multiplicities in the jellium model were defined by visual inspection as (n_x, n_y, n_z), where n_x, n_y, and n_z indicate the number of nodes along the x, y, and z dimensions of the models shown in Figure 1.
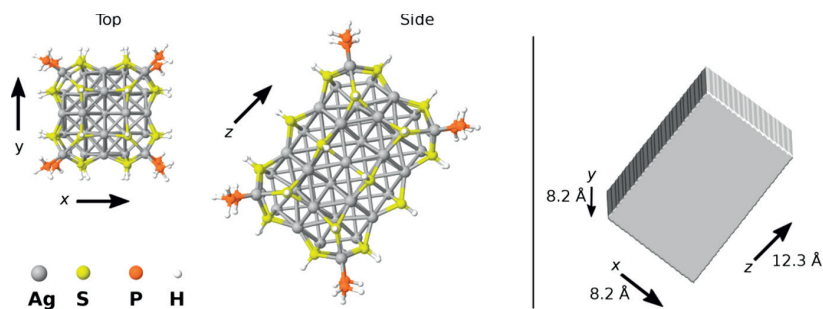

Figure 1. (Left) top and side views of the atomistic $[Ag_{67}(SH)_{32}(PH_3)_8]^{3+}$ model. (Right) shape of the background density of the jellium model consisting of 32 electrons and a net charge of $+12e$. The dimensions of the jellium system correspond to the dimensions of the silver core in the atomistic model.

The linear response time-dependent density functional theory (LR-TDDFT) was used to calculate the optical spectrum and the oscillator strengths of the individual transitions.[28,29] The electronic transitions were analyzed using the transition contribution maps (TCMs) based on the time-dependent density functional perturbation theory (TD-DFPT)[30,31] by using the photon with the same energy as the absorption peak of interest and a dipole moment μ directed either along the longest dimension (z) of the metal core or along one of the shorter ones (y) (see Figure 1). All the excited state calculations were performed using the PBE functional.

■ RESULTS AND DISCUSSION

In the optimized $[Ag_{67}(SH)_{32}(PH_3)_8]^{3+}$ nanocluster, the Ag–Ag bond distances are ~1% larger than the ones from the experimental structure. The S–Ag and P–Ag bonds, however, retained the same lengths (2.5 and 2.4 Å, respectively) as in the crystal structure. The comparison between the experimental and the calculated optical spectra shown in Figure 2,
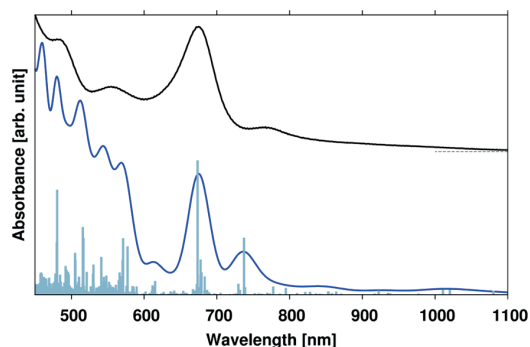

Figure 2. (Black) Experimental absorption spectrum of the $[Ag_{67}(SPhMe_2)_{32}(PPh_3)_8]^{3+}$ nanocluster, and (blue) the calculated spectrum of the $[Ag_{67}(SH)_{32}(PH_3)_8]^{3+}$ model. (Gray) The oscillator strength of individual transitions is plotted as delta-function-like peaks. The calculated spectrum is the sum of Gaussian smoothed individual transitions (width of 0.05 eV). The oscillator strengths and calculated spectrum are red-shifted by 87 nm to compare the main spectral features with the experimental data.

reveals that removing the phenyl ligands does not modify the main spectral features within the range of 650–1100 nm, but it significantly changes the spectrum at higher energy region. Moreover, the lack of the true ligands produces a blue-shifting of the spectrum by 87 nm as a consequence of the confinement of the electron density within the boundaries of the metal core. This was already reported in the paper of Alhilaly et al.[17]

To understand the nature of the molecular orbitals delocalized inside the metal core and to identify those that are involved in the electronic transitions with high oscillator strengths, we analyzed the symmetry of the electronic states formed in a jellium system of same charge density, shape, and size as in the metal core of the $[Ag_{67}(SH)_{32}(PH_3)_8]^{3+}$ nanocluster. The symmetry of the jellium states was determined by the number of nodes along the x, y, and z dimensions of the jellium model. The total number of nodes is given then by the sum of the nodal multiplicities as $n_x + n_y + n_z$. The projection of the Kohn–Sham molecular orbitals of the $[Ag_{67}(SH)_{32}(PH_3)_8]^{3+}$ nanocluster onto the "clean" jellium states allowed us to identify the symmetry of the metal core states. This new method is

comparable to the known approach of projecting the wave functions to spherical harmonics, but also allows studying nonspherical nanoclusters. The assignment of the state symmetries is based on the weights given by the overlap integrals as described in the SI text. In Figure 3 we depict the shape and indicate the symmetry of nine occupied molecular orbitals (HOMO to HOMO−8, and HOMO−446), and 15 unoccupied ones (LUMO to LUMO+13, and LUMO+17). The values (between 0 and 1) above the arrows correspond to the highest weights found from the square of the overlap integrals. Remembering that the overlap integrals were calculated for whole nanocluster including the ligand layer, the values between 0.19 and 0.67 in Figure 3 indicate a good correspondence between the symmetries of the jellium state and the corresponding molecular orbital of the $[Ag_{67}(SH)_{32}(PH_3)_8]^{3+}$ nanocluster. In comparison, the states located between −1.0 eV and −2.25 eV show very low overlap values (below 0.08) to any of the jellium states. Therefore, these states are assigned as ligand states (LS). An exceptional case is observed for the molecular orbitals at −0.84 eV and −0.83 eV whose symmetry is uncertain. These two states together resemble the jellium state with nodal multiplicities (1,1,1), which seems to get split in the atomistic system.

The weights from overlap integrals were broadened (with a Gaussian function of width = 0.01 eV) and plotted as projected local density of states (PLDOS) for sets of electronic states with the same number of total nodes. The PLDOS and TCMs are plotted together in Figure 4 to gain insight into the metal-to-metal electronic transitions analyzed for the spectral peaks at 587 nm (2.11 eV) and 648 nm (1.91 eV). The excitation profiles were analyzed along the y- and z- dimensions of the atomistic model by using a laser field with dipole moment μ_y and μ_z in each respective case. The transitions are labeled with the letters A−N in the TCMs.

The relative intensities of the electronic transitions (calculated with respect to the total intensity) are shown in percentages in Table 1. The results indicate that at 587 nm (2.11 eV), the most intense metal-to-metal electronic transitions (with relative intensity >7%) occurring along the y dimension involve the states with nodal multiplicities (2,0,1) → (0,3,1), and (0,2,1) → (0,3,1). Using the same photon energy but a dipole moment oriented along the z dimension of the metal core, the strongest transitions are between the states with symmetries (1,1,1) → (1,1,2), (2,0,0) → (2,0,3), and (0,0,3) → (0,0,4). Similarly, for the absorption peak at 648 nm (1.91 eV) the transitions in the metal core along the y dimension involve the states with nodal multiplicities (1,1,1) → (3,0,0), (0,2,0) → (0,3,0), and (1,1,1) → (1,2,1), and along the z dimension the transitions are between the states with symmetries (2,0,0) → (2,0,3) (see Table 1). The electronic transitions for the spectral peaks at 751 nm (1.65 eV) and 928 nm (1.33 eV) are also analyzed and the results are provided in the SI (see Figure S1 and Table S1).

With the exception of the cases that involve the states labeled with the (1,1,1) symmetry, in the metal-to-metal electronic transitions displayed in Table 1, the total number of nodes change from the ground state to the excited state by an odd number. Moreover, the number of nodes in the direction of the applied field changes by either ±1 or 3 and also, in many cases, by an even number in any of the other two directions. These results are partially in agreement with the transitions selection rule of a particle in an infinite 3D well model (see derivation in SI). The difference is that while the infinite well model predicts
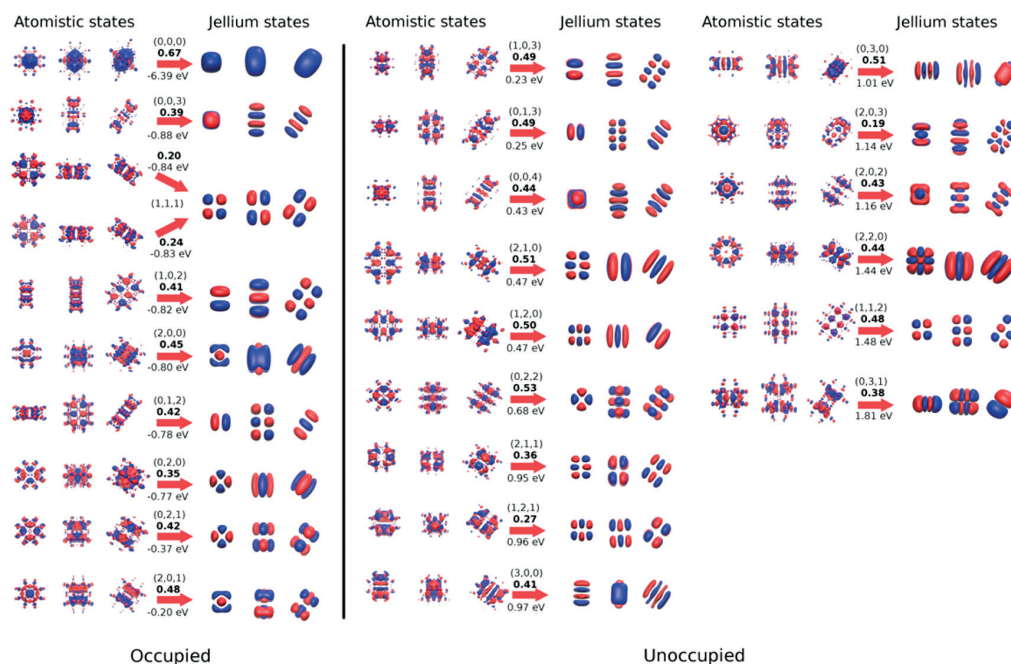
Figure 3. (Left) Occupied and (right) unoccupied Kohn−Sham states of the atomistic $[Ag_{67}(SH)_{32}(PH_3)_8]^{3+}$ and jellium models located close to the HOMO−LUMO region. The energy and nodal multiplicities (n_x, n_y, n_z) of the states are indicated below and above the arrows. The weights of the overlap between the molecular orbitals and the jellium quantum states are indicated in bold letters above the arrow. The states with $(2,0,1)$ and $(1,0,3)$ symmetry are the HOMO and LUMO, respectively. The most spherical state with no nodes $(0,0,0)$ is located 6.39 eV below the Fermi level (first in the list on the left).

allowed transitions when only one node multiplicity changes (the one in the direction of the field) by an odd number, here we obtained that a simultaneous change by an even number in any of the other two nodal multiplicities is also allowed. The reasons for this are the electron−electron interactions and the finite potential well of the real nanocluster that cause a distortion of the wave functions leading to nonzero transition dipole moment integrals. This is illustrated in Figure 5 in an example that shows the wave functions of the states with symmetries $(0,0,0)$ and $(0,2,1)$ calculated from the atomistic and jellium models, and compares them with the analytical solutions of infinite 3D potential well. The product of the $(0,0,0)$ and $(0,2,1)$ states is plotted at the right side of the figure, and the value of the integral relevant to the transition dipole moment (see SI) is also given for each case. Based on the infinite potential well model, transitions akin to $(0,0,0) \rightarrow (0,2,1)$ are forbidden since the integral over the product of the two curves is 0. However, in the jellium and atomistic calculations, the integral does not vanish as a consequence of the distortion of the wave functions beyond the box borders, indicating that this type of transitions is allowed. The derivation of the transition selection rule for a particle in a 3D infinite well is contrasted with the selection rule of more realistic models in the SI text. Briefly, the results of that analysis can be summarized as follows. The selection rules for an atomistic cluster with a box-like core shape become the following: (i) such transitions are forbidden where, in the direction of the electric field, the number of nodes is changed by an even number, (ii) in addition, such transitions are forbidden, where one other number of nodes changes by an odd number. In combination, this means that for an allowed transition, exactly in one direction (of the three possibilities) the number of nodes changes by an

odd number. Thus, the sum of the nodal multiplicities changes by an odd number (since odd + even + even = odd).

Since each delocalized state in the atomic cluster has either an even or an odd number of nodes in each direction x, y, z, there are in total eight combinations. Nonzero transitions between the states can be organized in an octant-shape "topography map"; see Figure S2, which also demonstrates again the TCM analysis of the 2.11 eV absorption peak when the occupied and empty states are classified by (odd/even ; odd/even ; odd/even) combinations.

Although in this work we focus on the particular case of the box-like $[Ag_{67}(SR)_{32}(PR_3)_8]^{3+}$ nanocluster, the strategy presented here to analyze the electronic states of an atomistic structure based on their projection onto the states of a jellium system is a general approach that can be applied to metal nanoclusters of any core shape or aspect ratio. As an example, a few recently reported ligand-stabilized noble metal nanoclusters have polyhedral core shapes such as bipyramidal or Ino's deca-hedral shapes.[32] Nodal symmetries of the states in the metal core in such cases can be expected to match better with jellium states in a volume of a similar background shape rather than spherical superatom angular momentum states.[1]

Finally, we performed electronic calculations on two fictive box-like structures with equally good geometric stability and coordination as in the synthesized $[Ag_{67}(SPhMe_2)_{32}(PPh_3)_8]^{3+}$ nanocluster. In these two systems, a block of $Ag_{21}(SH)_8$ atoms have been added or removed to/from the $[Ag_{67}(SH)_{32}(PH_3)_8]^{3+}$ model to form the compounds with chemical formulas $[Ag_{46}(SH)_{24}(PH_3)_8]^{2+}$ and $[Ag_{88}(SH)_{40}(PH_3)_8]^{2−}$, whose structures are shown in Figure 6. Based on the electron counting formula, the number of valence electrons in the former is 20, and 50 in the latter. For these two clusters, we get
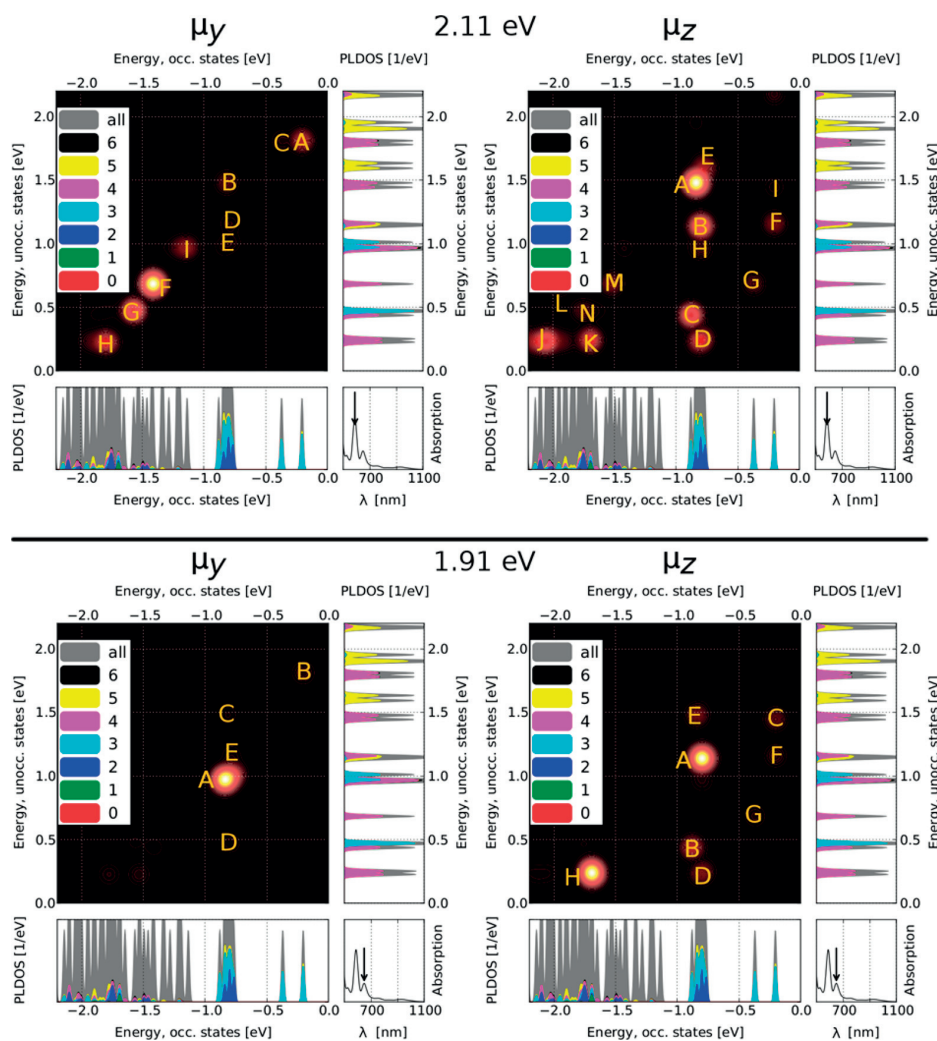
Figure 4. Transition contribution maps (TCMs) for the spectral features of the $[Ag_{67}(SH)_{32}(PH_3)_8]^{3+}$ cluster. The electronic transitions are analyzed by using photon energy of 2.11 eV (top) and 1.91 eV (bottom) and dipole moment μ directed either along the y- (μ_y) or z- (μ_z) dimension of metal core. The bright spots labeled with the letters A-N highlight the strongest contributions. The PLDOS based on the overlap between the jellium states and the molecular orbitals of the $[Ag_{67}(SH)_{32}(PH_3)_8]^{3+}$ cluster are plotted below (occupied) and next to (unoccupied) the TCM. The colors indicate the total number of nodes. Gray shows the total density of states of the cluster. The arrow in the optical spectrum (bottom-right) points to the analyzed absorption peak. Note that the optical spectra shown in the bottom right part of each panel does not include the red-shift used in Figure 2.

HOMO−LUMO band gaps of 1.0 and 0.46 eV. This result may indicate even higher electronic stability compared to the known $[Ag_{67}(SPhMe_2)_{32}(PPh_3)_8]^{3+}$ nanocluster whose HOMO−LUMO band gap is 0.36 eV. These results could motivate the experimentalist to search for similar structures where the Ag_{67} extends periodically to form clusters with different aspect ratios and even longer nanorod-like structures.

■ CONCLUSIONS

In this work we introduced a new approach to analyze the electronic shell structure of metal nanoclusters of nonspherical shape. In this approach, the symmetry of the Kohn−Sham molecular orbitals of the atomistic structure is determined based on their projection onto the "clean" states of a jellium system of similar background charge density and dimensions as in the real system. We used this strategy to determine the symmetry of the

electronic states of the box-like $[Ag_{67}(SH)_{32}(PH_3)_8]^{3+}$ nanocluster and to identify the states that are involved in the most intense metal-to-metal electronic transitions. As an outcome of this work we found that in real systems consisting of multiple electrons confined in a finite potential well, the electronic transitions are governed by a slightly different transition selection rule from the one of a particle in an infinitely deep 3D well model. Particularly, we found that in nanoclusters with rectangular cuboid-like core, such as in the $[Ag_{67}(SH)_{32}(PH_3)_8]^{3+}$ system, the electronic transitions are allowed when the nodal multiplicities in the direction of the applied field changes by an odd number, as predicted by the infinite well model, but also when the other nodal multiplicities change simultaneously by an even number, leading thus to an odd number for the overall change in the total number of nodes. The deviation of this new selection rule from the one of a particle in an infinite well model demonstrates the importance of the electron−electron

Table 1. Nodal Multiplicities (n_x, n_y, n_z) of the Kohn−Sham Molecular Orbitals of the $[Ag_{67}(SH)_{32}(PH_3)_8]^{3+}$ Nanocluster Involved in the Most Intense Electronic Transitions[a]

energy of the transition	direction of the μ	A	B	C	D	E	F	G	H	I	J,K	L,M	N
2.11 eV	y	(2,0,1)→(0,3,1) [7.5%] (0,2,1)→(0,3,1) [7.5%]	(1,0,2)→(1,1,2) [3.2%]	(0,2,1)→(0,3,1) [1.4%]	(0,1,2)→(2,0,2) [1.3%]	(0,2,0)→(0,3,0) [0.7%] (1,1,1)→(3,0,0) [0.3%] (2,0,0)→(0,3,0) [0.3%]	LS→(0,2,2) [42%]	LS→(1,2,0) [17%] LS→(0,0,4) [0.3%]	LS→(1,0,3) [11%] LS→(0,1,3) [0.3%]	LS→(1,2,1) [5.3%] LS→(3,0,0) [0.9%]	-	-	-
	z	(1,1,1)→(1,1,2) [23.9%]	(2,0,0)→(2,0,3) [9.9%]	(0,0,3)→(0,0,4) [8.9%]	(0,1,2)→(0,1,3) [3.2%] (1,0,2)→(1,0,3) [3.0%]	(0,2,0)→(0,2,3) [2.9%]	(2,0,1)→(2,0,2) [2.6%]	(0,2,1)→(0,2,2) [1.7%]	(0,1,2)→(2,1,1) [0.7%]	(2,0,1)→(2,2,0) [1.1%]	LS→(1,0,3) [8.3%] and [2.0%] LS→(0,1,3) [2.7%] and [3.5%]	LS→(0,2,2) [1.6%] and [2.6%]	LS→(1,2,0) [0.7%]
1.91 eV	y	(1,1,1)→(3,0,0) [29%] (0,2,0)→(0,3,0) [11%] (1,1,1)→(1,2,1) [11%] (0,0,3)→(2,1,1) [1.5%] (0,1,2)→(2,0,2) [1.9%]	(2,0,1)→(0,3,1) [3.3%]	(1,0,2)→(1,1,2) [1.4%]	(2,0,0)→(2,1,0) [1.6%] (0,2,0)→(2,1,0) [0.3%]	-	-	-	-	-	-	-	-
	z	(2,0,0)→(2,0,3) [33.5%]	(0,0,3)→(0,0,4) [6.1%]	(2,0,1)→(2,2,0) [2.8%]	(0,1,2)→(0,1,3) [2.1%] (1,0,2)→(1,0,3) [2.1%]	(1,1,1)→(1,1,2) [1.8%]	(2,0,1)→(2,0,2) [1.8%]	(0,2,1)→(0,2,2) [1.2%]	LS→(1,0,3) [19.4%] LS→(0,1,3) [16.3%]	-	-	-	-

[a]The transitions are analyzed for the absorption spectral peaks at 587 nm (2.11 eV) and 648 nm (1.91 eV) by using a laser field with the same photon energy and a dipole moment (μ) directed towards either the y (μ_y) or the z (μ_z) dimension. The letters from A to N refer to the bright spots shown in the TCMs. The values in the square brackets show the relative intensity (in percentage) of the transitions with respect to the total intensity. LS is used to indicate "ligand states".
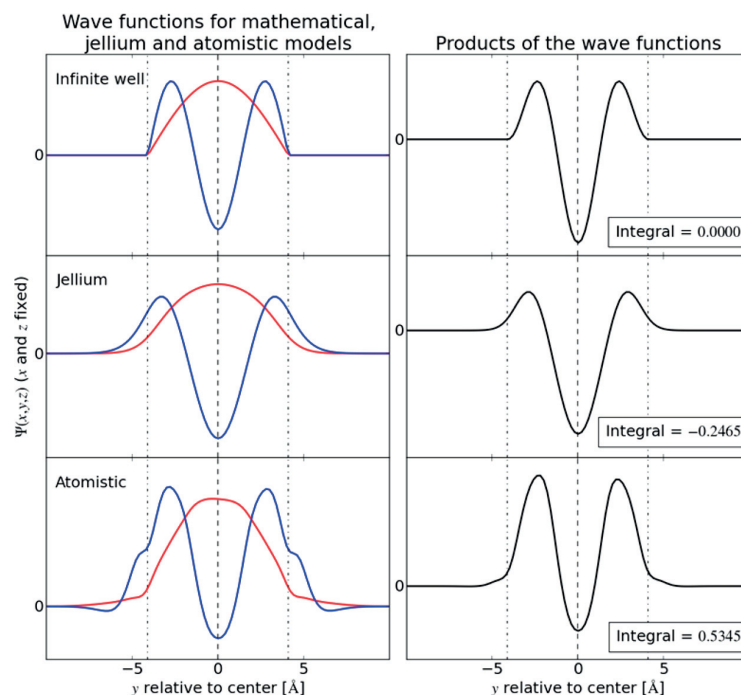
Figure 5. Wave functions for the mathematical, jellium, and atomistic models are plotted on the left for the states with symmetries (0,0,0) (in red) and (0,2,1) (in blue), and their product (in black) with the corresponding integral values are shown at the right. The curves are plotted along the y axis. The dashed line and dashed-dotted lines indicate the center and the borders of the box-like models.
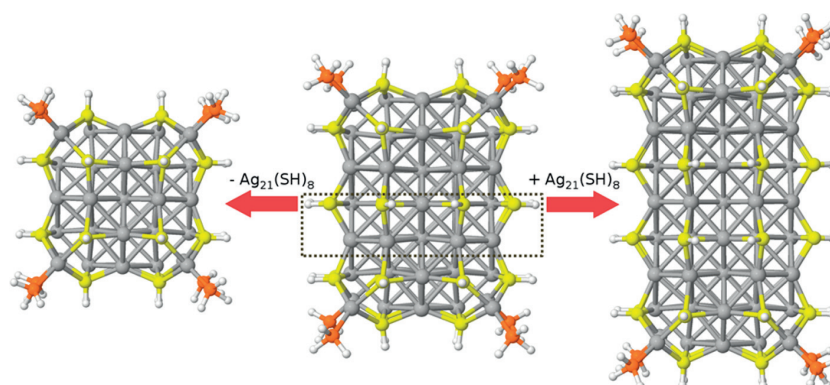

Figure 6. Side views of the (left) $[Ag_{46}(SH)_{24}(PH_3)_8]^{2+}$, (middle) $[Ag_{67}(SH)_{32}(PH_3)_8]^{3+}$, and (right) $[Ag_{88}(SH)_{40}(PH_3)_8]^{2-}$ structures. The atoms within the dashed-frame indicate the $Ag_{21}(SH)_8$ block that is added or removed to/from the $[Ag_{67}(SH)_{32}(PH_3)_8]^{3+}$ model to build the fictive nanoclusters.

interactions and the finite potential of the real nanoclusters in determining allowed transitions. Furthermore, all these results demonstrate the great potential of the new approach introduced here to investigate and understand electronic shell structure, optical properties, and stability of any nonspherical nanocluster, and even to do predictions for new electronically stable nanoparticles of nonspherical structures.

■ ASSOCIATED CONTENT

Ⓢ Supporting Information

The Supporting Information is available free of charge on the ACS Publications website at DOI: 10.1021/acs.jpcc.6b10618.

Additional analysis of optical transitions of the Ag$_{67}$ cluster (Figures S1, S2, and Table S1), technical dis-

cussion of overlap integrals, and the selection rules for box-like systems (SI text) (PDF)

■ AUTHOR INFORMATION

Corresponding Author
*E-mail: hannu.j.hakkinen@jyu.fi.

ORCID Ⓘ
Hannu Häkkinen: 0000-0002-8558-5436

Author Contributions
§These authors contributed equally.

Notes
The authors declare no competing financial interest.

REFERENCES

(1) Häkkinen, H. Electronic Shell Structures in Bare and Protected Metal Nanoclusters. *Adv. Phys. X* **2016**, *1*, 467−491.

(2) Jena, P. Beyond the Periodic Table of Elements: The Role of Superatoms. *J. Phys. Chem. Lett.* **2013**, *4*, 1432−1442.

(3) de Heer, W. A. The Physics of Simple Metal Clusters: Experimental Aspects and Simple Models. *Rev. Mod. Phys.* **1993**, *65*, 611−676.

(4) Brack, M. The Physics of Simple Metal Clusters: Self-Consistent Jellium Model and Semiclassical Approaches. *Rev. Mod. Phys.* **1993**, *65*, 677−732.

(5) Watanabe, H.; Inoshita, T. Superatom: A Novel Concept in Materials Science. *Optoelectronics* **1986**, *1*, 33−40.

(6) Leuchtner, R. E.; Harms, A. C.; Castleman, A. W. Thermal Metal Cluster Anion Reactions: Behavior of Aluminum Clusters with Oxygen. *J. Chem. Phys.* **1989**, *91*, 2753−2754.

(7) Leuchtner, R. E.; Harms, A. C.; Castleman, A. W. Aluminum Cluster Reactions. *J. Chem. Phys.* **1991**, *94*, 1093−1101.

(8) Luo, Z.; Reber, A. C.; Jia, M.; Blades, W. H.; Khanna, S. N.; Castleman, A. W. What Determines If a Ligand Activates or Passivates a Superatom Cluster? *Chem. Sci.* **2016**, *7*, 3067−3074.

(9) *Protected Metal Clusters: From Fundamentals to Applications*, 1st ed.; Tsukuda, T., Häkkinen, H., Eds.;Elsevier: Amsterdam, 2015.

(10) Fernando, A.; Weerawardene, K. L. D. M.; Karimova, N. V.; Aikens, C. M. Quantum Mechanical Studies of Large Metal, Metal Oxide, and Metal Chalcogenide Nanoparticles and Clusters. *Chem. Rev.* **2015**, *115*, 6112−6216.

(11) Häkkinen, H. The Gold-Sulfur Interface at the Nanoscale. *Nat. Chem.* **2012**, *4*, 443−455.

(12) Jin, R. Quantum Sized, Thiolate-Protected Gold Nanoclusters. *Nanoscale* **2010**, *2*, 343−362.

(13) Tsukuda, T. Toward an Atomic-Level Understanding of Size-Specific Properties of Protected and Stabilized Gold Clusters. *Bull. Chem. Soc. Jpn.* **2012**, *85*, 151−168.

(14) Negishi, Y. Towards the Creation of Functionalized Metal Nanoclusters and Highly Active Photocatalytic Materials UsingThiolate-Protected Magic Gold Clusters. *Bull. Chem. Soc. Jpn.* **2014**, *87*, 375−389.

(15) Sardar, R.; Funston, A. M.; Mulvaney, P.; Murray, R. W. Gold Nanoparticles: Past, Present, and Future. *Langmuir* **2009**, *25*, 13840−13851.

(16) Häkkinen, H. Atomic and Electronic Structure of Gold Clusters: Understanding Flakes, Cages and Superatoms from Simple Concepts. *Chem. Soc. Rev.* **2008**, *37*, 1847−1859.

(17) Alhilaly, M. J.; Bootharaju, M. S.; Joshi, C. P.; Besong, T. M.; Emwas, A.-H.; Juarez-Mosqueda, R.; Kaappa, S.; Malola, S.; Adil, K.; Shkurenko, A.; et al. [Ag67(SPhMe2)32(PPh3)8]3+: Synthesis, Total Structure, and Optical Properties of a Large Box-Shaped Silver Nanocluster. *J. Am. Chem. Soc.* **2016**, *138*, 14727−14732.

(18) Zeng, C.; Chen, Y.; Iida, K.; Nobusada, K.; Kirschbaum, K.; Lambright, K. J.; Jin, R. Gold Quantum Boxes: On the Periodicities and the Quantum Confinement in the Au28, Au36, Au44, and Au52 Magic Series. *J. Am. Chem. Soc.* **2016**, *138*, 3950−3953.

(19) Chen, Y.; Zeng, C.; Liu, C.; Kirschbaum, K.; Gayathri, C.; Gil, R. R.; Rosi, N. L.; Jin, R. Crystal Structure of Barrel-Shaped Chiral Au130(p-MBT)50 Nanocluster. *J. Am. Chem. Soc.* **2015**, *137*, 10076−10079.

(20) Das, A.; Li, T.; Nobusada, K.; Zeng, Q.; Rosi, N. L.; Jin, R. Total Structure and Optical Properties of a Phosphine/Thiolate-Protected Au24 Nanocluster. *J. Am. Chem. Soc.* **2012**, *134*, 20286−20289.

(21) Häkkinen, H.; Walter, M.; Grönbeck, H. Divide and Protect: Capping Gold Nanoclusters with Molecular Gold−Thiolate Rings. *J. Phys. Chem. B* **2006**, *110*, 9927−9931.

(22) Walter, M.; Akola, J.; Lopez-Acevedo, O.; Jadzinsky, P. D.; Calero, G.; Ackerson, C. J.; Whetten, R. L.; Grönbeck, H.; Häkkinen, H. A Unified View of Ligand-Protected Gold Clusters as Superatom Complexes. *Proc. Natl. Acad. Sci. U. S. A.* **2008**, *105*, 9157−9162.

(23) Enkovaara, J.; Rostgaard, C.; Mortensen, J. J.; Chen, J.; Dułak, M.; Ferrighi, L.; Gavnholt, J.; Glinsvad, C.; Haikola, V.; Hansen, H. A.; et al. Electronic Structure Calculations with GPAW: A Real-Space Implementation of The Projector Augmented-Wave Method. *J. Phys.: Condens. Matter* **2010**, *22*, 253202−1−24.

(24) Mortensen, J. J.; Hansen, L. B.; Jacobsen, K. W. Real-Space Grid Implementation of the Projector Augmented Wave Method. *Phys. Rev. B: Condens. Matter Mater. Phys.* **2005**, *71*, 35109−1−11.

(25) Henkelman, G.; Arnaldsson, A.; Jónsson, H. A Fast and Robust Algorithm for Bader Decomposition of Charge Density. *Comput. Mater. Sci.* **2006**, *36*, 354−360.

(26) Perdew, J. P.; Burke, K.; Ernzerhof, M. Generalized Gradient Approximation Made Simple. *Phys. Rev. Lett.* **1996**, *77*, 3865−3868.

(27) Perdew, J. P.; Wang, Y. Accurate and Simple Analytic Representation of the Electron-Gas Correlation Energy. *Phys. Rev. B: Condens. Matter Mater. Phys.* **1992**, *45*, 13244−13249.

(28) Casida, M. E.; Jamorski, C.; Bohr, F.; Guan, J.; Salahub, D. R. Theoretical and Computational Modeling of NLO and Electronic Materials. *Recent Advances in Density Functional Methods; ACS Press Washington, D.C* **1996**, *628*, 145.

(29) Walter, M.; Häkkinen, H.; Lehtovaara, L.; Puska, M.; Enkovaara, J.; Rostgaard, C.; Mortensen, J. J. Time-Dependent Density-Functional Theory in the Projector Augmented-Wave Method. *J. Chem. Phys.* **2008**, *128*, 244101−1−10.

(30) Malola, S.; Lehtovaara, L.; Enkovaara, J.; Häkkinen, H. Birth of the Localized Surface Plasmon Resonance in Monolayer-Protected Gold Nanoclusters. *ACS Nano* **2013**, *7*, 10263−10270.

(31) Andrade, X.; Botti, S.; Marques, M. A. L.; Rubio, A. Time-Dependent Density Functional Theory Scheme for Efficient Calculations of Dynamic (Hyper)Polarizabilities. *J. Chem. Phys.* **2007**, *126*, 184106−1−8.

(32) Yang, H.; Wang, Y.; Chen, X.; Zhao, X.; Gu, L.; Huang, H.; Yan, J.; Xu, C.; Li, G.; Wu, J.; et al. Plasmonic Twinned Silver Nanoparticles With Molecular Precision. *Nat. Commun.* **2016**, *7*, 12809−1−8.

Supporting information for:

Analysis of the Electronic Structure of Non-Spherical Ligand-Protected Metal Nanoclusters: The Case of a Box-Like Ag$_{67}$

Rosalba Juarez-Mosqueda,[†§] Sami Kaappa,[†§] Sami Malola,[†] Hannu Häkkinen[†‡]*

[†]Department of Physics and [‡]Department of Chemistry, Nanoscience Center, University of Jyväskylä, FI-40014 Jyväskylä, Finland

TABLE OF CONTENTS

Figure S1: Transition contribution maps for energies of 1.65 eV and 1.33 eV in the calculated optical spectrum of $[Ag_{67}(SH)_{32}(PH_3)_8]^{3+}$

Figure S2: Revision to the transition contribution map for energy of 2.11 eV with field direction z (along the long edge of the Ag core), with the PLDOS coloring referring to the nodal parities of the states

Table S1: The nodal multiplicities of the Kohn-Sham wavefunctions of $[Ag_{67}(SH)_{32}(PH_3)_8]^{3+}$ that are involved in the most intense electronic transitions with energies of 1.65 eV and 1.33 eV.

Technical discussion of overlap integrals and the selection rules for box-like systems.
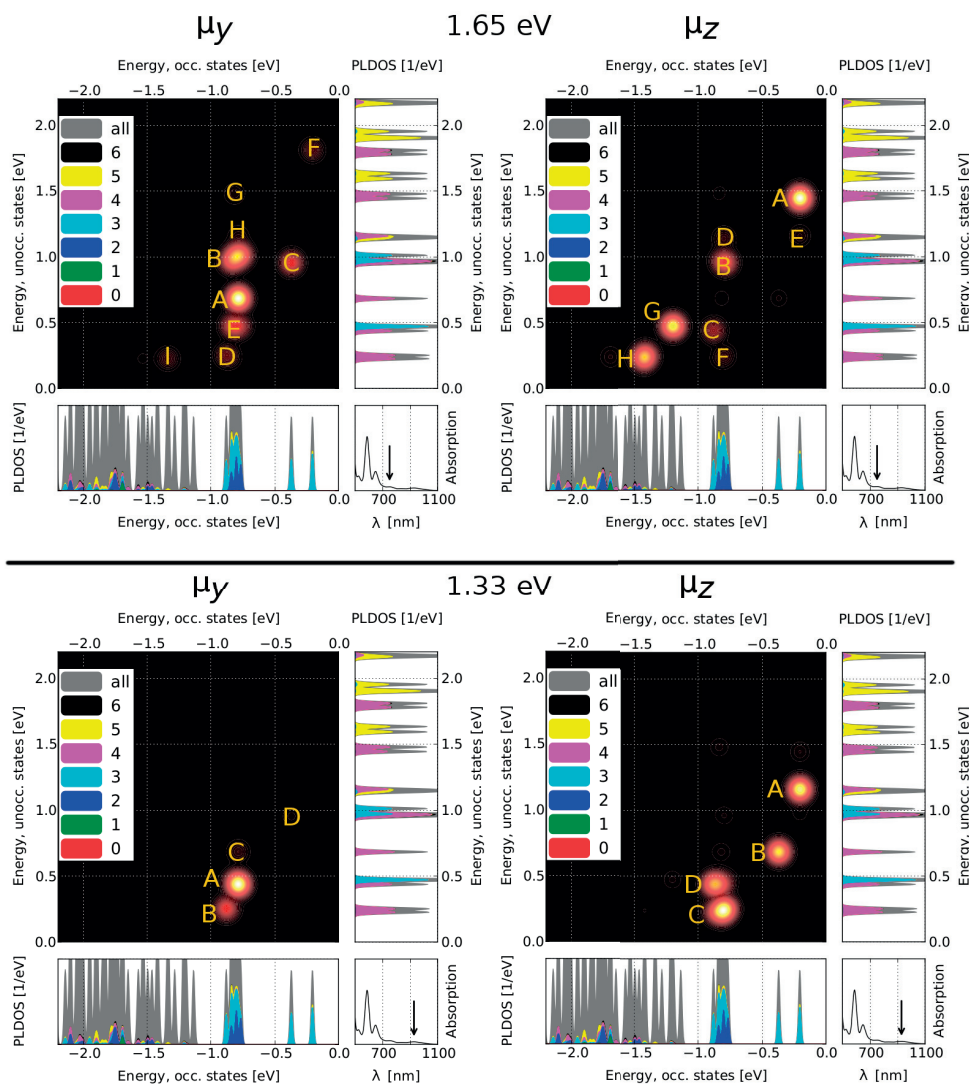
Figure S1. Transition contribution maps (TCMs) for the spectral features of the $[Ag_{67}(SH)_{32}(PH_3)_8]^{3+}$ cluster. The electronic transitions are analyzed by using photon energy of 1.65 eV (top) and 1.33 eV (bottom) and dipole moment μ directed either along the *y*- ($μ_y$) or *z*- ($μ_z$) dimension of metal core. The bright spots labeled with the letters A-I highlight the the strongest contributions. The PLDOS based on the overlap between the jellium states and the molecular orbitals of the $[Ag_{67}(SH)_{32}(PH_3)_8]^{3+}$ cluster are plotted below (occupied) and next to (unoccupied) the TCM. The colors indicate the total number of nodes. Gray shows the total density of states of the cluster. The arrow in the optical spectrum (bottom-right) points to the analyzed absorption peak.
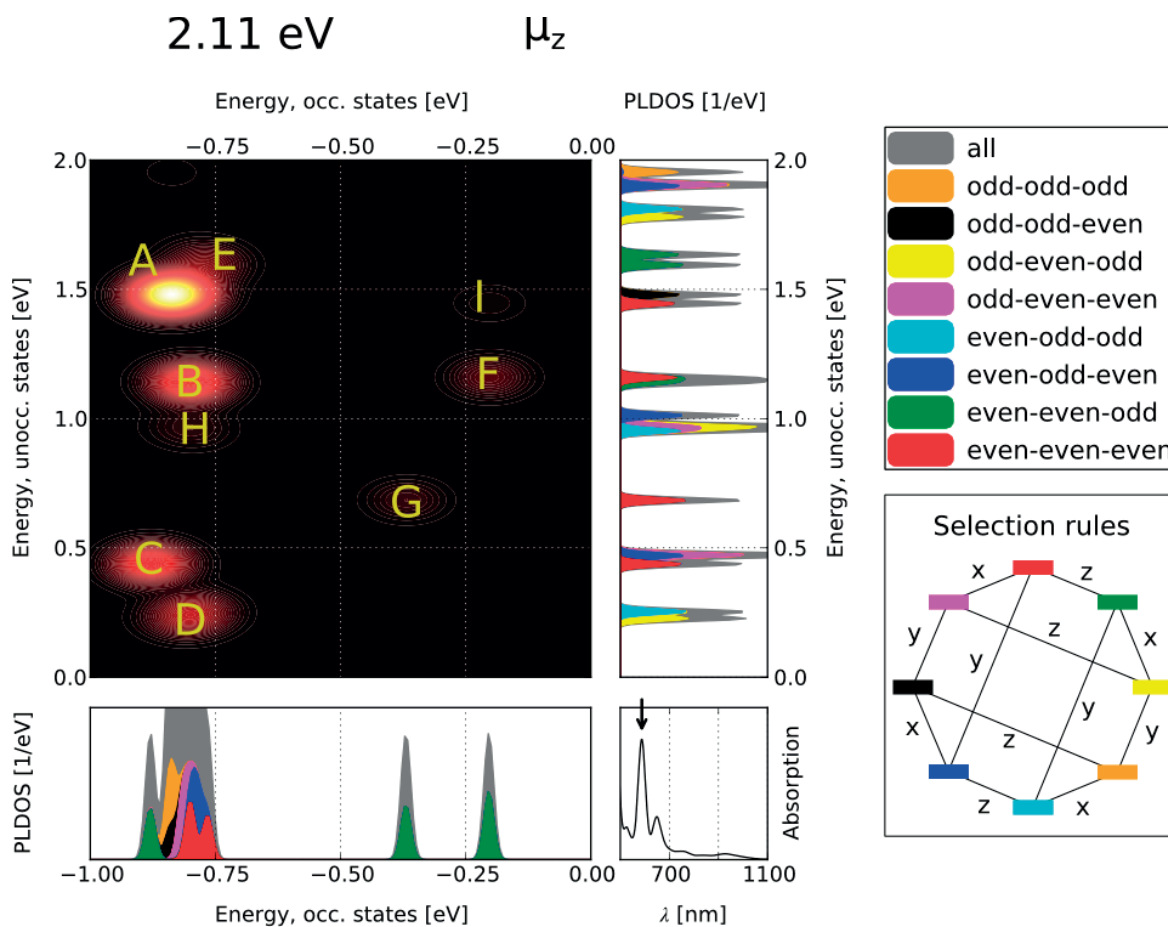
Figure S2. Transition contribution map (TCM) for 2.11eV transition with field direction along the longest edge of the Ag core, shown with different coloring of the PLDOS than the other TCM plots. The TCM corresponds to the same transitions as the upper right TCM in figure 4 (main text) with the similar labels A-I. The colors now indicate the nodal parities for each state as shown in the upper right corner. The selection rules for the nodal parities are illustrated in the lower right corner, where the lines indicate the possible transitions, for example between green and red, which denote the even-even-odd and even-even-even nodal structures, respectively. Also, the field direction in each type of allowed transition is shown, that is the direction where the parity of the nodal structure is changed. Therefore, for this TCM only the transitions with the label z are relevant. The gray area in the PLDOS, labelled as "all", refers to the nodal multiplicities with the total number of nodes more than 6.

Table S1. Nodal multiplicities (n_x, n_y, n_z) of the Kohn-Sham molecular orbitals of the $[Ag_{67}(SH)_{32}(PH_3)_8]^{3+}$ nanocluster involved in the most intense electronic transitions. The transitions are analyzed for the absorption spectral peaks at 751 nm (1.65 eV) and 928 nm (1.33 eV) by using a laser field with the same photon energy and a dipole moment (μ) directed towards either the y (μ_y) or the z (μ_z) dimension. The letters from A-I refer to the bright spots shown in the TCMs. The values in the square brackets show the relative intensity (in percentage) of the transitions with respect to the total intensity. LS is used to indicate "ligand states".

Energy of the transition	Direction of the μ	A	B	C	D	E	F	G	H	I
1.65 eV	y	(0,1,2)→(0,2,2) [31.8%]	(0,2,0)→(0,3,0) [11.4%] (2,0,0)→(0,3,0) [7.7%] (1,1,1)→(1,2,1) [5.3%] (1,1,1)→(3,0,0) [2.2%]	(0,2,1)→(2,1,1) [8.8%]	(0,0,3)→(0,1,3) [3.5%]	(0,2,0)→(2,1,0) [3.3%] (2,0,0)→(2,1,0) [3.2%] (1,1,1)→(1,2,0) [3.1%]	(2,0,1)→(0,3,1) [2.9%]	(1,1,1)→(1,2,1) [2.6%] (1,0,2)→(1,1,2) [1.2%]	(0,1,2)→(2,0,2) [1.2%]	LS→(1,0,3) [1.2%]
	z	(2,0,1)→(2,2,0) [24.7%]	(0,1,2)→(2,1,1) [6.6%] (1,0,2)→(1,2,1) [1.7%]	(0,0,3)→(0,0,4) [4.2%]	(2,0,0)→(2,0,3) [1.5%]	(2,0,1)→(2,0,2) [1.0%]	(0,1,2)→(0,1,3) [0.9%] (1,0,2)→(1,0,3) [0.8%]	LS→(2,1,0) [14.8%] LS→(1,2,0) [5.0%]	LS→(1,0,3) [11.0%] LS→(0,1,3) [6.4%]	-
1.33 eV	y	(0,1,2)→(0,0,4) [64.6%] (1,1,1)→(1,2,0) [2.3%] (2,0,0)→(2,1,0) [1.0%] (1,1,1)→(0,0,4) [0.4%]	(0,0,3)→(0,1,3) [19%] (1,0,2)→(0,1,3) [0.2%]	(0,1,2)→(0,2,2) [4.1%]	(0,2,1)→(2,1,1) [1.6%]	-	-	-	-	-
	z	(2,0,1)→(2,0,2) [22.5%]	(0,2,1)→(0,2,2) [18.8%]	(0,1,2)→(0,1,3) [13.8%] (1,0,2)→(1,0,3) [13.3%] (0,0,3)→(1,0,3) [3.8%]	(0,0,3)→(0,0,4) [13.8%] (1,0,2)→(0,0,4) [5.1%]	-	-	-	-	-

OVERLAP INTEGRALS

The overlap integral of $\phi_i(\vec{r})$ and $\psi_j(\vec{r})$ that are the wave functions for state i from the jellium calculation and state j from the atomistic calculations, respectively, is evaluated as

$$\mathcal{O}_{ij} = \int \phi_i(\vec{r}) \cdot \psi_j(\vec{r}) \; \mathrm{d}\vec{r}. \tag{S1}$$

Because the jellium wave functions form a proper orthonormal basis, we can write the atomistic wave functions as their linear combination

$$\psi_j(\vec{r}) = \sum_a c_a \phi_a(\vec{r}) \tag{S2}$$

with c_a as the coefficients. Since this must be an orthonormal set (as the set of functions $\psi_j(\vec{r})$ is), we have the relation

$$\begin{aligned}
1 &= \int \psi_j(\vec{r}) \cdot \psi_j(\vec{r}) \; \mathrm{d}\vec{r} \\
&= \int \left(\sum_a c_a \phi_a(\vec{r}) \right) \cdot \left(\sum_a c_a \phi_a(\vec{r}) \right) \mathrm{d}\vec{r} \\
&= \sum_a c_a^2 |\phi_a|^2 \\
&= \sum_a c_a^2.
\end{aligned} \tag{S3}$$

Substituting the linear combination (eq. S2) to equation S1, we notice that the overlap integrals give the coefficients for the linear combination of state j:

$$\begin{aligned}
\mathcal{O}_{ij} &= \int \phi_i(\vec{r}) \cdot \sum_a c_a \phi_a(\vec{r}) \; \mathrm{d}\vec{r} \\
&= \sum_a c_a \left(\int \phi_i(\vec{r}) \cdot \phi_a(\vec{r}) \; \mathrm{d}\vec{r} \right) \\
&= \sum_a c_a \delta_{i,a} \\
&= c_i
\end{aligned} \tag{S4}$$

For the coefficients c_i we know the property that the infinite sum of their squares equals to one (equation S3). The square of an overlap integral, $|\mathcal{O}_{ij}|^2$, thus gives the weight of a jellium state i for an atomistic state j.

SELECTION RULES FOR SYSTEMS WITH BOX-LIKE SYMMETRY

The transition dipole moment (TDM) for a transition between states i and f in the direction of the electric field $\hat{E}$ is defined as

$$\mu_{if} = \int \psi_f^*(x, y, z)(-e\hat{E} \cdot \vec{r}(x, y, z))\psi_i(x, y, z) \, \mathrm{d}x\mathrm{d}y\mathrm{d}z \qquad \text{(S5)}$$

with e as the elementary charge and $\vec{r}(x, y, z) = x\hat{e}_x + y\hat{e}_y + z\hat{e}_z$ as the position vector with the origin at the center of the box. For box-shaped systems, setting the coordinate axes to lie parallel to the edges of the system lets the integral of equation S5 be evaluated in terms of symmetry of the wave functions ψ in order to manifest the selection rules for these systems.

While the wave functions for a box-shaped system must obey the same symmetry, they are either symmetric or antisymmetric with respect to the planes that cross the center of the system and whose normal vectors are parallel to the edges of the box. It also holds that the factor $\hat{E} \cdot \vec{r}(x, y, z)$ is antisymmetric with respect to the center of the box.

The trivial multiplication rules for symmetric and antisymmetric functions are the following:

- symmetric $\times$ symmetric = symmetric

- symmetric × antisymmetric = antisymmetric

- antisymmetric × antisymmetric = symmetric

The principle of the selection rules is that an integral of an antisymmetric function vanishes. Knowing the symmetries of the functions in eq. S5 as described in the last paragraph, we can determine if the total integrand becomes antisymmetric and if the integral therefore becomes 0. If the integrand is symmetric with respect to the origin, the integral can still vanish, but this only happens when the integral goes to zero both at the positive side and negative side, independently.

Let's look at a system that has analytical solutions and that best describes the real system. The wave functions for a fermion in an infinitely deep, 3-dimensional potential well are described as

$$\Psi(x, y, z) = \sqrt{\frac{8}{L_x L_y L_z}} \sin\left(\frac{n_x \pi x}{L_x}\right) \sin\left(\frac{n_y \pi y}{L_y}\right) \sin\left(\frac{n_z \pi z}{L_z}\right) \tag{S6}$$

where (n_x, n_y, n_z) is the number of maxima along (x, y, z)-axis and (L_x, L_y, L_z) is the length of the potential well along (x, y, z)-axis. Inside the box, the sinusoidal functions are symmetric wrt. the center $L/2$ if the corresponding number of maxima is odd, and antisymmetric with an even number of maxima. For simplicity, let's consider the field direction $\hat{e}_x$. Then the TDM for these analytical states becomes

$$\begin{aligned}
\mu_{if} = \frac{-8e}{L_x L_y L_z} &\int_0^{L_x} \sin\left(\frac{n_{x,f} \pi x}{L_x}\right) x \sin\left(\frac{n_{x,i} \pi x}{L_x}\right) dx \\
&\times \int_0^{L_y} \sin\left(\frac{n_{y,f} \pi y}{L_y}\right) \sin\left(\frac{n_{y,i} \pi y}{L_y}\right) dy \\
&\times \int_0^{L_z} \sin\left(\frac{n_{z,f} \pi z}{L_z}\right) \sin\left(\frac{n_{z,i} \pi z}{L_z}\right) dz
\end{aligned} \tag{S7}$$

which indicates that if the number of maxima in direction $\hat{e}_x$ changes by an even number, the integral for x goes to zero and the transition is forbidden (antisymmetric integrand).

Also, due to orthogonality of the sinusoidal functions, the integrals for y and z vanish if the maximum number in $\hat{e}_y$ or $\hat{e}_z$ changes at all. Generalizing the result for any field direction, we can conclude that for functions of the form of equation S6, only such electronic transitions are allowed where one of the maximum numbers n_x, n_y and n_z is changed by an odd number.

For real systems, the rule becomes different due to the electron-electron interactions and the finite depth of the potential well. There, the wave functions are not anymore restricted to the volume of the metal core but spilled outside while losing their strict sinusoidal form. The nodal structure is preserved, however: we can label each wave function (that is delocalized in metal) with the numbers of nodes along each coordinate axis as (n_x, n_y, n_z). Note that we proceed by talking about nodes instead of maxima; the discussion ahead is valid for both cases since we are not dealing with the quantity itself but the change of the quantity in a transition, which is the same for nodes and maxima. Similar rules as for analytical solutions are valid considering antisymmetric integrands for real systems: If the node number in the direction of the field changes by an even number, the integrand becomes antisymmetric and the transition is forbidden. In addition, if the node number changes by an odd number in a direction that does not overlap with the field direction, the integrand becomes antisymmetric and the transition is forbidden.

The difference between real systems and the analytical solutions lies in transitions where one (or two) of the node numbers in a direction that is not the field direction changes by an even number. Both in real systems and in the analytical functions this results in a symmetric integrand, but in the case of the analytical solutions the integral vanishes

because of the properties of sinusoidal functions. While modelling real systems, those integrals are not necessarily zero and the corresponding transitions are not forbidden.

Therefore, the selection rules for real systems with box-like symmetry become the following:

- Such transitions are forbidden where, in the direction of the field, the number of nodes is changed by an even number

- In addition, such transitions are forbidden, where another number of nodes changes by an odd number.

To generalize, in an allowed transition exactly one node number (of the three numbers along the edges of the box-like system) changes by an odd number. It follows that in an allowed transition the total number of nodes changes by an odd number (odd + even + even = odd).

PII

POINT GROUP SYMMETRY ANALYSIS OF
THE ELECTRONIC STRUCTURE OF BARE AND
PROTECTED METAL NANOCRYSTALS

by

Sami Kaappa, Sami Malola & Hannu Häkkinen (2018)

The Journal of Physical Chemistry A, 122(43), 8576–8584

Point Group Symmetry Analysis of the Electronic Structure of Bare and Protected Metal Nanocrystals

Sami Kaappa,[†] Sami Malola,[†] and Hannu Häkkinen[*,†,‡]

[†]Department of Physics and [‡]Department of Chemistry, Nanoscience Center, University of Jyväskylä, FI-40014, Jyväskylä, Finland

S *Supporting Information*

ABSTRACT: The electronic structures of a variety of experimentally identified gold and silver nanoclusters from 20 to 246 atoms, either unprotected or protected by several types of ligands, are characterized by using point group specific symmetry analysis. The delocalized electron states around the HOMO−LUMO energy gap, originating from the metal s-electrons in the cluster core, show symmetry characteristics according to the point group that describes best the atomic arrangement of the core. This indicates strong effects of the lattice structure and overall shape of the metal core to the electronic structure, which cannot be captured by the conventional analysis based on identification of spherical angular momentum shells in the "superatom" model. The symmetry analysis discussed in this paper is free from any restrictions regarding shape or structure of the metal core, and is shown to be superior to the conventional spherical harmonics analysis for any symmetry that is lower than I_h. As an immediate application, we also demonstrate that it is possible to reach considerable savings in computational time by using the symmetry information inside a conventional linear-response calculation for the optical absorption spectrum of the Ag_{55} cluster anion, without any loss in accuracy of the computed spectrum. Our work demonstrates an efficient way to analyze the electronic structure of nonspherical, but atomically ordered nanocrystals and ligand-protected clusters with nanocrystal metal cores, and it can be viewed as the generalization of the superatom model demonstrated for spherical shapes 10 years ago (Walter, M.; et al. *Proc. Natl. Acad. Sci. U. S. A.* **2008**, *105*, 9157−9162).
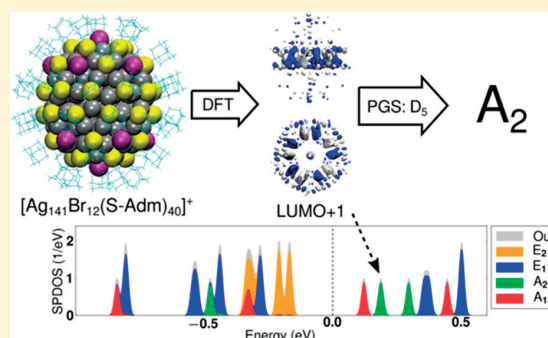
■ INTRODUCTION

Symmetry lays the foundation to understanding the electronic structure and spectroscopic transitions of small molecules, giving point group assignments of single-electron orbitals and dictating rules for allowed and forbidden dipole transitions between the quantum states.[1] Likewise, it can be used as an asset to predict properties of larger assemblies in the nanoscale even without explicit numerical computations, such as the high electronegativity of fullerene C_{60} or metal/semiconducting characteristics of carbon nanotubes.

During the past decade, the synthesis, structural determination, and characterization of atom−precise ligand-protected metal nanoclusters have taken great leaps forward, and currently over 100 structures of up to almost 400 metal atoms have been resolved (for recent reviews on experiments and theory, see refs 2−5). The current database of resolved structures reveals a multitude of shapes and atomic ordering in the metal cores, such as highly symmetric icosahedral or decahedral structures,[6−12] fcc-like packings,[13−15] and strongly nonspherical shapes such as elongated cuboids.[16,17]

Theoretical and computational research on chemical and optical properties of nanoclusters relies on examination of the electronic states and the corresponding wave functions computed from the density functional theory (DFT). As the

properties and interrelations of the electronic states are closely related to the symmetries of the wave functions, it is beneficial to extract these symmetry representations.

For a long time, the convention in analyzing the symmetries of the wave functions in the Kohn−Sham (KS) DFT scheme of bare and ligand-protected metal clusters has been the projection of the wave functions to metal-core-centered spherical harmonics. The calculated weights of the various Y_{lm} components in a given KS wave function are then used to characterize the "superatom character" of this particular KS wave function. The motivation lies in the superatom model, based on the spherically (or two-dimensional (2D) circularly) symmetric confining potential in which the electronic quantum states adapt similarly as the electron shells in a free atom.[18−24] In the ideal case of a perfect spherical symmetry, the allowed optical transitions can be evaluated directly from the angular momenta by using the dipole selection rule $\Delta l = \pm 1$. In practice, however, as the wave functions and consequently the electron density inherit the point group symmetry (if any) of the discrete atomic structure, this approach fails for shapes of

the atomic structure that are far from spherical, or in the case where the atomic lattice interacts strongly with the delocalized electron gas of the metal, splitting and intermixing the angular momentum shells.

Generally, small bare metal clusters and also many ligand-protected metal clusters are expected to be electronically stabilized with an electron count (electronic "magic number") that closes the highest occupied angular momentum shell. This creates a distinct energy gap between the highest occupied and lowest unoccupied single-electron levels (HOMO and LUMO, respectively). Larger clusters are expected to be stabilized by a favorable atomic packing of the metal, creating a series of atomic "magic numbers". Very recently, both stabilization mechanisms were demonstrated to be present simultaneously in cluster synthesis.[25] However, several known compositions and structures of ligand-protected gold and silver nanoclusters have strongly nonspherical core shapes and free-electron counts that do not match with expected electronic "magic numbers". Thus, deciphering the origin of the stabilization mechanisms of many known ligand-protected clusters creates continuing challenges to theory.

Attempts to generalize the "superatom" model[19] to take into account nonspherical shape and/or lattice effects are scarce. In 2017, we presented a scheme where the KS wave functions of the cuboidal-shape silver cluster $[Ag_{67}(SPhMe_2)_{32}(PPh_3)_8]^{3+}$ were projected onto the jellium wave functions of a three-dimensional (3D) quantum box, which aided the assignment of symmetries based on box quantization.[26] This method, however, was constrained to the cuboidal shape of the cluster core and required a reference calculation of the corresponding jellium box.

Here, we demonstrate the power of point group based symmetry analysis of the electronic structure of both unprotected and ligand-protected metal nanoclusters. We assign point group symmetry representations for KS wave functions of two bare and seven ligand-protected Ag and Au nanoclusters: (**1**) Ag_{55}^-, (**2**) Ag_{20}, (**3**) $[Ag_{136}(TBBT)_{64}Cl_3]^-$ (TBBT = *tert*-butylbenzenethiol), (**4**) $[Ag_{141}(SAd)_{40}Br_{12}]^+$ (SAd = adamantanethiol), (**5**) $Au_{70}S_{20}(PPh_3)_{12}$ (PPh$_3$ = triphenylphosphine), (**6**) $Au_{108}S_{24}(P(CH_3)_3)_{16}$, (**7**) $Au_{144}(SCH_3)_{60}$, (**8**) $[Au_{146}(p-MBA)_{57}]^{3-}$ (*p*-MBA = *p*-mercaptobenzoic acid), and (**9**) $Au_{246}(SPhCH_3)_{80}$. We refer to these systems later either by the metal atom count or by the compound number. We show that the point group symmetry analysis brings out the symmetry characteristics of the frontier orbitals of these clusters in a superior way compared to the conventional spherical harmonics based analysis for all symmetries that are lower than I_h. Furthermore, we demonstrate significant savings in CPU time when the symmetry information is used inside the linear-response calculation of the optical absorption spectrum of **1**.

METHODS

DFT and LR-TDDFT Calculations. The wave functions and eigenenergies for the KS states were solved using the real-space DFT code package GPAW.[27] The PBE (Perdew–Burke–Ernzerhof) functional[28] was used in all the calculations. The PAW setups for Ag and Au included relativistic effects. The wave functions were treated on a real-space grid with spacing of 0.20 Å. The systems were set in a computational cell with 5 Å of vacuum around the cluster. The structural optimization was deemed converged when the residual forces on atoms were below 0.05 eV/Å. The optical absorption spectrum of Ag_{55}^- was calculated by using the LR-TDDFT module
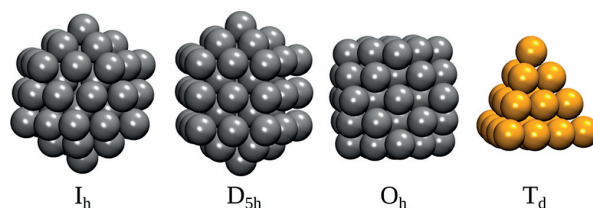

Figure 1. Bare metal clusters studied in this work. From left to right: icosahedral, decahedral, cuboctahedral Ag_{55}^-, and tetrahedral Au_{20}, with shown point group symmetries.

implemented in GPAW.[29] The PBE functional was used for the exchange–correlation kernel. The spacing of the real-space grid was 0.20 Å.

Experimental crystal structures were used directly for clusters **3**,[10] **4**,[11] **5**,[30] **8**,[15] and **9**.[12] For **6**, the PPh$_3$ ligand used in the experiment[31] was replaced by a simpler P(CH$_3$)$_3$, after which the ligand layer was optimized but the Au and S positions were kept fixed in the crystal structure. Cluster **7** is the theoretical model structure $Au_{144}(S(CH_3)_3)_{60}$ proposed by Lopez-Acevedo et al. in 2009 (ref 9). The correctness of this predictive structural model was very recently confirmed by the X-ray total structure discovery of $Au_{144}(SCH_2Ph)_{60}$ by Wu, Jin, and co-workers.[32]

Symmetry Analysis. The symmetry of a wave function is characterized via a set of overlap integrals

$$I_p = \int \psi^\dagger \hat{T}_p \psi \, d\tau \tag{1}$$

where $\hat{T}_p$ is the specific symmetry operator for operation p, such as rotation around the main axis. We calculate the overlap integrals by considering the wave functions as projected on a 3D grid, where each symmetry operation of the point group is carried out including cubic interpolation of the resulting function on the same grid. Finally, the overlap of the complex conjugate of the original wave function and the transformed function is calculated. After going through each operation, the resulting vector containing the overlap integrals is mapped into the basis of the character table rows, i.e., the symmetry representations.

The character tables for each point group are based on these integrals for perfectly symmetric objects, and they are given in the Supporting Information, Table S1. As metal nanoclusters very rarely possess perfectly symmetrical atomic structure, the integrals practically never give the exact symmetries as denoted by character tables. However, because the rows of a character table constitute a set of linearly independent basis vectors, we write the symmetry vector of the wave function (the vector consisting of the overlap integrals appointed with different operations) as a linear combination of the rows. Solving the linear equations gives the symmetry of the wave function in terms of numerical weights for each symmetry representation. While solving these linear equations, the rows for degenerate symmetries are normalized so that operating with the unit operator E on a normalized wave function gives 1; i.e., in practice the row elements are divided by the degeneracy of the row. Due to the properties of the irreducible character table matrix, the sum of the linear coefficients equals the first element of the overlap vector corresponding to the unit operation E and thus always giving 1. Weights that are determined this way for the point group symmetries are then compared to the conventional way of projecting the KS wave functions to spherical harmonics (Y_{lm} functions) as discussed in ref 19.
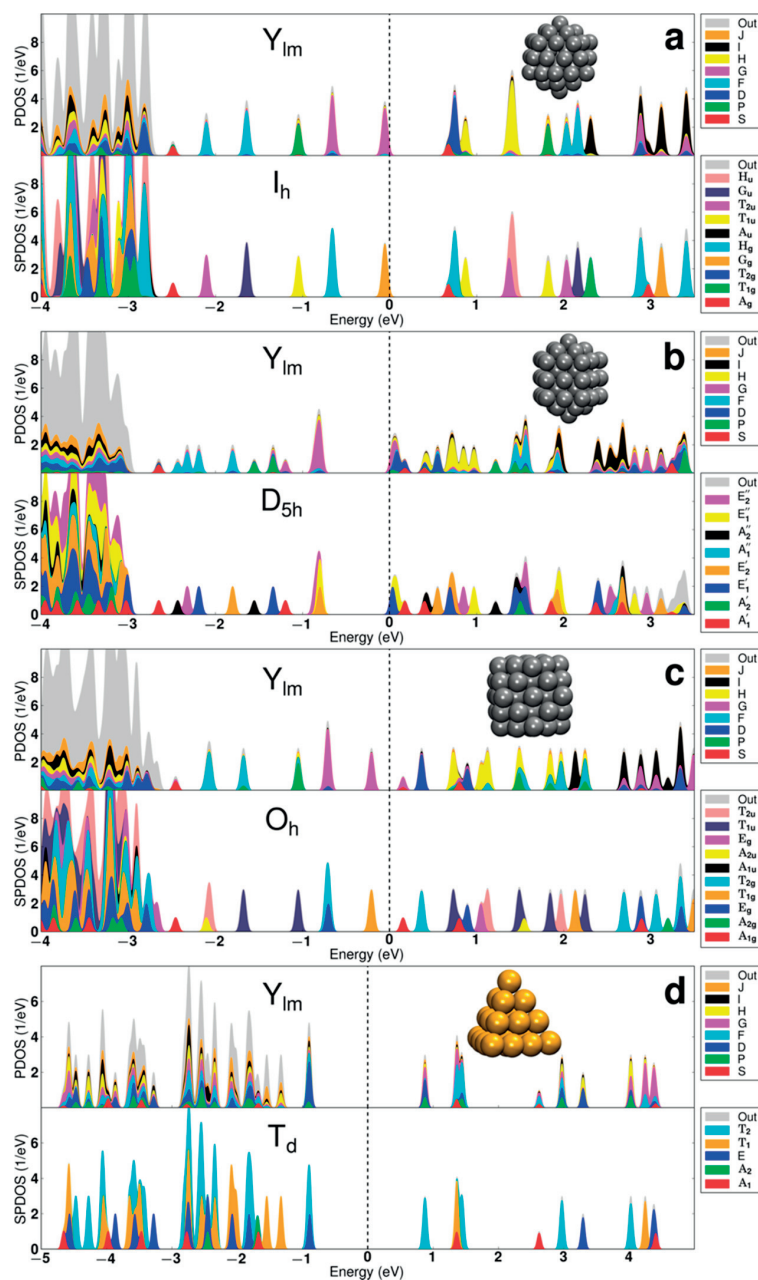
Figure 2. Analysis of KS states for clusters **1** and **2**. In each doublet of (a)–(d), the top panel shows the spherical harmonics (Y_{lm}) projected density of states (PDOS) and the bottom panel shows the PGS-analyzed DOS (SPDOS), with the point group symmetries shown in the panel. (a) Icosahedral, (b) decahedral, and (c) cuboctahedral Ag_{55}^-; (d) tetrahedral Au_{20}. The DOS curves are obtained by broadening each discrete KS state with a 0.03 eV Gaussian. The Fermi energy is at zero. The band of Ag(4d) states starts around −3 eV in (a)–(c) and the band of Au(5d) states starts around −1.5 eV in (d). The gray area (denoted by label "Out") shows electron densities that cannot be described by the projection to spherical harmonics (up to J symmetry) in the top panels. In the PGS analyses (bottom panels) the gray area denotes electron density that is outside the finite volume of the analysis.

■ RESULTS AND DISCUSSION

Bare Metal Clusters. We first compared the performance of the point group symmetry (PGS) analysis to Y_{lm} analysis for two bare metal clusters, Ag_{55}^- and Au_{20} (Figure 1). The projection to symmetry operators was done in a volume adding up atomic volumes of a radius of 3.0 Å from each atom. The Y_{lm} projections were done in a spherical volume of 12 Å radius. The ground-state atomic structure of both clusters in gas phase

has been determined previously. Based on comparison of photoelectron spectra and DFT calculations, Ag_{55}^- was determined to have an icosahedral (I_h) structure.[33] In addition to I_h symmetry, we studied Ag_{55}^- also in two other closed-shell atomic configurations, namely in cuboctahedral (O_h) and decahedral (D_{5h}) symmetries. For Au_{20}, we studied the tetrahedral T_d structure that was first suggested for the Au_{20} anion based on photoelectron spectroscopy data.[34] Later, it was also
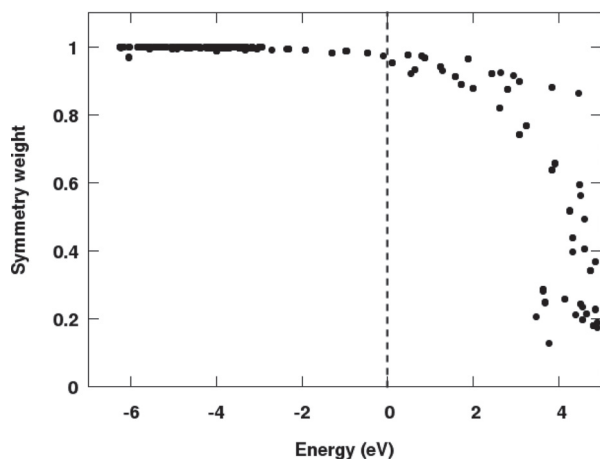
Figure 3. Maximum symmetry weights of each KS state of cuboctahedral Ag_{55}^-. Each dot represents one state. The Fermi energy is at zero. The Ag(4d) band starts at around −3 eV.

determined for the neutral Au_{20} based on experimental−theoretical study of IR vibrations.[35]

The comparison of the PGS analysis to the Y_{lm} analysis is shown in Figure 2. The free-electron count of Ag_{55} cluster anion is 56; i.e., it is two electrons shy from filling a magic-number electron shell at 58 electrons in a spherical system. In the perfectly spherical electron gas model (jellium), this corresponds to state fillings of $1S^2$ $1P^6$ $1D^{10}$ $2S^2$ $1F^{14}$ $2P^6$ $1G^{16}$. As can be seen in the top panel of Figure 2a, there is a set of well-defined discrete states between the upper edge of the Ag(4d) band (at about −3 eV) and the Fermi energy, displaying the spherical symmetries S, F, P, and G in the energetic order. These states correspond to the above jellium notations 2S, 1F, 2P, and 1G. However, one sees that the I_h symmetry splits the 1F and 1G shells very strongly. This was already noted in the early photoelectron spectroscopy study.[33] In the proper PGS I_h analysis (lower panel of Figure 2a), the split shells are identified as $1F^{14} \rightarrow T_{2u}(6) + G_u(8)$ and $1G^{16} \rightarrow H_g(10) + G_g(6)$, where the electron numbers are shown in parentheses in the symmetry notation. The decahedral cluster (Figure 2b) is seen to split almost all of the free-electron states very strongly, as revealed by the Y_{lm} analysis. The D_{5h} PGS analysis is successful in assigning the proper symmetry-dependent labels to these states, and the spherical symmetries are seen to split as follows: $1F^{14} \rightarrow A_2''(2) + E_2''(4) + E_1''(4) + E_2'(4)$ and $2P^6 \rightarrow A_2''(2) + E_1''(4)$. The major highly degenerate peak of $1G^{16}$ closest to the Fermi energy is seen to consist of D_{5h}-symmetric E_2', E_1'', and E_2'' states. The cuboctahedral cluster is PGS-analyzed in O_h symmetry, and the analysis reveals the following splitting: $1F^{14} \rightarrow A_{2u}(2) + T_{1g}(6) + T_{1u}(6)$ and $1G^{16} \rightarrow E_g(4) + T_{2g}(6) + T_{1g}(6)$.

For the T_d symmetric Au_{20} cluster, there is only one identifiable free-electron state between the upper edge of the Au(5d) band (at about −1.5 eV) and the Fermi energy. The Y_{lm} analysis yields the D symmetry for the HOMO manifold (10 electrons), indicating that in this cluster the energy order in the spherical model[36] between the 1D and 2S states is reversed. The T_d PGS analysis further reveals that the highly degenerate HOMO manifold is split to E(4) and $T_2(6)$.

When examining the d-band region in all systems, one sees a further interesting result. As expected, the Y_{lm} fails in all cases in capturing the "global" symmetries of any d-band states, as
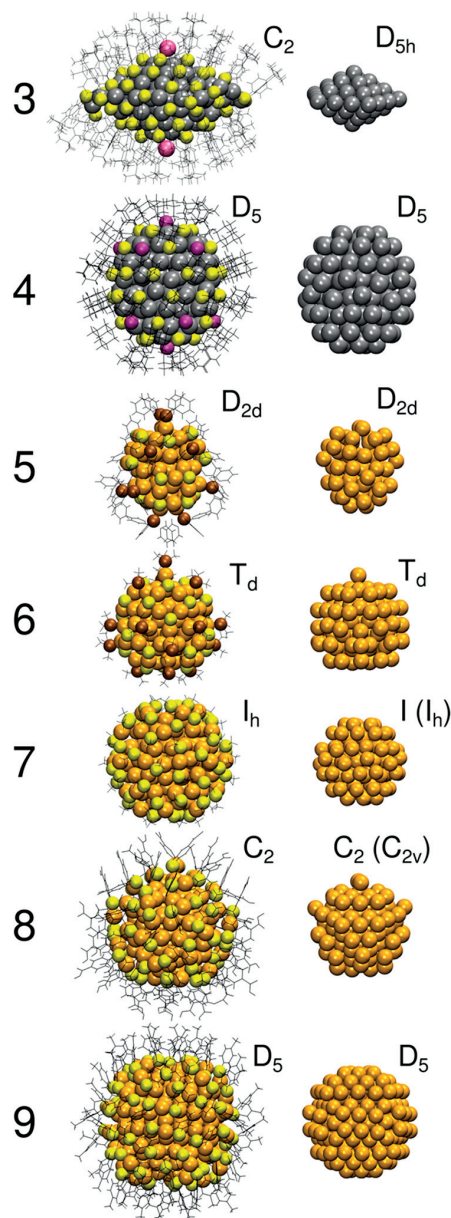

Figure 4. Clusters **3−9** (left to right, top row) and their metal cores with point group assignments (bottom row). The main symmetry axis of each cluster lies in the vertical direction. See text for chemical compositions. Ag, gray; Au, golden; S, yellow; P, brown; Cl, purple; Br, cyan. The ligand shells are indicated by the stick models.

they are very complicated linear combinations of atom-like d-orbitals. This is seen as the large gray areas in the PDOS in d-band regions in the top panels of Figure 2, which denote the electron density in the orbitals that cannot be described by the used spherical harmonics expansion (up to J symmetry). However, we found out that the PGS analysis works very well for O_h symmetric Ag_{55}^- and T_d symmetric Au_{20} clusters, being able to classify basically every state in the metal d-band to a given symmetry (see Figure 3 for O_h Ag_{55}^- and Figure S1 for Au_{20}). For I_h and D_{5h} Ag_{55}^-, the PGS analysis catches the symmetry of a large number of the d-band states (see Figures S2 and S3). This fact has an important consequence when we later discuss the

use of generalized dipole selection rules for optical transitions and demonstrate how our PGS analysis can greatly reduce the computational cost in identifying the nonzero oscillator matrix elements in the linear-response calculation of optical absorption of O_h Ag$_{55}^-$.

Ligand-Protected Clusters. We now turn the discussion to ligand-protected clusters. The total structures and the structures of the metal cores **3−8** are shown in Figure 4. The presence of ligands surrounding the metal core poses additional complications to the analysis of the electronic states in the metal core, since the electron density of a given KS state, while mostly residing in the core, may also spread out to ligands. Furthermore, the symmetry of the ligand layer may in some cases be lower than that of the metal core, as noted here for clusters **3** and **8**. This calls for judicious choices for selecting the volume(s) in which the overlaps with Y_{lm} functions or with the point group operators are computed. The Y_{lm} analysis needs a specification of a single sphere that reasonably contains the electron density in the metal core, and the chosen radii are given in Table 1 together with the point

Table 1. Point Group Symmetries for the Ligand-Protected Clusters Studied in This Work[a]

		core symm	ligand symm	$R(Y_{lm})$ (Å)
3	Ag$_{136}$	D_{5h}	C_2	10
4	Ag$_{141}$	D_5	D_5	10
5	Au$_{70}$	D_{2d}	D_{2d}	9
6	Au$_{108}$	T_d	T_d	9
7	Au$_{144}$	I (I_h)	I (I_h)	11
8	Au$_{146}$	C_2 (C_{2v})	C_2	9
9	Au$_{246}$	D_5	D_5	12

[a]For clusters **7** and **8**, we did the analysis of wave functions by using the symmetries shown in parentheses for the metal core.

group symmetries. In the PGS analysis, we kept the same definition for the volume as in the case of bare clusters; i.e., the overlaps to symmetry operators were calculated in a volume adding up atomic volumes of a radius of 3.0 Å from each core atom.

As Figure 5b shows for cluster **4**, the calculated wave functions manifest the symmetry representations with great accuracy for a cluster with well-defined symmetry of the total structure, i.e., where also the ligand layer possesses the symmetry (D_5) of the metal core. The assigned symmetries also show the degeneracy of the states correctly as the states labeled with "E" appear with higher degeneracy compared to the A symmetries. In contrast, **3** has a ligand layer that is of lower symmetry (C_2) than the 54-atom silver core (D_{5h}). Restricting the analysis to this smaller core gives rather clean symmetry states on both sides of the HOMO−LUMO energy gap (Figure 5a). The lower energy region (below −0.5 eV) can be ascribed to the ligand states with most of the electron density outside the analyzed volume, and consequently, the core symmetry analysis cannot assign any symmetry representations. For both **3** and **4**, the spherical angular momentum (Y_{lm}) analysis clearly indicates that the wave functions do not have spherical symmetry.

Clusters **5** and **6** are far from spherical and the Y_{lm} analyses show no distinct features as expected, but the analyses based on the point group symmetry of the Au cores are very clean as shown in Figure 5c for **5** (D_{2d}) and Figure 5d for **6** (T_d). It is again notable that, in both cases, the PGS analysis gives high

weights also to the lower states that are within the Au(5d) band.

Figure 6a shows the results for the icosahedral cluster **7**. Analysis based on the I_h group shows good performance in describing the symmetries of the states as it can attribute up to around 90% of the electron density to a single symmetry representation, while the corresponding ratio for Y_{lm} analysis is around 60%. The deviations from perfect I_h representations are due to the slightly chiral arrangement of the 60 Au atoms at the core−ligand interface and the RS−Au−SR moieties in the ligand layer. In fact, the proper symmetry is the chiral icosahedral I as noted already in 2009 when this structure model was proposed.[9] Figure S4 shows the comparison between I_h and I symmetric analyses. As expected, we note that the analysis in the I point group symmetry yields results that are very much related to the I_h classification. The only difference is that, due to lack of inversion symmetry in I group, "gerade" and "ungerade" subclassifications of I_h merge; e.g., the manifold of states just above the Fermi energy transform as (I_h: H$_g$, H$_u$) → (I: H). The I_h point group based analysis compares well with the spherical harmonics.[37] The spherical symmetries of Au$_{144}$ around the Fermi level are S, D, H, and I from the Y_{lm} analysis that correspond to S: A$_g$, D: H$_g$, H: T$_{1u}$ + T$_{2u}$ + H$_u$, and I: A$_g$ + T$_{1g}$ + G$_g$ + H$_g$ in the I_h representation. Our results are perfectly in line with this expected decomposition.

Regardless of the rather spherical shapes of clusters **8** and **9**, the Y_{lm} projections fail in finding any proper character of the states (Figure 6, parts b and c, respectively). Here again, PGS analysis based on the proper point group symmetry of their respective cores (C_{2v} of **8** and D_5 of **9**) reveals clean symmetries of states in a wide energy range around the HOMO−LUMO gap.

Selection Rules from Point Group Symmetry. As is well-known, symmetry is a defining factor behind selection rules for optical transitions. The selection rules similar to the spherical rule $\Delta l = \pm 1$ can be devised for each character table. According to Fermi's golden rule in quantum mechanics, the probability of an optical transition between two electronic states is proportional to the square of the transition dipole moment between the wave functions as

$$I \sim \left[\int \psi_f^\dagger \hat{\mu}_k \psi_i \, d\tau \right]^2 \tag{2}$$

where $\hat{\mu}_k = -e\hat{k}$ is the dipole moment operator. The intensity goes trivially to zero if the integrand is antisymmetric, Thus, consideration of the symmetries of the initial and final wave functions is sufficient to determine if the transition is forbidden. Using the symmetry representations of a point group corresponding to the molecule in question, the integral in eq 2 becomes a sum of the products of the rows in the character table

$$I_{i \to f} \sim \left[\sum s_f \circ \hat{\mu}_k \circ s_i \right]^2 \tag{3}$$

where the sum is taken over the elements of the vector that results from the element-wise products, denoted by the symbol "∘". The arrays s_i and s_f are the rows of the character table that correspond to the symmetry representation of the states i and f. The dipole moment operator $\hat{\mu}_k$ only consists of the character table rows corresponding to the translational vectors. For example, in the D_5 point group, the translation along the main axis (T_z) has A$_2$ symmetry representation and the translations T_x and T_y have both E$_1$ representation. The allowed and
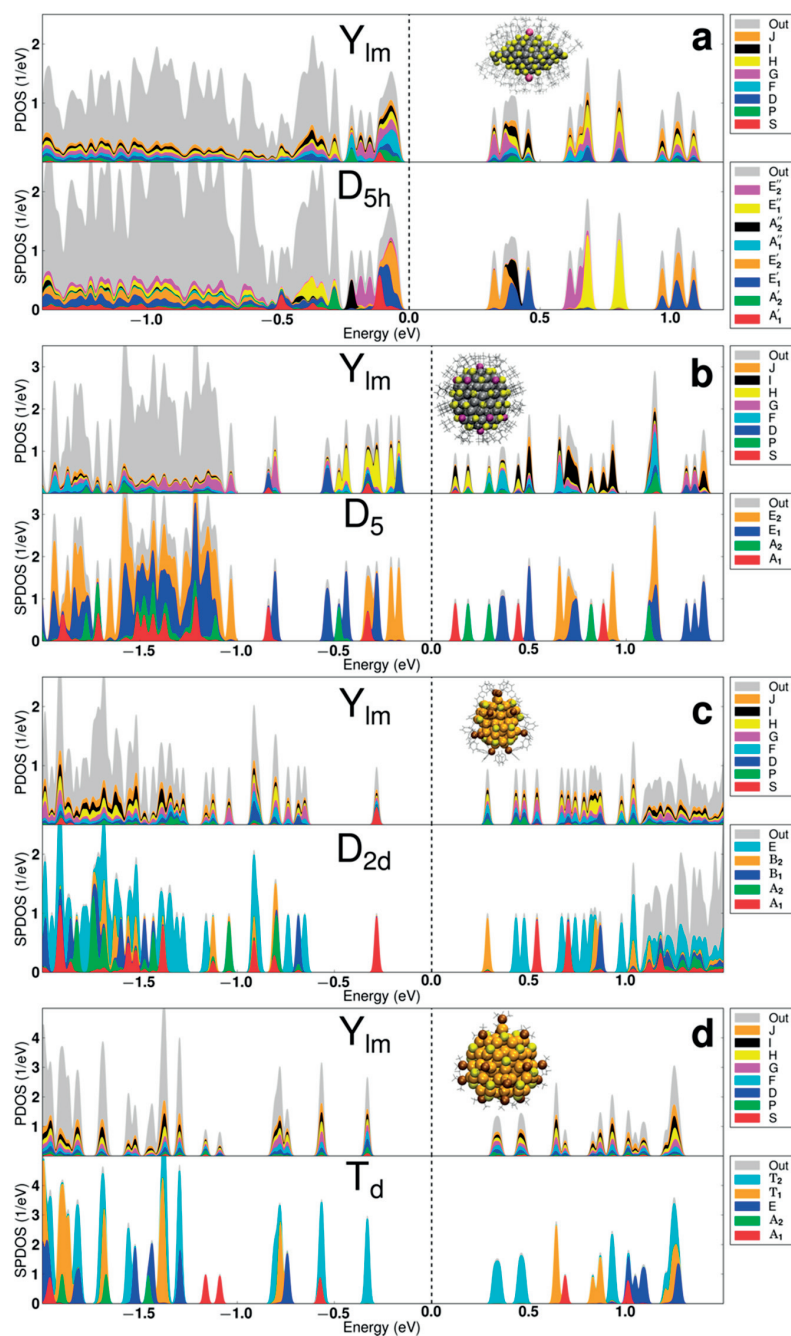
Figure 5. Analysis of the KS states for clusters (a) **3**, (b) **4**, (c) **5**, and (d) **6**. In each doublet of (a)−(d), the top panel shows the spherical harmonics (Y_{lm}) projected density of states (PDOS) and the bottom panel shows the PGS-analyzed DOS (SPDOS), with the point group symmetries shown in the panel. The gray area (denoted by label "Out") shows electron densities that cannot be described by the projection to spherical harmonics (up to J symmetry) in the top panels or by the PGS analyses (within the chosen symmetry group) in the lower panels. The DOS curves are obtained by broadening each discrete KS state with a 0.01 eV Gaussian. The Fermi energy is at zero.

forbidden transitions are determined directly by the symmetries: if the function inside the sum is antisymmetric, the sum over the values is 0, and the transition is always forbidden. Symmetric functions may lead to nonzero integral and to an allowed transition. This formulation also leads directly to Laporte's rule,[38] stating that if the point group of a molecule has an inversion center, transitions are allowed only between states of which the other carries g (gerade) symmetry and the

other has u (ungerade) symmetry. Transitions of types g → g and u → u are forbidden.

To generalize the selection rules for a point group over all directions, we used $\hat{\mu}_k = \hat{T}_x + \hat{T}_y + \hat{T}_z$ to tabulate the selection rules for the point group O_h (Table S2), although in this point group the symmetry representation of each Cartesian translation is the same, T_{1u}. In the table, the nonzero values from eq 3 are given as 1 (allowed) and the zero values are given as 0
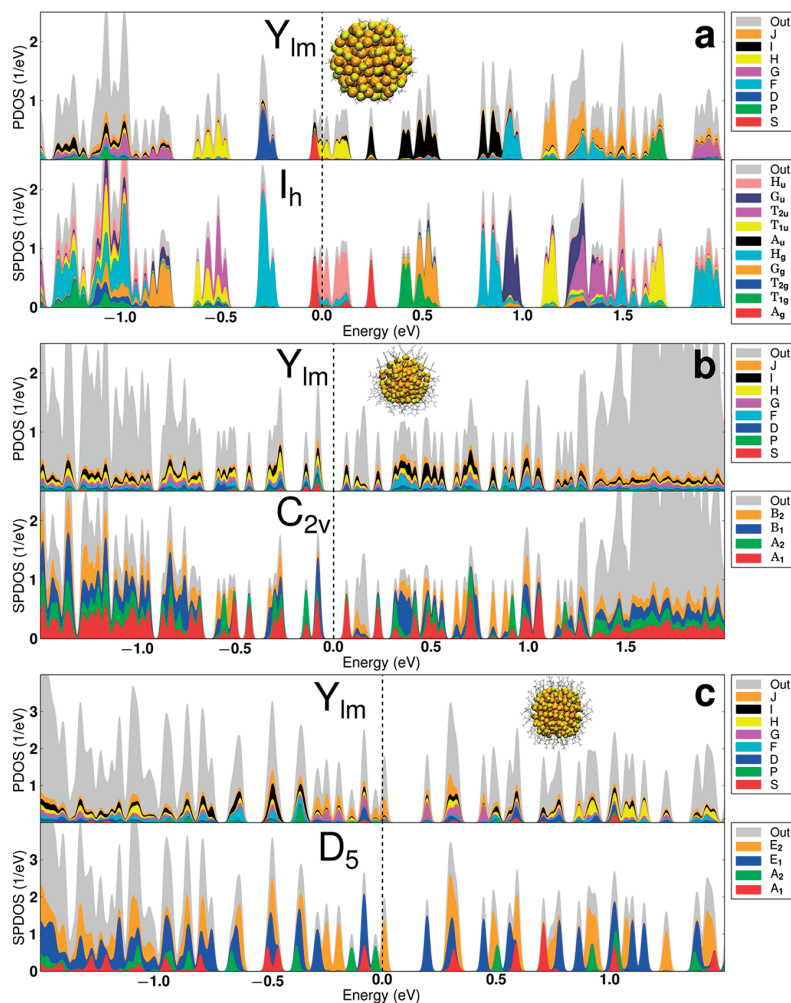
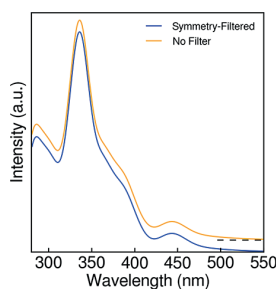**Figure 6.** Same as Figure 5, but for clusters (a) **7**, (b) **8**, and (c) **9**.

Figure 7. Computed optical spectra of the cuboctahedral Ag_{55}^- cluster by LR-TDDFT method. Brown curve, all transitions up to 4.5 eV included in the oscillator matrix; blue curve, only symmetry-filtered transition included. The brown curve is shifted up and decays to the dashed line.

(forbidden). These selection rules were then included in the linear-response time-dependent density functional theory (LR-TDDFT) calculation for the optical spectrum of the cuboctahedral Ag_{55}^- so that the optically forbidden transitions were removed from the calculation. Since the wave functions of Ag_{55}^- carry very clean symmetries even in the Ag(4d) band (Figures 2c and 3), the forbidden transitions were straightforwardly defined:

The states were assigned a single symmetry representation by their maximum symmetry weight, and a transition was excluded from the LR-TDDFT calculation if the selection rules denied the transition between these symmetry representations of the start and end states. The "symmetry-filtered" spectrum was practically identical to the one calculated without the symmetry filtering, as seen in Figure 7. The run time of the symmetry-filtered calculation was reduced to 21% compared to the nonfiltered calculation as a result from the fact that only 24 of the 100 intersymmetry transitions are allowed in the O_h point group. The very small differences of the spectra can be accounted for either by the numerical error due to the Cartesian grid on which the wave functions are projected or by the small deviations of the atomic structure from the idealized point group symmetry.

■ CONCLUSIONS

In this work, we have introduced an improved and generalized way to analyze electronic states of metal clusters that have nanocrystalline cores, i.e., atomic arrangements with specific point group symmetries. For such systems, it is straightforward to calculate weights of each KS state (or "molecular orbital") projected to symmetry operators of the point group in

question. We have shown that those electronic states of silver and gold clusters, both bare and ligand-protected, that reside mostly in the metal core, and close to the Fermi energy), are well classified to symmetry subgroups by the PGS analysis. Furthermore, in many cases also the electron states in the metal d-band carry one major symmetry component with almost 100% weight. This has important consequences in the calculation of optical transitions via the linear response method, since it may allow significant savings in CPU time when symmetry-filtering of the states is done before calculating the elements in the oscillator matrix, as demonstrated here for the O_h symmetric Ag_{55}^- cluster.

We found that $Au_{144}(SR)_{60}$ is the only cluster in this study for which the Y_{lm} projection gives reasonably good weights, so it is rather close to shell filling orders according to the spherical electron gas (jellium) model. The high spherical symmetry of the states there can be attributed to the high symmetry of the atomic configuration: the icosahedral point group I_h has 120 different symmetry operations, which can be regarded as a measure of how close the shape of the cluster is to a sphere. The second largest number of operations for point groups in this study is 48 for the octahedral O_h group.

The strong splitting of jellium-type electron shells by the point group symmetry of the metal core in ligand-protected clusters can explain also the electronic stability of compounds where the electron counting rule[19] for "superatoms" yields an unconventional electron number for spherical shell filling. The stabilization, that is, opening of the energy gap between the HOMO and LUMO states, is then a combined effect of the point group and the shape of the metal core. This effect can be surprisingly strong for clusters of size up to fairly large metal atom counts.

The rather large variety of systems analyzed here, consisting of two different noble metals, several different ligands, as well as several sizes, shapes, and symmetries of the metal core, shows the generality of our approach, which has never before been applied to study the electronic structure of larger metal nanoclusters. Our analysis presented here can be applied to any nanoparticle with any shape that has a core of an identifiable point group symmetry; thus it can be viewed as the generalization of the superatom model introduced for spherical ligand-protected clusters 10 years ago.[19] The code for performing the point group symmetry analysis will be uploaded for free use in the GPAW code repository at https://gitlab.com/gpaw/gpaw.

ASSOCIATED CONTENT

ⓢ Supporting Information

The Supporting Information is available free of charge on the ACS Publications website at DOI: 10.1021/acs.jpca.8b07923.

> Character tables for point group symmetries D_5, D_{5h}, I_h, T_d, D_{2d}, C_{2v}, and O_h; optical selection rules for O_h point group; maximum symmetry weights of each KS state of T_d Au_{20}, I_h Ag_{55}^-, and D_{5h} Ag_{55}^-; comparison of symmetry analyses of cluster 7 based on either I_h or I groups (PDF)

AUTHOR INFORMATION

Corresponding Author
*E-mail: hannu.j.hakkinen@jyu.fi.
ORCID
Hannu Häkkinen: 0000-0002-8558-5436

REFERENCES

(1) Willock, D. J. *Molecular Symmetry*; John Wiley & Sons: Chichester, U.K., 2009.

(2) Tsukuda, T.; Häkkinen, H. *Protected Metal Clusters: From Fundamentals to Applications*; Elsevier: Amsterdam, 2015.

(3) Jin, R.; Zeng, C.; Zhou, M.; Chen, Y. Atomically Precise Colloidal Metal Nanoclusters and Nanoparticles: Fundamentals and Opportunities. *Chem. Rev.* **2016**, *116*, 10346−10413.

(4) Chakraborty, I.; Pradeep, T. Atomically Precise Clusters of Noble Metals: Emerging Link between Atoms and Nanoparticles. *Chem. Rev.* **2017**, *117*, 8208−8271.

(5) Weerawardene, K. L. D. M.; Häkkinen, H.; Aikens, C. M. Connections Between Theory and Experiment for Gold and Silver Nanoclusters. *Annu. Rev. Phys. Chem.* **2018**, *69*, 205−229.

(6) Jadzinsky, P. D.; Calero, G.; Ackerson, C. J.; Bushnell, D. A.; Kornberg, R. D. Structure of a Thiol Monolayer-Protected Gold Nanoparticle at 1.1 Angstrom Resolution. *Science* **2007**, *318*, 430−433.

(7) Heaven, M. W.; Dass, A.; White, P. S.; Holt, K. M.; Murray, R. W. Crystal Structure of the Gold Nanoparticle (N(C8H17)4)(Au25-(SCH2CH2Ph)(18)). *J. Am. Chem. Soc.* **2008**, *130*, 3754−3755.

(8) Zhu, M.; Aikens, C. M.; Hollander, F. J.; Schatz, G. C.; Jin, R. Correlating the Crystal Structure of a Thiol-Protected Au25 Cluster and Optical Properties. *J. Am. Chem. Soc.* **2008**, *130*, 5883−5885.

(9) Lopez-Acevedo, O.; Akola, J.; Whetten, R. L.; Grönbeck, H.; Häkkinen, H. Structure and Bonding in the Ubiquitous Icosahedral Metallic Gold Cluster Au144(SR)60. *J. Phys. Chem. C* **2009**, *113*, 5035−5038.

(10) Yang, H.; Wang, Y.; Chen, X.; Zhao, X.; Gu, L.; Huang, H.; Yan, J.; Xu, C.; Li, G.; Wu, J.; Edwards, A. J.; Dittrich, B.; Tang, Z.; Wang, D.; Lehtovaara, L.; Häkkinen, H.; Zheng, N. Plasmonic Twinned Silver Nanoparticles with Molecular Precision. *Nat. Commun.* **2016**, *7*, 12809.

(11) Ren, L.; Yuan, P.; Su, H.; Malola, S.; Lin, S.; Tang, Z.; Teo, B. K.; Häkkinen, H.; Zheng, L.; Zheng, N. Bulky Surface Ligands Promote Surface Reactivities of [Ag141 × 12(S-Adm)40]3+ (X = Cl, Br, I) Nanoclusters: Models for Multiple-Twinned Nanoparticles. *J. Am. Chem. Soc.* **2017**, *139*, 13288−13291.

(12) Zeng, C.; Chen, Y.; Kirschbaum, K.; Lambright, K. J.; Jin, R. Emergence of Hierarchical Structural Complexities in Nanoparticles and Their Assembly. *Science* **2016**, *354*, 1580−1584.

(13) Azubel, M.; Koivisto, J.; Malola, S.; Bushnell, D.; Hura, G. L.; Koh, A. L.; Tsunoyama, H.; Tsukuda, T.; Pettersson, M.; Häkkinen, H.; Kornberg, R. D. Electron Microscopy of Gold Nanoparticles at Atomic Resolution. *Science* **2014**, *345*, 909−912.

(14) Azubel, M.; Koh, A. L.; Koyasu, K.; Tsukuda, T.; Kornberg, R. D. Structure Determination of a Water-Soluble 144-Gold Atom Particle at Atomic Resolution by Aberration-Corrected Electron Microscopy. *ACS Nano* **2017**, *11*, 11866−11871.

(15) Vergara, S.; Lukes, D. A.; Martynowycz, M. W.; Santiago, U.; Plascencia-Villa, G.; Weiss, S. C.; de la Cruz, M. J.; Black, D. M.; Alvarez, M. M.; Lopez-Lozano, X.; Barnes, C. O.; Lin, G.; Weissker, H. C.; Whetten, R. L.; Gonen, T.; Yacaman, M. J.; Calero, G. MicroED Structure of Au146(p-MBA)57 at Subatomic Resolution

Reveals a Twinned FCC Cluster. *J. Phys. Chem. Lett.* **2017**, *8*, 5523−5530.

(16) Yang, H.; Yan, J.; Wang, Y.; Su, H.; Gell, L.; Zhao, X.; Xu, C.; Teo, B. K.; Häkkinen, H.; Zheng, N. Embryonic Growth of Face-Center-Cubic Silver Nanoclusters Shaped in Nearly Perfect Half-Cubes and Cubes. *J. Am. Chem. Soc.* **2017**, *139*, 31−34.

(17) Alhilaly, M. J.; Bootharaju, M. S.; Joshi, C. P.; Besong, T. M.; Emwas, A. H.; Juarez-Mosqueda, R.; Kaappa, S.; Malola, S.; Adil, K.; Shkurenko, A.; Häkkinen, H.; Eddaoudi, M.; Bakr, O. M. [Ag67-(SPhMe2)32(PPh3)8]3+: Synthesis, Total Structure, and Optical Properties of a Large Box-Shaped Silver Nanocluster. *J. Am. Chem. Soc.* **2016**, *138*, 14727−14732.

(18) Häkkinen, H. Atomic and Electronic Structure of Gold Clusters: Understanding Flakes, Cages and Superatoms from Simple Concepts. *Chem. Soc. Rev.* **2008**, *37*, 1847−1859.

(19) Walter, M.; Akola, J.; Lopez-Acevedo, O.; Jadzinsky, P. D.; Calero, G.; Ackerson, C. J.; Whetten, R. L.; Grönbeck, H.; Häkkinen, H. A Unified View of Ligand-Protected Gold Clusters as Superatom Complexes. *Proc. Natl. Acad. Sci. U. S. A.* **2008**, *105*, 9157−9162.

(20) Häkkinen, H. Electronic Shell Structures in Bare and Protected Metal Nanoclusters. *Adv. Phys. X* **2016**, *1*, 467−491.

(21) Jena, P.; Sun, Q. Super Atomic Clusters: Design Rules and Potential for Building Blocks of Materials. *Chem. Rev.* **2018**, *118*, 5755−5870.

(22) Khanna, S. N.; Jena, P. Assembling Crystals from Clusters. *Phys. Rev. Lett.* **1992**, *69*, 1664−1667.

(23) Khanna, S. N.; Jena, P. Atomic Clusters: Building Blocks for a Class of Solids. *Phys. Rev. B: Condens. Matter Mater. Phys.* **1995**, *51*, 13705−13716.

(24) Janssens, E.; Tanaka, H.; Neukermans, S.; Silverans, R. E.; Lievens, P. Two-Dimensional Magic Numbers in Mass Abundancies of Photofragmented Bimetallic Clusters. *New J. Phys.* **2003**, *5*, 46.

(25) Yan, J.; Malola, S.; Hu, C.; Peng, J.; Dittrich, B.; Teo, B. K.; Häkkinen, H.; Zheng, L.; Zheng, N. Co-Crystallization of Atomically Precise Metal Nanoparticles Driven by Magic Atomic and Electronic Shells. *Nat. Commun.* **2018**, *9*, 3357.

(26) Juarez-Mosqueda, R.; Kaappa, S.; Malola, S.; Häkkinen, H. Analysis of the Electronic Structure of Non-Spherical Ligand-Protected Metal Nanoclusters: The Case of a Box-Like Ag67. *J. Phys. Chem. C* **2017**, *121*, 10698−10705.

(27) Enkovaara, J.; Rostgaard, C.; Mortensen, J. J.; Chen, J.; Dulak, M.; Ferrighi, L.; Gavnholt, J.; Glinsvad, C.; Haikola, V.; Hansen, H. A.; et al. Electronic Structure Calculations with GPAW: a Real-Space Implementation of the Projector Augmented-Wave Method. *J. Phys.: Condens. Matter* **2010**, *22*, 253202.

(28) Perdew, J.; Burke, K.; Ernzerhof, M. Generalized Gradient Approximation Made Simple. *Phys. Rev. Lett.* **1996**, *77*, 3865−3868.

(29) Walter, M.; Häkkinen, H.; Lehtovaara, L.; Puska, M.; Enkovaara, J.; Rostgaard, C.; Mortensen, J. J. Time-dependent density-functional theory in the projector augmented-wave method. *J. Chem. Phys.* **2008**, *128*, 244101.

(30) Kenzler, S.; Schrenk, C.; Frojd, A. R.; Häkkinen, H.; Clayborne, A. Z.; Schnepf, A. Au70S20(PPh3)12: An Intermediate Sized Metalloid Gold Cluster Stabilized by the Au4S4 Ring Motif and Au-PPh3 Groups. *Chem. Commun.* **2018**, *54*, 248−251.

(31) Kenzler, S.; Schrenk, C.; Schnepf, A. Au108S24(PPh3)16: A Highly Symmetric Nanoscale Gold Cluster Confirms the General Concept of Metalloid Clusters,. *Angew. Chem., Int. Ed.* **2017**, *56*, 393−396.

(32) Yan, N.; Xia, N.; Liao, L.; Zhu, M.; Jin, R.; Wu, Z.; Jin, F. Unravelling the Long-Pursued Au144 Structure by X-ray Crystallography. *Sci. Adv.* **2018**, *4*, eaat7259.

(33) Häkkinen, H.; Moseler, M.; Kostko, O.; Morgner, N.; Astruc Hoffman, M.; Issendorff, B. Symmetry and Electronic Structure of Noble-Metal Nanoparticles and the Role of Relativity. *Phys. Rev. Lett.* **2004**, *93*, 093401.

(34) Li, J.; Li, X.; Zhai, H. J.; Wang, L. S. Au20: A Tetrahedral Cluster. *Science* **2003**, *299*, 864−867.

(35) Gruene, P.; Rayner, D. M.; Redlich, B.; van der Meer, A. F. G.; Lyon, J. T.; Meijer, G.; Fielicke, A. Structures of Neutral Au7, Au19, and Au20 Clusters in the Gas Phase. *Science* **2008**, *321*, 674−676.

(36) Martin, T. P.; Bergmann, T.; Göhlich, H.; Lange, T. Shell Structure of Clusters. *J. Phys. Chem.* **1991**, *95*, 6421−6429.

(37) Gelessus, A.; Thiel, W.; Weber, W. Multipoles and Symmetry. *J. Chem. Educ.* **1995**, *72*, 505−508.

(38) Laporte, O.; Meggers, W. F. Some Rules of Spectral Structure. *J. Opt. Soc. Am.* **1925**, *11*, 459−463.

Point Group Symmetry Analysis of the Electronic Structure of Bare and Protected Metal Nanocrystals

Sami Kaappa, [1] Sami Malola[1] and Hannu Häkkinen[1,2,*]

[1] Department of Physics, Nanoscience Center, University of Jyväskylä, FI-40014, Jyväskylä, Finland

[2] Department of Chemistry, Nanoscience Center, University of Jyväskylä, FI-400014, Jyväskylä, Finland

A general reference to the theory of point group symmetries:
Kieran C Molloy: Group Theory for Chemists (Second Edition), Woodhead Publishing 2013.

Glossary for symbols used in Table S1:
- A and B: Singly degenerate. Symmetric and antisymmetric w.r.t. rotation around the main axis, respectively.
- E, T, G, H: 2-, 3-, 4- and 5-fold degeneracies, respectively
- subscript 1 and 2: Symmetric and antisymmetric w.r.t. C_2 perpendicular to the main axis, respectively.
- prime and double-prime: Symmetric and anti-symmetric w.r.t. σ_h
- g(erade) and u(ngerade): Symmetric and antisymmetric w.r.t. inversion, respectively.

Table S1. Character tables for point group symmetries D₅, D₅ₕ, Iₕ, Tₔ, D₂ₔ, C₂ᵥ, and Oₕ (source: http://symmetry.jacobs-university.de).

D_5

	E	$2\,C_5$	$2\,(C_5)^3$	$5\,C_2'$
A_1	1	1	1	1
A_2	1	1	1	−1
E_1	2	$2\cos(2\pi/5)$	$2\cos(4\pi/5)$	0
E_2	2	$2\cos(4\pi/5)$	$2\cos(2\pi/5)$	0

D_{5h}

	E	$2\,C_5$	$2\,(C_5)^2$	$5\,C_2'$	σ_h	$2\,S_5$	$2\,(S_5)^3$	$5\,\sigma_v$
A_1'	1	1	1	1	1	1	1	1
A_2'	1	1	1	−1	1	1	1	−1
E_1'	2	$2\cos(2\pi/5)$	$2\cos(4\pi/5)$	0	2	$2\cos(2\pi/5)$	$2\cos(4\pi/5)$	0
E_2'	2	$2\cos(4\pi/5)$	$2\cos(2\pi/5)$	0	2	$2\cos(4\pi/5)$	$2\cos(2\pi/5)$	0
A_1''	1	1	1	1	−1	−1	−1	−1
A_2''	1	1	1	−1	−1	−1	−1	1
E_1''	2	$2\cos(2\pi/5)$	$2\cos(4\pi/5)$	0	−2	$-2\cos(2\pi/5)$	$-2\cos(4\pi/5)$	0
E_2''	2	$2\cos(4\pi/5)$	$2\cos(2\pi/5)$	0	−2	$-2\cos(4\pi/5)$	$-2\cos(2\pi/5)$	0

I_h

	E	12 C$_5$	12 (C$_5$)^2	20 C$_3$	15 C$_2$	i	12 S$_{10}$	12 (S$_{10}$)^3	20 S$_6$	15 σ
A$_g$	1	1	1	1	1	1	1	1	1	1
T$_{1g}$	3	$-2\cos(4\pi/5)$	$-2\cos(2\pi/5)$	0	-1	3	$-2\cos(2\pi/5)$	$-2\cos(4\pi/5)$	0	-1
T$_{2g}$	3	$-2\cos(2\pi/5)$	$-2\cos(4\pi/5)$	0	-1	3	$-2\cos(4\pi/5)$	$-2\cos(2\pi/5)$	0	-1
G$_g$	4	-1	-1	1	0	4	-1	-1	1	0
H$_g$	5	0	0	-1	1	5	0	0	-1	1
A$_u$	1	1	1	1	1	-1	-1	-1	-1	-1
T$_{1u}$	3	$-2\cos(4\pi/5)$	$-2\cos(2\pi/5)$	0	-1	-3	$2\cos(2\pi/5)$	$2\cos(4\pi/5)$	0	1
T$_{2u}$	3	$-2\cos(2\pi/5)$	$-2\cos(4\pi/5)$	0	-1	-3	$2\cos(4\pi/5)$	$2\cos(2\pi/5)$	0	1
G$_u$	4	-1	-1	1	0	-4	1	1	-1	0
H$_u$	5	0	0	-1	1	-5	0	0	1	-1

T_d

	E	8 C$_3$	3 C$_2$	6 S$_4$	6 σ_d
A$_1$	1	1	1	1	1
A$_2$	1	1	1	-1	-1
E	2	-1	2	0	0
T$_1$	3	0	-1	1	-1
T$_2$	3	0	-1	-1	1

D_{2d}

	E	2 S$_4$	C$_2$	2 C$_2'$	2 σ_d
A$_1'$	1	1	1	1	1
A$_2'$	1	1	1	-1	-1
B$_1'$	1	-1	1	1	-1
B$_2'$	1	-1	1	-1	1
E	2	0	-2	0	0

C$_{2v}$

	E	C$_2$	σ_{v1}	σ_{v2}
A$_1$	1	1	1	1
A$_2$	1	1	−1	−1
B$_1$	1	−1	1	−1
B$_2$	1	−1	−1	1

O$_h$

	E	8 C$_3$	6 C$_2$	6 C$_4$	3 (C$_4$)^2	i	6 S$_4$	8 S$_6$	3 σ_h	6 σ_d
A$_{1g}$	1	1	1	1	1	1	1	1	1	1
A$_{2g}$	1	1	−1	−1	1	1	−1	1	1	−1
E$_g$	2	−1	0	0	2	2	0	−1	2	0
T$_{1g}$	3	0	−1	1	−1	3	1	0	−1	−1
T$_{2g}$	3	0	1	−1	−1	3	−1	0	−1	1
A$_{1u}$	1	1	1	1	1	−1	−1	−1	−1	−1
A$_{2u}$	1	1	−1	−1	1	−1	1	−1	−1	1
E$_u$	2	−1	0	0	2	−2	0	1	−2	0
T$_{1u}$	3	0	−1	1	−1	−3	−1	0	1	1
T$_{2u}$	3	0	1	−1	−1	−3	1	0	1	−1

Table S2. Optical selection rules for O_h point group. Ones and zeros denote allowed and forbidden transitions, respectively.

	A_{1g}	A_{2g}	E_g	T_{1g}	T_{2g}	A_{1u}	A_{2u}	E_u	T_{1u}	T_{2u}
A_{1g}	0	0	0	0	0	0	0	0	1	0
A_{2g}	0	0	0	0	0	0	0	0	0	1
E_g	0	0	0	0	0	0	0	0	1	1
T_{1g}	0	0	0	0	0	1	0	1	1	1
T_{2g}	0	0	0	0	0	0	1	1	1	1
A_{1u}	0	0	0	1	0	0	0	0	0	0
A_{2u}	0	0	0	0	1	0	0	0	0	0
E_u	0	0	0	1	1	0	0	0	0	0
T_{1u}	1	0	1	1	1	0	0	0	0	0
T_{2u}	0	1	1	1	1	0	0	0	0	0
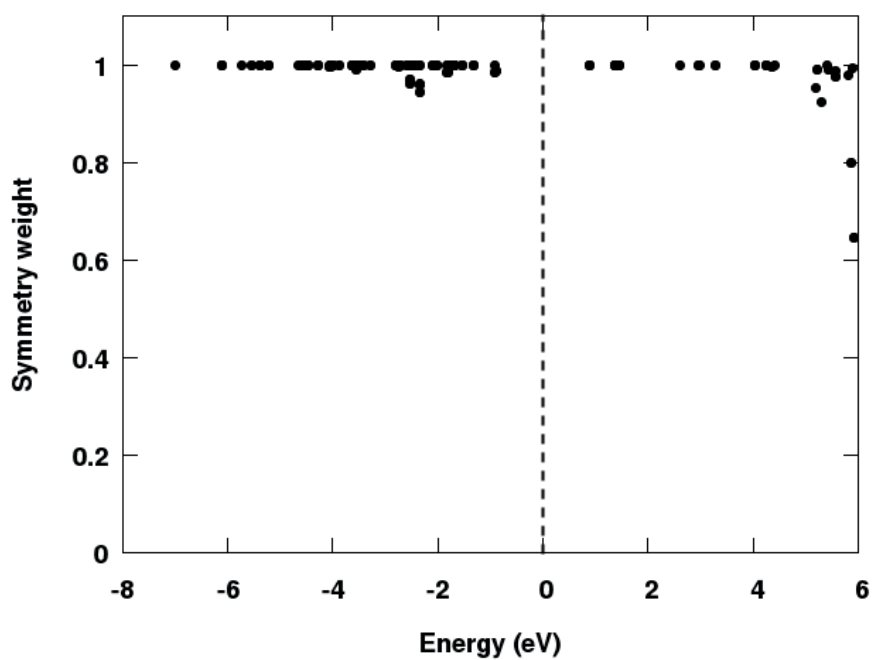
Figure S1. Maximum symmetry weights of each KS state of the T_d Au_{20}. Each dot represents one state. The Fermi energy is at zero. The Au(5d)-band starts at around -1.5 eV.
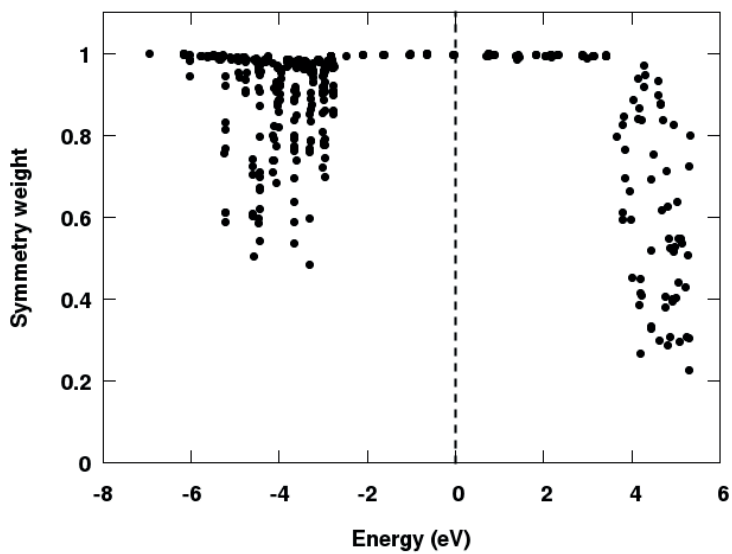
Figure S2. Maximum symmetry weights of each KS state of the I_h Ag_{55}^-. Each dot represents one state. The Fermi energy is at zero. The Ag(4d)-band starts at around -3 eV.
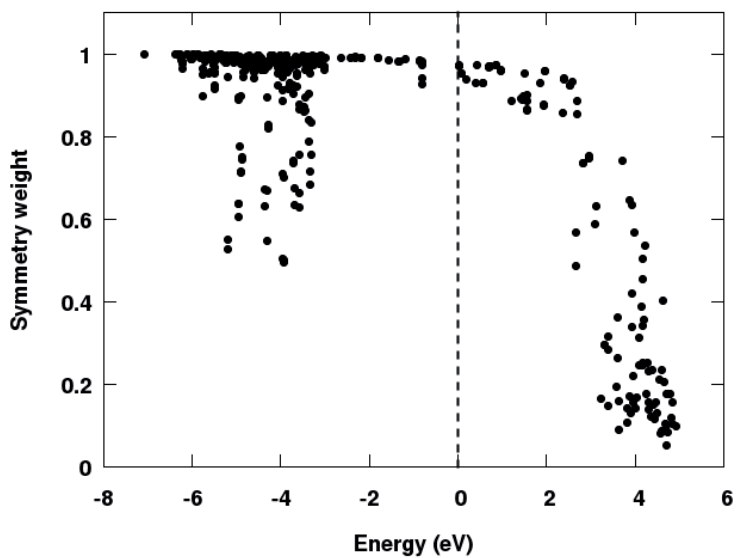
Figure S3. Maximum symmetry weights of each KS state of the D_{5h} Ag_{55}^-. Each dot represents one state. The Fermi energy is at zero. The Ag(4d)-band starts at around -3 eV.
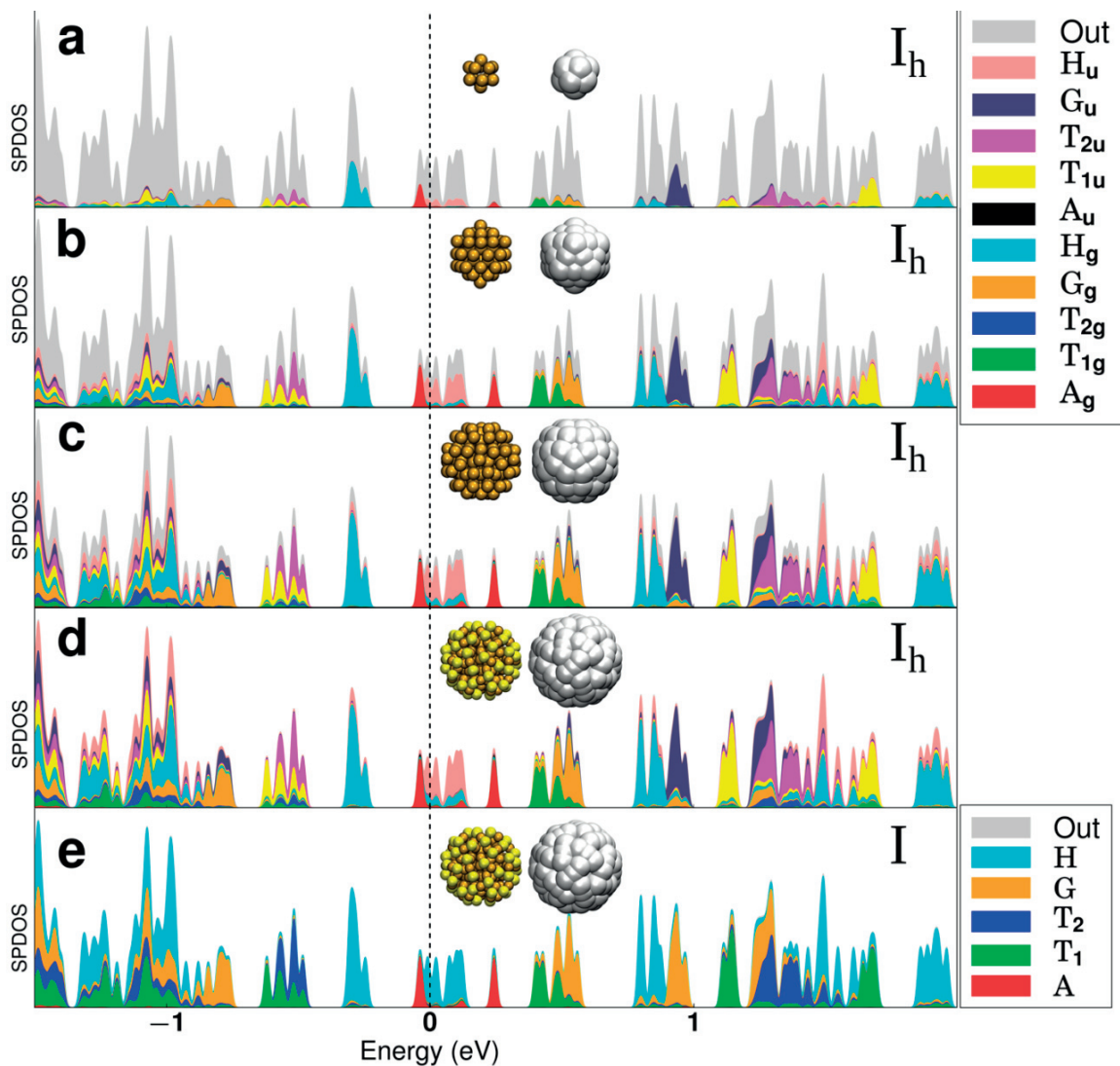
Figure S4. Comparison of symmetry analyses of cluster **7** based on either I_h or I groups. Panels a-d show the analyses based on sequential addition of the atom shells in the volume where the analysis is made. I_h analyses for (a) Au_{12} , (b) Au_{54} , (c) Au_{114} , (d) $Au_{144}S_{60}$. (e) is like (d) but using the chiral I point group symmetry. The volumes for the analyses are shown as insets in each panel alogn the atomic structure. The gray area labeled "out" denotes the electron density that is outside the volume of analysis. The character table for the I symmetry can be found at http://symmetry.jacobs-university.de/cgi-bin/group.cgi?group=905&option=4

PIII

N-HETEROCYCLIC CARBENE-FUNCTIONALIZED
MAGIC NUMBER GOLD NANOCLUSTERS

by

Mina R. Narouz, Kimberly M. Osten, Phillip J. Unsworth, ReneeW.Y. Man,
Kirsi Salorinne, Shinjiro Takano, Ryohei Tomihara, Sami Kaappa,
Sami Malola, Cao-Thang Dinh, J. Daniel Padmos, Kennedy Ayoo,
Patrick J. Garrett, Masakazu Nambo, J. Hugh Horton, Edward H. Sargent,
Hannu Häkkinen, Tatsuya Tsukuda & Cathleen M. Crudden (2019)

N-heterocyclic carbene-functionalized magic-number gold nanoclusters

Mina R. Narouz[1], Kimberly M. Osten[2], Phillip J. Unsworth[1], Renee W. Y. Man[2], Kirsi Salorinne[2], Shinjiro Takano[3], Ryohei Tomihara[3], Sami Kaappa[4], Sami Malola[4], Cao-Thang Dinh[5], J. Daniel Padmos[1], Kennedy Ayoo[1], Patrick J. Garrett[1], Masakazu Nambo[2], J. Hugh Horton[1], Edward H. Sargent[5], Hannu Häkkinen[4]*, Tatsuya Tsukuda[3,6]* and Cathleen M. Crudden[1,2]*

Magic-number gold nanoclusters are atomically precise nanomaterials that have enabled unprecedented insight into structure–property relationships in nanoscience. Thiolates are the most common ligand, binding to the cluster via a staple motif in which only central gold atoms are in the metallic state. The lack of other strongly bound ligands for nanoclusters with different bonding modes has been a significant limitation in the field. Here, we report a previously unknown ligand for gold(0) nanoclusters—N-heterocyclic carbenes (NHCs)—which feature a robust metal–carbon single bond and impart high stability to the corresponding gold cluster. The addition of a single NHC to gold nanoclusters results in significantly improved stability and catalytic properties in the electrocatalytic reduction of CO_2. By varying the conditions, nature and number of equivalents of the NHC, predominantly or exclusively monosubstituted NHC-functionalized clusters result. Clusters can also be obtained with up to five NHCs, as a mixture of species.

Magic-number gold nanoclusters stabilized by organic ligands are intriguing species that bridge the gap between molecules and materials[1–3]. Although clearly nanomaterials, with size-dependent properties, they can be described with a single molecular formula, have discrete electronic transitions due to their well-defined molecular orbitals and can be characterized by techniques usually employed in molecular science. Kornberg and colleagues' determination of the precise structure of the cluster $Au_{102}(SR)_{44}$ (SR = p-mercaptobenzoic acid) using single-crystal X-ray diffraction (XRD) was a watershed moment in understanding these nanomaterials[4]. The crystallographically determined structure partially confirmed earlier computational predictions on the bonding at the gold–thiolate interface and provided strong support for the 'superatom' theory of closed electronic shells, first described by Häkkinen and colleagues to explain why certain cluster sizes are over-represented among known species, and hence 'magic'[2,5].

Since the seminal paper by Kornberg, research into magic-number nanoclusters featuring different thiolates, metals, core configurations and applications has abounded[6–10]. However, with few exceptions, thiols and phosphines remain virtually the only organic ligands used to stabilize these structures (other than some work on alkynes)[11–17].

N-heterocyclic carbenes (NHCs) are phosphine analogues that have attracted considerable attention in organometallic chemistry and recently in surface science[18–31]. In organometallics, these ligands are known for their ability to form strong, substitutionally inert bonds to various metals[32,33]. Recently they have been shown to form highly robust self-assembled monolayers (SAMs) on Au(111) surfaces and nanoparticles[20,30]; however, their use as stabilizing ligands in magic-number nanoclusters has not been described previously.

NHCs have, however been described as stabilizing ligands in small, mixed-valency clusters of three to four atoms in seminal works by the Corrigan[34,35], Sadighi[36] and Bertrand[37] groups.

Here, we report the first example of NHC-stabilized Au(0) nanoclusters. Au_{11} nanoclusters functionalized by up to five NHC ligands have been prepared and characterized. Remarkably, the addition of even one NHC to the Au_{11} cluster significantly increases the thermal stability of this important nanocluster and improves its activity in the electrochemical reduction of CO_2 to CO, which is a critically important reaction in the valorization of CO_2.

Results and discussion

Development of cluster synthesis. Our studies began with preformed phosphine-stabilized undecagold clusters $Au_{11}(PPh_3)_7Cl_3$ and $[Au_{11}(PPh_3)_8Cl_2]Cl$ (ref. [38]). Phosphine-stabilized clusters were chosen because NHC and phosphine ligands are both neutral and thus require no change in oxidation state or cluster charge to accompany an exchange reaction. Furthermore, phosphine-stabilized clusters do not have a layer of Au(I) atoms on the exterior, as is the case for thiolate-stabilized clusters. Treatment of $[Au_{11}(PPh_3)_8Cl_2]Cl$ (**2**) with di-isopropyl benzimidazolium hydrogen carbonate **1a·H₂CO₃** (Fig. 1a) in THF at 66 °C gave predominantly a single NHC-containing cluster (**3a**, Table 1, entry 1). This cluster results from substitution of one phosphine ligand for the NHC (Fig. 1b). The less stable cluster $Au_{11}(PPh_3)_7Cl_3$ was not effective as a substitution partner.

Conclusive information about the cluster identity was obtained by mass spectrometry, which demonstrated that mono-substituted cluster **3a** is the predominant product, accompanied by small amounts of di-substituted cluster **4a** and starting material **2**

[1]Department of Chemistry, Queen's University, Kingston, Ontario, Canada. [2]Institute of Transformative Bio-Molecules (WPI-ITbM), Nagoya University, Nagoya, Japan. [3]Department of Chemistry, School of Science, The University of Tokyo, Bunkyo-ku, Tokyo, Japan. [4]Departments of Chemistry and Physics, Nanoscience Center, University of Jyväskylä, Jyväskylä, Finland. [5]Department of Electrical and Computer Engineering, The University of Toronto, Toronto, Ontario, Canada. [6]Elements Strategy Initiative for Catalysts and Batteries (ESICB), Kyoto University, Katsura, Kyoto, Japan.
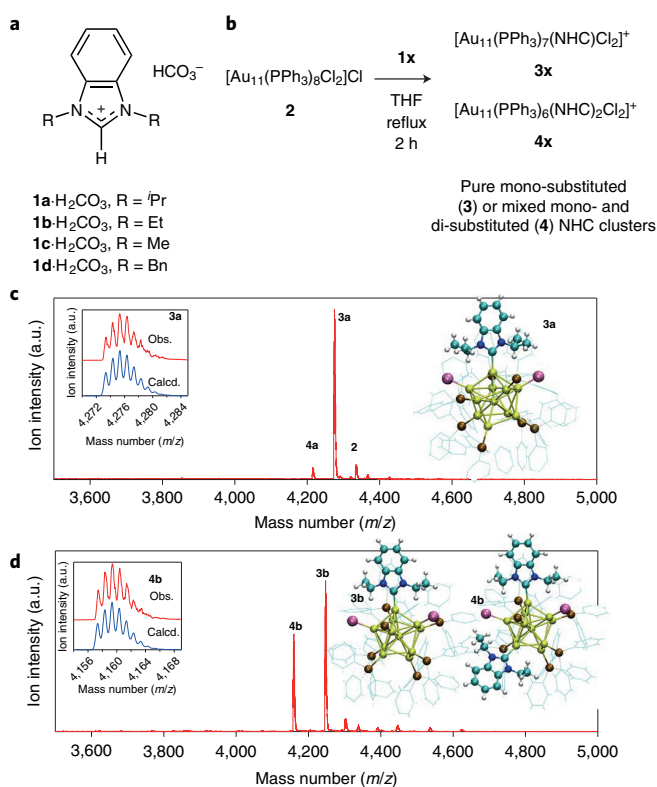*e-mail: hannu.j.hakkinen@jyu.fi; tsukuda@chem.s.u-tokyo.ac.jp; cruddenc@chem.queensu.ca

Fig. 1 | Synthesis and characterization of NHC-modified Au₁₁ nanoclusters.
a, Structure of NHC precursors employed in this study featuring a variety of organic substituents on the nitrogen atoms flanking the key carbon.
b, Reaction of undecagold cluster $[Au_{11}(PPh_3)_8Cl_2]Cl$ (**2**) with NHC precursors from **a**, resulting in formation of new NHC-containing clusters.
c, Mass spectrometric characterization of the reaction mixture leading to $[Au_{11}(PPh_3)_7(NHC^{i-Pr})Cl_2]Cl$ **3a**, along with the structure obtained by X-ray crystallography. Inset, observed versus calculated isotope pattern. The high level of purity is notable from the mass spectrum, which shows **3a** as the major product, along with small quantities of starting cluster **2** and di-substituted cluster $[Au_{11}(PPh_3)_6(NHC^{i-Pr})_2Cl_2]Cl$ **4a**. Colours in the atomistic structures: yellow, Au; purple, Cl; brown, P; blue, N; cyan, C; white, H.
d, Mass spectrometric characterization of the reaction of **1b** with **2**, showing a mixture of **3b** and **4b** along with DFT-predicted structures. Note that the structure of **3a** shown in **c** is an actual crystal structure while **3b** and **4b** are DFT-simulated.

(Fig. 1c). Quantification of the cluster purity was accomplished by detailed ¹H NMR spectroscopic analysis. For precise details and replicate runs, see Supplementary Section 2. NHC nanoclusters were analysed before and after purification by chromatography on silica gel, which indicated that there was no change in the cluster distribution after chromatography and highlighted the stability of the cluster to chromatography (Supplementary Fig. 33). The main effect of purification was to remove molecular by-products such as $[Au(NHC)_2]^+$ and $OPPh_3$ (Supplementary Fig. 12).

Increasing the amount of $1a·H_2CO_3$ to 5 equiv. resulted in larger amounts of the di-substituted cluster **4a**, with the addition of water attenuating reactivity and giving a more selective process (Table 1, entries 2 and 3). The use of the free NHC in place of the bicarbonate salt gave similar overall yields, but a mixture of clusters was obtained (entry 4). The mono-substituted cluster **3a** still predominated, but di-substituted cluster **4a** was observed along with tri-substituted cluster **5a**. ESI-MS (electrospray ionization mass spectrometry) revealed the presence of trace amounts of the tetra- and

penta-substituted clusters **6a** and **7a**. Thus, the use of the bicarbonate salt $1a·H_2CO_3$ at ~1 equiv. is important to produce clusters that are predominantly mono-substituted.

With conditions in hand for the preparation of NHC-stabilized clusters **3a** and **4a**, we then examined the effect of the NHC structure (Table 1). NHC precursors $1b–d·H_2CO_3$ were used, where the nitrogen atoms of the NHC are substituted with Et, Me and Bn groups. Each of these relatively minor changes in NHC structure had an influence on the reaction. NHC precursor $1b·H_2CO_3$ (R = Et) consistently gave a mixture of mono- and di-substituted clusters, regardless of the conditions or stoichiometry, suggesting that the initial substitution activates the cluster for a second displacement reaction (Fig. 1d and Table 1, entries 5—8). Again, increasing the amount of the NHC gave greater substitution (Supplementary Section 2).

NHC precursor $1c·H_2CO_3$ (R = Me) behaved more like $1a·H_2CO_3$ and allowed for the isolation of clean, mono-substituted cluster **3c** with no evidence for formation of the di-substituted cluster **4c** under optimized conditions. On average, lower isolated yields were observed in comparison to reactions with $1a·H_2CO_3$ and $1b·H_2CO_3$, and the reaction was best run at lower temperatures (Table 1, entries 9 and 10). The addition of larger quantities of this small NHC gave cluster degradation rather than increased substitution (Supplementary Sections 2 and 3).

Finally, benzylated NHC precursor $1d·H_2CO_3$ behaved similarly to $1b·H_2CO_3$, giving a mixture of mono-, di- and tri-substituted clusters **3d**, **4d** and **5d** even at 1.2 equiv. of the precursor. At higher loadings (9.0 equiv.), a mixture of clusters including mono- (**3d**), di- (**4d**), tri- (**5d**) and tetra- (**6d**) NHC-containing clusters was observed (Table 1, entries 11 and 12 and Supplementary Figs. 45–48).

Computational studies and structure prediction. Density functional theory (DFT, implemented as described in ref. [39]; for technical details see Supplementary Information) was used to investigate the energetics of substitution of the various phosphines in cluster **2** by NHCs (Fig. 2a). Introduction of NHC (**1a**) into cluster **2** was found to be thermodynamically favourable at most sites, with the exception of phosphine **8** (P8), which gave an unfavourable reaction energy change of +0.05 eV, probably due to steric constraints at this site (Fig. 2b). Introduction of the NHC by displacement of phosphines adjacent to the Au–Cl sites was uniformly preferred, with the single most favourable exchange predicted to occur at P2 for all NHCs examined. Differences between exchange at P2 and the next favourable phosphine energetically were 0.18 eV, 0.07 eV and 0.06 eV for **3a**, **3b** and **3c**, respectively (Fig. 2b and Supplementary Table 7). The calculated highest occupied molecular orbital–lowest unoccupied molecular orbital gaps for the mono-substituted clusters were largest for substitution at P2 for each NHC type, showing that the trends in electronic stability followed exchange energetics (Supplementary Table 8).

For NHC precursor $1b·H_2CO_3$ with **2** to form di-substituted clusters, the four lowest-energy isomers were found within a 0.1 eV window. Three of these included introduction of the NHC at P2 (Supplementary Table 9). NHC precursors $1a·H_2CO_3$ and $1c·H_2CO_3$ were also predicted to have favourable energetics for the production of di-substituted clusters. For example, substitution of **1a** and **1c** at P2 and P7 led to energy changes of −1.39 eV and −1.43 eV, respectively, suggesting that kinetic control rather than thermodynamics must play a role in the observation of predominantly or exclusively mono-substitution for these NHCs.

In the later stages of this work we were able to determine the atomistic structure of **3a** from a single-crystal X-ray analysis (vide infra). The crystal structure confirmed our DFT predictions that it is energetically optimal to replace phosphine P2 with an NHC in cluster **3a** (see the comparison of the predicted and observed structures in Supplementary Fig. 52). Three computational structure

Table 1 | Preparation of NHC-containing clusters by reaction of phosphine-containing cluster 2 with benzimidazolium hydrogen carbonates 1a–d

$[Au_{11}(PPh_3)_8Cl_2]^+ \xrightarrow[\text{Conditions}]{\text{1x}} [Au_{11}(PPh_3)_{8-n}(NHC)_nCl_2]^+$

Entry	1x·H$_2$CO$_3$ (equiv.)	Additive	Cluster(s) produced[a]	Yield[b] (%)
1	**1a** (1.2)	None	**3a,4a** (9:1)	22[c]
2	**1a** (5.0)	H$_2$O[d]	**3a,4a** (3:1)	26[c]
3	**1a** (5.0)	None	**3a,4a** (1:1)	38
4	**1a** (1.2)[e]	None	**3a,4a,5a** (2.6:1:1)	24
5	**1b** (1.2)	H$_2$O	**3b,4b** (2:1)	41
6	**1b** (1.2)	None	**3b,4b** (2:1)	20
7	**1b** (5.0)	H$_2$O	**3b,4b** (1:1)	64
8	**1b** (5.0)	None	**3b,4b** (1:1)	43
9	**1c** (1.2)	H$_2$O	**3c**	6[c]
10	**1c** (1.2)	H$_2$O[f]	**3c**	10[c]
11	**1d** (1.2)	None	**3d,4d,5d**[g]	18
12	**1d** (9.0)	None	**3d,4d,5d,6d**[g]	38

[a]Conditions: THF solvent, 66 °C, 2 h. **3x** clusters contain 1 NHC ($n=1$), **4x** ($n=2$), **5x** ($n=3$), **6x** ($n=4$), ratios determined by ^{1}H NMR spectroscopy, traces of starting cluster **2** present in some cases. [b]Isolated yields. [c]Average of 3–5 runs. [d]Water added at 500 ppm unless otherwise noted. [e]Free carbene employed. [f]40 °C, 1,000 ppm H$_2$O. [g]Exact ratios difficult to elucidate by NMR. Electrospray ionization mass spectrometry (ESI-MS) analysis shows decreasing amounts of more substituted clusters.

Phosphine	Energy (eV)[a]
P1	−0.64
P2	−0.93
P3	−0.73
P4	−0.55
P5	−0.41
P6	−0.40
P7	−0.75
P8	+0.05

[a]Changes in potential energy for reaction of **2** with **3a** by DFT.

Fig. 2 | DFT and UV–vis spectroscopic prediction of structure for NHC-modified nanoclusters. a, Labelling of phosphines in [Au$_{11}$(PPh$_3$)$_8$Cl$_2$]Cl (**2**) and exchange with **1a**. **b**, DFT-predicted changes in potential energy for reaction shown in **a** at each phosphine. **c**, Comparison of calculated optical spectra (red, blue, green curves) of cluster **3a** to experimental data (black). Three computed spectra are calculated for the initial DFT-predicted structure obtained by replacing phosphine P2 in cluster **2** by NHC **1a** (red), for the experimentally determined crystal structure (CS) (blue) and for DFT-optimization of the experimentally determined crystal structure (green). The computed spectra are blueshifted by 0.4 eV for better visual comparison to the experimental data.

models for **3a** were now in our hands: one based upon the structure predicted prior to obtaining an experimental crystal structure (red), one employing exact coordinates from the experimentally obtained crystal structure (blue) and one applying DFT optimization to the experimentally derived crystal structure (green).

The computed optical absorption spectra from these models are compared to the experimental data measured for **3a** in Fig. 2c. We notice that all computed spectra have spectral features that match the experimental data very well; however, the computed spectra systematically underestimate all transition energies by ~0.4 eV. This is understandable based on the properties of the DFT functional used in the calculation. The shift is corrected in Fig. 2c to enable a better visual comparison to experiment. The nature of the dominant two absorption features in the computed spectra (close to 300 nm and 450 nm in the shifted spectra) are further analysed in Supplementary Fig. 53. The dominant transitions were found to be either from Au s-type (450 nm) or Au d-type (300 nm) states to the empty states of the phenyl rings of the phosphines.

Spectroscopic characterization. The clusters were also extensively characterized by NMR spectroscopy, examining ^{1}H, ^{31}P and ^{13}C nuclei (Supplementary Section 3). The NHC carbon bound to Au could not be observed by ^{13}C NMR spectroscopy at natural abundance, but when cluster **3a** was prepared with ^{13}C enrichment at C2 of the NHC, the Au–C bond could be observed at 209 ppm. This signal appeared as an octet, indicating equivalent coupling to each of the seven phosphines (Fig. 3a). Because there are at least two unique environments for phosphines in any NHC-containing cluster, exchange processes must be happening on the timescale of the NMR experiment. ^{31}P NMR spectroscopy supports the presence of exchange phenomena at room temperature because a clean singlet was observed (Fig. 3b). To address this further, low-temperature ^{31}P NMR spectra were obtained for both **2** and **3a** (Supplementary Figs. 50 and 51). These spectra confirm the presence of an exchange phenomenon (or phenomena) on the NMR time scale. Interestingly,
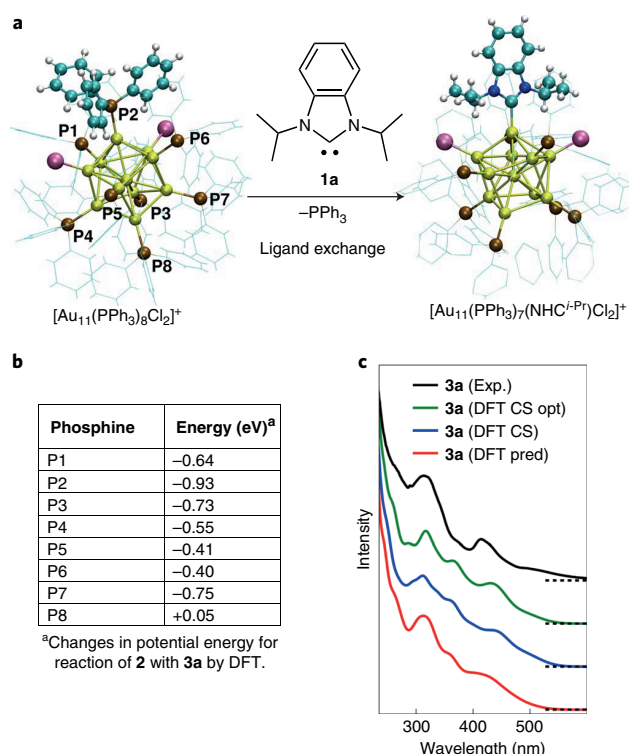
the NHC-functionalized cluster starts to show decoalescence at −10 °C, while the all-phosphine cluster **2** does not begin to decoalesce until close to −70 °C.

Information on the bonding and electronic properties of the clusters was also obtained through Au L$_3$-edge X-ray absorption spectroscopy (XAS). X-ray absorption near edge structure (XANES) spectra show a decrease in intensity when the NHC is introduced into the clusters (Supplementary Fig. 55), particularly for the Me derivative **3c**, which may be due to the electron-donating ability of NHCs[33,40,41].

Extended X-ray absorption fine structure (EXAFS) R-space spectra of the clusters revealed information on Au–C, Au–P and Au–Cl bonding, and Au–Au bonding within the cluster (Supplementary Fig. 54 and Supplementary Table 10). Analysis of Au–C bond lengths revealed that the Au–C(NHC) bond length in **3c** is 11.4 pm shorter than the corresponding Au–C bond in **3a**, consistent with steric differences between the NHC types. Most importantly, the introduction of NHC **1a** resulted in a 3 pm increase in the average Au–Au bond length for gold atoms on the exterior of the cluster relative to the all-phosphine cluster **2**, which suggests that NHC ligation leads to expansion of the outermost Au atoms in the cluster. A similar cluster expansion was not observed on ligation of the smaller NHC in cluster **3c**, which is interesting considering that this cluster has higher stability than **3a** (vide infra), suggesting an interplay between the experimental observations of cluster structure and stability.
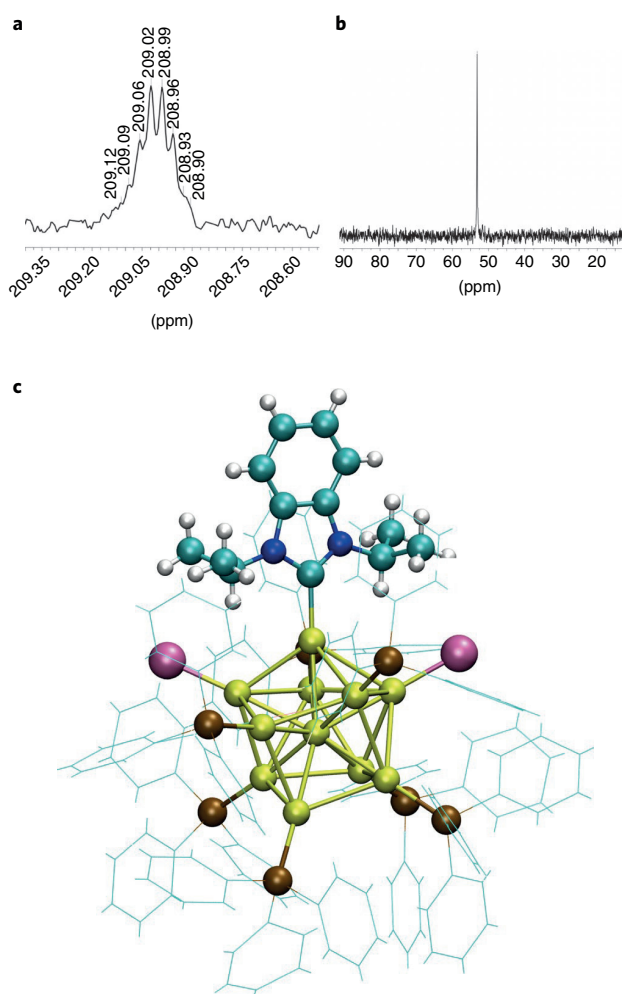
Fig. 3 | Spectroscopic and XRD characterization of NHC-substituted cluster 3a. a, ^{13}C {^{1}H} NMR spectrum of **3a** bearing ^{13}C-labelled NHC, which enables identification of the Au–C resonance. The signal appears as an octet from equal coupling to all seven phosphines. **b**, ^{31}P {^{1}H} NMR spectrum showing a single resonance at room temperature consistent with rapid exchange. **c**, Single-crystal XRD structure for NHC cluster **3a** showing NHC incorporation at P2 as proposed from DFT studies.

The longer Au–C bond and its effect on the underlying structure has precedent in prior DFT studies, which have proposed that binding of an NHC results in restructuring of the surface Au atoms in Au(111) systems[20,42,43]; however, this effect has been difficult to observe experimentally. The EXAFS results reported herein represent a direct measurement of the NHC influence on the underlying structure in metallic Au materials.

DFT calculations supported the trends observed experimentally by EXAFS. When the bond lengths were averaged over each of the optimized clusters, DFT studies predicted a 1.9 pm shorter Au–C bond in **3c** compared to **3a**. Similarly, the averaged calculated Au–Au bond length for the exterior gold atoms increased by 1.0 pm for cluster **3a** compared to **2**, while cluster **3c** showed no core expansion (within error).

Single-crystal XRD study of nanocluster 3a. X-ray quality single crystals of **3a** were grown by layering of *n*-hexane onto a solution of **3a** in dichloromethane at room temperature. After several days, reddish prisms of **3a** could be observed. Because dichloromethane co-crystallizes with **3a**, degradation of the crystal was observed on drying.
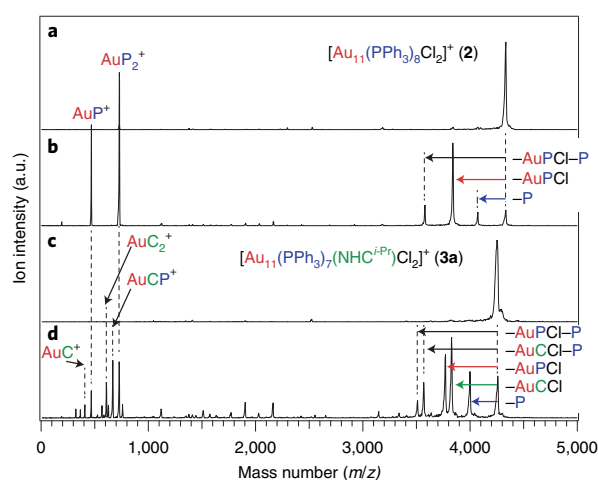
Fig. 4 | Assessment of stability and ligand dissociation by CID mass spectrometry. a, In-source CID mass spectra of cluster **2** recorded at the CID voltage of 0 V. Notations C and P represent NHC$^{i\text{-}Pr}$ and PPh$_3$, respectively. **b**, In-source CID mass spectra of cluster **2** recorded at 200 V. **c**, In-source CID mass spectra of cluster **3a** recorded at the CID voltage of 0 V. **d**, In-source CID mass spectra of cluster **3a** recorded at 200 V.

The structure of the cluster obtained from this study was found to be the same as that predicted by DFT, resulting from displacement of P2 (Fig. 3c). Although static disorder in the region of the NHC ligand complicates a detailed analysis of the Au–C bond length, the value obtained (2.09(2) Å) is in the same range as that predicted by EXAFS analysis (2.161(6) Å, Supplementary Table 10). Taken in aggregate, the Au–Au bonds in the cluster were seen to contract upon introduction of the NHC ligand; however, localized bonds experience contractions and expansions that may be significant for catalysis (Supplementary Figs. 56 and 57 and Supplementary Tables 11 and 12).

Stability and catalytic activity of nanoclusters. Stability and ligand dissociation were also assessed using collision-induced dissociation mass spectrometry (CID-MS). In Fig. 4 we compare the in-source CID mass spectra of **2** and **3a**, recorded under identical conditions. Cluster **2** undergoes loss of Au(PPh$_3$)Cl and PPh$_3$ as major CID paths (Fig. 4a). In contrast, loss of the Au(NHC$^{i\text{-}Pr}$)Cl unit was the most dominant CID pathway for **3a** (Fig. 4b), even though the ratio of NHC$^{i\text{-}Pr}$ to PPh$_3$ in the cluster is 1:7. In addition, direct dissociation of the NHC$^{i\text{-}Pr}$ ligand by Au–C bond cleavage was not observed under any conditions, in sharp contrast to **2**, where the loss of PPh$_3$ was observed. These results suggest that NHC$^{i\text{-}Pr}$ has significantly higher binding affinity to Au than PPh$_3$ does. These conclusions were supported by thermogravimetric analysis–mass spectrometry (TGA–MS) data, which also showed that phosphines are the first ligands to be lost (Supplementary Table 13 and Supplementary Figs. 61–64).

The thermal stability of the clusters was assessed by heating clusters in various solvents and monitoring the molecular transitions by UV–vis spectroscopy. The all-phosphine cluster **2** was used as a benchmark, which underwent complete decomposition after heating to 70 °C in pentanol (12 h) and toluene at 70 °C (24 h). By contrast, NHC-stabilized clusters showed dramatically improved stability, with **3c** displaying virtually no change over 24 h at 70 °C in toluene (Supplementary Fig. 58). Stability was reduced in the polar solvent pentanol, which allowed us to differentiate between the different NHC-functionalized clusters (Fig. 5a,b and Supplementary Fig. 59). Among the clusters examined, cluster stability tracked with sterics, with **3c** being the most stable, showing virtually no decomposition after 12 h at 70 °C in pentanol (Fig. 5a,b). Clusters **2**, **3a** and **3b**
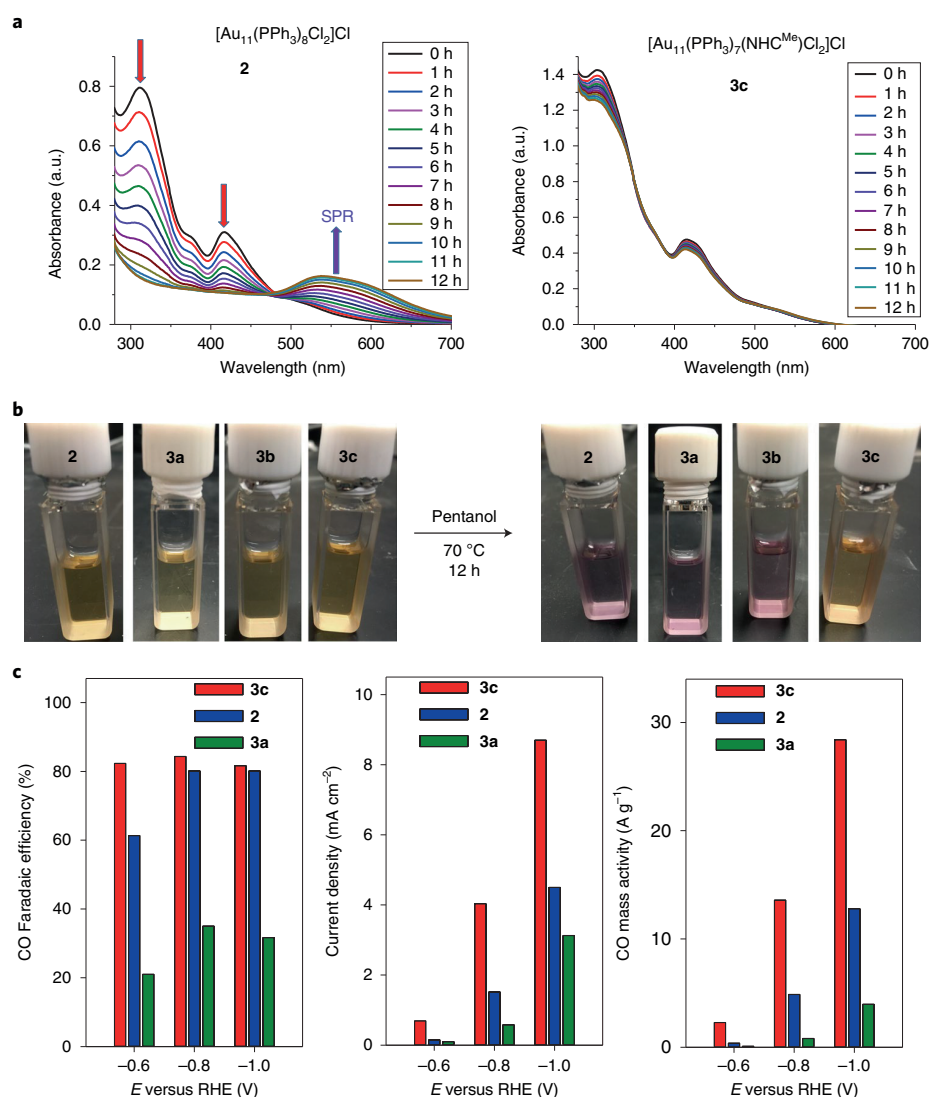
Fig. 5 | Nanocluster stability and activity in the electrocatalytic reduction of CO_2 to CO. a, UV–vis spectra of clusters **2** and **3c** in pentanol at 70 °C over 12 h. Cluster **2** decomposes to nanoparticles, evident by the loss of molecular signals at 405 and 310 nm and growth of the signal at 550 nm, while **3c** is completely stable. **b**, Nanoclusters **2**, **3a**, **3b** and **3c** before and after thermal treatment showing the decomposition of **2**, **3a** and **3b** while nanocluster **3c** remains intact. **c**, Catalytic activity and selectivity of nanoclusters **2**, **3a** and **3c** in the CO_2 to CO reduction showing that nanocluster **3c** has the highest Faradaic efficiency for CO, the highest current density and the highest mass activity among the nanoclusters tested. Although Faradaic efficiency seems independent of applied current, catalytic activity (as assessed through current density and mass activity) is highest at −1.0 V (versus reversible hydrogen electrode, RHE).

change colour from yellow (clusters) to purple (nanoparticles) after heating in pentanol (Fig. 5b). The relative stability of the clusters is thus **2** < **3a** < **3b** < **3c**. TGA–MS studies also showed that **3c** was the most stable of all clusters, with onset of ligand loss occurring 15–20 °C higher than all other clusters (Supplementary Figs. 60–64).

With a detailed understanding of structure and stability in hand, we examined these clusters as catalysts for the electrocatalytic reduction of CO_2 to CO (Fig. 5c)[44–49]. This is an important reaction because CO is the key component in many high-volume carbon–carbon bond-forming reactions such as the oxo reaction and the Cativa process.

Nanoclusters **2**, **3a** and **3c** were dissolved in a mixture of isopropanol and toluene (1:2 vol/vol) and deposited on carbon-paper electrodes with a catalyst loading of 0.25 mg cm^{-2}. The electrodes were then dried at room temperature before activating in air by heating

to 180 °C for 2 h. This temperature was coincident with changes in the TGA-MS of the nanoclusters that are attributed to loss of a phosphine ligand (Supplementary Table 13 and Supplementary Figs. 61–64). Lower temperatures resulted in significantly lower activity, and longer treatment (6 h) at 180 °C was also detrimental (Supplementary Fig. 66).

Electroreduction of CO_2 was performed using a three-electrode system, with Ag/AgCl and Pt mesh used as reference and counter electrodes, which were submerged in a CO_2-saturated, 0.1 M $KHCO_3$ electrolyte solution. During the reaction, CO_2 was introduced by bubbling the gas through the electrolyte at 15 standard cubic centimetres per minute, and the product gases were analysed by gas chromatography.

As shown in Fig. 5c, nanocluster **3c** outperformed all-phosphine cluster **2** and cluster **3a** bearing an isopropylated NHC. Nanocluster

3c affected the electrocatalytic CO_2 reduction with the highest Faradaic efficiency (selectivity for CO production versus H_2). Similarly, cluster **3c** had the highest current density (mA cm^{-2}) and mass activity (A g^{-1}) of all clusters tested, at all voltages employed (Fig. 5c), with the greatest differences being observed at −1.0 V (versus RHE). Higher loadings of this nanocluster on the surface led to decreased performance, suggesting that more highly dispersed nanoclusters are more active than any agglomerated species that may form (Supplementary Fig. 67).

Compared with previously reported related NHC-functionalized nanoparticles, nanocluster **3c** displays similar levels of Faradaic efficiency and current density, although at more negative voltages[43,44]. The best nanostructured catalysts in the literature again give similar results, but at lower overpotentials, as a consequence of high catalyst loadings[43,47]. With the high mass activity already observed for **3c**, performance improvements would be expected through the use of higher-surface-area supports such as carbon nanoparticles[43].

To ensure that CO_2 is the source of the observed CO, the reaction was carried out with ^{13}C-labelled CO_2. Analysis of this reaction by gas chromatography–mass spectrometry (GC–MS) analysis (Supplementary Fig. 65) shows clear incorporation of the isotope into carbon monoxide (^{13}CO, $m/z = 29$), confirming that the CO is produced from CO_2 by comparison with CO obtained from $^{12}CO_2$ where GC-MS analysis gave an m/z of 28 mass units for ^{12}CO. Only trace amounts of formate were observed after prolonged exposure (1%), illustrating the high selectivity of the reaction (Supplementary Fig. 68).

Interestingly, cluster **3c** is the only cluster of those examined that retained its structure and did not decompose to nanoparticles following extended thermal treatment. This observation leads to the intriguing possibility that having an intact nanocluster is important for catalytic activity, and illustrates the advantage of employing molecular species such as clusters as catalysts. It should be noted that NHC substitution does not uniformly lead to improved catalysts because cluster **3a** was outperformed by all-phosphine cluster **2**. Although the precise reasons for this difference are not presently clear, it may be that comparisons across cluster types are not as valid as comparisons within the NHC series **3a**, **3b** and **3c**. However, it is clear that the most stable cluster examined (**3c**) also gives the highest activity.

Conclusion

We have reported an example of the use of NHCs to stabilize gold(0) nanoclusters. The introduction of the NHC can be accomplished by a simple displacement reaction employing benzimidazolium hydrogen carbonate salts. The number of NHCs introduced is controllable by NHC structure, equivalents and reaction conditions. The structures of the NHC-containing clusters were predicted by DFT and confirmed by a combination of mass spectrometry, NMR, EXAFS, XANES, UV–vis spectroscopy and single-crystal XRD. The stability of the NHC-containing clusters was assessed by treatment at high temperature in a variety of solvents and by CID-MS and TGA–MS. NHC-containing clusters were found to be more stable than the all-phosphine clusters, with absolute stability dictated by the nature of the NHC. The performance of various clusters in electrocatalytic CO_2 reduction was found to correlate with cluster stability, with the most stable cluster having the highest Faradaic efficiency, catalytic activity and current density. These observations suggest that these novel NHC-stabilized gold clusters can have quantifiable benefits for electrocatalytic performance, which can be enhanced even further due to an atomically precise understanding of their structure.

Methods

In a two-neck flask equipped with a condenser and an argon balloon, a mixture of $[Au_{11}(PPh_3)_8Cl_2]Cl$ (**2**) and the corresponding benzimidazolium hydrogen carbonate (**1x**) were dissolved in THF (1 ml of THF per 1 mg of **2**). The resulting mixture was heated at 70 °C for 2 h before being cooled to room temperature.

The solvent was removed in vacuo to give an orange solid, which was dissolved in dichloromethane (DCM) and passed through a Celite plug to remove any insoluble orange particles. The solvent was evaporated under an air stream or by rotary evaporator and the resulting orange solid was triturated with Et_2O (2 × 5 ml) to remove triphenylphosphine oxide. The resulting clusters were dissolved in a minimum amount of DCM to give a red solution, which was loaded onto a silica gel column packed with DCM/MeOH (25:1 vol/vol). The product was eluted with DCM/MeOH (9:1 v/v) to give the desired cluster as a red solid after solvent evaporation in vacuo. For details of specific experiments see Supplementary Information.

References

1. Bürgi, T. Properties of the gold–sulphur interface: from self-assembled monolayers to clusters. *Nanoscale* **7**, 15553–15567 (2015).
2. Häkkinen, H. The gold–sulfur interface at the nanoscale. *Nat. Chem.* **4**, 443–455 (2012).
3. Yamazoe, S., Koyasu, K. & Tsukuda, T. Nonscalable oxidation catalysis of gold clusters. *Acc. Chem. Res.* **47**, 816–824 (2014).
4. Jadzinsky, P. D., Calero, G., Ackerson, C. J., Bushnell, D. A. & Kornberg, R. D. Structure of a thiol monolayer-protected gold nanoparticle at 1.1 Å resolution. *Science* **318**, 430–433 (2007).
5. Häkkinen, H., Walter, M. & Grönbeck, H. Divide and protect: capping gold nanoclusters with molecular gold–thiolate rings. *J. Phys. Chem. B* **110**, 9927–9931 (2006).
6. Qian, H., Zhu, M., Wu, Z. & Jin, R. Quantum sized gold nanoclusters with atomic precision. *Acc. Chem. Res.* **45**, 1470–1479 (2012).
7. Hesari, M., Workentin, M. S. & Ding, Z. NIR electrochemiluminescence from Au_{25}^- nanoclusters facilitated by highly oxidizing and reducing co-reactant radicals. *Chem. Sci.* **5**, 3814–3822 (2014).
8. Jensen, K. M. Ø. et al. Polymorphism in magic-sized $Au_{144}(SR)_{60}$ clusters. *Nat. Commun.* **7**, 11859 (2016).
9. Chevrier, D. M., Yang, R., Chatt, A. & Zhang, P. Bonding properties of thiolate-protected gold nanoclusters and structural analogs from X-ray absorption spectroscopy. *Nanotechnol. Rev.* **4**, 193–206 (2015).
10. Chevrier, D. M., Zeng, C. J., Jin, R. C., Chatt, A. & Zhang, P. Role of Au_4 units on the electronic and bonding properties of $Au_{28}(SR)_{20}$ nanoclusters from X-ray spectroscopy. *J. Phys. Chem. C* **119**, 1217–1223 (2015).
11. Jin, R. Quantum sized, thiolate-protected gold nanoclusters. *Nanoscale* **2**, 343–362 (2010).
12. Tsukuda, T. & Häkkinen, H. *Protected Metal Clusters: From Fundamentals to Applications* (Elsevier, Amsterdam, 2015).
13. Wang, Y. et al. Atomically precise alkynyl-protected metal nanoclusters as a model catalyst: observation of promoting effect of surface ligands on catalysis by metal nanoparticles. *J. Am. Chem. Soc.* **138**, 3278–3281 (2016).
14. Wang, Y. et al. Site preference in multimetallic nanoclusters: incorporation of alkali metal ions or copper atoms into the alkynyl-protected body-centered cubic cluster $[Au_7Ag_8(C\equiv C^tBu)_{12}]^+$. *Angew. Chem. Int. Ed.* **55**, 15152–15156 (2016).
15. Wang, Y. et al. An intermetallic $Au_{24}Ag_{20}$ superatom nanocluster stabilized by labile ligands. *J. Am. Chem. Soc.* **137**, 4324–4327 (2015).
16. Wan, X. K., Tang, Q., Yuan, S. F., Jiang, D. E. & Wang, Q. M. Au_{19} nanocluster featuring a V-shaped alkynyl-gold motif. *J. Am. Chem. Soc.* **137**, 652–655 (2015).
17. Maity, P., Tsunoyama, H., Yamauchi, M., Xie, S. H. & Tsukuda, T. Organogold clusters protected by phenylacetylene. *J. Am. Chem. Soc.* **133**, 20123–20125 (2011).
18. Weidner, T. et al. NHC-based self-assembled monolayers on solid gold substrates. *Aust. J. Chem.* **64**, 1177–1179 (2011).
19. Zhukhovitskiy, A. V., Mavros, M. G., Voorhis, T. V. & Johnson, J. A. Addressable carbene anchors for gold surfaces. *J. Am. Chem. Soc.* **135**, 7418–7421 (2013).
20. Crudden, C. M. et al. Ultra stable self-assembled monolayers of N-heterocyclic carbenes on gold. *Nat. Chem.* **6**, 409–414 (2014).
21. Crudden, C. M. et al. Simple direct formation of self-assembled N-heterocyclic carbene monolayers on gold and their application in biosensing. *Nat. Commun.* **7**, 12654 (2016).

22. Zhukhovitskiy, A. V., MacLeod, M. J. & Johnson, J. A. Carbene ligands in surface chemistry: from stabilization of discrete elemental allotropes to modification of nanoscale and bulk substrates. *Chem. Rev.* **115**, 11503–11532 (2015).
23. Larrea, C. R. et al. N-heterocyclic carbene self-assembled monolayers on copper and gold: dramatic effect of wingtip groups on binding, orientation and assembly. *ChemPhysChem* **18**, 3536–3539 (2017).
24. MacLeod, M. J. & Johnson, J. A. Pegylated N-heterocyclic carbene anchors designed to stabilize gold nanoparticles in biologically relevant media. *J. Am. Chem. Soc.* **137**, 7974–7977 (2015).
25. Kim, H. K. et al. Reduction of the work function of gold by N-heterocyclic carbenes. *Chem. Mater.* **29**, 3403–3411 (2017).
26. Wang, G. et al. Ballbot-type motion of N-heterocyclic carbenes on gold surfaces. *Nat. Chem.* **9**, 152–156 (2016).
27. Engel, S., Fritz, E. C. & Ravoo, B. J. New trends in the functionalization of metallic gold: from organosulfur ligands to N-heterocyclic carbenes. *Chem. Soc. Rev.* **46**, 2057–2075 (2017).
28. Moller, N. et al. Stabilization of high oxidation state upconversion nanoparticles by N-heterocyclic carbenes. *Angew. Chem. Int. Ed.* **56**, 4356–4360 (2017).
29. Salorinne, K. et al. Water-soluble N-heterocyclic carbene-protected gold nanoparticles: size-controlled synthesis, stability and optical properties. *Angew. Chem. Int. Ed.* **56**, 6198–6202 (2017).
30. Man, R. W. Y. et al. Ultrastable gold nanoparticles modified by bidentate N-heterocyclic carbene ligands. *J. Am. Chem. Soc.* **140**, 1576–1579 (2018).
31. Rühling, A. et al. Modular bidentate hybrid NHC–thioether ligands for the stabilization of palladium nanoparticles in various solvents. *Angew. Chem. Int. Ed.* **55**, 5856–5860 (2016).
32. Crudden, C. M. & Allen, D. A. Stability and reactivity of N-heterocyclic carbene complexes. *Coord. Chem. Rev.* **248**, 2247–2273 (2004).
33. Hopkinson, M. N., Richter, C., Schedler, M. & Glorius, F. An overview of N-heterocyclic carbenes. *Nature* **510**, 485–496 (2014).
34. Polgar, A. M., Weigend, F., Zhang, A., Stillman, M. J. & Corrigan, J. F. A N-heterocyclic carbene-stabilized coinage metal–chalcogenide framework with tunable optical properties. *J. Am. Chem. Soc.* **139**, 14045–14048 (2017).
35. Azizpoor Fard, M., Levchenko, T. I., Cadogan, C., Humenny, W. J. & Corrigan, J. F. Stable -ESiMe$_3$ complexes of Cu^I and Ag^I (E = S, Se) with NHCs: synthons in ternary nanocluster assembly. *Chem. Eur. J* **22**, 4543–4550 (2016).
36. Robilotto, T. J., Bacsa, J., Gray, T. G. & Sadighi, J. P. Synthesis of a trigold monocation: an isolobal analogue of [H$_3$]$^+$. *Angew. Chem. Int. Ed.* **51**, 12077–12080 (2012).
37. Jin, L. et al. Trinuclear gold clusters supported by cyclic (alkyl)(amino) carbene ligands: mimics for gold heterogeneous catalysts. *Angew. Chem. Int. Ed.* **53**, 9059–9063 (2014).
38. McKenzie, L. C., Zaikova, T. O. & Hutchison, J. E. Structurally similar triphenylphosphine-stabilized undecagolds, Au$_{11}$(PPh$_3$)$_7$Cl$_3$ and [Au$_{11}$(PPh$_3$)$_8$Cl$_2$]Cl, exhibit distinct ligand exchange pathways with glutathione. *J. Am. Chem. Soc.* **136**, 13426–13435 (2014).
39. Enkovaara, J. et al. Electronic structure calculations with GPAW: a real-space implementation of the projector augmented-wave method. *J. Phys. Condens. Matter* **22**, 253202 (2010).
40. Zhang, P. & Sham, T. K. X-ray studies of the structure and electronic behavior of alkanethiolate-capped gold nanoparticles: the interplay of size and surface effects. *Phys. Rev. Lett.* **90**, 245502 (2003).
41. Lopez-Cartes, C. et al. Gold nanoparticles with different capping systems: an electronic and structural XAS analysis. *J. Phys. Chem. B* **109**, 8761–8766 (2005).
42. Tang, Q. & Jiang, D.-E. Comprehensive view of the ligand–gold interface from first principles. *Chem. Mater.* **29**, 6908–6915 (2017).
43. Rodríguez-Castillo, M. et al. Reactivity of gold nanoparticles towards N-heterocyclic carbenes. *Dalton Trans.* **43**, 5978–5982 (2014).
44. Tang, Q. et al. Lattice-hydride mechanism in electrocatalytic CO$_2$ reduction by structurally precise copper-hydride nanoclusters. *J. Am. Chem. Soc.* **139**, 9728–9736 (2017).
45. Cao, Z. et al. A molecular surface functionalization approach to tuning nanoparticle electrocatalysts for carbon dioxide reduction. *J. Am. Chem. Soc.* **138**, 8120–8125 (2016).
46. Cao, Z. et al. Chelating N-heterocyclic carbene ligands enable tuning of electrocatalytic CO$_2$ reduction to formate and carbon monoxide: surface organometallic chemistry. *Angew. Chem. Int. Ed.* **57**, 4981–4985 (2018).
47. Gray, H. B. Powering the planet with solar fuel. *Nat. Chem.* **1**, 7 (2009).
48. Liu, M. et al. Enhanced electrocatalytic CO$_2$ reduction via field-induced reagent concentration. *Nature* **537**, 382–386 (2016).
49. Zhang, L., Zhao, Z.-J. & Gong, J. Nanostructured materials for heterogeneous electrocatalytic CO$_2$ reduction and their related reaction mechanisms. *Angew. Chem. Int. Ed.* **56**, 11326–11353 (2017).

Acknowledgements

Author contributions

C.M.C., P.J.U., M.R.N. and K.S. designed and carried out the synthesis of the nanoclusters, assisted by K.A., P.J.G., M.N., K.M.O. and R.W.Y.M. K.M.O. and R.W.Y.M. optimized the synthetic procedures and purifications and acquired TGA–MS data. MS analysis was performed and interpreted by S.T., R.T. and T.T., including CID MS. Crystallization of **3a** was carried out by M.N. and S.T. on a sample prepared and purified by K.M.O. DFT studies, including prediction of structure and optical spectra, were carried out by S.K., S.M. and H.H. EXAFS and XANES studies were carried out and interpreted by J.H.H. and J.D.P. Electrocatalytic studies were performed and interpreted by C.-T.D. and E.H.S. The manuscript was written by C.M.C. with assistance from co-authors.

Competing interests

The authors declare no competing interests.

Additional information

Supplementary information is available for this paper at https://doi.org/10.1038/s41557-019-0246-5.

Reprints and permissions information is available at www.nature.com/reprints.

Correspondence and requests for materials should be addressed to H.H., T.T. or C.M.C.

Publisher's note: Springer Nature remains neutral with regard to jurisdictional claims in published maps and institutional affiliations.

In the format provided by the authors and unedited.

N-heterocyclic carbene-functionalized magic-number gold nanoclusters

Mina R. Narouz[1], Kimberly M. Osten[2], Phillip J. Unsworth [1], Renee W. Y. Man[2], Kirsi Salorinne[2], Shinjiro Takano [3], Ryohei Tomihara[3], Sami Kaappa [4], Sami Malola[4], Cao-Thang Dinh [5], J. Daniel Padmos[1], Kennedy Ayoo[1], Patrick J. Garrett[1], Masakazu Nambo[2], J. Hugh Horton[1], Edward H. Sargent [5], Hannu Häkkinen [4]*, Tatsuya Tsukuda [3,6]* and Cathleen M. Crudden [1,2]*

[1]Department of Chemistry, Queen's University, Kingston, Ontario, Canada. [2]Institute of Transformative Bio-Molecules (WPI-ITbM), Nagoya University, Nagoya, Japan. [3]Department of Chemistry, School of Science, The University of Tokyo, Bunkyo-ku, Tokyo, Japan. [4]Departments of Chemistry and Physics, Nanoscience Center, University of Jyväskylä, Jyväskylä, Finland. [5]Department of Electrical and Computer Engineering, The University of Toronto, Toronto, Ontario, Canada. [6]Elements Strategy Initiative for Catalysts and Batteries (ESICB), Kyoto University, Katsura, Kyoto, Japan.
*e-mail: hannu.j.hakkinen@jyu.fi; tsukuda@chem.s.u-tokyo.ac.jp; cruddenc@chem.queensu.ca

Supplementary Information

N-Heterocyclic carbene-functionalized magic-number gold nanoclusters

Mina R. Narouz[1], Kimberly M. Osten[2], Phillip J. Unsworth[1], Renee W. Y. Man[2], Kirsi Salorinne[2], Shinjiro Takano[3], Ryohei Tomihara[3], Sami Kaappa[4], Sami Malola[4], Cao-Thang Dinh[5], J. Daniel Padmos[1], Kennedy Ayoo[1], Patrick J. Garrett[1], Masakazu Nambo[2], J. Hugh Horton[1], Edward H. Sargent[5], Hannu Häkkinen*[4], Tatsuya Tsukuda*[3,6], Cathleen M. Crudden*[1,2]

[1]Department of Chemistry, Queen's University, Chernoff Hall, Kingston, Ontario K7L 3N6 Canada
[2]Institute of Transformative Bio-Molecules (WPI-ITbM), Nagoya University, Nagoya, 464-8601, Japan
[3]Department of Chemistry, School of Science, The University of Tokyo, 7-3-1 Hongo, Bunkyo-ku, Tokyo 113-0033, Japan
[4]Departments of Chemistry and Physics, Nanoscience Center, University of Jyväskylä, 40014 Jyväskylä, Finland
[5]Department of Electrical and Computer Engineering, The University of Toronto, Toronto, Ontario M5S 3G4, Canada
[6]Elements Strategy Initiative for Catalysts and Batteries (ESICB), Kyoto University, Katsura, Kyoto 615-8520, Japan

4   Computational studies

DFT calculations were run as implemented in the GPAW package.[12] The wave functions were converged in a real-space grid basis with spacing of 0.2 Å, and the exchange-correlation effects were modelled using the PBE functional.[13] The optimal exchange site was investigated by replacing the phosphines of $Au_{11}(PPh_3)_8Cl_2$ by carbene ligands manually one by one and finding the minimum-energy atomic configuration for each species. The relaxation was performed in a computational cell with 6 Å of vacuum around the outermost atoms of the cluster, and the configuration with maximum force of 0.05 eV/Å on a single atom was sought. To compensate for the absence of the counter-ion, the calculations were run with +1 charge for each cluster. The atomic coordinates for the initial structure of $Au_{11}(PPh_3)_8Cl_2$ were obtained by relaxing the crystal structure reported.[2] While all eight single substitutions for different sites were examined for all the three types of NHC (**1a–c**), only the most plausible isomers were studied of the di-substituted species (**4c**), the choice being based on the energetics of the mono-substitutions. To obtain the energy changes in **Table 7** and **Table 8**, the molecules in formula (1) were relaxed and the sum of potential energies of the reactants was subtracted from the sum of potential energies of the products. The optical spectra were calculated for the relaxed atomic structures using linear-response time-dependent DFT (LR-TDDFT), as implemented in GPAW.[14] The transitions were calculated up to 5 eV (~ 250 nm) and the delta peaks for each transition were broadened as a Gaussian function with a width of 0.1 eV.

Table 7: Reaction energies from DFT calculations for the formation of mono-substituted clusters (**3a-c**) via reactions of the type $[Au_{11}(PPh_3)_8Cl_2]^+ + NHC^R \rightarrow [Au_{11}(PPh_3)_7NHC^RCl_2]^+ + PPh_3$ at different ligand sites P1–8 (ligand site labelling is shown in **Error! Reference source not found.**).

Position	Potential energy (eV)		
	3a (R = iPr)	**3b** (R = Et)	**3c** (R = Me)
P1	−0.64	−0.37	−0.47
P2	**−0.93**	**−0.82**	**−0.80**
P3	−0.73	−0.75	−0.74
P4	−0.55	−0.59	−0.60
P5	−0.41	−0.16	−0.54
P6	−0.40	−0.32	−0.47
P7	−0.75	−0.44	−0.67
P8	+0.05	−0.25	−0.46

Table 8: DFT-based HOMO–LUMO gaps of the mono-NHC substituted clusters (**3a-c**) with NHC-substitution at different ligand sites P1-8 (ligand site labelling is shown in **Error! Reference source not found.**).

Position	HOMO-LUMO gap (eV)		
	3a (R = iPr)	**3b** (R = Et)	**3c** (R = Me)
P1	1.91	1.92	1.90
P2	**1.96**	**2.00**	**2.01**
P3	1.90	1.89	1.91

P4	1.81	1.83	1.82
P5	1.86	1.97	1.95
P6	1.81	1.88	1.86
P7	1.81	1.94	1.95
P8	1.95	1.91	1.89

*un-substituted cluster **2** has a HOMO-LUMO gap of 1.95 eV
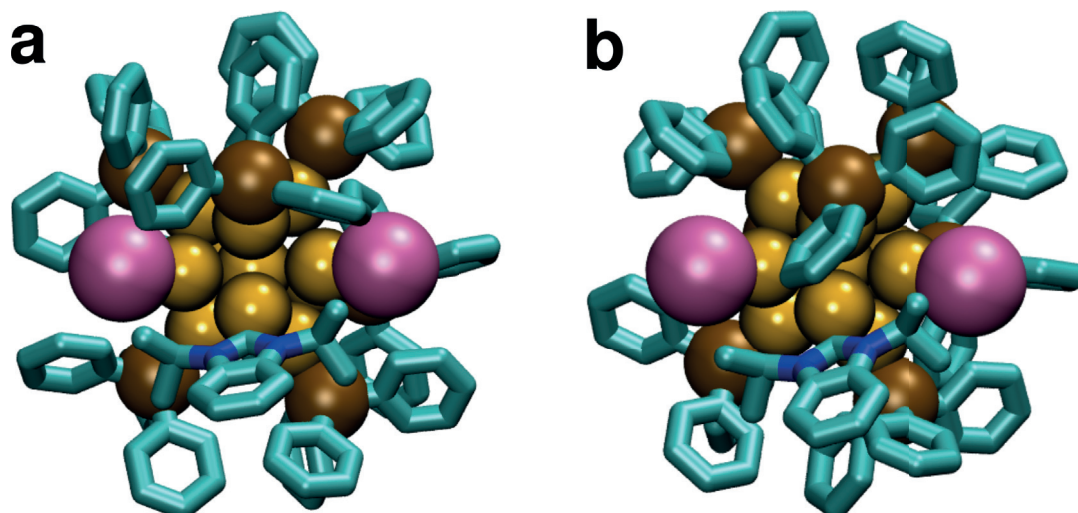
Figure 52: a: DFT-predicted structure and b: observed crystal structure of cluster **3a**. The NHC is substituted to the phosphine position P2. The only difference in the structures a and b are in the packing of the phosphine phenyl rings in the ligand layer.
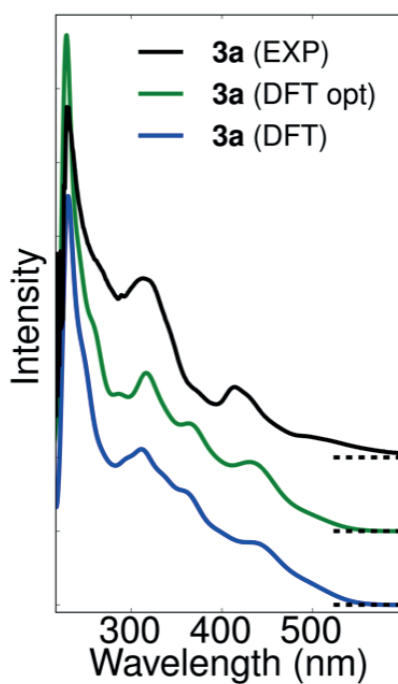
Figure 52: Calculated UV-Vis spectra of NHC^{iPr}-substituted clusters **3a** (blue) using the X-ray structure, and experimental UV-Vis spectrum of **3a** (black). The green curve (labeled as DFT opt) is calculated for the structure that is relaxed before the optical response calculation. The calculated spectra are shown for the most energetically favourable isomers of the substituted clusters.
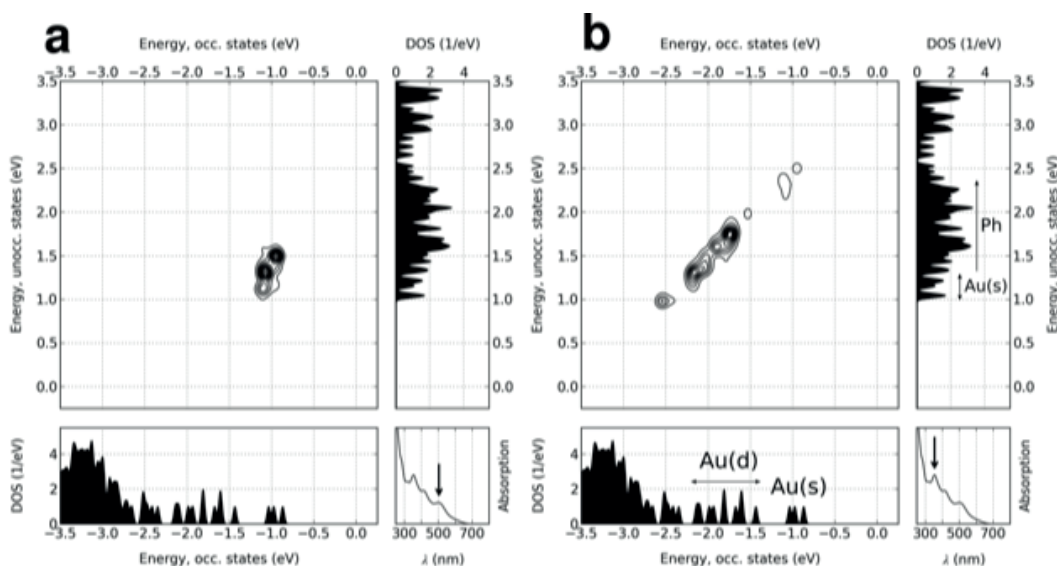
Figure 53: Transition contribution map (TCM) images of (a) the 500 nm peak and (b) the 350 nm peak in the computed, non-shifted UV-Vis spectrum of **3a**. The unshifted peak at around 500nm in Figure a corresponds to transitions from the HOMO states, that are s-valence states of Au, to the unoccupied states of the phenyl rings of the PPh$_3$ groups. The peak in Figure b shows that the absorption at 350 nm mostly comprises of transitions from the Au d-states to the same phenyl states. Spectral analysis of the relaxed structure was conducted using the time-dependent density functional perturbation theory DFPT.[15]

Table 9: Reaction energies from DFT calculations for the formation of di-substituted cluster (**4b**) via a reaction of the type [Au$_{11}$(PPh$_3$)$_8$Cl$_2$]$^+$ + 2 NHC^{Et} → [Au$_{11}$(PPh$_3$)$_6$(NHC^{Et})$_2$Cl$_2$]$^+$ + 2 PPh$_3$ at different ligand sites P1–8.

Positions		Potential energy (eV) 4b (R = Et)
P2	P3	**−1.33**
P3	P7	−1.29
P2	P4	−1.25
P2	P7	−1.24
P3	P4	−1.14
P4	P5	−1.06
P1	P4	−1.04
P1	P7	−1.01
P4	P7	−0.91

PIV

N-HETEROCYCLIC CARBENE-STABILIZED AU₁₃ SUPERATOM CLUSTERS

by

Mina R. Narouz, Shinjiro Takano, Paul A. Lummis, Tetyana I. Levchenko,
Ali Nazemi, Sami Kaappa, Sami Malola, Seyedehgoonay Yousefalizadeh,
Kevin G. Stamplecoskie, Hannu Häkkinen, Tatsuya Tsukuda &
Cathleen Crudden (2018)

N-heterocyclic carbene-stabilized Au$_{13}$ superatom clusters

Mina R. Narouz[†], Shinjiro Takano[¶], Paul A. Lummis[†], Tetyana I. Levchenko[†], Ali Nazemi[†], Sami Kaappa[fl], Sami Malola[fl], Seyedehgoonay Yousefalizadeh[†], Kevin G. Stamplecoskie[†*], Hannu Häkkinen[fl*], Tatsuya Tsukuda[¶§*] and Cathleen M. Crudden[†‡*]

[†]Department of Chemistry, Queen's University, Chernoff Hall, Kingston, Ontario, Canada, K7L 3N6 [¶]Department of Chemistry, School of Science, The University of Tokyo, 7-3-1 Hongo, Bunkyo-ku, Tokyo 113-0033, Japan [§]Elements Strategy Initiative for Catalysts and Batteries (ESICB), Kyoto University, Katsura, Kyoto 615-8520, Japan [fl]Departments of Chemistry and Physics, Nanoscience Center, University of Jyväskylä, 40014 Jyväskylä, Finland [‡]Institute of Transformative Bio-Molecules (WPI-ITbM), Nagoya University, Chikusa, Nagoya, Japan, 464-8602.

Supporting Information Placeholder

ABSTRACT: Magic number Au$_{13}$ nanoclusters stabilized entirely by N-heterocyclic carbenes (NHCs) have been prepared by the bottom-up reduction of well-defined molecular NHC–Au–Cl complexes with sodium borohydride. The nature of the wingtip groups was shown to be critical in the preparation of stable clusters. The all NHC-clusters are prepared in high yield by this straightforward method, display higher stability than related all phosphine clusters, and possess extremely high emission quantum yield. DFT analysis of these clusters based on the resolved crystal structure reveals their electronic structure as 8-electron superatoms.

Metal nanoclusters are atomically-precise class of nanomaterials that, unlike metal nanoparticles, feature precise structures and discrete molecular orbitals and electronic transitions.[1] Since the ground-breaking report from Kornberg of a crystallographically characterized Au$_{102}$(SR)$_{44}$ cluster in 2007,[22] nanoclusters containing up to 333 Au atoms have been reported.[3] The stability of these clusters is explained with the "superatom" theory first described by Häkkinen and collaborators, which predicts structure based on closed electronic shell configurations.[1a, 4] This property differentiates "magic number" clusters from coordination clusters, the latter featuring Au(I) centers held together via aurophillic interactions and bridging X-type ligands.[5]

Thiols have long been the ligands of choice for superatom nanoclusters.[6] L-type ligands such as phosphines can also be employed, although these ligands are not as omnipresent as thiolates.[7] Clusters in which the only ligands are NHCs are limited to a handful of examples. In seminal work, Sadighi[8] and Bertrand[9] showed that mixed valence NHC clusters (Au(0/1)) can be prepared by reaction of carbon monoxide with Au carboxylates or μ$_3$-oxo Au clusters (Figure 1A). NHC-stabilized coordination clusters with gold atoms in the +1 state have been reported by Corrigan[5a] and Shionaya,[10] but thus far, there have been no examples of all-NHC magic number

Au(0) nanoclusters. Considering the high activity of Au(0) clusters in catalysis[1c] biomedicine, sensing, imaging, optics and energy conversion[6b], and the rising interest in the use of NHCs as stabilizing ligands for metal surfaces,[11] access to these unique structures is of significant importance. Our groups recently succeeded in introducing NHCs into the known phosphine-stabilized Au$_{11}$ nanoclusters via a ligand exchange approach (Figure 1B).[12] The number of NHCs introduced could be tuned in the range of 1–5, but complete replacement was not possible.

Herein we describe a straightforward, high yielding synthesis of gold (0) superatom clusters functionalized by all NHCs along with their structure determination by X-ray crystallography (Figure 1C). These clusters have unique photophysical properties, including among the highest quantum yields reported for gold nanoclusters.[13]

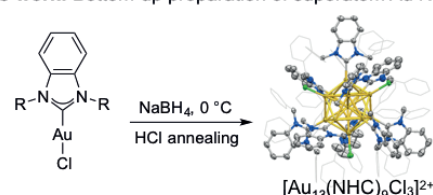**Figure 1**: NHC-containing Au clusters. **A**: NHC-stabilized mixed valence Au(0/1) clusters; **B**: Mixed phosphine/NHC–stabilized Au(0) clusters; **C**: All NHC-stabilized Au(0) clusters.

We and others have previously shown that the wingtip groups on the NHC are of paramount importance in terms of bonding modes to planar gold surfaces.[11g, 11k, 14] In the synthesis of NHC-containing nanoclusters, we also showed that the nature of the NHC ligand had a large effect on the substitution chemistry, with benzyl substituents providing the cluster with the highest extent of NHC for phosphine subsitution.[12] In a key computational paper, Tang and Jiang[15] have predicted that aromatic wing–tip groups will provide considerable stabilization when NHCs bind to surfaces of all types, but that when unusually bulky NHCs are employed, the number that can be introduced around a gold core is limited.

In recent work from our group where a displacement reaction was used to prepare mixed NHC/phosphine gold clusters, we found that the use of benzylated NHCs gave the largest number of NHCs on the cluster under comparable conditions. Based on this, the Jiang predictions, and the likelihood of π-π interactions stabilizing the cluster, we targeted benzylated NHC **1a** as our first choice for the first de novo synthesis of Au–NHC nanoclusters.

Precursor synthesis began with the preparation of molecular NHC–Au–Cl complexes. In addition to benzimidazolium salt **1a**, we also examined related salts **1b-f**, which have aromatic substituents on the wing-tip groups. The desired gold complexes could be produced easily and in high yield by the reaction of commercially available Me$_2$S–Au–Cl with benzimidazolium salts (**1a-e**) in the presence of K$_2$CO$_3$, following the work of Nolan and co-workers for the preparation of related Au–NHC complexes (Equation 1).[16] The use of these simple complexes as starting materials for cluster synthesis already presents an advantage vs. thiolate chemistry, where reduction is performed on an ill-characterized and likely polymeric mixture of sulfur-bridged species.[6b]

(a) R = Bn (b) R = CH$_2$(4-MeC$_6$H$_4$)
(c) R = CH$_2$(2-MeC$_6$H$_4$) (d) R = Ph (as BF$_4$ salt)
(e) R = CH$_2$(2-Np)
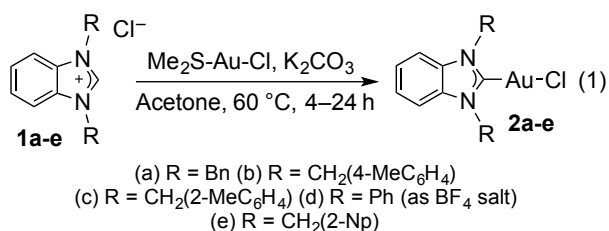
With NHC–Au–Cl complexes **2a-e** in hand, we optimized the conditions for cluster synthesis with **2a** using NaBH$_4$ as the reducing agent. Initial results were promising, with UV-vis data indicative of the presence of clusters rather than nanoparticles. After investigating a variety of conditions, we eventually settled on reduction at 0 °C, followed by warming to room temperature and treatment with HCl, taking inspiration from the work of Konishi on phosphine-Au clusters (Equation 2).[17]

Examining the clusters by UV-visible spectroscopy

and ESI-MS before and after HCl treatment was highly instructive (see S.I.). ESI-MS analysis showed that even the crude material contained only molecular species and Au$_{13}$ clusters, with no other significant cluster species detected. No significant changes were detected by ESI-MS after HCl treatment. The UV-vis spectra, however, were significantly sharper after HCl treatment (see S.I.). This suggests that the effect of HCl is not to focus cluster size, but rather to enhance the purity of the cluster in terms of ligand arrangement.[18]
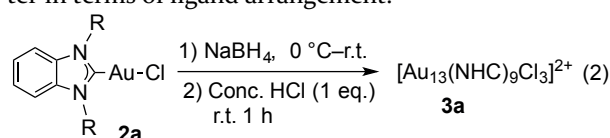
The molecular formula of the cluster was determined to be [Au$_{13}$(NHC)$_9$Cl$_3$]$^{2+}$, by ESI-MS analysis (Figure 2). This formula yields 8 delocalized electrons left in the gold core, in agreement with the predictions for an enhanced stability from the superatom theory,[3] and is also closely related to the cluster [Au$_{13}$(NHC)$_{10}$Cl$_2$]$^{3+}$ predicted by Tang and Jiang.[15]
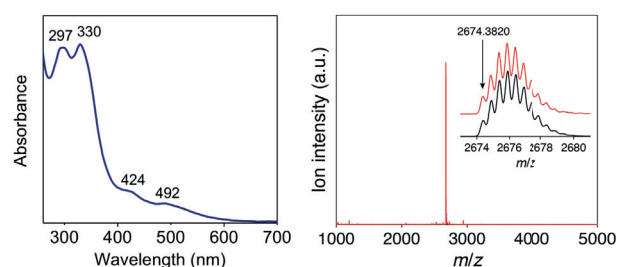
Figure 2: UV-vis spectrum (left) and ESI-MS (right) of [**3a**][PF$_6$]$_2$

Structural characterization of cluster **3a** was achieved by anion exchange to yield the related PF$_6^-$ cluster, [**3a**][PF$_6$]$_2$, followed by crystallization from a supersaturated acetonitrile/diethyl ether solution. Under these conditions, single crystals of suitable quality for X-ray diffraction analysis were obtained. As shown in Figure 3, the cluster is comprised of an icosahedral Au$_{13}$ core with one gold atom at the center, with the remaining gold atoms bound to either chloride or NHC ligands.
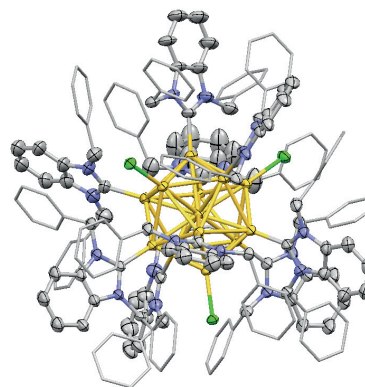
Figure 3: Molecular structure of [**3a**][PF$_6$]$_2$ with ellipsoids shown at 30% probability level. Anions and hydrogen atoms

have been removed, and phenyl rings from wingtip groups shown as wireframe for additional clarity. For additional representations, and all bond lengths and angles, please see Supporting Information. Colour key: carbon (grey); nitrogen (blue); chlorine (green); gold (yellow).

As expected, the NHCs are bound via a single Au–C bond, with Au-C and Au-Au bond lengths within expected values (For more details, see Supporting Information). In addition to providing clarity on the core Au structure, the X-ray crystallographic data also show the importance of interactions between the ligands. The cluster contains multiple CH–π and π-π interactions between the benzyl substituents and both rings of the benzannulated NHC core (see Supporting Information). The structural rigidity implicated by these interactions is likely responsible for the presence of long lived excited states (*vide infra*).

Through the use of ^{13}C labeled NHC precursors, we were able to identify the carbon-gold bonds as occurring in the 200–214 ppm range, consistent with the observation of the ^{13}C NMR signal for the single NHC in the mixed cluster $[Au_{11}(NHC)(PPh_3)_7Cl_2]Cl$ at 209 ppm.[12]

In order to test the generality of the cluster synthesis, and the importance of the benzyl groups, we subjected NHC–Au–Cl complexes **2b-2e** to the same reducing conditions followed by HCl treatment. The procedure was found to be general, but the clusters produced are highly sensitive to the steric constraints of the wingtip groups. For example, Au complex **2b**, in which methyl groups are introduced onto the para position of the benzyl groups, still gives Au_{13} clusters, as judged by UV-vis spectra and ESI–MS analysis. Complex **2c**, which contains an ortho methylated benzyl group, was also examined. This more hindered precursor gave slightly different clusters with the molecular formula $[Au_{13}(NHC^{oTol})_8Cl_4]^+$, accompanied by other species, indicating the significant effect of sterics. Consistent with this, aryl rings attached directly to the ring as in **2d** were completely ineffective, giving no nanoclusters and illustrating the importance of flexibility in the NHC wingtip groups. NaphthylCH$_2$– substituents were tolerated, with complex **2e** giving Au_{13} cluster **3e** in good yield.

With three new NHC-stabilized Au_{13} clusters in hand, we turned to a study of their properties. The thermal stability of the various clusters was assessed by heating acetonitrile solutions of the clusters while examining changes to their UV-vis spectra. For comparison, the all phosphine cluster $[Au_{11}(PPh_3)_8Cl_2]Cl$ (**4**)[19] was subjected to the same thermal treatment. As shown in Figure 4A, the all phosphine–protected cluster underwent full decomposition, while clusters **3a** and **3e** retained much of their initial colour. Further analysis by UV-vis spectroscopy (Figure 4, panels B-D) illustrated that phosphine cluster **4** completely decomposed after 4 hours. By comparison, all NHC-protected cluster **3a** showed only slight decomposition over the same time frame, and

cluster **3e** shows virtually no decomposition (Figure 4, panel D).

This improved stability is consistent with TGA analysis of the clusters, which demonstrate some loss of ligand at 235 °C and complete desorption at 585 °C. In contrast, for cluster **4**, ligand loss begins at 150 °C and complete loss of ligand is complete at 245 °C (see S.I.).
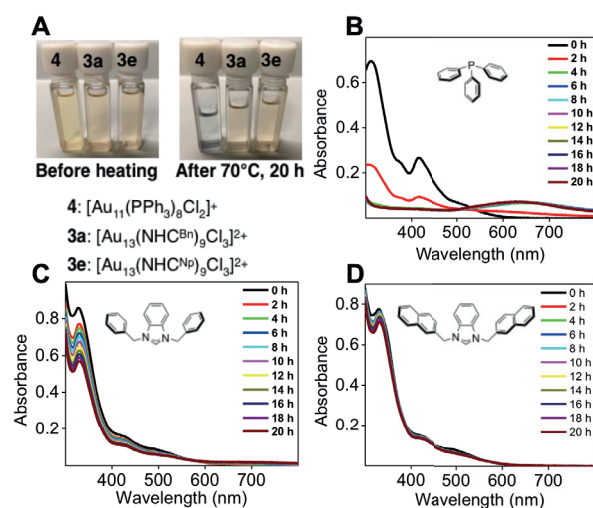

Figure 4: Study of Au clusters **4**, **3a** and **3e** before and after 20h of heating in acetonitrile at 70 °C. **A**: visuals of clusters before and after heating; **B**: UV-vis spectra of $[Au_{11}(PPh_3)_8Cl_2]Cl$ from 0-20h heating; **C** UV-vis spectra of $[Au_{13}(NHC^{Bn})_9Cl_3]^{2+}$ (**3a**) from 0-20h heating; **D** UV-vis spectra of $[Au_{13}(NHC^{Np})_9Cl_3]^{2+}$ (**3e**) from 0-20h heating.

The structural and electronic properties of **3a**, **3c**, and **3e** were examined by DFT, using the crystal structure of **3a** as a starting point (technical details in SI). The binding energy of the NHC ligand in **3a** evaluated from the PBE functional (1.99 eV) is about the same magnitude as a typical Au-SR bond, but being clearly higher than a typical Au-PR$_3$ bond (by about 1 eV). When van der Waals interactions in the ligand layer are accounted for (BEEF-vdW functional), the predicted Au-NHC bond strength increases to 2.62 eV in **3a**.

Compounds **3a**, **3c**, and **3e** all have a very similar HOMO-LUMO energy gap of about 2.0 eV, reflecting the expected electronic stability of the 8-electron configuration (Figures 5, S.I.). The Kohn-Sham orbitals near the Fermi level show distinct symmetry properties when projected to the I_h point group in the volume of the gold core (see S.I.). The HOMO, HOMO-1 and HOMO-2 states have triply degenerate T_{1u} symmetry corresponding to the *p*-type spherical orbitals as expected for an 8-electron superatom. The first few unoccupied states have H_g symmetry corresponding to five-fold degenerate *d*-states in spherical representation, Cl ligands break both the T_{1u} and H_g states by lowering the symmetry from the core-I_h to C_3.

The calculated UV-vis spectra of **3a**, **3c**, and **3e** were in good agreement with the experimental data concerning

the location of the optical gap and the few visible absorption peaks (see S.I.). The superatom electronic structure predicts dipole-allowed HOMO→LUMO as the lowest optical transition as also confirmed from the spectral analysis (see S.I.). We also examined the first excited states where an electron is excited from the HOMO to the LUMO state by forcing the occupation numbers accordingly in the spin-polarized DFT calculation and relaxing the system with the PBE functional. The excited states of **3a** and **3e** were 1.68 eV and 1.61 eV higher in energy compared to the ground state, respectively. These energies correspond to 738-770 nm in wave length, in a excellent agreement with the observed emission spectra as discussed next.
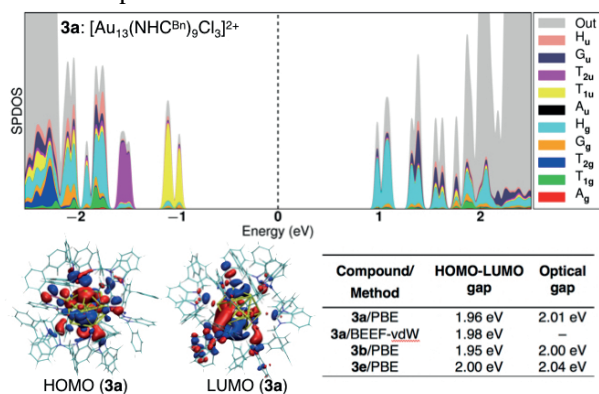
Figure 5: I_h symmetry-projected electronic density of states (SPDOS) of **3a.** Energy zero is at the center of the HOMO-LUMO gap. HOMO and LUMO orbitals are visualized.

Fluorescence excitation emission matrix (EEM) spectroscopy studies on **3e** are shown in Figure 6. Importantly, the excitation spectrum of **3e** matches very well with the absorbance spectrum for the same compound (Figure 4D). The quantum yield of fluorescence was also determined from EEM spectra (Figure 6B) with excitation matched to the standard, zinc phthalocyanine. Clusters **3e** and **3a** boast impressive emission quantum yields of 27% and 10%, respectively, making these some of the highest quantum yields ever recorded for gold clusters. The absorbance and/or emission onset can be used to estimate the HOMO/LUMO energy gap to be 616 nm (2.03 eV), in excellent agreement with DFT results (see S.I.), (see supporting information for more detailed analysis).[20] This is a further indicator of the purity of the clusters, and confirms that de-excitation of the superatom excited-state is responsible for the intense emission observed.[21]

In conclusion, we have reported the preparation of an all-NHC stabilized superatom Au$_{13}$ cluster as a novel example of an 8-electron superatom with unusually high emission quantum yield and superior thermal stability to related phosphine-protected gold clusters.
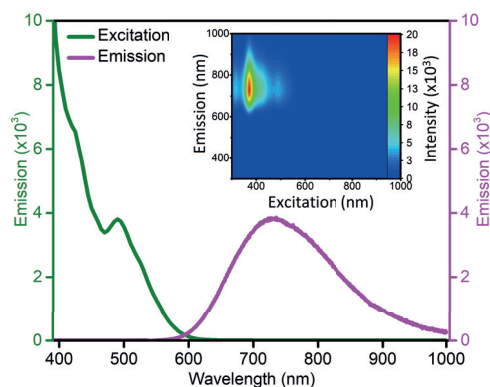
Figure 6. Fluorescence characterization of compound **3e**, Emission spectrum (with 420 nm excitation) and excitation spectrum (monitoring 730 nm emission) for **3e**. Inset: 3D EEM spectra of **3e**. illustrating the colour and the high quantum yield of emission under visible and UVA light.

AUTHOR INFORMATION

Corresponding Authors

*cruddenc@chem.queensu.ca
*hannu.j.hakkinen@jyu.fi
*tsukuda@chem.s.u-tokyo.ac.jp
*kevin.stamplecoskie@queensu.ca

ORCID

Hannu Häkkinen: 0000-0002-8558-5436
Tatsuya Tsukuda 0000-0002-0190-6379
Cathleen Crudden 0000-0003-2154-8107
Paul Lummis: 0000-0002-9212-3678

REFERENCES

1. (a) Häkkinen, H., *Nature Chem.* **2012,** *4*, 443; (b) Tsukuda, T.; Häkkinen, H., *Protected Metal Clusters: From Fundamentals to Applications* Elsevier: Amsterdam, 2015; (c) Yamazoe, S.; Koyasu, K.; Tsukuda, T., *Acc. Chem. Res.* **2014,** *47*, 816–824; (d) Li, G.; Jin, R., *Acc. Chem. Res.* **2013,** *46*, 1749–1758; (e) Bürgi, T., *Nanoscale* **2015,** *7*, 15553-15567.
2. Jadzinsky, P. D.; Calero, G.; Ackerson, C. J.; Bushnell, D. A.; Kornberg, R. D., *Science* **2007,** *318*, 430-433.

3. Zhou, M.; Zeng, C.; Chen, Y.; Zhao, S.; Sfeir, M. Y.; Zhu, M.; Jin, R., *Nature Commun.* **2016**, *7*, 13240.
4. (a) Häkkinen, H.; Walter, M.; Grönbeck, H., *J. Phys. Chem. B* **2006**, *110*, 9927-9931; (b) Walter, M.; Akola, J.; Lopez-Acevedo, O.; Jadzinsky, P. D.; Calero, G.; Ackerson, C. J.; Whetten, R. L.; Grönbeck, H.; Häkkinen, H., *Proc. Natl. Acad. Sci.* **2008**, *105*, 9157.
5. (a) Polgar, A. M.; Weigend, F.; Zhang, A.; Stillman, M. J.; Corrigan, J. F., *J. Am. Chem. Soc.* **2017**, *139*, 14045-14048; (b) Azizpoor Fard, M.; Levchenko, T. I.; Cadogan, C.; Humenny, W. J.; Corrigan, J. F., *Chem. Eur. J.* **2016**, *22*, 4543-4550; (c) Khalili Najafabadi, B.; Corrigan, J. F., *Dalton Trans.* **2014**, *43*, 2104-2111.
6. (a) Chakraborty, I.; Pradeep, T., *Chem. Rev.* **2017**, *117*, 8208-8271; (b) Jin, R.; Zeng, C.; Zhou, M.; Chen, Y., *Chem. Rev.* **2016**, *116*, 10346-10413.
7. (a) McKenzie, L. C.; Zaikova, T. O.; Hutchison, J. E., *J. Am. Chem. Soc.* **2014**, *136*, 13426-13435; (b) Konishi, K., *Struct. Bond.* **2014**, *161*, 49-86.
8. Robilotto, T. J.; Bacsa, J.; Gray, T. G.; Sadighi, J. P., *Angew. Chem., Int. Ed.* **2012**, *51*, 12077 –12080.
9. Jin, L.; Weinberger, D. S.; Melaimi, M.; Moore, C. E.; Rheingold, A. L.; Bertrand, G., *Angew. Chem., Int. Ed.* **2014**, *53*, 9059-9063.
10. Ube, H.; Zhang, Q.; Shionoya, M., *Organometallics* **2018**, *37*, 2007-2009.
11. (a) Crudden, C. M.; Horton, J. H.; Ebralidze, I. I.; Zenkina, O. V.; McLean, A. B.; Drevniok, B.; She, Z.; Kraatz, H. B.; Mosey, N. J.; Seki, T.; Keske, E. C.; Leake, J. D.; Rousina-Webb, A.; Wu, G., *Nature Chem.* **2014**, *6*, 409-414; (b) Crudden, C. M.; Horton, J. H.; Narouz, M. R.; Li, Z. J.; Smith, C. A.; Munro, K.; Baddeley, C. J.; Larrea, C. R.; Drevniok, B.; Thanabalasingam, B.; McLean, A. B.; Zenkina, O. V.; Ebralidze, I. I.; She, Z.; Kraatz, H. B.; Mosey, N. J.; Saunders, L. N.; Yagi, A., *Nature Commun.* **2016**, *7*, 1-7; (c) Zhukhovitskiy, A. V.; Mavros, M. G.; Van Voorhis, T.; Johnson, J. A., *J. Am. Chem. Soc.* **2013**, *135*, 7418-7421; (d) Zhukhovitskiy, A. V.; MacLeod, M. J.; Johnson, J. A., *Chem. Rev.* **2015**, *115*, 11503-11532; (e) Weidner, T.; Baio, J. E.; Mundstock, A.; Grosse, C.; Karthauser, S.; Bruhn, C.; Siemeling, U., *Aust. J. Chem.* **2011**, *64*, 1177-1179; (f) Engel, S.; Fritz, E.-C.; Ravoo, B. J., *Chem. Soc. Rev.* **2017**, *46*, 2057-2075; (g) Wang, G.; Rühling, A.; Amirjalayer, S.; Knor, M.; Ernst, J. B.; Richter, C.; Gao, H.-J.; Timmer, A.; Gao, H.-Y.; Doltsinis, N. L.; Glorius, F.; Fuchs, H., *Nat Chem* **2017**, *9*, 152-156; (h) Man, R. W. Y.; Li, C.-H.; MacLean, M. W. A.; Zenkina, O. V.; Zamora, M. T.; Saunders, L. N.; Rousina-Webb, A.; Nambo, M.; Crudden, C. M., *J. Am. Chem. Soc.* **2018**, *140*, 1576–1579; (i) Rühling, A.; Schaepe, K.; Rakers, L.; Vonhören, B.; Tegeder, P.; Ravoo, B. J.; Glorius, F., *Angew. Chem., Int. Ed.* **2016**, *55*, 5856-5860; (j) Salorinne, K.; Man, R. W. Y.; Li, C.-H.; Taki, M.; Nambo, M.; Crudden, C. M., *Angew. Chem., Int. Ed.* **2017**, *56*, 6198-6202; (k) Larrea, C. R.; Baddeley, C. J.; Narouz, M. R.; Mosey, N. J.; Horton, J. H.; Crudden, C. M., *ChemPhysChem* **2017**, *18*, 3536-3539.
12. Narouz, M. R. O., K. M.; Unsworth, P. J.; Man, R. W. Y.; Salorinne, K.; Takano, S.; Tomihara, R.; Kaappa, S.; Malola, S.; Dinh, C. T.; Padmos, J. D.; Ayoo, K.; Patrick, G. J.; Nambo, M.; Horton, J. H.; Sargent, E. H.; Häkkinen, H.; Tsukuda, T.; Crudden, C.M. *ChemRxiv Preprint* **2018**
13. (a) Zheng, J.; Petty, J. T.; Dickson, R. M., *J. Am. Chem. Soc.* **2003**, *125*, 7780-7781; (b) Zheng, J.; Nicovich, P. R.; Dickson, R. M., *Annu. Rev. Phys. Chem.* **2007**, *58*, 409-431.
14. (a) Jiang, L.; Zhang, B.; Medard, G.; Seitsonen, A. P.; Haag, F.; Allegretti, F.; Reichert, J.; Kuster, B.; Barth, J. V.; Papageorgiou, A. C., *Chem. Sci.* **2017**, *8*, 8301-8308; (b) Kim, H. K.; Hyla, A. S.; Winget, P.; Li, H.; Wyss, C. M.; Jordan, A. J.; Larrain, F. A.; Sadighi, J. P.; Fuentes-Hernandez, C.; Kippelen, B.; Brédas, J.-L.; Barlow, S.; Marder, S. R., *Chem. Mater.* **2017**, *29*, 3403-3411; (c) Bakker, A.; Timmer, A.; Kolodzeiski, E.; Freitag, M.; Gao, H. Y.; Mönig, H.; Amirjalayer, S.; Glorius, F.; Fuchs, H., *J. Am. Chem. Soc.* **2018**, *140*, 11889-11892.
15. Tang, Q.; Jiang, D.-E., *Chem. Mater.* **2017**, *29*, 6908-6915.
16. Collado, A.; Gómez-Suárez, A.; Martin, A. R.; Slawin, A. M. Z.; Nolan, S. P., *Chem Commun* **2013**, *49*, 5541-5543.
17. Shichibu, Y.; Konishi, K., *Small* **2010**, *6*, 1216-1220.
18. Note we cannot rule out the influence of smaller or less stable clusters that do not survive ESI-MS analysis.
19. McKenzie, L. C.; Zaikova, T. O.; Hutchison, J. E., *J. Am. Chem. Soc.* **2014**, *136*, 13426-13435.
20. Tauc, J.; Grigorovici, R.; Vancu, A., *Phys. Status Solidi B* **1966**, *15*, 627-637.
21. Ramsay, H.; Simon, D.; Steele, E.; Hebert, A.; Oleschuk, R. D.; Stamplecoskie, K. G., *RSC Adv.* **2018**, *8*, 42080-42086.

PV

**REAL-SPACE IMAGING WITH PATTERN RECOGNITION OF
A LIGAND-PROTECTED AG$_{374}$ NANOCLUSTER AT
SUB-MOLECULAR RESOLUTION**

by

Qin Zhou, Sami Kaappa, Sami Malola, Hui Lu, Dawei Guan, Yajuan Li,
Haochen Wang, Zhaoxiong Xie, Zhibo Ma, Hannu Häkkinen,
Nanfeng Zheng, Xueming Yang & Lansun Zheng (2018)

Nature Communications, 9(1), 2948

ARTICLE

Real-space imaging with pattern recognition of a ligand-protected Ag$_{374}$ nanocluster at sub-molecular resolution

Qin Zhou[1,2], Sami Kaappa [3], Sami Malola[3], Hui Lu[2], Dawei Guan[2], Yajuan Li[2], Haochen Wang[2], Zhaoxiong Xie[1], Zhibo Ma[2], Hannu Häkkinen [3], Nanfeng Zheng [1], Xueming Yang[2,4] & Lansun Zheng[1]

High-resolution real-space imaging of nanoparticle surfaces is desirable for better understanding of surface composition and morphology, molecular interactions at the surface, and nanoparticle chemical functionality in its environment. However, achieving molecular or sub-molecular resolution has proven to be very challenging, due to highly curved nanoparticle surfaces and often insufficient knowledge of the monolayer composition. Here, we demonstrate sub-molecular resolution in scanning tunneling microscopy imaging of thiol monolayer of a 5 nm nanoparticle Ag$_{374}$ protected by *tert*-butyl benzene thiol. The experimental data is confirmed by comparisons through a pattern recognition algorithm to simulated topography images from density functional theory using the known total structure of the Ag$_{374}$ nanocluster. Our work demonstrates a working methodology for investigations of structure and composition of organic monolayers on curved nanoparticle surfaces, which helps designing functionalities for nanoparticle-based applications.

[1] State Key Laboratory of Physical Chemistry of Solid Surfaces, Collaborative Innovation Center of Chemistry for Energy Materials,and National & Local Joint Engineering Research Center for Preparation Technology of Nanomaterials, College of Chemistry and Chemical Engineering, Xiamen University, Xiamen 361005, China. [2] State Key Laboratory of Molecular Reaction Dynamics, Dalian Institute of Chemical Physics, Chinese Academy of Science, Dalian 116023, China. [3] Departments of Physics and Chemistry, Nanoscience Center (NSC), University of Jyväskylä, FI-40014 Jyväskylä, Finland. [4] Department of Chemistry, Southern University of Science and Technology, 1088 Xueyuan Road, Guangdong, Shenzhen 518055, China. Correspondence and requests for materials should be addressed to Z.M. (email: zhbma@dicp.ac.cn) or to H.Häk. (email: hannu.j.hakkinen@jyu.fi) or to N.Z. (email: nfzheng@xmu.edu.cn)

Real-space imaging of nanoparticles is instrumental for understanding the correlations between size, shape, composition, structure, and stability. These fundamental properties define functionalities for applications in areas, such as catalysis, drug delivery, bio-sensing, and theranostics[1,2]. Most metal and semiconductor nanoparticles are made by wet chemistry using surface-stabilizing molecules that build an organic overlayer on the nanoparticle surface; consequently, knowing the detailed properties of this overlayer is crucial for understanding how nanoparticles interact with their environment[3]. While great progress has been made in imaging organic molecules on flat surfaces via atomic force (AFM) and scanning tunneling (STM) microscopies, with resolution extending down to a single intramolecular covalent bond[4–9], achieving even a molecular resolution at nanoparticle organic surface has proven to be extremely challenging[10–17]. These challenges arise from the highly curved nanoparticle surface leading to spatially dependent tip-convolution, inhomogeneity of nanoparticle size and shape, insufficient knowledge of the composition of the nanoparticle organic surface, and from the difficulty to produce accurate theoretical modeling for AFM or STM imaging due to lack of reliable atomic-scale nanoparticle models.

Atomically precise metal nanoclusters, composed of 1–3 nm noble metal cores and an organic monolayer of thiols, phosphines, or alkynyls, have emerged in recent years as an interesting sub-class of extremely well-defined nanoparticles with total structures available from single crystal X-ray crystallography[18–20]. Recently, synthesis and the total structure of a large silver nanocluster of composition $Ag_{374}(SR)_{113}Br_2Cl_2$ ($SR = SPhC(CH_3)_3$ = tert-butyl benzenethiol, TBBT) was reported[21]. The Ag_{374} nanocluster has a decahedral silver core of about 3 nm in diameter, and the total diameter of the particle is about 5 nm (Fig. 1a, b). Density functional theory (DFT) calculations on this cluster indicated a metallic behavior with a continuous density of electron states at the Fermi level, and experimental UV–Vis spectroscopy revealed a strong plasmonic absorption at 465 nm (2.67 eV)[21]. The Ag_{374} nanocluster serves thus as a model of a large metallic nanoparticle, yet structurally known to atomic precision.

Here, we show that it is possible to achieve a sub-molecular spatial resolution in STM imaging of topography of the TBBT surface of Ag_{374} nanoclusters in ultra-high vacuum (UHV) conditions at both liquid Helium (LHe) and liquid Nitrogen (LN$_2$) temperatures. Spatial recognition of single CH_3 units of $SPhC(CH_3)_3$ at the nanocluster surface is corroborated by comparisons to a set of STM images of individual TBBT molecules at various orientations on Au(111) surface, as well as to DFT simulations of topography images based on the known atomic structure of $Ag_{374}(SPhC(CH_3)_3)_{113}Br_2Cl_2$. We demonstrate, provide, and discuss an algorithm to automatically suggest the closest matches between simulated STM images and the experimental data, based on principles in "facial recognition".

Results

Nanocluster synthesis and characterization. The Ag_{374} nanoclusters were synthesized and characterized (Supplementary Fig. 1) as described previously[21], deposited on dithiol-modified Au(111) surface at ambient conditions and quickly transformed to a UHV-STM chamber (see Methods for details). The clusters formed a disordered monolayer as shown in Fig. 1c. The particles show almost the same apparent height (about 3 nm) but present rather different widths and shapes induced by tip convolution effect depending on the surrounding as well as their orientations. We applied a simple method to extract the real nanocluster diameter from STM images. First, we located an area containing

an ordered compact nanocluster array with at least three particles at the same altitude, as shown in Fig. 1c. Second, each Ag_{374} was identified (indicated by blue dashed circles in Fig. 1c). Excluding the last particle of the array, the height profile along the row of clusters exhibits regular oscillations at about 5 nm intervals which is taken as the true size, free from convolution effects (red line, profile (1), in Fig. 1d). This size corresponds well to the cluster diameter determined from the crystal structure. On the other hand, height profile taken across the cluster line indicates cluster diameter of about 10 nm; this value includes the tip convolution effect (black line, profile (2), in Fig. 1d).

We found that continuous scanning of the same sample area improved both the sample stability and the spatial resolution (Fig. 2). We started with higher setpoint currents of 40–30 pA for a typical bias voltage of −1.2 V (meaning that the STM tip scans closer to clusters) and eventually reduced the setpoint current to 10 pA. During the scans at higher currents, we noticed movement of less stable clusters away from the sample area (removed by the tip), as well as gradual increase of the spatial resolution of topography features at the cluster surfaces. With the final setpoint values of −1.2 V and 10 pA, the images were stable at 20 min time scale over a few scans. This pertained to the individual topography features at the same cluster surface to a very high degree independent of the scanning directions (Supplementary Fig. 2).

DFT calculations and STM topography simulations. Large-scale DFT calculations by using the GPAW software[22] were made to solve the ground-state electron density of $Ag_{374}(SPhC(CH_3)_3)_{113}Br_2Cl_2$ in its determined X-ray structure[21], and the Tersoff–Haman method[23] was used to simulate STM topography of Ag_{374}'s organic surface (see Methods for details). Representative DFT-topography image and height profile across the cluster surface, calculated using typical bias voltage and current values of the experiment, are shown in Fig. 3a, b, respectively. DFT gave an apparent size of one TBBT ligand as 0.6 nm and indicated that each methyl group in the ligand is visible, with peak-to-peak distance of about 0.3 nm. Imaging of single TBBT molecules adsorbed on Au(111) surface provided valuable additional information of various modes of appearance (Supplementary Fig. 3). As shown in Fig. 3c, in most cases only one or two of the methyl groups were seen due to the tilt angle between TBBT and the surface, but the peak-to-peak distance was in the range of 0.3–0.4 nm (Fig. 3d), consistent with the DFT results in Fig. 3a, b.

Confirmation of sub-molecular resolution. Encouraged by these observations, we turned to systematic analysis of several high-resolution STM images of Ag_{374} taken at LHe temperature; a typical example is shown in Fig. 3e–h. As shown in Fig. 3e, the topography at the center area of the cluster, where tip convolution effects are minimal, featured rather regular maxima and minima, with peak-to-peak distances ranging from 0.3 to 0.6 nm (Fig. 3f). Concentrating on 11 locations at the cluster surface, we were additionally able to identify local configurations of maxima/minima that closely resemble individual TBBT molecules on the Au(111) surface (Fig. 3g, h). All this evidence points unambiguously that single methyl groups produced the topography variations in our image data, i.e., we achieved the sub-molecular resolution.

We did a similar analysis of Ag_{374} topography data taken at LN$_2$ temperature (Supplementary Figs. 4–6). Comparison of images taken from the same sample area during continuous scanning showed fewer sharply identifiable ligands and somewhat less sharp peaks in the height profile compared to data measured at LHe temperature, as expected. However, the main features of
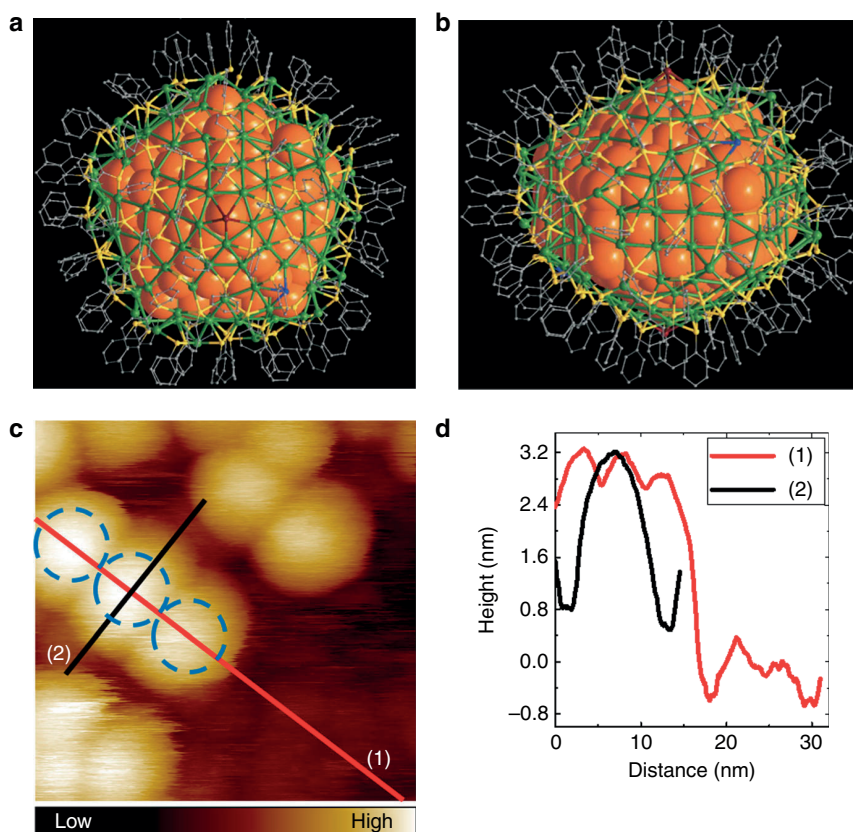
Fig. 1 Total structure of Ag_{374} nanoparticle and its appearance in STM imaging. **a**, **b** Complete cluster structure shown in a plane perpendicular to a five-fold rotation axis and a plane parallel to the five-fold axis, respectively (from ref.[21], copyright 2016 SpringerNature). **c** STM topography image of Ag_{374} at LHe temperature. Scan size: 25.1×25.1 nm^2, bias and setpoint current: 1.2 V and 30 pA. Blue dashed circles indicate nanoclusters with a defined size (diameter 5 nm) and their locations. **d** Height profiles taken along the red and black lines in **c**
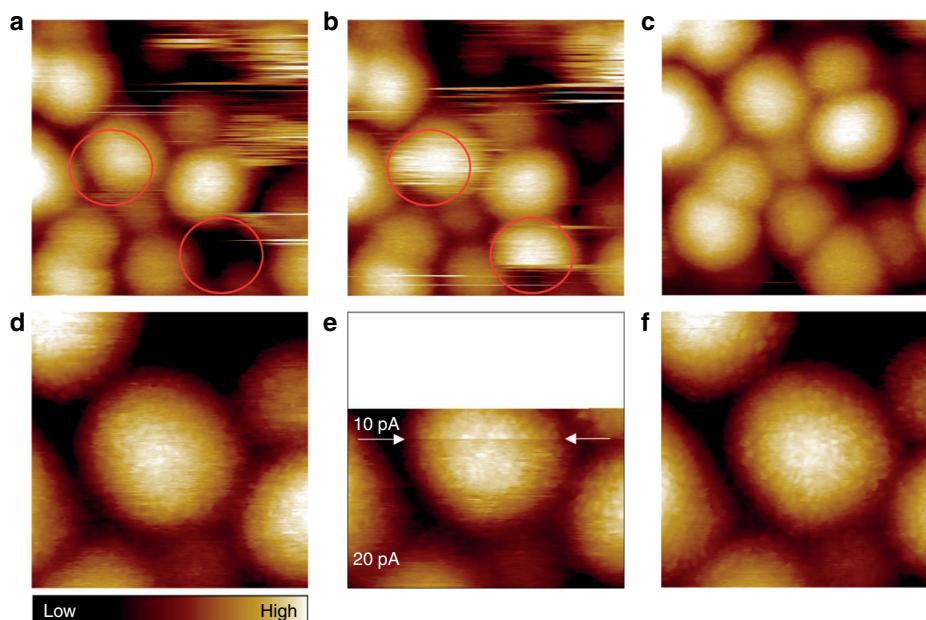
Fig. 2 Repeated imaging of the same sample area increases the resolution. Bias, setpoint current, scan size: **a**, **b** −1.2 V, 30 pA, 23.7×23.7 nm^2 **c** −1.2 V, 20 pA, 23.7×23.7 nm^2 **d** −1.2 V, 20 pA, 12.0×12.0 nm^2 **e** −1.2 V, setpoint current change from 20 to 10 pA at the marked scan line, 12.0×7.8 nm^2; and **f** −1.2 V, 10 pA, 12.0×12.0 nm^2. Red circles indicate unstable clusters and some were removed by tip in in **a**, **b**. Repeated imaging of the same area with decreasing setpoint current improved the spatial resolution markedly. Images taken at the LHe temperature over the course of 7 min/image
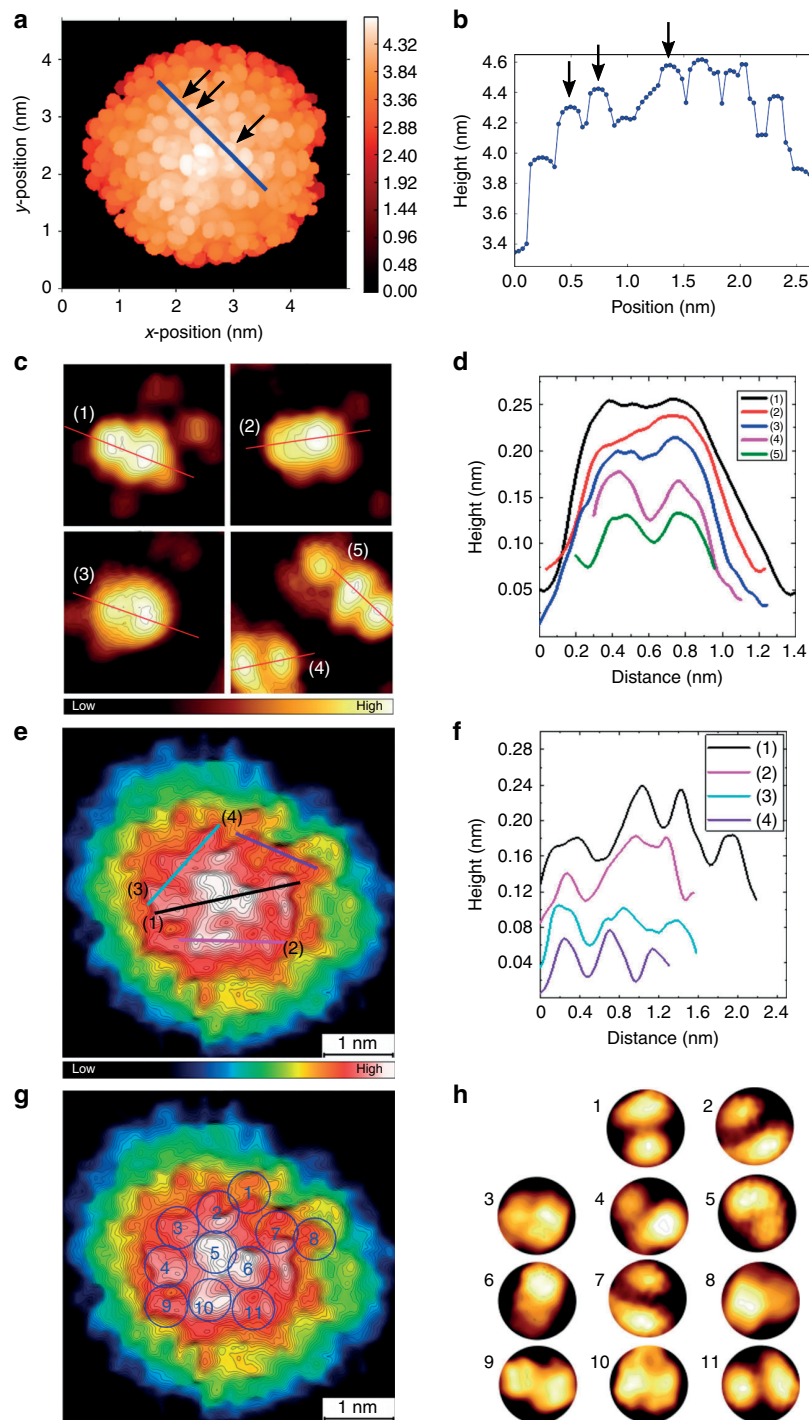
Fig. 3 DFT simulations and high-resolution imaging. **a** DFT calculated STM image for Ag_{374} by using the known atomistic structure of the nanocluster[17]. Image area: 5×5 nm^2. The image has been simulated by using voltage and current settings of -1.4 V and 20 pA, respectively. Black arrows indicate individual methyl groups. **b** Height profile taken along the blue line in **a**. The three arrows show positions of the same methyl groups as shown in **a**. **c** STM topography images of single TBBT molecules in various orientations bound to an Au(111) surface. Image settings: (**1,2**) 1.0 V, 30 pA, 1.51×1.51 nm^2; (**3–5**) 1.2 V, 60 pA, 1.50×1.50 nm^2, all at LN$_2$ temperature. (Zoomed in from different large images, the resolution had small deviation.) **d** shows height scans of the molecules as marked in **c** by numbers 1–5. **e** A topography image of Ag_{374} at submolecular resolution (bias: -1.2 V, current: 10 pA, scan size: 4.81×4.81 nm^2). **f** Height profiles of the cluster along the lines marked in **e**. **g** The same cluster as in **e**, with 11 detailed features showing similarity to the ligand configurations at Au(111) shown in **h**. STM imaging at LHe temperature
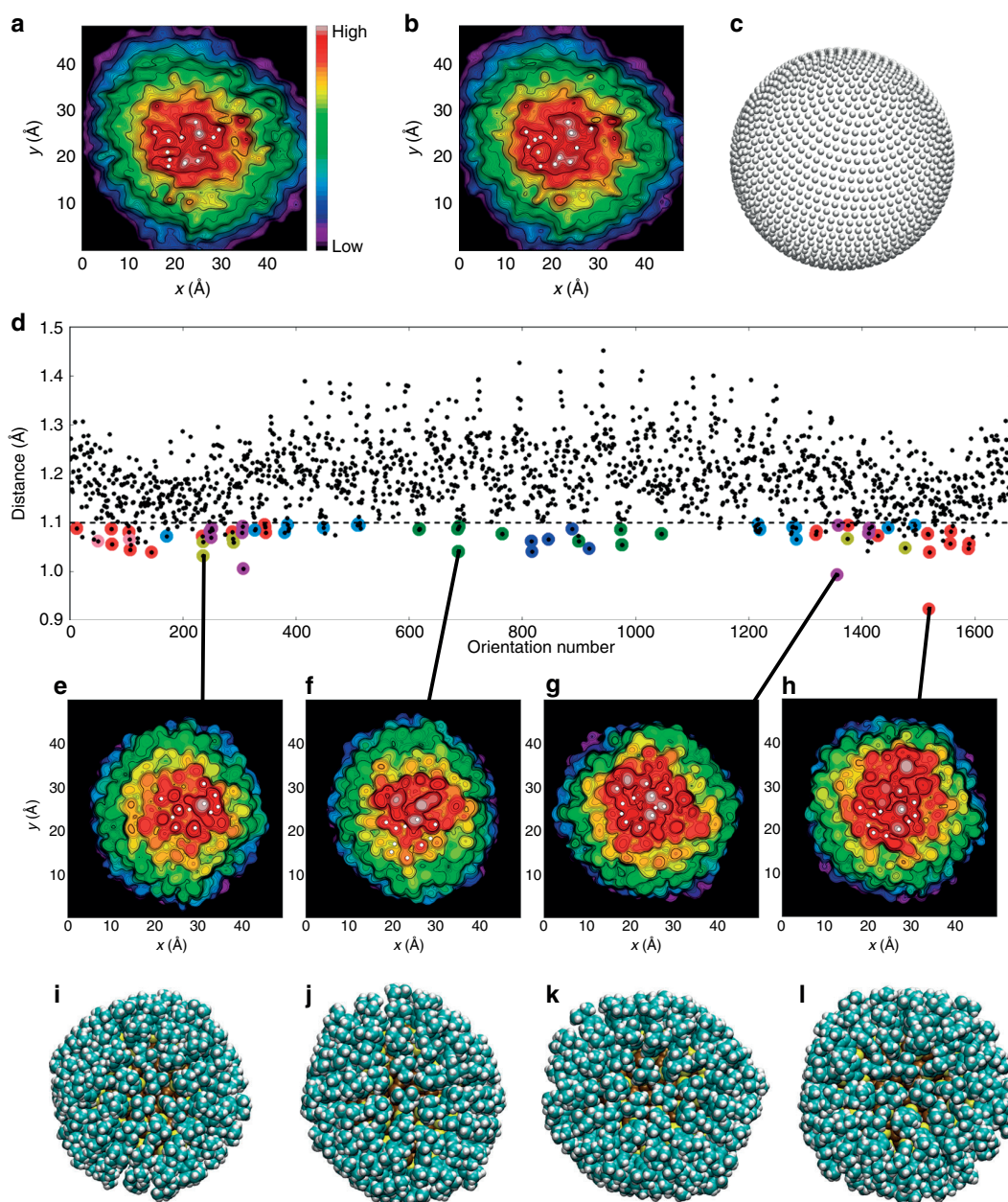
Fig. 4 "Facial recognition" of experimental STM topography by an automated matching of simulated images. **a**, **b** Two consecutive scans (trace and retrace) of the same Ag_{374} cluster at LHe temperature (bias voltage: −1.2 V, current: 10 pA). The white dots represent the extrema of the data. **c** Visualization of the set of perspectives used to prepare the simulated STM image from the computational data. Each dot corresponds to a perspective when the cluster lies at the center of the sphere. **d** Minimum correlation distances for each perspective, resulting from comparison to the extremum points of **a**. The dashed line is drawn below the major feature formed by the data points. Below this threshold, the data points with the same color correspond to a perspective very close to each other that consequently give relatively small correlation distances. Selected small-distance perspectives are connected with lines to the respective calculated STM images (**e**–**h**) with white dots showing the extrema. **i**–**l** The atomistic models of the cluster in similar orientations to **e**–**h**, respectively. X–Y scales are the same in experimental and simulated images, and are shown in Å. The STM simulations were done for the voltage and current values used in the experiment

the topography remained stable showing that sub-molecular resolution could be achieved.

Pattern recognition between experimental and simulated topographies. The sub-molecular resolution in the experimental topography data encouraged us to go one step further in comparison between experiment and theory, by applying an idea of

"facial recognition". By projecting the DFT-calculated local density of electronic states of Ag_{374} to 1665 different space orientations (Fig. 4c), we calculated 1665 simulated topography images and compared them to experimental data (Fig. 4a), looking for the best match with help of an automated algorithm that used ideas for pattern recognition in machine learning. We determined a generalized rms-distance between each simulated topography image and experimental data based on locations of extrema
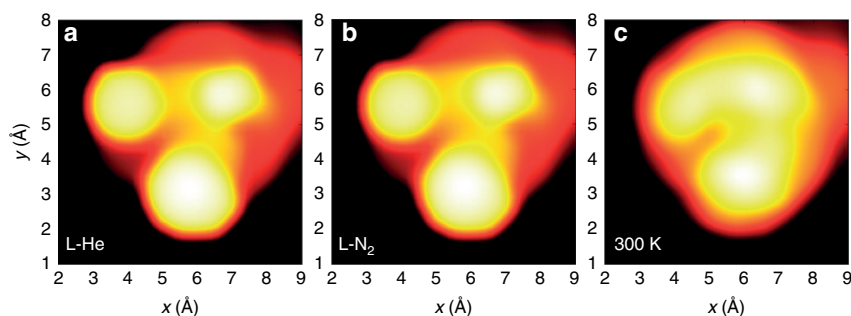
Fig. 5 Temperature effect on simulated STM topography images of a single TBBT molecule on Au(111) surface. The images show the simulated STM topography images by taking into account the ensemble effect of various positions of the t-butyl group at LHe (**a**) and LN$_2$ temperatures (**b**), and at 300 K (**c**). The ensemble averages are calculated in each case as a weight-averaged of 20 images corresponding one 120° rotation from one potential minimum to the next one, separated by the energy barrier of 80 meV, the weight factors coming from Boltzmann term exp($-E/kT$). The averaged positions of single methyl groups are clearly resolved at LHe and LN$_2$ temperatures but are blurred at 300 K

points in the central region of the image (where the experimental tip convolution effects are minimal). Minimal values of the generalized distance were used as a criterion to find the best candidates in the simulated images. As Fig. 4d shows, only a handful of good matches out of 1665 candidates were identified by this algorithm, shown in Fig. 4e–h with the corresponding atomic visualizations in Fig. 4i–l. A similar result was achieved when we analyzed the STM topography data achieved by re-tracing (Fig. 4b) the same Ag$_{374}$ cluster as shown in Fig. 4a: a small sub-set from the possible 1665 orientations stands out as giving a close correlation to the experimental data (Supplementary Fig. 7). Self-consistent tests of the reliability of the matching algorithm, performed by taking one simulated image (out of 1665) as a reference ("experimental") data, adding random noise to the data and comparing that data to all other 1664 possible simulated images, showed that the true image is found while the random noise is kept within reasonable bounds (Supplementary Fig. 8).

As Fig. 4 shows, the closest matches between the "best" simulated and experimental topography images yield a typical rms-value of 1 Å for the distance (that is, an extremal point in the best simulated image is on average within 1 Å from a corresponding point in the experimental data). As the simulations pertain to strictly one ($T = 0$) configuration of the Ag$_{374}$ cluster, it is natural to question the role of thermal dynamics of the ligand layer in producing noise to the experimental data in the time scale of imaging. To address this question, we calculated by DFT energy barriers for three different modes of motion of a single TBBT ligand on a flat Au(111) surface: (i) rotation of the tert-butyl group around the C–C bond, (ii) rotation of the phenyl ring around the S–C bond, and (iii) flipping motion of TBBT with respect to an underlying Au–Au bridge of the surface. The results are summarized in Supplementary Fig. 9. We found that the rotational barriers are very low for mechnisms (i), (ii) described above (80 and 40 meV, respectively), while the barrier for the flipping motion is large, 0.27 eV. In order to apply an Arrhenius-type estimate for the rate of rotational motion at various temperatures, we took a typical rotational frequency of 10^9 1/s considering the tert-butyl group/phenyl group as a rigid rotor. This implies that at the LHe temperature, even the rotational motion with the lowest barrier (rotation (ii), 40 meV) is effectively hindered (rate of the order of 10^{-42} 1/s). Rotations can easily take place at the LN2 temperature during the imaging timescale (rates of 10^3–10^6 1/s) and certainly at the room temperature, where the initial handling of the nanoparticle sample takes place. At room temperature, a flipping motion can in principle contribute as well, although in the tightly packed

TBBT monolayer of Ag$_{374}$ its energy barrier is probably significantly larger than shown here for an isolated TBBT/Au (111). Rotations give an average uncertainty of 0.8 Å in the rms-distance over one 120° rotation from one potential energy minimum to the next one (Supplementary Fig. 9e, f). We also studied the ensemble effect of rotations on the simulated STM images by weight-averaging 20 STM images of evenly spaced rotational configurations around the 120° rotation, by using the Boltzmann weight factors exp($-E/kT$). The results in Fig. 5 show interestingly, that single CH$_3$ groups still produce distinct intensity maxima also at LN$_2$ temperature, but at 300 K the sub-molecular resolution is blurred since the high-energy configurations are thermally populated by significant weights.

Discussion

Previously, successful STM imaging of individual metal atoms[24–26], small metal and metal-oxide clusters[27,28], and metal nanoparticles at near-atomic resolution[29] on well-prepared flat supports have been reported. Hybrid nanoparticles, consisting of metal core and organic ligand layer, have been notoriously challenging to image to high spatial resolution due to the highly curved surface and uncertainties in the ligand monolayer composition. Our work demonstrates a successful approach for investigations of the structure of organic monolayers on curved nanoparticle surfaces at sub-molecular spatial resolution, by combining low-temperature STM imaging with high-level DFT simulations of STM topography data and automated comparison of large simulated data sets to experimental data via an algorithm based on pattern recognition. We believe that this approach will facilitate various studies of physical and chemical properties of ligand monolayers, such as conductance, ligand–ligand interactions, and chemical reactivity with the environment, at an unprecedented level of spatial resolution. The improved understanding of composition, morphology, and functionalities of ligand layers of hybrid nanoparticles will help designing nanoparticles for applications.

Methods

Nanocluster synthesis. Ag$_{374}$ nanoclusters were prepared and crystallized as reported in ref.[17]. The crystals were stored at 4 °C in fridge to keep stable. 4,4′-Biphenyldithiol (Alfa, 97%) and 4-(t-butyl)phenylthiol (Alfa, 97%) were used without further purification. Ethanol (HPLC) and dichloromethane (HPLC) were used as solvent. 1 M HCl and 0.5 M H$_2$SO$_4$ were prepared by directly diluting concentrated HCl (37%) and H$_2$SO$_4$ (98%), respectively, to electrochemically polish Au(111).

Au(111)/dithiol/Ag$_{374}$ sample preparation. Au(111) substrate (MaTeck, 5 × 5 cm^2) was cleaned by Ar$^+$ sputtering (at 1.5 keV and 10^{-6} mbar) and

annealing (at about 700 K) in UHV chamber after electrochemical polish in the air. Dithiol modified Au(111) was achieved by immersing the substrate to 1 mM 4,4′-Biphenyldithiol/CH₃CH₂OH solution at 60 °C for 4 h in a sealed vessel isolated from light and cleaned with pure ethanol for several times. Then 5 μL 10^{-7} M Ag₃₇₄/CH₂Cl₂ solution was dropped to the dithiol-modified Au(111) substrate. After the solvent automatically and slowly evaporated from the surface, the sample was transferred to UHV-STM chamber.

Au(111)/4-(t-butyl)phenylthiol sample preparation. Clean Au(111) substrate was immersed in the atmosphere of 4-(t-butyl)phenylthiol in a sealed vessel at 60 °C for 1 h. Then it was transferred to UHV-STM chamber.

STM measurements. STM measurements were performed with a low-temperature STM system (Scientaomicron), operating at a base pressure of 10^{-11} mbar. The sample temperatures were either 7 K (LHe) or 79 K (LN₂). Tungsten tip was electrochemically etched in 5 M NaOH solution. Image processing was performed by SPIP 6.6.0 software.

DFT calculations and STM topography simulations. The electronic structure and STM topography images were calculated using the DFT as implemented in the real-space code-package grid-based projector augmented-wave method (GPAW)[22]. The experimentally determined[21] crystal structure of Ag₃₇₄[SPhC(CH₃)₃]₁₁₃Br₂Cl₂ was used directly without atomic relaxation. The ground state electron density was solved by using 0.25 Å grid spacing and the Perdew–Burke–Ernzerhof (PBE) xc-functional[30]. STM topographs were calculated from the partial local density of states by using the Tersoff–Hamann method[23]. 1665 orientations were used, distributed evenly with 5° separation either in azimuthal or polar direction. Bias voltage and tunneling current were selected according to the experimental setups.

DFT calculations on TBBT molecules on Au(111) surface were done in a *x*–*y* periodic supercell of four Au layers in the *z*-direction and 64 atoms in the cell, with one TBBT molecule relaxed at an initial Au–Au bridge position when the bottom Au(111) was fixed. The energy calculations were done with the gamma-point approximation. PBE functional and 0.20 Å grid spacing were used. Rotations of either the tert-butyl headgroup around the C–C bond or the phenyl group around the S–C bond were considered (Supplementary Fig. 9a, b). In addition, an energy barrier for a motion that flips the molecular axis to a symmetrically identical position around the surface Au–Au bridge (Supplementary Fig. 9c) was studied using the nudged elastic band method[31] with nine intermediate images and the spring constant of 0.1 eV/Å, and four closest Au atoms to S being dynamic.

Numerical comparison of STM images for pattern recognition. For each calculated STM image, we determined the coordinates of the 20 largest local maxima and 20 largest local minima after Gaussian smoothing of the data with standard deviation of 0.23 Å. The smoothing was performed in order to obtain more well-defined gradients of the numerical data and thus to model the experimental data in a more sophisticated way considering the local extremum points. A point was accepted as a local maximum (minimum) if it had the maximum (minimum) value of the data within a radius of 0.7 Å. Similarly, we determined a few well-defined extrema from the experimental data (all of the extrema are shown in Fig. 4a, b in the main text). We concentrated the analysis to the central part of the cluster due to aberrations near the cluster edges caused by the tip-convolution effect.

We compared an experimental set of extremum coordinates to each computational set as follows. The extremum coordinates were first placed into the same coordinate system by setting the maximum height coordinates to origin. The nearest neighbor for each experimental coordinate was sought from the computational set, separately for local maxima and minima. Denoting the set of extremum coordinates from the experimental data as Q and the nearest neighbors from the calculated data as P (correspondingly ordered), the rotation and translation matrices R and T, respectively, were sought that minimize the root-mean-square distance between the sets Q and $P' = RP + T$, using the algorithm introduced in ref.[32]. The fitted distance between the coordinate sets Q and P is thus read as

$$D = \left(\Sigma_i |P'_i - Q_i|^2 / N \right)^{1/2} \tag{1}$$

where the summation index i runs from 1 to N that is the number of coordinates in Q. The distance D was minimized with respect to rotations of the experimental set of points around full circle to consider all the reasonable nearest-neighbors between the sets of coordinates. These minima are documented in Fig. 4d for each calculated image, compared to one of the experimental images.

Code availability. For DFT calculations and system preparation we used open-source software available at https://wiki.fysik.dtu.dk/gpaw/. The custom-made computer code used in comparison of simulated and experimental STM images can be downloaded from the web link http://r.jyu.fi/uNF.

Data availability

References

1. Daniel, M.-C. & Astruc, D. Gold nanoparticles: assembly, supramolecular chemistry, quantum-size-related properties, and applications toward biology, catalysis, and nanotechnology. *Chem. Rev.* **104**, 293–346 (2004).
2. Giljohann, D. A. et al. Gold Nanoparticles for biology and medicine. *Angew. Chem. Int. Ed.* **49**, 3280–3294 (2010).
3. Colangelo, E. et al. Characterizing self-assembled monolayers on gold nanoparticles. *Bioconj. Chem.* **28**, 11–22 (2016).
4. Hou, J. G. et al. Topology of two-dimensional C60 domains. *Nature* **409**, 304–305 (2001).
5. de Oteyza, D. G. et al. Direct imaging of covalent bond structure in single-molecule chemical reactions. *Science* **340**, 1434–1437 (2013).
6. Zhang, J. et al. Real-space identification of intermolecular bonding with atomic force microscopy. *Science* **342**, 611–614 (2013).
7. He, J. H., Mao, W., Tok, E. S. & Xu, G. Q. Orbital resolution of molecules covalently attached to a clean semiconductor surface. *Nat. Commun.* **5**, 3721 (2014).
8. Gross, L. Recent advances in submolecular resolution with scanning probe microscopy. *Nat. Chem.* **3**, 273–278 (2011).
9. Han, Z. et al. Imaging the halogen bond in self-assembled halogenbenzenes on silver. *Science* **358**, 206–210 (2017).
10. Jackson, A., Myerson, J. & Stellacci, F. Spontaneous assembly of subnanometre-ordered domains in the ligand shell of monolayer-protected nanoparticles. *Nat. Mater.* **3**, 330–336 (2004).
11. Cesbron, Y., Shaw, C. P., Birchall, J. P., Free, P. & Lévy, R. Stripy nanoparticles revisited. *Small* **8**, 3714–3719 (2012).
12. Yu, M. & Stellacci, F. Response to "Stripy Nanoparticles Revisited". *Small* **8**, 3720–3726 (2012).
13. Ong, Q. K. et al. High-resolution scanning tunneling microscopy characterization of mixed monolayer protected gold nanoparticles. *ACS Nano* **7**, 8529–8539 (2013).
14. Biscarini, F. et al. Quantitative analysis of scanning tunneling microscopy images of mixed-ligands-functionalized nanoparticles. *Langmuir* **29**, 13723–13734 (2013).
15. Moglianetti, M. et al. Scanning tunneling microsocpy and small angle neutron scattering study of mixed monolayer protected gold nanoparticles in organic solvents. *Chem. Sci.* **5**, 1232–1240 (2014).
16. Luo, Z. et al. Quantitative 3D determination of self-assembled structures on nanoparticles using small angle neutron scattering. *Nat. Commun.* **9**, 1343 (2018).
17. Kano, S., Tada, T. & Majima, Y. Nanoparticle characterization based on STM and STS. *Chem. Soc. Rev.* **44**, 970–987 (2015).
18. Jadzinsky, P. D., Calero, G., Ackerson, C. J., Bushnell, D. A. & Kornberg, R. D. Structure of a thiol monolayer-protected gold nanoparticle at 1.1 angstrom resolution. *Science* **318**, 430–433 (2007).
19. Tsukuda, T. & Häkkinen, H. *Protected Metal Clusters: From Fundamentals to Applications.* (Elsevier, Amsterdam, 2015).
20. Chakraborty, I. & Pradeep, T. Atomically precise clusters of noble metals: emerging link between atoms and nanoparticles. *Chem. Rev.* **117**, 8208–8271 (2017).
21. Yang, H. et al. Plasmonic twinned silver nanoparticles with molecular precision. *Nat. Commun.* **7**, 12809 (2016).
22. Enkovaara, J. et al. Electronic structure calculations with real-space implementation of the projector augmented-wave method. *J. Phys.-Condens. Matter* **22**, 253202 (2010).
23. Tersoff, J. & Hamann, D. Theory and application for the scanning tunneling microscope. *Phys. Rev. Lett.* **50**, 1998–2001 (1983).
24. Repp, J. et al. Controlling the charge state of individual gold adatoms. *Science* **305**, 493–495 (2004).
25. Yulikov, M. et al. Binding of single gold atoms on thin MgO(001) films. *Phys. Rev. Lett.* **96**, 146804 (2006).
26. Olsson, F. E., Paavilainen, S., Persson, M., Repp, J. & Meyer, G. Multiple charge states of Ag atoms on ultrathin NaCl films. *Phys. Rev. Lett.* **98**, 176803 (2007).
27. Lin, X. et al. Quantum well states in two-dimensional gold clusters on MgO thin films. *Phys. Rev. Lett.* **102**, 206801 (2009).

28. Fu, Q. et al. Interface-confined ferrous centers for catalytic oxidation. *Science* **328**, 1141–1143 (2010).
29. Schouteden, K. et al. Probing the atomic structure of metallic nanoclusters with the tip of a scanning tunneling microscope. *Nanoscale* **6**, 2170–2176 (2014).
30. Perdew, J., Burke, K. & Ernzerhof, M. Generalized gradient approximation made simple. *Phys. Rev. Lett.* **77**, 3865–3868 (1996).
31. Berne, B. J., Cicotti, G. & Coker, D. F. (eds). *Classical and Quantum Dynamics in Condensed Phase Simulations,* 385–404 (World Scientific, Singapore, 1998).
32. Arun, K. S., Huang, T. S. & Blostein, S. Least-squares fitting of two 3-D point sets. *IEEE Trans. Pattern Anal. Mach. Intell.* **PAMI-9**, 698–700 (1987).

Author contributions

N.F.Z. and L.S.Z. designed the study and supervised the project. Q.Z. carried out the STM experiments and analyzed the STM data, assisted by H.L., D.W.G., Y.J.L. and H.C.W. Z.B.M. and X.M.Y. supported the experiment and Z.X.X. supported the STM data analysis. S.M. carried out the DFT calculations of the electronic structure of Ag_{374}. S.K. carried out the STM topography simulations and built the algorithm of pattern recognition for comparison to experimental topography data. H.H. supervised the theoretical and computational work and analyzed the computational results together with S.K. and S.M. The first manuscript draft was compiled by Q.Z., H.H. edited and finalized the manuscript based on comments from co-authors.

Additional information
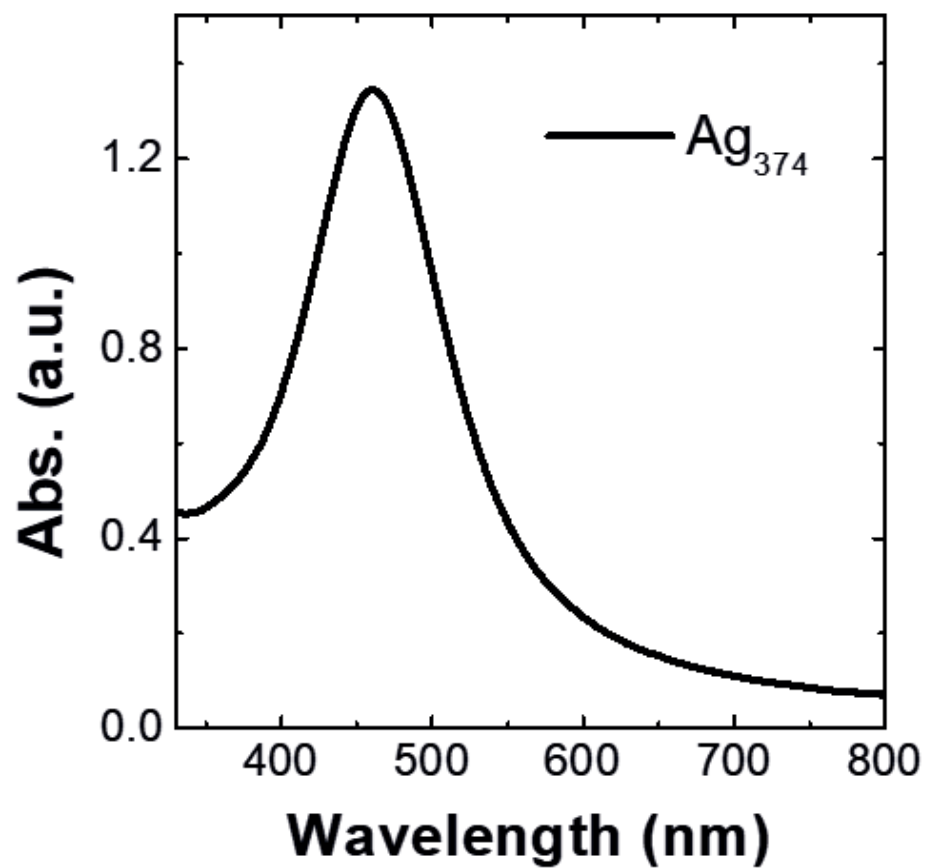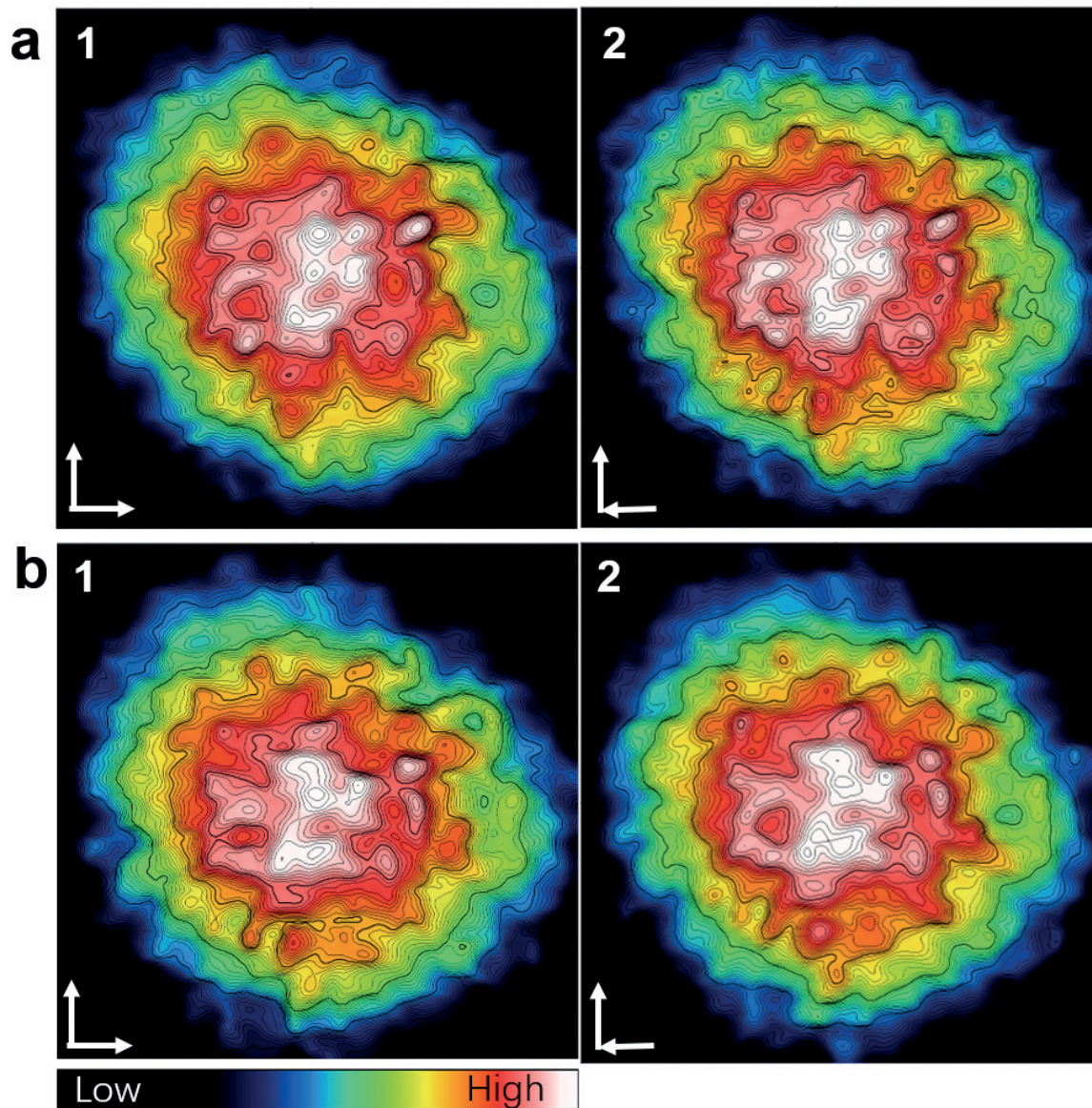
SUPPLEMENTARY INFORMATION FOR

Real-Space Imaging with Pattern Recognition of a Ligand-Protected Ag$_{374}$ Nanocluster at Sub-Molecular Resolution

Zhou et al.

SUPPLEMENTARY FIGURES

Supplementary Figure 1. Optical absorption of Ag$_{374}$ as dissolved from crystalline phase before depositing on the dithiol-modified gold surface.
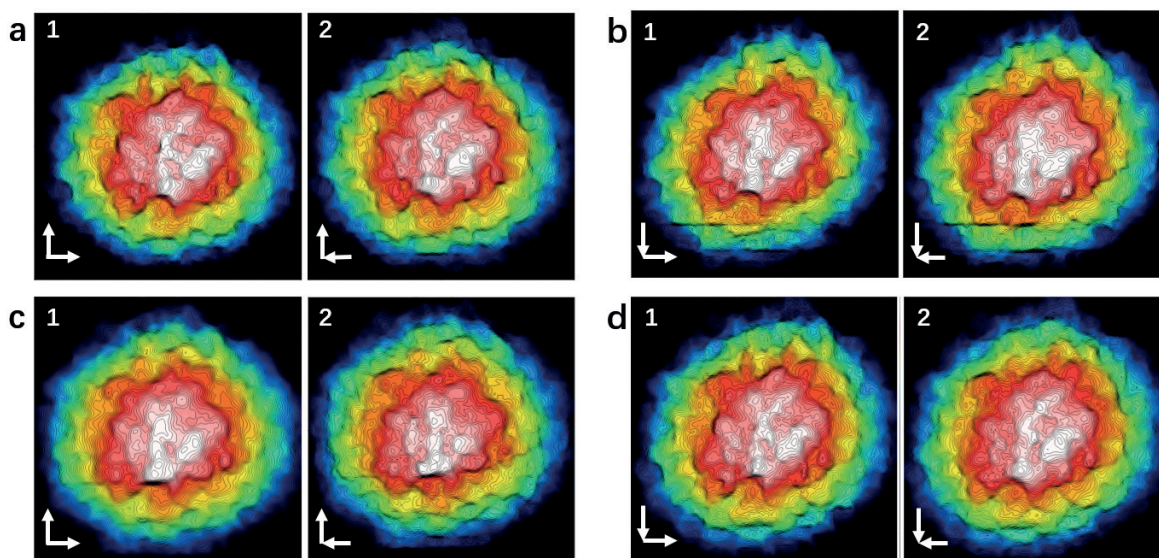
Supplementary Figure 2. Repeated scans of the same Ag_{374} cluster at LHe temperature. Scan directions are shown by the arrows. **(1)** and **(2)** in (**a,b**) refer to up (or down) images with opposite scanning directions (trace and retrace) marking at left bottom which were recorded simultaneously at a time scale of 7min. Bias voltage: -1.2V, 10pA. 5.0 $\times$ 5.0 nm. Images in **(b)** （**1,2**） were selected in calculation in Fig. 4 as the references.
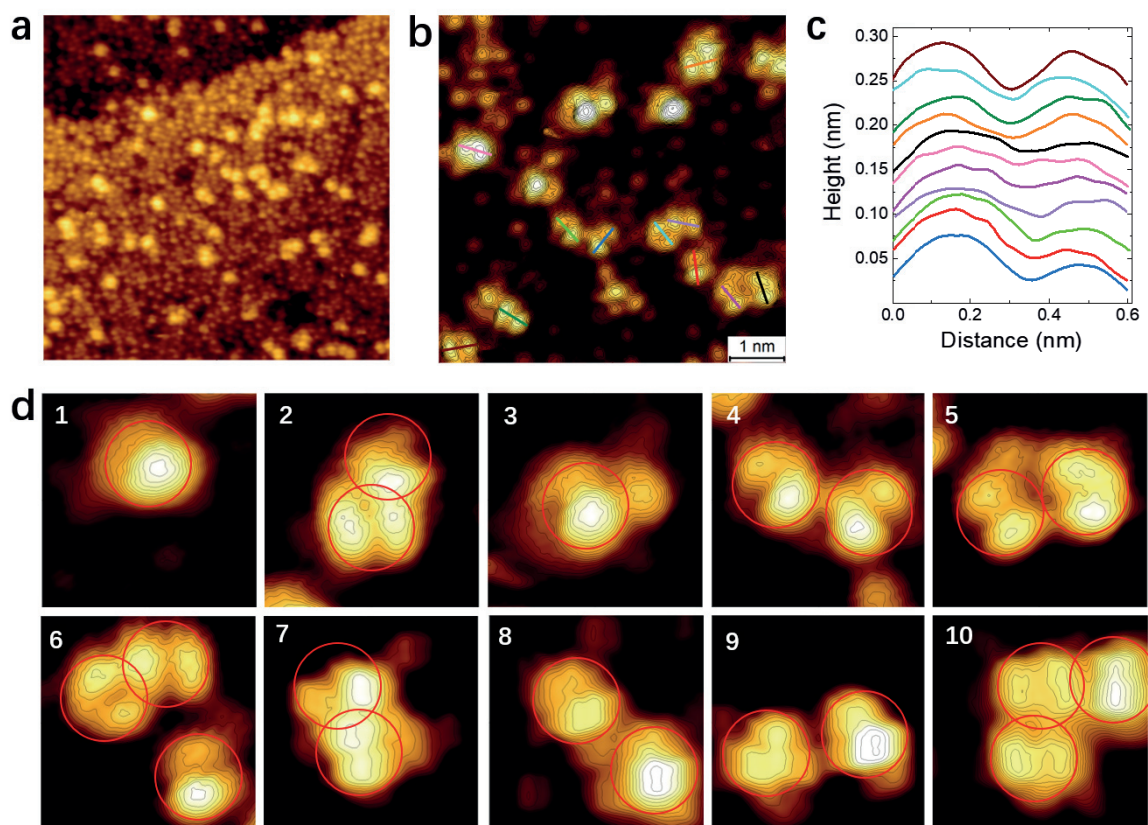
Supplementary Figure 3. STM images of the ligand database. (**a**) large scale image where TBBT molecules adsorbed on Au(111) surface with multilayers. Size: 21.5 x 21.5 nm^2, bias and setpoint current: 1.2 V, 40 pA. (**b**) Zoom-in image with bright individual TBBT molecules on the outmost surface. Size: 6.38 ×6.38 nm^2, bias and setpoint current: 1.2 V, 60 pA. (**c**) Height profile for colored lines marked in (**b**), which were shifted for good visual. (**d**) Part of TBBT image database, each red circle (0.6 nm diameter) indicates one TBBT molecule. All the images were digitally zoomed-in from large area images. Size, bias and setpoint current**: (1-6)** 1.51 × 1.51 nm, 1.2V, 60pA, **(7-10)** 1.50 × 1.50 nm, 1.0V, 30pA. Measured at LN$_2$ temperature.
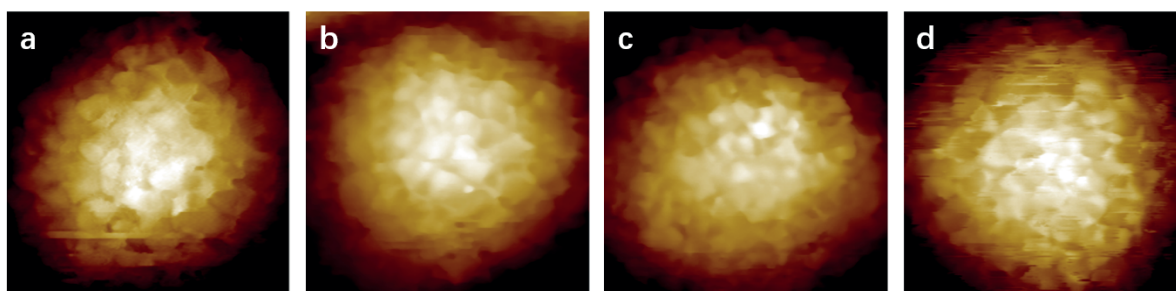
Supplementary Figure 4. High-resolution images of Ag$_{374}$ at LN$_2$ temperature. Four different clusters showing a similar degree of high sub-molecular resolution as shown in Fig. 3 of the main text at LHe temperature. Bias, setpoint current, scanning angle, size: **(a)** -1.4 V, 20 pA, 0°, 4.81 × 4.81 nm^2; **(b)** -1.5 V, 40 pA, 0°, 4.81 × 4.81 nm^2; **(c)** -1.5 V, 30 pA, 90°, 4.80 × 4.80 nm^2; **(d)** -1.2 V, 30 pA, 45°, 4.80 × 4.80 nm^2.


Supplementary Figure 5. Continuous scanning of the same Ag$_{374}$ cluster at LN$_2$ temperature. Scan directions are shown by the arrows. **(1)** and **(2)** in (**a-d**) refer to up (or down) images with opposite scanning directions (trace and retrace) marking at left bottom which were recorded simultaneously at a timescale of 8 min 45 sec. Size: 4.81 × 4.81 nm^2. Bias and setpoint current: -1.4 V, 20 pA.
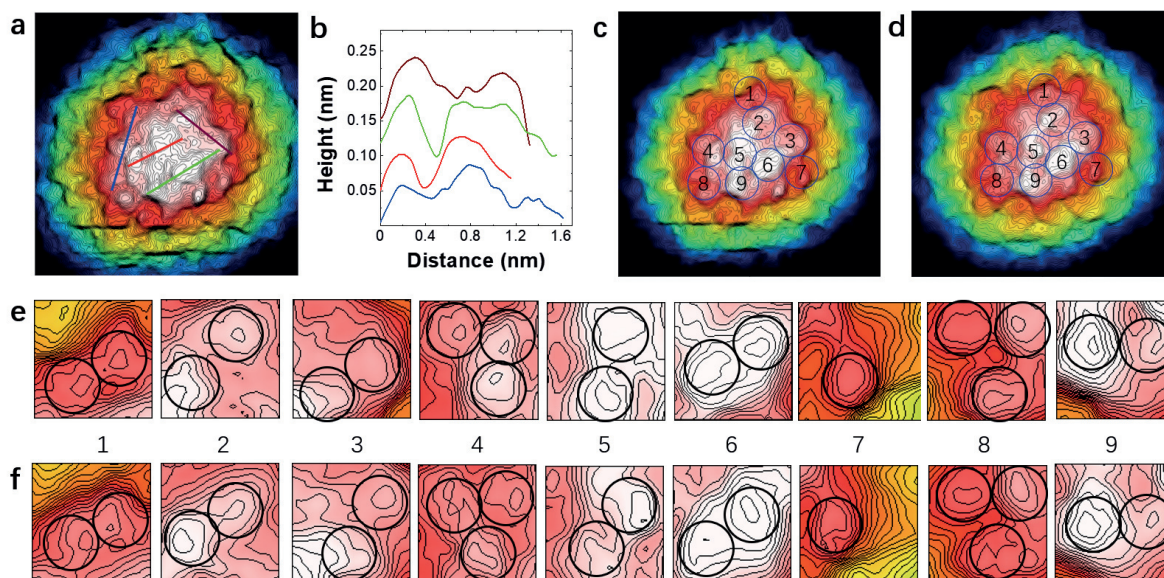
Supplementary Figure 6. High resolution image of Ag_{374} and the detailed ligand information. **(a)** the same as Fig. S5 b2. **(c)** and **(d)** same as Fig. S5 b2 and d2, respectively. **(b)** Height profile of colored lines marked in **(a).** The numbered circles 1-9 (diameter 0.6 nm) refer to local areas shown zoomed-in in **(e,f).** Size: 4.81×4.81 nm^2. Bias and setpoint current: -1.4 V, 20 pA. **(e,f)** blow-up of areas 1-9 from **(c)** and **(d),** respectively. Black circles denote local maxima.
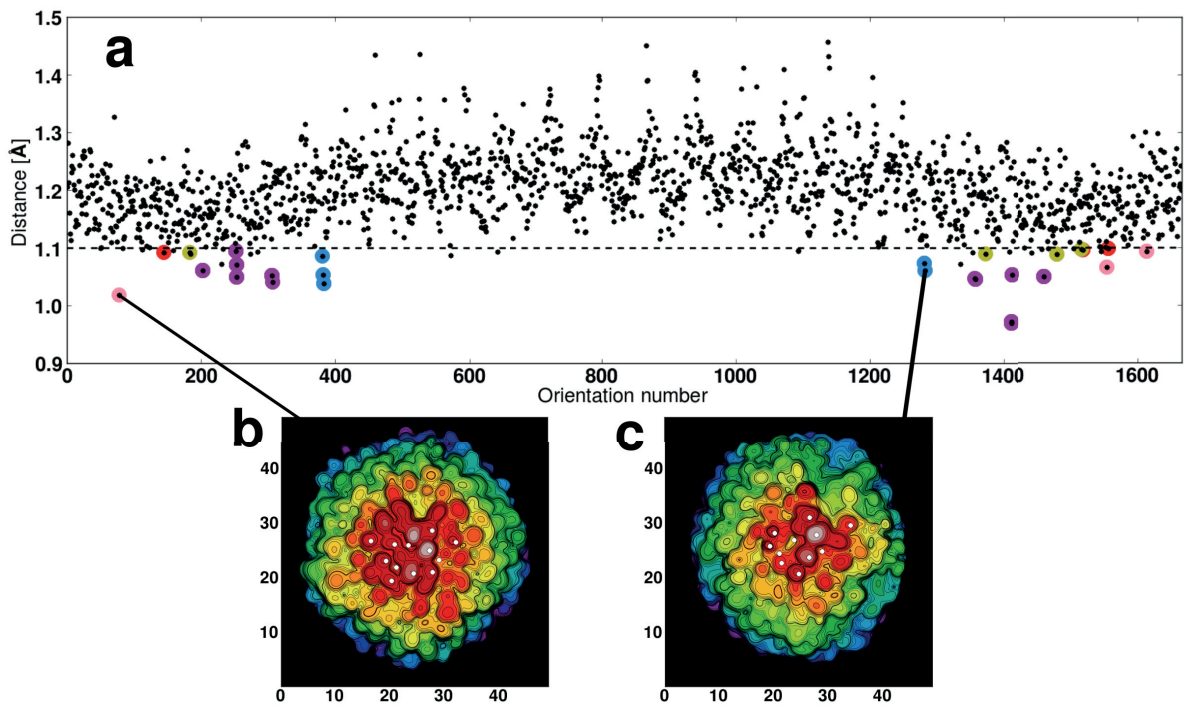
Supplementary Figure 7. The facial recognition of the retrace STM data (Fig. 4b). (**a**) Distance analysis for the STM image in figure 4b. Selected small-distance perspectives are connected with lines to the respective calculated STM images (**b**,**c**). The colors are the same as in figure 4d.
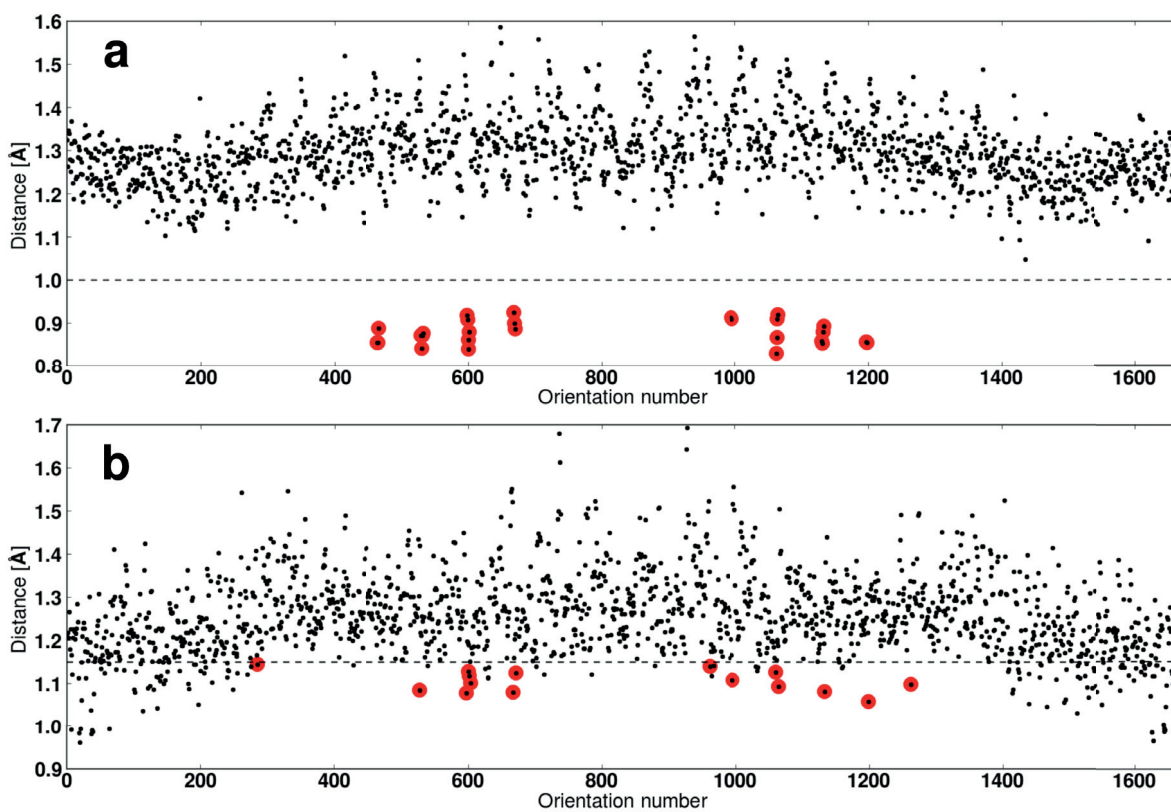
Supplementary Figure 8. A test for the facial recognition algorithm. (**a**) The reference set of coordinates was obtained by determining 10 maxima and 3 minima from the calculated STM image number 600, each of which were then randomly deviated in the range [0, 1] Å to a random direction. This set of points was compared to each calculated STM image. (**b**) Similar to (**a**) with the deviation range of [0, 2] Å. The red data points correspond to a perspective very close to the reference ie. orientation number 600.
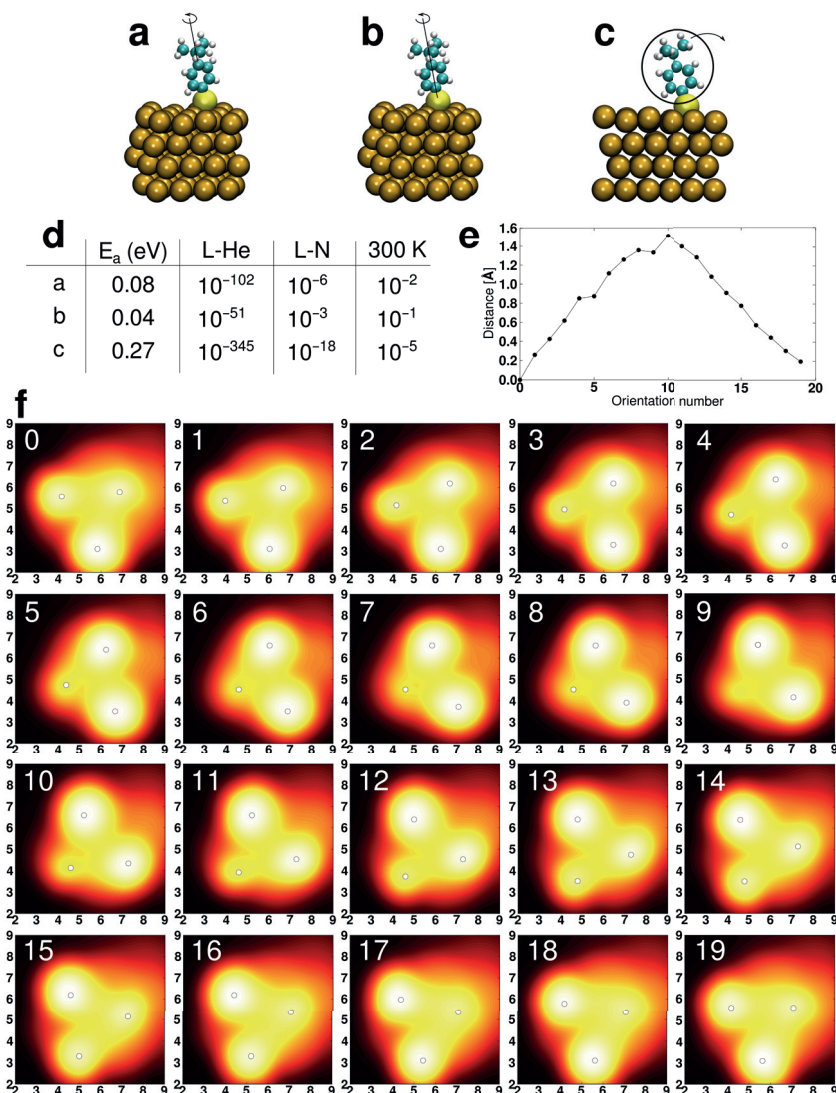
Supplementary Figure 9. Determining the rotational barriers and rotation probabilities of a single TBBT molecule absorbed onto bridge site of Au111 surface. (**a**,**b**,**c**) Illustrations of the different rotations that were considered: (**a**) Rotation of the tert-butyl head group. (**b**) Rotation of the thiol around the principal axis. (**c**) Rotation of the thiol around the axis parallel to the surface. (**d**) Rotational barriers and temperature-dependent Boltzmann factors in the Arrhenius equation for rotations a, b and c, referring to the corresponding images. The factors are shown for temperatures of liquid Helium, liquid Nitrogen and 300 K. (**e**) Results of the extremum coordinate comparison for 20 rotations of type **a** where the coordinates of the three maxima, shown for each state in the calculated STM images (**f**), are compared to the initial state (state number 0) without minimizing with respect to rotations. The maximum distance in (**e**) is 1.5 Å and the mean value 0.8 Å. X-Y scales in (**f**) are shown in Å.